EVOLUTION OF MULTI-OXIDANT AND HETEROGENEOUS CHEMISTRY IN BIOMASS BURNING PLUMES

by

Zachary C.J. Decker

B.A., New College of Florida, 2016

A thesis submitted to the

Faculty of the Graduate School of the

University of Colorado in partial fulfillment

of the requirement for the degree of

Doctor of Philosophy

Department of Chemistry

2021

Committee Members

Steven S. Brown

Ralph Jimenez

Emily V. Fischer

Gregory B. Rieker

Joost de Gouw

ABSTRACT

Decker, Zachary (Ph.D., Chemistry; Department of Chemistry)

Evolution of Multi-Oxidant and Heterogeneous Chemistry in Biomass Burning Plumes

Thesis directed by Professor Steven S. Brown

Biomass burning (BB) has an increasing impact on air quality as wildfires increase in the western U.S. Atmospheric chemistry of urban plumes suggests that during the daytime volatile organic compounds (VOCs) are oxidized by O_3 and the hydroxyl radical (OH), but during the nighttime by O_3 and the nitrate radical (NO_3). However, BB emissions are unique because they include large amounts of aerosols, BBVOCs, and nitrogen oxides (NO_x = NO + NO_2), creating a highly reactive environment.

We study the formation, competition, and fate of oxidants (NO_3, N_2O_5, O_3, and OH) reacting with BBVOCs using an analysis of daytime and nighttime BB plume observations. Toward this goal, we 1) developed a detailed BBVOC emissions and kinetics inventory, 2) conducted aircraft observations of wildfire plumes, 3) used a detailed 0-D chemical box model (0-DBM), and 4) created a novel model, the Gaussian Observational Model for Edge to Center Heterogeneity (GOMECH), to quantify chemical differences between plume center and edge.

We present 1) the first analysis of nighttime aircraft observations of an agricultural BB plume sampled by the NOAA WP-3D aircraft during the South East Nexus (SENEX 2013) campaign, 2) an analysis of daytime, sunset, and nighttime plumes sampled by the NOAA Twin Otter, and NASA DC-8 aircraft during the Fire Influence on Regional to Global Environments and Air Quality (FIREX-AQ 2019) campaign, and 3) the first analysis to quantify plume center to edge phenolic oxidation and nitrophenolic formation in BB plumes.

We show that, unlike urban plumes, >98% of NO_3 loss in BB plumes, even under sunlight, is due to BBVOCs at plume center. Reactions with phenolics dominate NO_3 reactions and NO_x loss overnight from the formation of nitrophenolics. Using GOMECH, we show that NO_3 chemistry may be a major, even dominant, source of nitrophenolics in daytime BB plumes, even on plume edges.

Overall, our work suggests that BB plumes are large sources of reactivity for OH, O_3 and NO_3 under sunlight and in the dark, unlike more conventional atmospheric chemistry that separates the role of OH and NO_3 into photochemistry and nighttime chemistry.

DEDICATION

For my Grandma, Joan Decker, a second mother to me.

ACKNOWLEDGEMENTS

With any thesis, or body of scientific work, there are numerous contributors that deserve to be mentioned. Including those who directly contributed to the science, and those who influenced the scientist. I will attempt to acknowledge them all here.

Thank you to the educators I had as a child, including Mrs. Ursrey, Mrs. Harvilchuck, Madame Redden, Mrs. Atkinson, and Mrs. Peteranecz. Not all of you are science teachers, but you assured I was well-rounded, and were generous with your time and friendship.

Thank you to New College of Florida, an institution that, no doubt, changed my view on the world and made me a better human-being all around – as it does to most of those who pass through. Specifically, thank you to the chemistry professors, Dr. Steven Shipman, Dr. Paul Scudder, and Dr. Suzanne Sherman. Your introduction to chemistry research, along with your patience and guidance, are why I am a chemist today.

Thank you to Dr. Fabien Goulay and Dr. Talitha Selby, for fighting for my placement at West Virginia University for a summer, and providing a wonderful independent research project and soft guidance in the world of Science. As well as Dr. Leonid Sheps, for providing the means and leadership that lead to my first peer-reviewed paper and my undergraduate thesis. Lastly, thank you to Prof. Hynes for your intuitive instruction, inspiring view on chemistry, and role-model type professorship.

Thank you to all of those at NOAA including Erin McDuffie, Dorothy Fibiger, Kyle Zarzana, Patrick Veres, Rebecca Washenfelder, Carrie Womack, Aaron Lamplugh, Carsten Warneke, Jessica Gilman, and Jane August. Your contributions are worth pages, but briefly: you were all always willing to help when I needed advice on a paper, Igor code, booking a plane ticket,

using a wrench, operating an instrument, navigating science, navigating people, and sometimes navigating the DSRC building.

A special thank you to Andy Neuman for continuous advice on the operation and intricacies of mass spectrometry; to Jeff Peischl for your company in the heat of Las Vegas, your amazing memory, your keen scientific advice, and of course your unmatched ability to edit papers; to Bill Dubé for your brilliant engineering advice and instruction, frank conversations, and warm friendship; to the trio of Ilann Bourgeois, Georgios Gkatzelis, and Matt Coggon for your academic advice, comradery and continued friendship; to Dimitrios Papanastasiou for your leadership in the investigation of chemical mechanisms and flow tube studies that were ended too soon, but more importantly for your friendship; to Mike Robinson for your friendship, conversations and shared struggle with the FIREX-AQ campaign and analysis; finally thank you to the Thornton group for generously allowing me to operate and use their I^- CIMS on the NOAA Twin Otter, from which the majority of this thesis originates.

A BIG thank you to my graduate thesis advisor Dr. Steven S. Brown. Thank you for fighting for my position at NOAA CSL even during a turbulent time when some questioned the permanence of the lab. As a result, I had an awesome graduate experience that many could only hope for. Through your guidance and excitement, you got me hooked on atmospheric chemistry, where I plan to stay and hope to make meaningful contributions.

Finally, thank you to those outside of academia who offered me an escape from research. Thank you to the Science Buffs team, for teaching me how to get excited about communicating science, as well as how to communicate science. Thank you to the CU Hiking Club, for fostering important friendships and many backcountry memories. Thank you to my family who made it clear you were proud, even if you weren't always sure what I was doing. Most important of all, thank

you to Katie for supporting my growth, and for growing with me as we tackled high school, college, and graduate school together as partners. Without you, I am not confident this dissertation would exist.

Acknowledgements for specific Chapters are as follows.

Chapter 3

Thank you to my coauthors who contributed both data and scientific insight: Kyle Zarzana, Matthew Coggon, Kyung-Eun Min, Ilana Pollack1, Thomas B. Ryerson, Jeff Peischl, Pete Edwards, William P. Dubé, Milos Z. Markovic1, James M. Roberts, Patrick R. Veres, Martin Graus1, Carsten Warneke, Joost de Gouw, Lindsay E. Hatch, Kelley C. Barsanti, and Steven S. Brown. As well as Charles A. Brock for aerosol surface area measurements**.**

Chapter 4

Thank you to the CIRES Graduate Student Research Award Program for one year of funding, during which time I participated in the FIREX-AQ campaign that produced the data for Chapters 4-6. Another Thank you to the coauthors who contributed both data and scientific insight: Michael A. Robinson, Kelley C. Barsanti, Ilann Bourgeois, Matthew M. Coggon, Joshua P. DiGangi, Glenn S. Diskin, Frank M. Flocke, Alessandro Franchin, Carley D. Fredrickson, Samuel R. Hall, Hannah Halliday, Christopher D. Holmes, L. Gregory Huey, Young Ro Lee, Jakob Lindaas, Ann M. Middlebrook, Denise D. Montzka, Richard Moore, J. Andrew Neuman, John B. Nowak, Brett B. Palm, Jeff Peischl, Pamela S. Rickly, Andrew W. Rollins, Thomas B. Ryerson, Rebecca H. Schwantes, Lee Thornhill, Joel A. Thornton, Geoffrey S. Tyndall, Kirk Ullmann, Paul Van Rooy, Patrick R. Veres, Rebecca A. Washenfelder, Andrew J. Weinheimer, Elizabeth Wiggins, Edward Winstead, Caroline Womack, and Steven S. Brown. Further, thank you to Alan

Fried, Dirk Richter, Jim Walega, and Petter Weibring for use of their HCHO measurements. A big thank you to all of those who helped organize and participated in the 2019 FIREX-AQ field campaign, specifically the NOAA Aircraft Operations, including Francisco Fuenmayor, Joe Greene, Conor Maginn, Rob Miletic, Joshua Rannenberg, and David Reymore. Carley D. Fredrickson, Brett B. Palm, and Joel A. Thornton were supported by NOAA OAR Climate Program Office Award Number NA17OAR4310012.

Chapter 5

Another Thank you to the coauthors who contributed both data and scientific insight: Siyuan Wang, Ilann Bourgeois, Pedro Campuzano Jost, Matthew M. Coggon, Joshua P. DiGangi, Glenn S. Diskin, Frank M. Flocke, Alessandro Franchin, Carley D. Fredrickson, Georgios I. Gkatzelis, Samuel R. Hall, Hannah Halliday, Katherine Hayden, Christopher D. Holmes, L. Gregory Huey, Jose L. Jimenez, Young Ro Lee, Jakob Lindaas, Ann M. Middlebrook, Denise D. Montzka, J. Andrew Neuman, John B. Nowak, Demetrios Pagonis, Brett B. Palm, Jeff Peischl, Felix Piel, Pamela S. Rickly, Michael A. Robinson, Andrew W. Rollins, Thomas B. Ryerson, Kanako Sekimoto, Joel A. Thornton, Geoff S. Tyndall, Kirk Ullmann, Patrick R. Veres, Carsten Warneke, Rebecca A. Washenfelder, Andrew J. Weinheimer, Armin Wisthaler, Caroline Womack, Steven S. Brown. Further, thank you to Reed Meyerson for his assistance in deriving an early version of GOMECH and Charlie Edelson for his thoughtful conversation on the intricacies of multivariable regression. The UIBK PTR-ToF-MS instrument was partly funded by the Austrian Federal Ministry for Transport, Innovation and Technology (bmvit) through the Austrian Space Applications Programme (ASAP) of the Austrian Research Promotion Agency (FFG). Instrumental support came from Ionicon Analytik; Tomas Mikoviny provided technical assistance. Laura Tomsche and John Nowak supported the UIBK PTR-ToF-MS team. Felix Piel received

funding from the European Union's Horizon 2020 research and innovation program under grant agreement no. 674911 (IMPACT EU ITN). The Jimenez group (CU Boulder) acknowledges funding from NASA grant 80NSSC18K0630. The Thornton group (Univ. Washington) was supported by grants from the National Oceanic and Atmospheric Administration (NA17OAR4310012) and the National Science Foundation (AGS 1652688)

Table of Contents

LIST OF FIGURES

LIST OF TABLES

LIST OF PUBLICATIONS

First Author Publications

5. Zachary C.J. Decker, …., Brown S.S. $ClNO_2$ Yields and Heterogeneous N_2O_5 Uptake from Aircraft Measurements of Western U.S. Wildfire Plumes – *in preparation*

4. Zachary C.J. Decker, Siyuan Wang, Ilann Bourgeois, Pedro Campuzano Jost, Matthew M. Coggon, Joshua P. DiGangi, Glenn S. Diskin, Frank M. Flocke, Alessandro Franchin, Carley D. Fredrickson, Georgios I. Gkatzelis, Samuel R. Hall, Hannah Halliday, Katherine Hayden, Christopher D. Holmes, L. Gregory Huey, Jose L. Jimenez, Young Ro Lee, Jakob Lindaas, Ann M. Middlebrook, Denise D. Montzka, J. Andrew Neuman, John B. Nowak, Demetrios Pagonis, Brett B. Palm, Jeff Peischl, Felix Piel, Pamela S. Rickly, Michael A. Robinson, Andrew W. Rollins, Thomas B. Ryerson, Kanako Sekimoto, Joel A. Thornton, Geoff S. Tyndall, Kirk Ullmann, Patrick R. Veres, Carsten Warneke, Rebecca A. Washenfelder, Andrew J. Weinheimer, Armin Wisthaler, Caroline Womack, Steven S. Brown. A Novel Analysis to Quantify Plume Crosswind Heterogeneity Applied to Biomass Burning Smoke – *in review*

3. Zachary C.J. Decker, Michael A. Robinson, Kelley C. Barsanti, Ilann Bourgeois, Matthew M. Coggon, Joshua P. DiGangi, Glenn S. Diskin, Frank M. Flocke, Alessandro Franchin, Carley D. Fredrickson, Samuel R. Hall, Hannah Halliday, Christopher D. Holmes, L. Gregory Huey, Young Ro Lee, Jakob Lindaas, Ann M. Middlebrook, Denise D. Montzka, Richard Moore, J. Andrew Neuman, John B. Nowak, Brett B. Palm, Jeff Peischl, Pamela S. Rickly, Andrew W. Rollins, Thomas B. Ryerson, Rebecca H. Schwantes, Lee Thornhill, Joel A. Thornton, Geoffrey S. Tyndall, Kirk Ullmann, Paul Van Rooy, Patrick R. Veres, Rebecca A. Washenfelder, Andrew J. Weinheimer, Elizabeth Wiggins, Edward Winstead, Caroline Womack, and Steven S. Brown. Nighttime and Daytime Dark Oxidation Chemistry in Wildfire Plumes: An Observation and Model Analysis of FIREX-AQ Aircraft Data. *Atmos. Chem. Phys, Discussions* doi:10.5194/acp-2021-267 – *in review*

2. Zachary C. J. Decker, Kyle J. Zarzana, Matthew Coggon, Kyung-Eun Min, Ilana Pollack, Thomas B. Ryerson, Jeff Peischl, Pete Edwards, William P. Dubé, Milos Z. Markovic, James M. Roberts, Patrick R. Veres, Martin Graus, Carsten Warneke, Joost de Gouw, Lindsay E. Hatch, Kelley C. Barsanti, Steven S. Brown, Nighttime chemical transformation in biomass burning plumes: a box model analysis initialized with aircraft observations. *Environ. Sci. Technol.* 2019, 53, 5, 2529-2538. doi:10.1021/acs.est.8b05359

1. Zachary. C. J. Decker, Kendrew, Au, Luc, Vereecken, and Leonid Sheps. Direct Experimental Probing and Theoretical Analysis of the Reaction between the Simplest Criegee Intermediate CH_2OO and Isoprene. *Phys. Chem. Chem. Phys.,* 2017,19, 8541-8551 doi: 10.1039/C6CP08602K

Co-authored Publications

4. Michael A. Robinson, **Zachary C.J. Decker**, Kelley C. Barsanti, Matthew M. Coggon, Frank M. Flocke, Alessandro Franchin, Carley D. Fredrickson, Jessica B. Gilman, Georgios Gkatzelis, Christopher Holmes, Aaron Lamplugh, Avi Lavi, Ann M. Middlebrook, Denise M. Montzka, Brett B. Palm, Bradley Pierce, Rebecca H. Schwantes, Geoffrey S. Tyndall, Joel A. Thornton, Paul Van Rooy, Carsten Warneke, Andrew J. Weinheimer, and Steven S. Brown. Variability and Diurnal Dependence of Ozone Photochemistry in Western Wildfire Plumes

3. Li Zhang, Meiyun Lin, Andrew O. Langford, Larry W. Horowitz, Christoph J. Senff, Elizabeth Klovenski, Yuxuan Wang, Raul J. Alvarez, Irina Petropavlovskikh, Patrick Cullis, Chance W. Sterling, Jeff Peischl, Thomas B. Ryerson, Steven S. Brown, **Zachary C. J. Decker**, Guillaume Kirgis, and Stephen Conley. Characterizing sources of high surface ozone events in the southwestern U.S. with intensive field measurements and two global models. *Atmos. Chem. Phys*. doi:10.5194/acp-20-10379-2020

2. Daniel Stone, Kendrew Au, Samantha Sime, Diogo J. Medeiros, Mark Blitz, Paul W. Seakins, **Zachary C.J. Decker** and Leonid Sheps Unimolecular decomposition kinetics of the stabilised Criegee intermediates CH_2OO and CD_2OO *Phys. Chem. Chem. Phys.*, 2018,20, 24940-24954 doi: 10.1039/c8cp05332d

1. Caroline C. Womack, J. Andrew Neuman, Patrick R. Veres, Scott J. Eilerman, Charles A. Brock, **Zachary C. J. Decker**, Kyle J. Zarzana, William P. Dube, Robert J. Wild, Paul J. Wooldridge, Ronald C. Cohen, and Steven S. Brown. Evaluation of the accuracy of thermal dissociation CRDS and LIF techniques for atmospheric measurement of reactive nitrogen species. *Atmos. Meas. Tech.,* 10, 1911–1926, 2017. doi:10.5194/amt-10-1911-2017

Chapter 1: Introduction to Wildfire Chemistry

1.1 Wildfires are Growing

It is well known that biomass burning (BB), including wildfires and agricultural burning, can have large impacts on air quality at local, regional and global scales (Jaffe et al., 2020). The relative impact and importance of wildfire smoke on air quality in the western U.S. is increasing with decreasing anthropogenic volatile organic compound (VOC) and nitrogen oxide (NO_x = NO + NO_2) emissions (Bishop and Haugen, 2018; McClure and Jaffe, 2018; O'Dell et al., 2019; Silvern et al., 2019; Warneke et al., 2012; Xing et al., 2015). This increase is compounded by growing wildfire emissions caused by anthropogenic influences such as human-caused climate change and past wildland management practices. Twentieth century suppression of western U.S. wildfires has led to increased fuel loadings and thus fire potential (Higuera et al., 2015; Marlon et al., 2012; Parks et al., 2015). A warmer and drier climate in the western U.S. resulting from human-caused climate change has exacerbated fire potential and has resulted in an increase in the frequency of large wildfires since the 1980s (Abatzoglou and Williams, 2016; Balch et al., 2017; Barbero et al., 2015; Brey and Fischer, 2016; Dennison et al., 2014; Marlon et al., 2012; Westerling et al., 2006; Westerling, 2016; Williams et al., 2019). Further, there is consensus that increased smoke exposure in the western U.S. is significantly associated with increased respiratory morbidity and risk of cardiovascular disease (Liu et al., 2015). Recent studies have associated smoke exposure with respiratory infections such as influenzas and SARS-CoV-2 (Navarro et al., 2021).

1.2 Atmospheric Chemistry of Biomass Burning

Wildfires emit NO_x, nitrous acid (HONO), biomass burning VOCs (BBVOCs) and particulate matter (PM) that evolve chemically on a range of time scales, from seconds to weeks downwind (Akagi et al., 2011; Andreae and Merlet, 2001b; Decker et al., 2019; Hatch et al., 2015, 2017; Koss et al., 2018; Palm et al., 2020). These emissions and their chemical products influence air quality through ozone (O_3) production, emitted PM, and secondary organic aerosol formation (SOA) (Brey et al., 2018; Brey and Fischer, 2016; Jaffe et al., 2020; Jaffe and Wigder, 2012; Lu et al., 2016; Palm et al., 2020; Phuleria et al., 2005). However, the evolution of the smoke downwind is influenced by several variables such as fuel type, burn conditions, moisture content, nitrogen content, meteorology, and time of day.

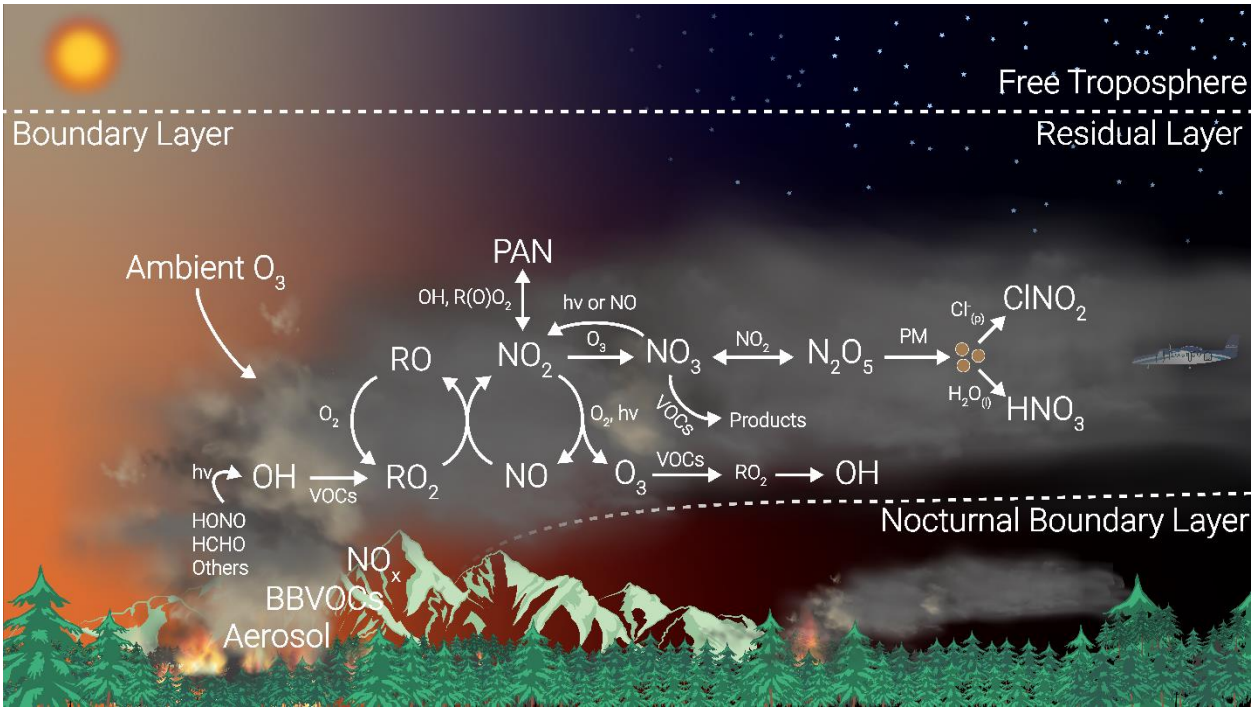

Figure 1.1: Schematic of BB chemistry. Boundary layer dynamics are illustrated by dashed lines.

Like most atmospheric oxidation processes, the oxidation of BBVOCs is influenced by three key atmospheric oxidants: O_3, the hydroxyl radical (OH), and the nitrate radical (NO_3),

highlighted in Figure 1.1. The amount of each oxidant present in a plume is influenced by emissions of NO_x, plume mixing with background air, and the amount of sunlight that penetrates a plume.

The OH radical is typically considered to be a daytime oxidant because it is formed through the photolysis of compounds such as formaldehyde (HCHO) and HONO (Peng et al., 2020; Trentmann et al., 2003). Indeed, the photolysis of HONO was found to be the dominant source of HO_x (= OH + HO_2) in the first three hours of aging for wildfires sampled in the western U.S. (Peng et al., 2020).

$$HONO + hv \rightarrow OH + NO \quad \text{R1.1}$$

However, at night, or in optically thick plumes, OH can also be formed by the ozonolysis of unsaturated hydrocarbons, or alkenes, which form Criegee intermediates and subsequently decompose (Khan et al., 2018). The OH radical can react with BBVOCs to from RO_2, or secondary products.

$$RO_2\bullet \rightarrow OH + RO\bullet \quad \text{R1.2}$$

$$OH + VOC \rightarrow Products \quad \text{R1.3}$$

Ozone formation in the atmosphere typically occurs through the photolysis of NO_2, a prominent emission of BB. BB plumes also contain large amounts of NO, which reacts quickly with O_3. Under sufficient sunlight, NO is in a rapid cycle with NO_2 photolysis and regeneration of O_3 in which odd oxygen, $O_x = NO_2 + O_3$, is conserved.

$$NO_2 + hv \rightarrow NO + O(^3P) \quad \text{R1.4}$$

$$O(^3P) + O_2 \rightarrow O_3 \quad \text{R1.5}$$

$$NO + O_3 \rightarrow NO_2 + O_2 \quad \text{R1.6}$$

Therefore, in young BB plumes O_3 is often reduced in the plume-center compared to the ambient air outside of the plume. On the edge of a plume, O_3 can be greater than plume-center due to ambient O_3 entrainment and photochemical O_3 production. In aged BB plumes, when NO is depleted, O_3 is often enhanced throughout the plume relative to ambient O_3. Lastly, both the entrainment of atmospheric background levels of O_3 and photochemical O_3 production within a smoke plume, provide O_3 for oxidation of BBVOCs (Jaffe and Wigder, 2012).

$$O_3 + \text{BBVOC} \rightarrow \text{products} \qquad \text{R1.7}$$

In comparison to O_3 and the OH radical, the role of NO_3 oxidation in BB plumes is variable. NO_3 is produced within a smoke plume by the gas-phase reaction of O_3 and NO_2 (R1.8) and is a precursor for N_2O_5 (R1.9), which may serve as a NO_x reservoir (Brown and Stutz, 2012). N_2O_5 may undergo heterogeneous uptake to form $ClNO_2$ and HNO_3 according to the branching ratio ϕ (R1.10) (Chang et al., 2011; McDuffie et al., 2018). NO_3 can also be directly taken up by aerosol (R1.11) or react with BBVOCs (R1.12).

$$NO_2 + O_3 \rightarrow NO_3 + O_2 \qquad \text{R1.8}$$
$$NO_3 + NO_2 \rightleftharpoons N_2O_5 \qquad \text{R1.9}$$
$$N_2O_5(g) + \text{aerosol} \rightarrow \phi ClNO_2 + (2 - \phi)HNO_3 \qquad \text{R1.10}$$
$$NO_3 + \text{aerosol} \rightarrow \text{products} \qquad \text{R1.11}$$
$$NO_3 + \text{BBVOCs} \rightarrow \text{products} \qquad \text{R1.12}$$

In urban plumes during daytime, NO_3 is rapidly destroyed by photolysis (R1.13 & R1.14) and even more rapidly by reaction with NO (R1.15, τ<10 s) (Brown and Stutz, 2012; Wayne et al., 1991).

$$NO_3 + h\nu \rightarrow NO_2 + O(^3P) \qquad \text{R1.13}$$

$NO_3 + hv \rightarrow NO + O_2$ R1.14

$NO_3 + NO \rightarrow 2NO_2$ R1.15

Therefore, the role of NO_3 in daytime BB plumes might be expected to be small and limited to the darkest parts of a plume. Despite the potential for rapid loss of NO_3 from sunlight and NO, wildfire plumes provide a unique environment which promotes NO_3 chemistry. Wildfire emissions typically peak in the mid-afternoon to evening, and continue to emit smoke into the night (Giglio, 2007; Li et al., 2019). Furthermore, large smoke plumes can be optically thick, with little photolysis at their center. This means that most smoke plumes will undergo dark oxidation processes during some, if not all, of their transport (Kodros et al., 2020).

The fate of NO_3 and N_2O_5 has important implication for O_3 production the following day. If N_2O_5 persists throughout the night, N_2O_5 thermal dissociation and subsequent photolysis of NO_3, after sunrise the next day, will provide NO_x and thus contribute to photochemical O_3 production. However, if N_2O_5 reacts heterogeneously with aerosol to form $ClNO_2$, then the photo-labile $ClNO_2$ will dissociate to form NO_2 and Cl•, which can further contribute to oxidation of BBVOCs and O_3 production the following morning. Understanding the potential for O_3 production due to BB emissions is important because O_3 is considered a threat to health and the environment and is a criteria pollutant designated by the U.S. EPA (EPA, 2021). For example O_3 has been linked to increased mortality rates (e.g. Bell et al., 2006), is a potent green-house gas, and is responsible for over 10 billion dollars in annual crop loss (e.g. Avnery et al., 2011).

That fate of O_3, OH, and NO_3 will depend on the BB emissions, which are highly variable. Laboratory burns have worked to catalog biomass burning emissions for a multitude of fuel types (Hatch et al., 2015; Koss et al., 2018; Stockwell et al., 2014; Veres et al., 2010). Among others,

these emissions include saturated and unsaturated hydrocarbons, aromatics, and oxygenated aromatics with a distribution that changes based on fuel type (Hatch et al., 2017, 2018; Koss et al., 2018) and burn temperature (Sekimoto et al., 2018).

As we show later, the suite of BBVOCs emitted from BB are highly reactive, especially toward NO_3. This is the result of elevated concentrations of several highly reactive BBVOCs within the plume. Specifically, directly emitted aromatic alcohols (phenolics) react with NO_3 at near the gas-kinetic limit to form nitrophenolics, a subset of nitroaromatics, and secondary organic aerosol (Finewax et al., 2018; Lauraguais et al., 2014; Liu et al., 2019; Xie et al., 2017). Nitrophenolics absorb strongly in the ultraviolet and visible regions of the solar spectrum, and are expected to significantly contribute to brown carbon (BrC) absorption (Palm et al., 2020; Selimovic et al., 2020). Phenolic reactions with OH in the presence of NO_x also form nitrophenolics, but at one third the yield (Finewax et al., 2018). Therefore, understanding BBVOC reactivity, oxidant competition, and chemical fate of both is imperative to understanding the air quality impacts of BB smoke downwind.

1.3 Research Approach

Here, we outline our approach to sampling and studying the multi-oxidant and heterogeneous chemical evolution of both wildfire and agricultural burning plumes. To better understand the role each oxidant plays in the chemical evolution of BB plumes downwind, and within a plume, we use four main methodologies 1) aircraft observations of agricultural and wildfire plumes both day and night, 2) an emissions database of fire emissions from previous lab studies, including bimolecular rate coefficients, 3) observationally constrained and chemically detailed 0-D box models, and 4) a novel quantitative method, the Gaussian Observational Model

for Center to Edge Heterogeneity (GOMECH), to study plume center vs plume edge chemical heterogeneity in plumes.

Dark chemistry may occur in lofted BB plumes, or in smoke that subsides to lower altitudes (Figure 1.1). Boundary layer dynamics may cause concentrated and potentially inactive chemistry near the ground surface (Brown et al., 2017; Brown and Stutz, 2012), although these dynamics are complex and may lead to a range of chemical regimes. Aircraft sampling captures dark chemistry in lofted plumes, which has not previously been studied.

However, aircraft studies of BB plumes, especially after sunset, are limited. More data must be collected of both wildfire and agricultural burning plumes during both day and night. These observations require measurements of a large suite of BBVOCs, as well as O_3, NO_x, CO, and aerosol properties. A combination of both Iodide chemical ionization mass spectrometry (I^- CIMS) and proton transfer reaction mass spectrometry (PTR MS) provide for measurements of oxygenated and aliphatic semi-volatile and volatile BBVOCs, which are often highly reactive.

Due to safety and logistical limits, aircraft can only sample smoke sufficiently far from the fire. Further, aircraft sampling of nighttime smoke is difficult to achieve because of low visibility in potentially mountainous terrain and complex meteorology, with variable windspeeds that result in plume structures that may be difficult to predict. Therefore, we use the aircraft observations of young smoke to initialize and constrain a chemically detailed 0-D box model that simulates plume chemistry from the time of emission, through the night, until sunrise the next morning.

To accurately model BB plume chemistry, knowledge of the emissions and chemical reactions are required. We construct a detailed emissions database of the most reactive 302 BBVOCs sampled during previous lab studies (Hatch et al., 2017; Koss et al., 2018) of BB

emissions, combined with bimolecular rate coefficients for reactions with NO_3, O_3, and OH. We use our database to both study reactivity of BB plumes as well as initiate our box models.

Even so, our box model analysis is a plume-center Lagrangian model. Therefore, it does not capture chemistry occurring at plume edges. In order to understand and quantify the chemical difference between the plume center and edge, we developed a novel methodology, the Gaussian Observational Model for Center to Edge Heterogeneity (GOMECH), to model chemical plume structures relative to a plume tracer compound. CO is emitted at high concentration from BB, is readily and accurately measured, and is inert relative to more reactive VOC and nitrogen compounds. Though, GOMECH is general and can be applied to any type of plume. We use GOMECH to explore the spatial relationship of NO_3 and OH as well as their oxidation of phenolic compounds, and subsequent formation of nitrophenolics.

1.4 Thesis Overview

In this thesis, the results from two field campaigns that observed both agricultural burning and wildfire plume emissions both day and night are analyzed. The chapters are as follows:

Chapter 2: Methodologies

In this chapter the methods common to multiple chapters are described. These include 1) common analysis metrics of BB and NO_3 chemistry, 2) a 0-D Detailed Chemical Box Model coupled with the master chemical mechanism and updated phenolic mechanisms, 3) a detailed BB chemical emissions and kinetics inventory, and 4) observations made by the NOAA WP-3D during the SENEX 2013 campaign, and the NASA DC-8 and NOAA Twin Otter aircraft during the FIREX-AQ campaign.

Chapter 3: Nighttime Chemical Transformation in Biomass Burning Plumes: A Box Model Analysis Initialized with Aircraft Observations

While the daytime photochemistry of BB emissions has been studied in some detail, there has been little focus on nighttime reactions despite the potential for substantial oxidative and heterogeneous chemistry. Here, we present the first analysis of nighttime aircraft intercepts of agricultural BB plumes using observations from the NOAA WP-3D aircraft during the 2013 Southeast Nexus (SENEX) campaign. We use these observations in conjunction with detailed chemical box modeling to investigate the formation and fate of oxidants (NO_3, N_2O_5, O_3, and OH) and BBVOCs, using emissions representative of agricultural burns (rice straw) and western wildfires (ponderosa pine).

Chapter 4: Nighttime and Daytime Dark Oxidation Chemistry in Wildfire Plumes: An Observation and Model Analysis of FIREX-AQ Aircraft Data

The impact of BB smoke, including wildfires, on regional air quality depends on emissions and chemistry that varies depending on the time of day. This includes the oxidation of emitted BBVOCs by OH, NO_3, and O_3. This chapter focuses on the transition between daytime and nighttime oxidation, which has significant implications for the formation of secondary pollutants and loss of NO_x and has been understudied. We present wildfire plume observations made during FIREX-AQ (Fire Influence on Regional to Global Environments and Air Quality), a field campaign involving multiple aircraft, ground, satellite, and mobile platforms that took place in the United States in the summer of 2019 to study both wildfire and agricultural burning emissions and atmospheric chemistry. We use observations from two research aircraft, the NASA DC-8 and the

NOAA Twin Otter, with a detailed chemical box model, including updated phenolic mechanisms, to analyze smoke sampled during mid-day, sunset, and nighttime.

Chapter 5: A Novel Analysis to Quantify Plume Crosswind Heterogeneity Applied to Phenolic Oxidation in Biomass Burning Smoke.

BB plumes undergo chemical evolution that is influenced by sunlight and background air entrainment in the horizontal crosswind dimension. We present a novel method, termed the Gaussian Observational Model for Edge to Center Heterogeneity (GOMECH), to quantitatively describe the aircraft observed horizontal chemical structure of plumes as a function of a conserved tracer (CO). GOMECH can be used to fit observations and provides metrics for plume width and center. We demonstrate GOMECH with an analysis of plumes sampled during FIREX-AQ. We investigate the oxidation of phenolics by the OH radical (by analysis of nitrous acid and maleic anhydride) and the nitrate radical (NO_3, by analysis of NO_3 production) to form nitrophenolics, a source of secondary organic aerosol in BB plumes. In a campaign-wide analysis and case study of large plumes, our model suggests phenolic loss is most associated with OH, but nitrophenolic formation is most associated with NO_3. This result is further corroborated by an LES model of an observed large plume, indicating the majority of nitrocatechol is formed via NO_3 on plume edges while OH controls formation at plume center.

Chapter 6: Summary and Conclusions.

Chapter 2: Research Methods

2.1 Common Analysis Metrics

We report our observations for each species (X) relative to CO in the form of normalized excess missing ratios (NEMR) (Yokelson et al., 2013).

$$\mathrm{NEMR} = \frac{\mathrm{X_{Plume} - X_{Background}\ (ppbv)}}{\mathrm{CO_{Plume} - CO_{Background}\ (ppmv)}} \quad \text{E2.1}$$

Instantaneous reactivity, referred to simply as reactivity here on, is used as a simplified metric to predict the competition of reactions between oxidant and BBVOC

$$k_X = \sum_i k_{X+BBVOC_i}[BBVOC_i] \quad \text{E2.2}$$

where, $k_{X+BBVOC}$ is a bimolecular rate coefficient for the reaction of X + BBVOC (where X is O_3, NO_3 or OH) and k_X is an instantaneous first order rate coefficient.

While reactivity is a useful metric to predict the competition between reactions, it does not account for oxidant concentration, which can vary widely depending on photolysis rates, emissions, and competing oxidants. The oxidation rate is related to reactivity through the oxidant concentration as shown below

$$R_x = \sum k_{X+BBVOC_i}[BBVOC_i][X] = k_x[X] \quad \text{E2.3}$$

where R_x is the BBVOC oxidation rate for a BBVOC + X.

2.1.1 Common NO_3 Analysis Metrics

The NO_3 production rate, $P(NO_3)$, is the instantaneous source of NO_3 from the reaction of NO_2 with O_3 and is given in E2.4 (Brown and Stutz, 2012).

$$P(NO_3) = k_{NO_3}[NO_2][O_3] \quad \text{E2.4}$$

The NO_3 + N_2O_5 lifetime (τ) is the ratio of NO_3 and N_2O_5 concentration to the NO_3 production rate (E2.5) (Brown, 2003). The summed lifetime is useful because NO_3 and N_2O_5 reach an equilibrium state in which interconversion between the two species is typically more rapid than the individual sink reactions for either, such that they can be regarded as a sum.

$$\tau(NO_3 + N_2O_5) = \frac{NO_3 + N_2O_5}{P(NO_3)} \quad \text{E2.5}$$

The total heterogeneous NO_3 loss (i.e., reaction by aerosol uptake) is given as the sum of the 1st-order NO_3 and N_2O_5 heterogeneous rate coefficients. By assuming steady state (Brown et al., 2003) for both NO_3 and N_2O_5, we estimate the total heterogeneous uptake, and therefore NO_3 heterogeneous reactivity, as

$$k_{NO_3}^{het} = K_{eq}[NO_2]k_{uptake\ N_2O_5} + k_{uptake\ NO_3} \quad \text{E2.6}$$

where $k_{NO_3}^{het}$ is a first order rate coefficient, K_{eq} is the equilibrium constant between NO_3 and N_2O_5 (R1.9), and $k_{uptake\ x}$ is the first order rate coefficient for N_2O_5 or NO_3 heterogeneous uptake expressed below.

$$k_{uptake\ x} = \frac{\gamma \cdot \bar{c} \cdot SA}{4} \quad \text{E2.7}$$

Here, γ is the uptake coefficient, $\bar{c}$ is the mean molecular speed, and SA is the aerosol surface area. The expression in E2.7 is approximate in the limit of small uptake coefficient and particle diameter (Dentener and Crutzen, 1993). Calculations use uptake coefficients of $\gamma_{N_2O_5} = 10^{-2}$ for N_2O_5 (Chang et al., 2011) and $\gamma_{NO_3} = 10^{-3}$ for NO_3 (Brown and Stutz, 2012; McDuffie et al., 2018). However, γ_{NO_3} values have a potentially wide range, and therefore we include calculations with $\gamma_{NO_3} = 1$, even though this is an unrealistic upper limit, as discussed in Chapters 3 and 4, but find similar results when using $\gamma_{NO_3} = 10^{-3}$ (Brown and Stutz, 2012).

2.2 0-D Detailed Chemical Box Model

Box modeling was performed using the Framework for 0-D Atmospheric Modeling (F0AM). Chemical mechanisms were adopted from the MCM (v3.3.1, Bloss et al., 2005; Jenkin et al., 1997, 2003, 2012, 2015), via website: http://mcm.york.ac.uk) along with additional mechanisms specific to each analysis, which are explicitly stated in their respective chapters. Initial, background, and dilution conditions varied depending on the study, and are specified in each box modeling chapter. However, in all box model studies we initiated BBVOCs in the model with emissions ratios from our emissions database, described below.

2.3 Emissions Database

Our emissions database including emission ratios, rate coefficients, and rate coefficient references can be found on the SENEX publications page under "Nighttime Chemical Transformation in Biomass Burning Plumes: A Box Model Analysis Initialized with Aircraft Observations": https://esrl.noaa.gov/csd/projects/senex/pubs/. The methods of constructing the database are described below.

We report our emissions in the form of laboratory-derived emission ratios (ER), which is the background subtracted emitted compound (x) normalized to background subtracted CO (Hatch et al., 2015; Koss et al., 2018).

$$ER_x = \frac{x\ (ppbv)}{CO(ppmv)} \qquad \text{E2.8}$$

These emissions are integrated over the entirety of the laboratory fires and therefore contain emissions from all stages of the fire.

Hatch et al., 2017 report emission factors (EF), which is the ratio of the mass of BBVOC emitted (g) to mass of fuel burned (kg). We used CO emission factors from Stockwell et al., 2014 as well as molecular mass to convert the reported emission factors to emission ratios.

$$EF_x = \frac{x(g)}{fuel(kg)} \quad \text{E2.9}$$

Databases from Koss et al., 2018 and Hatch et al., 2017 were combined in the form ERs. ERs for identical isomers were averaged and the errors added in quadrature. For both inventories all unidentified masses were excluded. Compounds were only included if an isomer, or isomer group was explicitly named. The inventory by Koss et al., 2018 gives assignments based on gas-chromatography (if available), literature evidence, inter-comparisons, and the peak's appearance in the time series. We used all isomers regardless of the confidence ratings. Five compounds (designated in our inventory) had little to no evidence for their assignment.

Two-dimensional gas chromatography used by Hatch et al., 2017 allows for isomer speciation; however, it is less able to detect highly polar isomers that are detectable by PTR-ToF, which can lead to discrepancies in the total emission ratios for some groups of isomers between the two datasets (Hatch et al., 2017). Occasionally the inventory from Hatch et al., 2017 included more isomers for a given mass than the inventory from Koss et al., 2018. Any additional isomers only identified by Hatch et al., 2017 were summed into one group name. The rate coefficient used is dependent on the compound group and is explicitly stated in the inventory. For example, at m/z = 96.1, Koss et al., 2018 report 2,5-dimethylfuran, 2-ethylfuran, and "Other furans (C2)" while Hatch et al., 2017 report an additional three isomers. The emission ratios for these three additional isomers from Hatch et al. were summed and grouped under "Other furans (C2)". Some masses had more than one identification, but an unknown fractional contribution to the ion signal for each. In

these cases, an even distribution is assumed. For example, at m/z = 110.1 both catechol and methylfurfural are reported for a single emission ratio and we assume a 50/50 contribution.

Rate coefficients for the reactions of O_3 + BBVOC and OH + BBVOC were collected for only the top 63 compounds in the NO_3 reactivity sum. Rate coefficient estimations for NO_3 + BBVOC reactions were performed using the structure activity relationships (SAR) (Kerdouci et al., 2010, 2014). There are several compounds for which the SAR is not developed, such as hetero-aromatics or complex oxygenated aromatics. For these compounds, as well as O_3 + BBVOC and OH + BBVOC reactions without published rate coefficients, we estimated the rate coefficient based on structural similarity to compounds with available rate coefficients.

Due to limited literature on NO_3 + BBVOC rate coefficients, our inventory excludes many nitriles, amines, alkynes, acids, and other compounds whose rate coefficients were unavailable and could not be estimated. We also removed saturated hydrocarbons because they are generally unreactive toward NO_3 (Atkinson, 1991). Despite this, our merged inventory retains about 87% of the total inventory carbon mass, or 96% by mass, with 235 compounds from Hatch et al., 2017 and 171 compounds from Koss et al., 2018 with 103 compounds shared in both inventories for a total of 302 unique compounds.

2.3.1 Emissions Uncertainties

Emission uncertainties were taken as the reported error (1-σ from multiple burns within a single database) when available and 30% when unavailable. In general, the emissions from each database have disagreements, which is expected due to variability in fuel composition and combustion conditions. While there are several compounds that agree within a factor of two, the majority differ by more than a factor of two (Figure 2.1). These uncertainties were combined in

quadrature when both databases were averaged and treated as uncertainty in BBVOC concentration, which propagate to significant uncertainty in initial NO_3 reactivity and model results.

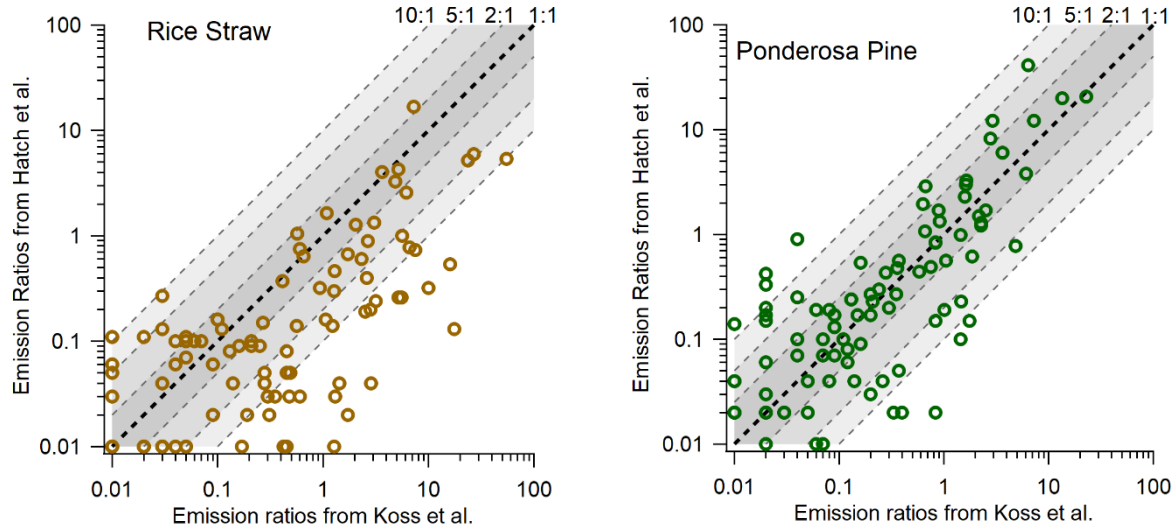

Figure 2.1: Comparison of emission ratios, relative to CO, shared in inventories from both Hatch et al. and Koss et al. for rice straw (left) and ponderosa pine (right) fuels.

2.3.2 Rate Coefficient Uncertainties

Kerdouci et al. report that 90% of calculated rate coefficients for compounds they validated were within a factor of two of the experimental values (Kerdouci et al., 2010). We assume a conservative factor of 3 uncertainty for both rate coefficients estimated by the SAR and structural similarity alone, however it is possible that some of these compounds fall outside of this range. We use the reported uncertainty for published rate coefficients. See the "Details on model parameters and sensitivities" for details on how these propagate in the model results.

2.4 Aircraft Measurements

2.4.1 SENEX 2013 Aircraft Measurements

SENEX (Southeast Nexus) was a 2013 field campaign focused on studying the interactions between biogenic and anthropogenic emissions to form secondary pollutants in the southeastern U.S. Field data were taken from multiple instruments deployed on the NOAA WP-3D aircraft during the SENEX 2013 (Warneke et al., 2016) flight on July 2-3, 2013 (20:00-03:00 CDT), which are used in the analysis presented in Chapter 3. Our analysis utilizes data from the NOAA nitrogen oxide cavity ring-down spectrometer (CRDS) for NO_2, NO_3, N_2O_5, and O_3, (Brown et al., 2002; Dubé et al., 2006; Fuchs et al., 2008; Wild et al., 2014) as well as the NO_yO_3 chemiluminescence instrument (CL) for NO, NO_2, O_3, and NO_y (Ryerson et al., 1999) with 1 Hz acquisition resolution. Within the plume regions we study, the measurements of NO_2 and O_3 from the CRDS and CL instruments agree within 7%. We also use data from an ultra-high sensitivity aerosol spectrometer (UHSAS) for aerosol size measurements (1Hz, Brock et al., 2000, 2011) and a proton-transfer-reaction mass spectrometer (PTR-MS) for VOC measurements (1 s every 17 s, De Gouw and Warneke, 2007).

BB intercepts were identified by the enhancement above background of four species: black carbon (BC), glyoxal (CHOCHO), CO, and acryloyl peroxynitrate (APAN) (Bond et al., 2013; Zarzana et al., 2017). BB identifier data were provided by the NOAA airborne cavity enhanced spectrometer (ACES, Min et al., 2016) for glyoxal, iodide chemical ionization mass spectrometer (I^- CIMS) for APAN (Zheng et al., 2011), single particle soot photometer (SP2) for black carbon (Schwarz et al., 2006), and vacuum ultra-violet fluorimeter for CO (Holloway et al., 2000).

2.4.2 FIREX-AQ Aircraft Measurements

FIREX-AQ was a large-scale multi-platform campaign that took place during the summer of 2019 in the United States to study both wildfire and agricultural burning smoke. Both the NOAA Twin Otter and the NASA DC-8 aircraft executed a series of research flights sampling smoke plumes as part of this campaign. A main science goal of the NOAA Twin Otter was to investigate nighttime plume chemistry. However, due to a less active fire season in 2019 (NIFC, 2019) and to the decreasing smoke injection height with time of day for the sampled fires, smoke emitted after dark proved difficult to sample reliably within the altitude range of the NOAA Twin Otter. While the NOAA Twin Otter sampled over a dozen plumes after sunset, plume age estimates (described below) suggest these plumes were emitted before or at sunset. The NASA DC-8 aircraft sampled plumes both mid-day and near sunset.

In the following sections we describe the instrumentation used for this analysis, which are listed in Table 2.1. More information and data can be found at https://csl.noaa.gov/projects/firex-aq/twinotterCHEM/, https://espo.nasa.gov/firex-aq, and https://www-air.larc.nasa.gov/missions/firex-aq/index.html.

2.4.2.1 NOAA Twin Otter Instrument Descriptions

The NOAA Twin Otter sampled nine wildfires with 39 flights between 3 August 2019 and 5 September 2019 in the western U.S. The aircraft was based mainly in Boise, Idaho and briefly in Cedar City, Utah. The NOAA Twin Otter payload limited flight duration to 3.0 h or less and the aircraft typically flew 2 – 3 times in a day to achieve plume sampling from mid-afternoon into the night. Campaign-wide aircraft speed was 71.2 $\pm$ 4.7 m s^{-1} (average $\pm$ 1σ), which yields a

horizontal resolution of ~70 m for the in situ 1 s measurements. Attempts to probe the same airmass downwind, known as Lagrangian sampling, proved difficult to achieve due to complex plume structure, terrain and airspace. Therefore, we define the sampling strategy as semi-Lagrangian.

In Chapter 4 and 5 we use NOAA Twin Otter observations of BBVOCs and HONO from a University of Washington Iodide High Resolution Time of Flight Chemical Ionization Mass Spectrometer (UW I^- HR ToF CIMS, 2 Hz, Lee et al., 2014) as well as a Tenax cartridge sampler with subsequent GCxGC analysis for speciated BBVOCs (intermittent transect integrations, Hatch et al., 2015; Mondello et al., 2008), which we use to support mass assignments from the UW I^- HR ToF CIMS for some phenolic compounds (see section 2.4.2.4 on page 22).

We use data from a commercial cavity ringdown spectrometer (Picarro G2401-m) for measurements of CO, CO_2, and CH_4 (0.5 Hz, Crosson, 2008). We use measurements from a custom chemiluminescence instrument (1 Hz) for NO, NO_2 and O_3 (Sparks et al., 2019). Aerosol surface area measurements were collected by an ultra-high sensitivity aerosol spectrometer (UHSAS, 1 Hz, Kupc et al., 2018). The aircraft had a standard meteorological probe (Aventech ARIM 200) for temperature, pressure, relative humidity, wind speed and direction. We use NO_2 photolysis rates (jNO_2) collected by upward and downward facing filter radiometers (Metcon, GmbH , 1 Hz, Kupc et al., 2018; Warneke et al., 2016). Measurements of a group of nitrophenolic masses are from an HR-ToF Aerosol Mass Spectrometer (HR-ToF AMS, 1 Hz, Decarlo et al., 2006; Liggio et al., 2016; Palm et al., 2020).

Measurements Used	Method	Platform	Sample Frequency	Reference
HONO, C_6H_6O, C_7H_8O, $C_6H_6O_2$, $C_7H_8O_2$, $C_6H_5NO_4$, $C_7H_7NO_4$, $C_6H_5NO_3$, $C_7H_7NO_3$.	University of Washington Iodide High Resolution Time of Flight Chemical Ionization Mass Spectrometer (UW I^- HR-ToF-CIMS)	Twin Otter	2 Hz	(Lee et al., 2014)
Guaiacol and methylcatechol.	Tenax cartridge sampler with subsequent GCxGC analysis	Twin Otter	~ 5 min	(Hatch et al., 2015; Mondello et al., 2008)
CO	Picarro G2401-m, cavity ringdown spectrometer.	Twin Otter	0.5 Hz	(Crosson, 2008)
NO, NO_2 and O_3.	NCAR chemiluminescence instrument	Twin Otter	1 Hz	(Sparks et al., 2019)
Nitrophenolic ions $C_6H_5NO_3$ + $C_6H_5NO_4$ + $C_7H_7NO_3$ + $C_7H_7NO_4$	HR-ToF AMS (high-resolution time-of-flight aerosol mass spectrometer)	Twin Otter	1 Hz	(Decarlo et al., 2006; Liggio et al., 2016; Palm et al., 2020)
Aerosol surface area	Ultra-high sensitivity aerosol spectrometer (UHSAS)	Twin Otter	1 Hz	(Kupc et al., 2018)
jNO_2	Meteorologie Consult, GmbH upward and downward facing jNO_2 filter radiometers	Twin Otter	1 Hz	(Kupc et al., 2018; Warneke et al., 2016)
CO	Tunable diode laser spectrometer	DC-8	1 Hz	(Sachse et al., 1991)
CO	Cavity enhanced spectrometer	DC-8	1 Hz	(Eilerman et al., 2016)
NO_2 NO_y and O_3	NOAA chemiluminescence	DC-8	1 Hz	(Pollack et al., 2010; Ridley et al., 1992; Stedman et al., 1972)
NO_2	NOAA broadband Airborne Cavity Enhanced Spectrometer (ACES)	DC-8	1 Hz	(Min et al., 2016)
NO	NOAA laser induced fluorescence	DC-8	1 Hz	(Rollins et al., 2020)
HONO, $C_4H_2O_3$, $C_6H_6O_2$, $C_6H_5NO_4$	NOAA Iodide Time of Flight Chemical Ionization Mass Spectrometer (I^- ToF-CIMS)	DC-8	1 Hz	(Neuman et al., 2016; Veres et al., 2020)
peroxyacetyl nitrate (PAN)	Thermal dissociation Chemical Ionization Mass Spectrometer	DC-8	1 Hz	(Ro Lee et al., 2020)
$C_6H_5NO_4$	Extractive Electrospray Ionization Rime-of-Flight Mass Spectrometer (EESI-MS)	DC-8	1 Hz	(Pagonis et al., 2020)
Photolysis rates listed in their respective chapter	Charged-coupled device Actinic Flux Spectroradiometer (CAFS)	DC-8	1 Hz	(Shetter and Müller, 1999)
$C_4H_2O_3$, C_4H_4O	NOAA Proton Transfer Reaction Time of Flight Mass Spectrometer (NOAA-PTR-ToF-MS)	DC-8	1 Hz	(Coggon et al., 2019; Koss et al., 2018)
$C_4H_2O_3$	University of Innsbruck Proton Transfer Reaction Time of Flight Mass Spectrometer (UIBK-PTR-ToF-MS)	DC-8	1 Hz	(Müller et al., 2014; Piel et al., 2019, 2021)

Table 2.1: List of instruments and measurements used in this thesis from FIREX-AQ.

2.4.2.2 NASA DC-8 Instrument Descriptions

The NASA DC-8 aircraft sampled 14 wildfires in the western U.S. while based in Boise, Idaho as well as about 90 prescribed agricultural southeastern U.S. fires while based in Salina, Kansas between 22 July 2019 and 5 September 2019. Aircraft speed campaign-wide was 296.9 $\pm$ 24.3 m s^{-1}, which yields a horizontal resolution of ~297 m for the in situ 1 s measurements. Similar to the NOAA Twin Otter, sampling was semi-Lagrangian.

In this analysis we use measurements of CO from a tunable diode laser spectrometer (1 Hz, Sachse et al., 1991) when available and from an integrated cavity output spectrometer (ICOS, 1 Hz, Eilerman et al., 2016) when unavailable. In the fires investigated here both instruments agree well within <2 %. Measurements of NO_2, NO_y and O_3 are provided by a NOAA chemiluminescence (CL, 1 Hz, Pollack et al., 2010; Ridley et al., 1992; Stedman et al., 1972) instrument. When measurements of NO_2 by the NOAA CL instrument are unavailable we use measurements by a NOAA CES (1 Hz, Min et al., 2016). These two measurement methods of NO_2 agree within 11 % for the fires we investigate. We use measurements of NO by a laser induced fluorescence instrument (1 Hz, Rollins et al., 2020).

Measurements of $C_4H_2O_3$ (likely maleic anhydride, MA) were taken from three instruments at 1 Hz 1) the NOAA Proton Transfer Reaction ToF-MS (Coggon et al., 2019; Koss et al., 2018, NOAA PTR-ToF-MS) for all flights except 7 Aug when data is unavailable 2) the University of Innsbruck PTR-ToF-MS (Müller et al., 2014; Piel et al., 2019, 2021, UIBK PTR-ToF-MS) on 7 Aug, and 3) from the NOAA I^- ToF-CIMS (Neuman et al., 2016; Veres et al., 2020) on 7 Aug. The UIBK PTR-ToF-MS and NOAA I^- ToF-CIMS agree within 3% for the mass $C_4H_2O_3$ on a normalized scale, and results for both instruments are reported.

Measurements of other BBVOCs and HONO are also taken from the NOAA I^- ToF CIMS (1 Hz, Neuman et al., 2016; Veres et al., 2020). PAN measurements were performed by a thermal dissociation CIMS (1 Hz, Ro Lee et al., 2020). Aerosol surface area measurements are taken from a scanning mobility particle sizer and laser aerosol spectrometer (SMPS and LAS, 1 Hz, LAS, n.d.; Moore et al., 2021; SMPS, n.d.). Spectrally resolved actinic flux was measured with separate upward and downward facing actinic flux optics (CAFS, 1 Hz, Shetter and Müller, 1999). These fluxes were used to calculate photolysis rates using the photochemistry routine contained in the NCAR TUV model (v5.3.2). Measurements of nitrocatechol aerosol, measured as $C_6H_5NO_4$, were taken from the Extractive Electrospray Ionization ToF-MS (Pagonis et al., 2020, EESI-MS, 1 Hz).

2.4.2.3 Plume Age Determination

Plume age estimates are made by air parcel trajectories computed in the HYSPLIT trajectory model with multiple high-resolution meteorological datasets (HRRR 3 km, NAM CONUS nest 3 km, and GFS 0.25°). These estimates account for buoyant plume rise as well as horizontal advection. Uncertainties in plume age are determined from spread between the meteorological datasets, mismatch between observed and archived winds, and trajectory spatial error in missing the known fire source. Typical uncertainties are 25 % of the estimated age (Holmes et al., 2020).

2.4.2.4 Mass Assignments for $C_7H_8O_2$

From the FIREX-AQ Twin Otter dataset we see significant signal at the mass corresponding to $C_7H_8O_2$ from the UW I^- HR ToF CIMS. There are at least two explanations for

this mass: methylcatechol or guaiacol or any mixture in-between. The time series of $C_7H_8O_2$ suggests it is a primary emission (Figure B.1 and Figure B.2 on page 187). Current BB emissions literature does not list methylcatechol as a detected gas-phase emission (Hatch et al., 2015; Koss et al., 2018), however emissions collected on Teflon filters with subsequent GCxGC analysis show evidence for methylcatechol (Hatch et al., 2018). Both guaiacol and methylcatechol are highly reactive to NO_3, OH, and O_3. Therefore, accurately determining its identity and thus mixing ratio, is important to both constraining the model and comparing it to observations. Collection of smoke during the Castle and Cow plume by a Tenax cartridge sampler with subsequent GCxGC analysis shows no evidence for methylcatechol or guaiacol above detection limits in the Castle plume, but some evidence for guaiacol at roughly ~0.06 ppbv in the Cow plume. Using calibrations for the UW I^- HR ToF CIMS $C_7H_8O_2$ signal for guaiacol and methylcatechol (described in the SI of Palm et al., 2020), we determined that methycatechol is the most likely assignment despite its absence by the Tenax cartridge sampler. If the mass was entirely due to guaiacol, then ~0.06 ppbv would appear as < 1 normalized count per second on the UW I^- HR ToF CIMS, while we observe 1,000 – 10,000 normalized counts per second. In other words, iodide is very weakly sensitive to guaiacol and we do not expect to detect a mixing ratio of 0.06 ppbv. Assigning $C_7H_8O_2$ to methylcatechol corresponds to observations of 0.1 – 1 ppbv (Figure B.1 and Figure B.2) and an emission ratio of 0.4 ppbv $ppmv^{-1}$ CO, or $1/3^{rd}$ that of the catechol emission ratio. This is consistent with the same assignment of $C_7H_8O_2$ and emission ratios observed in (Palm et al., 2020). Lastly, while we expect formation of methylcatechol from cresol oxidation by OH, our box model shows this formation pathway is negligible.

2.5 Fire Descriptions

The analyses in Chapter 4 and 5 focus on seven semi-Lagrangian experiments from three separate fire complexes: the Castle Fire plume in northern Arizona, the 204 Cow Fire plume in central Oregon (referred to as Cow from here on), and four from the Williams Flats Fire plume in eastern Washington. In Chapter 4 we refer to the first and second pass of the Williams Flats Fire on 7 Aug as WF1 and WF2, respectively. In Chapter 5 we use an additional two passes of the Williams Flats Fire from 3 Aug. Table 2.2 summarizes fire locations, sampling platform, and fuel types (Inciweb, 2019b, 2019c, 2019a). Figure 2.2 displays flight paths for flights used.

2.5.1 Williams Flats

The Williams Flats Fire started on 2 August 2019 and grew to a total of 44,446 acres before it was contained on 25 August 2019. The fuel was mostly short grass (1 ft tall) as well as ponderosa and mixed conifer timber (Inciweb, 2019c). The DC-8 aircraft performed three semi-Lagrangian smoke transect patterns on 3 and 7 August 2019.

2.5.2 Castle

The Castle Fire began on 12 July 2019 and was allowed to burn the mixed conifer fuel in a defined area that eventually reached 19,368 acres, and burned out on 15 October 2019 (Inciweb, 2019b). The Twin Otter aircraft performed one semi-Lagrangian transect pattern during sunset on 21 August 2019 when small pockets of remaining fuels were burning. The sampled smoke varied in age from approximately 2 min – 1.5 h. The Castle Fire had a neighboring fire named Ikes. Smoke from the Ikes fire visually mixed (Figure 2.3) with the Castle Fire plume after the fourth transect downwind of the Castle Fire. For that reason, this analysis focuses on the first four transects only.

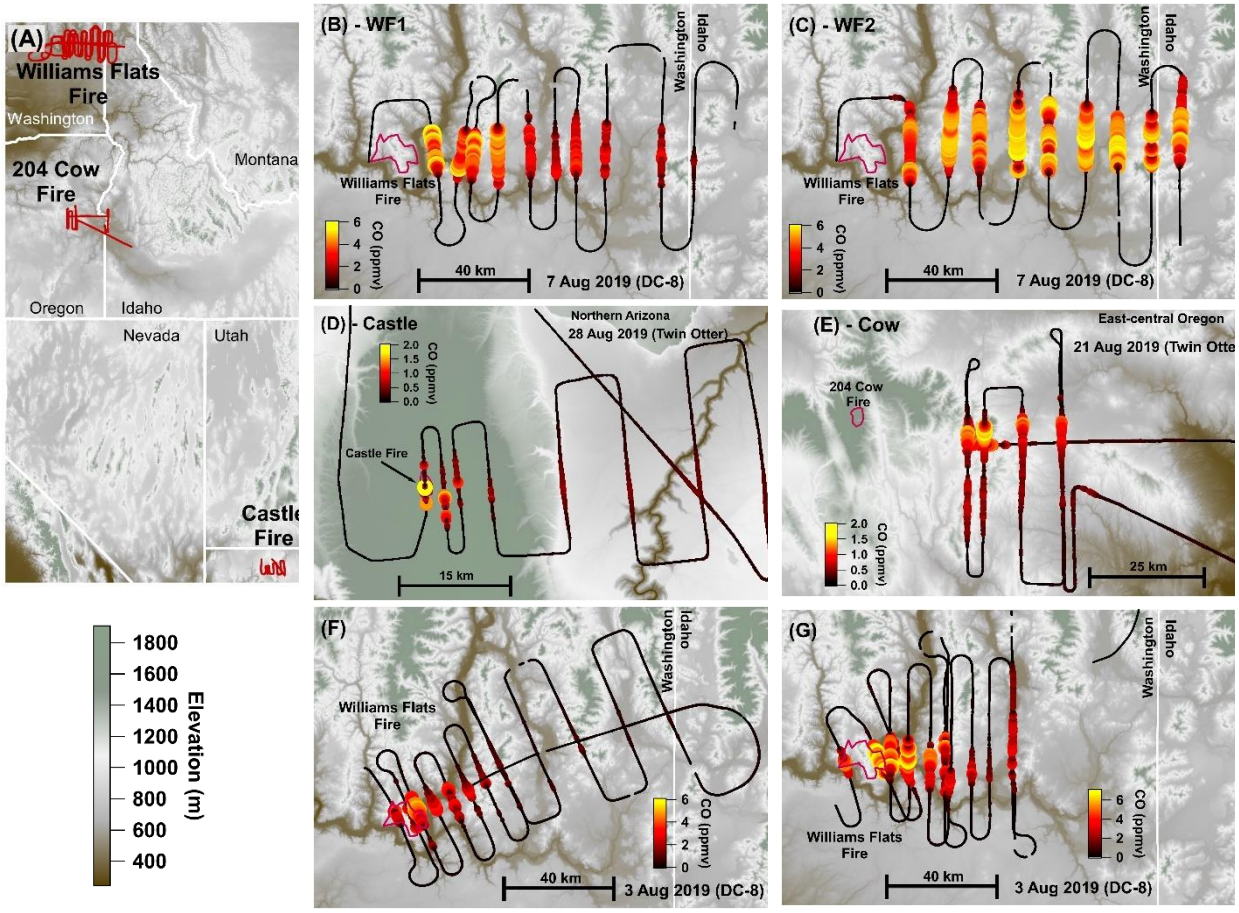

Figure 2.2: Flight maps on top of a topographic model. Overview Map (A) showing flight tracks (red), 7 Aug Williams Flats first pass (B), 7 Aug Williams Flats second pass (C), Castle (D), 204 Cow (E), 3 Aug Williams Flats first pass (F), 3 Aug Williams Flats second pass (G). Panels B–G are colored and sized by CO. Fire boundaries are approximate and indicated by red outlines. The flight path is shown in black colored and sized by CO.

Fire Name	County/State	Latitude	Longitude	Date sampled	Time sampled	Aircraft	Fuel
Williams Flats	Ferry/Washington	47.9392	-118.6183	Aug 07 & Aug 03	16:30–17:45 PDT & 18:00–19:30 PDT	DC-8	Short grass, ponderosa timber
Castle	Coconino/Arizona	36.5312	-112.2281	Aug 21	18:00–19:15 MST	Twin Otter	Mixed conifer
204 Cow	Grant/Oregon	44.2851	-118.4598	Aug 28	20:00–22:00 PDT	Twin Otter	Primarily lodgepole pine with conifer

Table 2.2: Details of fires studied.

2.5.3 204 Cow

The Cow Fire started on 9 August 2019 and was allowed to burn eventually reaching 9,668 acres by 15 September 2019. The fuel was mainly lodgepole pine at lower elevations and mixed conifer at higher elevations with abundant downed timber. The Twin Otter aircraft performed three semi-Lagrangian transect patterns on 28 August 2019, by which time the fire had burned 3,441 acres (Inciweb, 2019a). This study focuses on the third semi-Lagrangian transect pattern, which was conducted after sunset. The sampled smoke in this analysis had aged approximately 2 – 3 h.

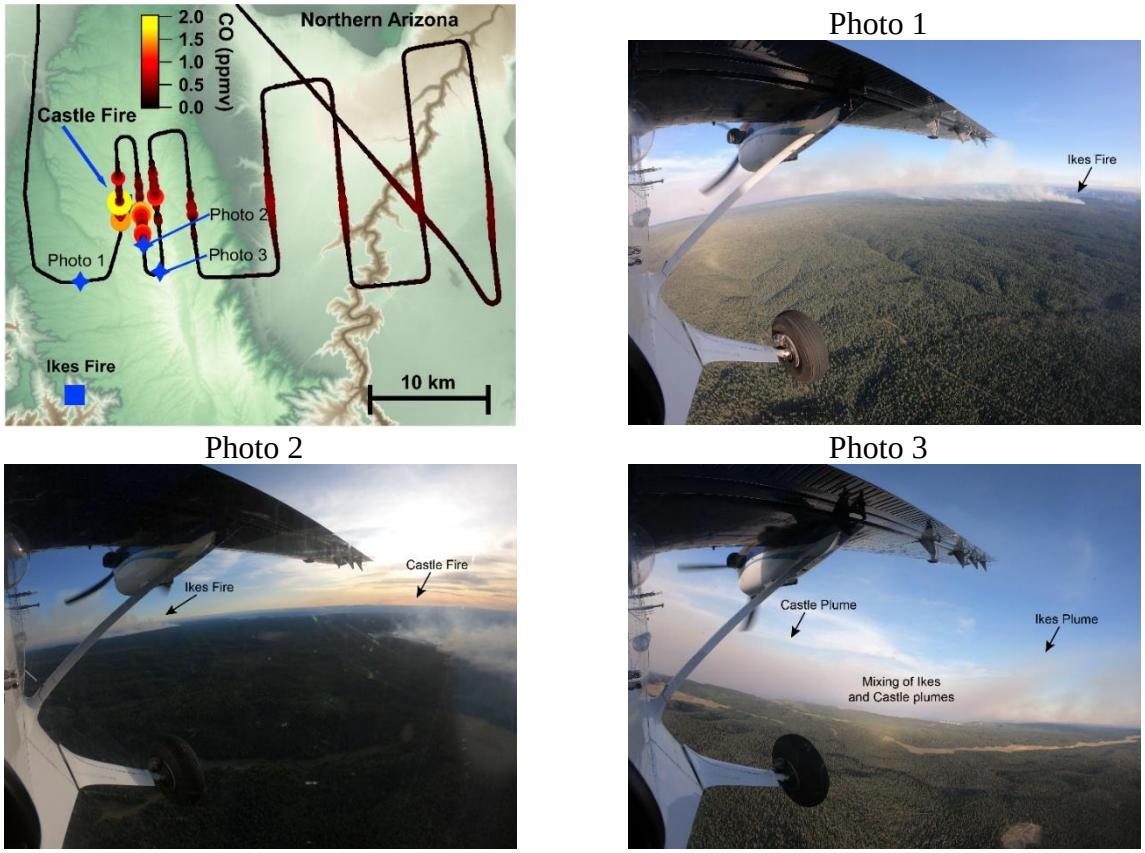

Figure 2.3: Flight map and photos of the Castle plume. Photos indicate the Ikes and Castle Fires, which burned near each other and eventually mixed plumes. The first four (of 8) transects of the Castle plume are unmixed with the Ikes plume.

Chapter 3: Nighttime Chemical Transformation in Biomass Burning Plumes: A Box Model Analysis Initialized with Aircraft Observations

Abstract

Biomass burning (BB) is a large source of reactive compounds to the atmosphere. While the daytime photochemistry of BB emissions has been studied in some detail, there has been little focus on nighttime reactions despite the potential for substantial oxidative and heterogeneous chemistry. Here we present the first analysis of nighttime aircraft intercepts of agricultural BB plumes using observations from the NOAA WP-3D aircraft during the 2013 Southeast Nexus (SENEX) campaign. We use these observations in conjunction with detailed chemical box modeling to investigate the formation and fate of oxidants (NO_3, N_2O_5, O_3, and OH) and BB volatile organic compounds (BBVOCs), using emissions representative of agricultural burns (rice straw) and western wildfires (ponderosa pine). Field observations suggest NO_3 production was approximately 1 ppbv hr^{-1}, while NO_3 and N_2O_5 were at or below 3 pptv, indicating rapid NO_3/N_2O_5 reactivity. Model analysis shows that >99% of NO_3/N_2O_5 loss is due to BBVOC + NO_3 reactions rather than aerosol uptake of N_2O_5. Nighttime BBVOC oxidation for rice straw and ponderosa pine fires is dominated by NO_3 (72, 53%, respectively), but O_3 oxidation is significant (25, 43%) leading to roughly 55% overnight depletion of the most reactive BBVOCs and NO_2.

3.1 Introduction

Biomass burning (BB), including wildfires, prescribed burning, and agricultural burning, represents a large, imperfectly characterized and chemically complex source of reactive material to the troposphere. BB releases reactive species and particulate matter that impact the radiative balance of the atmosphere, air quality, and human health on local to global scales (Andreae and

Merlet, 2001a; Hatch et al., 2017; Koss et al., 2018; Pope and Dockery, 2006; Rotstayn and Penner, 2001). The gas-phase components of BB plumes include volatile organic compounds (BBVOCs) as well as nitrogen oxides (NO_x = NO + NO_2), oxidants, and oxidant precursors. The air quality and climate effects of BB emissions are defined in part by the oxidative processes and atmospheric chemical cycles that occur as the smoke is transported, diluted, and exposed to oxidants over the hours and weeks following emission.

The photochemistry of BB plumes has been studied previously in a number of field and laboratory studies. Daytime BB plumes can have OH concentrations 5-10 times higher than background air (Yokelson et al., 2009) and daytime reactions of NO_x, BBVOCs, and OH involve complex pathways that generally lead to O_3 formation, but in some cases to near-field O_3 titration (Bruns et al., 2015, 2016; Hennigan et al., 2010, 2011; Jaffe and Wigder, 2012; Ortega et al., 2013). Much less is known about nighttime BB plume oxidative processes, which are expected to be dominated by nitrate radicals (NO_3) and O_3 (Brown and Stutz, 2012). NO_3 is formed by O_3 oxidation of NO_2 (R1.8) but is rapidly (τ < 10 s) destroyed in the daytime by NO and photolysis (Brown and Stutz, 2012; Wayne et al., 1991). NO_3 is a precursor for N_2O_5 (R1.9), a NO_x reservoir. N_2O_5 may undergo heterogeneous uptake to form $ClNO_2$ and HNO_3 (R1.10). The former is a daytime Cl radical precursor affecting both marine and continental environments and influencing next-day O_3 production (Ahern et al., 2018; Chang et al., 2011; Osthoff et al., 2008; Thornton et al., 2010). NO_3 can also be directly taken up onto aerosol (R1.11).

Mixing of background or smoke-derived (Jaffe and Wigder, 2012) O_3 with NO_x in a BB plume leads to the production of NO_3, which may be rapid (>0.5 ppbv hr^{-1}). Recent laboratory measurements conducted during both the Fire Lab at Missoula Experiment (FLAME-4) and the

on-going Fire Influence on Regional and Global Environments Experiment (FIREXLab) have provided detailed identification and quantification of emissions for a range of BBVOCs (Hatch et al., 2015, 2017; Koss et al., 2018; Selimovic et al., 2017; Stockwell et al., 2014). Emissions inventories from these experiments indicate that the compounds emitted and their relative concentrations depend on the fuel type (e.g., pine vs. grass), combustion process (e.g., smoldering or flaming), ignition procedure (fast or slow), and pyrolysis temperature (e.g., high or low) (Hartikainen et al., 2018; Hatch et al., 2015; Koss et al., 2018; Sekimoto et al., 2018). Generally, primary BBVOC emissions include oxygenated hydrocarbons and aromatics (e.g., phenols), as well as unsaturated hydrocarbons, biogenic and hetero-aromatic species (Hatch et al., 2015, 2017; Koss et al., 2018). Many such compounds are very reactive toward NO_3 (Atkinson, 1991; Atkinson and Arey, 2003b, 2003a; Cabañas et al., 2004; Grosjean and Williams, 1992; Kerdouci et al., 2014; Martínez et al., 1999; El Zein et al., 2015) and may significantly limit its lifetime, promote secondary organic aerosol formation (SOA), and alter nighttime oxidative budgets (Harrison et al., 2005; Laskin et al., 2015).

The co-emission of NO_x, highly reactive VOCs, and aerosol particles leads to the potential for significant nighttime chemical transformations. Despite this potential, there has been only one aircraft campaign to date from which sampling of nighttime biomass burning plumes has been reported (Neuman et al., 2016; Zarzana et al., 2017). The Southeast Nexus (SENEX) campaign in 2013 included 20 research flights of an instrumented NOAA WP-3D aircraft and one of the goals was to study the interactions between anthropogenic and biogenic emissions (Warneke et al., 2016). A night flight on July 2-3 targeted the emissions and nighttime chemistry from a power plant plume near the Mississippi river. During this flight the WP-3D also targeted and intercepted

agricultural BB plumes yielding the first airborne study of nighttime smoke that included NO_3 and N_2O_5 measurements (Zarzana et al., 2017). Even so there has been no previous analysis of BB NO_3 chemistry using nighttime aircraft intercepts.

Here, we present the first analysis of nighttime smoke oxidation based on aircraft intercepts of fire plumes using data from this flight. With these observations we initiate a detailed chemical box model to understand the chemical evolution of oxidants (NO_3, N_2O_5, O_3, and OH) and BBVOCs over one night (10 hours) using emissions for rice straw to model a generic agricultural burning plume. We then use this analysis to model nighttime chemistry in western wildfires using emissions for a ponderosa pine fire.

3.2 Methods

3.2.1 Field and Laboratory Measurements

We use data from multiple instruments deployed on the NOAA WP-3D aircraft during the SENEX 2013 (Warneke et al., 2016) flight on July 2-3, 2013 (20:00-03:00 CDT). Details on the instrumentation and measurements are described in section 2.4.1 on page 17. Below, we describe the BB plumes used in this analysis.

3.2.1.1 Details on BB Tracers, Plume Selection, and Plume Calculations

We use four biomass burning tracers: black carbon (BC), glyoxal (CHOCHO), CO, and acryloyl peroxynitrate (APAN). APAN is primarily formed by oxidation of acrolein or oxidation of 1,3-butadiene (Tanimoto, 2001). APAN is expected to account for <1% of total PAN in both urban and rural environments, unless there are unusually large emissions of these precursors from, for example, petrochemical sources (Roberts et al., 2003, 2001; Tanimoto, 2001; Tanimoto et al., 2002; Wolfe et al., 2007). Acrolein and 1,3-butadiene account for more than 3% of rice straw and

ponderosa pine BBVOC emissions (Hatch et al., 2015, 2017; Koss et al., 2018) and it is therefore expected for APAN to be enhanced within BB plumes. During the SENEX nighttime BB intercepts we calculate that APAN is 5.3 $\pm$ 0.7% of total PAN, suggesting it is appropriate as a BB tracer.

We define a BB intercept as any period of time during which at least three of the four BB tracers are present above background. We chose only three of four in order to include plumes that were intercepted when at most one tracer instrument is not operating or is zeroing. Specifically, we consider above background to be 5-σ above the total average signal for CO, CHOCHO, and BC or 2-σ above the average signal for APAN. We use a lower threshold for APAN because APAN mixing ratios are far smaller and the uncertainty far larger than CO, CHOCHO, and BC. Lastly, the modified combustion efficiency (MCE) was calculated for each plume.

$$MCE = \frac{CO_2 - CO_{2_{bkg}}}{\left(CO_2 - CO_{2_{bkg}}\right) + (CO - CO_{bkg})} \quad \text{E3.1}$$

During plume intercepts, the average MCE was 95 $\pm$ 6%, which is consistent with previous MCE calculations of the July 2/3 night flight (Zarzana et al., 2017).

Background and plume measurements were calculated as the average of a series of representative BB and power plant plume intercepts. Background measurements were taken outside the bounds of both BB and power plan plume types. Table 3.1 provides a summary of plume and background averages of species used in this analysis and Table 3.2 provides a list of data sections used for the analysis.

Figure 3.1 shows altitude profiles of CO, NO_2, NO_y, and O_3 from aircraft observations. Figure 3.1E shows potential temperature in yellow near the Missouri/Kentucky/Tennessee border, which is the same region as the BB intercepts. Figure 3.1E suggests the BB plume

intercepts were likely above the surface layer and within the residual layer, which we estimate extended to 1000-1400 meters based on the steeper gradient of potential temperature with height in that range.

	Plume Enhancement		**Background**	
	average	***σ***	**average**	***σ***
O_3 (ppbv)	-14.2	3.6	43.9	0.5
CO (ppbv)	543.4	87.7	188.4	5.6
Black carbon (μg m^{-3})	2.0	0.3	0.2	0.1
Glyoxal (ppbv)	0.6	0.1	<0.1	<0.1
NO (ppbv)	0.0	0.0	0.0	0.0
NO_2 (ppbv)	10.0	2.7	0.9	0.5
NO_y (ppbv)	13.2	3.1	2.0	0.2
Relative Humidity (%)			88.2	1.0
APAN (ppbv)	0.026	0.003	0.006	0.001
PAN (ppbv)	0.363	0.030	457	24
PPN (ppbv)	0.09	0.01	70	6
Total aerosol (μg m^{-3})	58.7	8.4	12.7	1.0
RH corrected aerosol surface area density (μm^2 cm^{-3})	1950	234	166.7	18.4

Table 3.1: BB plume averages and background averages used.

	Start Time	Stop Time	Average Altitude (m)
Background	21:48:16	21:51:46	702
	21:52:36	21:54:29	695
BB Plume	21:44:51	21:45:21	930
	21:45:47	21:46:11	740
	21:46:16	21:46:32	739
	21:52:06	21:52:27	694
	21:58:21	21:57:49	695

Table 3.2: Sections of data used for plume and background measurements.

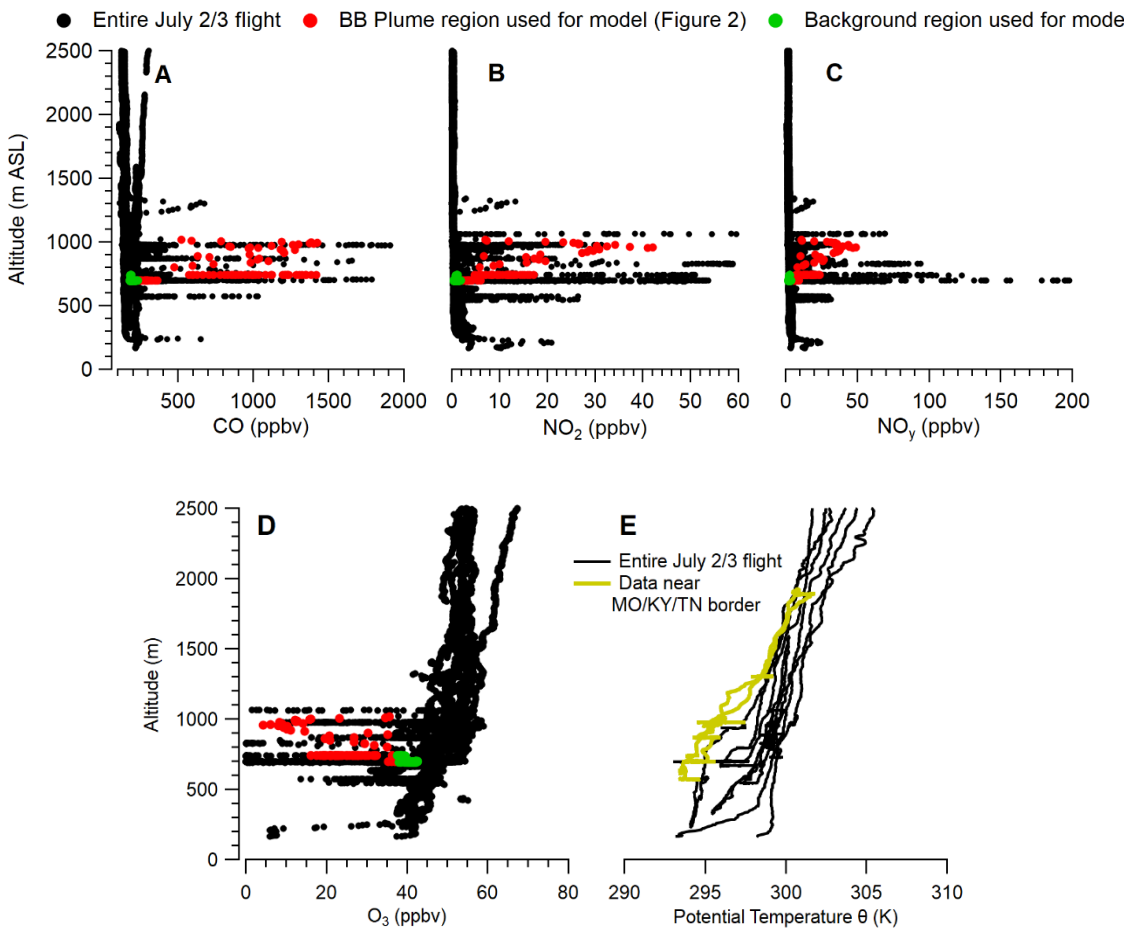

Figure 3.1. Panels A (CO), B (NO_2), C (NO_y), D (O_3), and E (potential temperature θ) include altitude profiles of aircraft observations for the entire July 2/3 flight (black). Panels A-D are overlaid by the BB plume intercept (red) and background region data (green) which are aircraft observations used to initialize our model and are also shown in Figure 2. Panel E is overlaid by potential temperature near the Missouri/Kentucky/Tennessee border (yellow), which is the same region as the BB intercepts.

3.2.1.2 Plume Age Estimates

Figure 3.2 shows a flight map colored by NO_x/NO_y ratio with four boxed plume regions (seven plume intercepts total). Plume intercepts from these regions along a north to south distance exhibit a systematic change in NO_x/NO_y with distance from the fire plume, although the change is within the combined errors in the NO_x and NO_y instruments (Figure 3.2B).

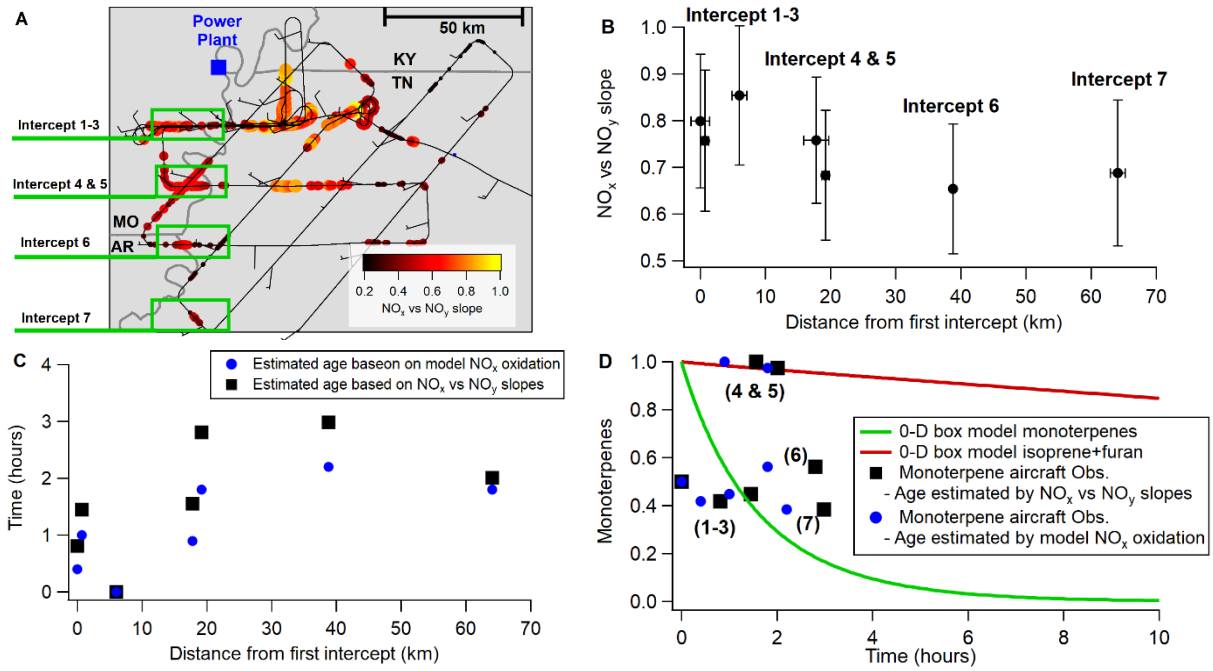

Figure 3.2: Panel A: Flight map colored by NO_x/NO_y ratio. Intercept regions used for plume aging estimates are shown by green boxes. Panel B: NO_x/NO_y ratios as determined by NO_x vs. NO_y correlations as a function of distance from the first intercept. Panel C: Plume age estimates based on the NO_x/NO_y ratio (black squares) and comparing the modeled NO_x/NO_y ratio to aircraft observations (blue circles). Panel D: Box model time trace of monoterpenes (green) and isoprene+furan (red) overlaid by monoterpene observations with age estimates based on the NO_x/NO_y ratio (black squares) and by comparing the modeled NO_x/NO_y ratio to aircraft observations (blue circles).

Error bars in Figure 3.2B are large and incorporate a stated accuracy of 5% in NO_x and 12% in NO_y. The wind direction is variable, but roughly northwesterly at 2.5 ± 0.9 m s^{-1} for these regions. We have estimated the plume age (Figure 3.2C black) by the oxidation of NO_x by O_3

$$t = \ln\frac{NO_x}{NO_y}\,(k[O_3])^{-1} \qquad \text{E3.2}$$

where t is time (plume age) and k is the bimolecular rate coefficient for the reaction of $NO_2 + O_3$ (R1.8). Plume age estimation from NO_x/NO_y ratios is not well established because components of NO_y are emitted during combustion, such as HONO. In addition, the NO_yO_3 chemiluminescence instrument is a gas phase instrument and may not capture HNO_3 that is in the particle phase, meaning we would expect the NO_x/NO_y ratio to be less than one at the fire source (Akagi et al.,

2011; Neuman et al., 2016). Therefore, we have normalized the NO_x/NO_y ratios to the greatest NO_x/NO_y ratio observed before estimating plume age and discuss only the aging observed after the first intercept region (intercepts 1-3).

We have also estimated plume age by comparing the NO_x/NO_y ratio in our 0-D box model (excluding dilution) to the normalized ratio observed during aircraft observations (Figure 3.2C blue). Both plume age estimates are variable, but generally agree within a factor of two and suggest that roughly two hours of oxidation occurs after the first intercept region. All estimated plume ages are roughly equal to or less than the time elapsed since sunset (SZA=90°). Our 0-D box model suggests monoterpenes is the only VOC aircraft measurement whose oxidation rate is sufficiently rapid to observe a change in VOC greater than the factor of two variability seen in plume age estimates over two hours. For example, changes in isoprene + furan decay (red in Figure 3.2D) are small compared to the variability in estimated plume age.

In Figure 3.2D we compare the normalized model time trace of monoterpenes to the NEMR (E2.1) aircraft measurements of monoterpenes using both plume age estimation methods. Normalizing monoterpenes to CO gives similar results. Without knowledge of the initial monoterpene concentration at the fire source we have also normalized the monoterpene aircraft observations to the greatest monoterpene/acetonitrile ratio observed. There is large variability in the monoterpene aircraft observations, and there is no apparent decaying trend in monoterpenes. While some monoterpene measurements fall near the 0-D box model line, the majority do not. Little knowledge of the fire location or the number of fire sources combined with the variability in aircraft measurements makes plume age estimation and aircraft to model comparisons difficult. We find that plume age estimates and the aircraft to model comparison are highly uncertain.

3.2.2 0-D Chemical Box Model Description

As mentioned in section 2.2 on page 13, we use the Framework for 0-D Atmospheric Modeling (F0AM, Wolfe et al., 2016). to investigate the evolution of oxidized mass and oxidant fractions over 10 hours (the approximate duration of one night in July in the Southeastern U.S.).

3.2.2.1 Chemistry and Emissions

As described in section 2.3 on page 13, our detailed chemical box model uses emission inventories from Hatch *et al.*, (2015, 2017) and Koss *et al.*, (2018) for the ponderosa pine and rice straw fuels. The BBVOC emissions from Hatch *et al.*, (2015, 2017) were measured during FLAME-4 using the following instruments: two-dimensional gas chromatography–time-of-flight mass spectrometry, open-path Fourier-transform infrared spectroscopy (Stockwell et al., 2014), whole-air sampling with one-dimensional gas chromatography–mass spectrometry, and PTR time-of-flight mass spectrometry (PTR-ToF, Stockwell et al., 2015). BBVOC emissions from Koss et al., 2018 were measured by PTR-ToF during FIREXLab.

As shown in the Results and Discussion on page 43, BBVOC is likely the main sink of NO_3; therefore, the extent of BBVOC oxidation by NO_3 will be limited by the NO_x/BBVOC ratio as NO_x is the source for NO_3 (R1.8). Furthermore, the relative oxidative importance between O_3 and NO_3 depends on the NO_x/BBVOC ratio as explained by Edwards et al., 2017. Therefore, we initiate our box model with fire emissions scaled to NO_x in order to preserve the NO_x/VOC ratio observed during the fire lab experiments.

To estimate the emitted NO_x at the fire source we assume that the total reactive nitrogen (NO_y, which does not include NH_3) is equivalent to the emitted NO_x. The NO_x/NO_y ratio as measured during SENEX fire plume intercepts was 0.84. We calculated the observed NO_y

emission ratio (E2.1 on page 11) using NO_y (13.2 $\pm$ 3.1 ppbv) and CO (543.4 $\pm$ 87.7 ppbv) enhancements above background. The calculated NO_y emission ratio, which we assume to be the NO_x emission ratio at the fire source, was determined to be 24.3 $\pm$ 6.4 ppbv NO_y/ppmv CO for the plume intercept. We compared the estimated observed NO_x emission ratio to the NO_x emission ratios reported by Selimovic et al., 2017 for rice straw (43.9 ppbv NO_x/ppmv CO) and ponderosa pine (26.9$\pm$4.3 ppbv NO_x/ppmv CO). We then scaled the BBVOC emissions by this ratio (E3.3), effectively scaling the fire emissions to the NO_x of the observed fire plume.

$$[BBVOC]^{model} = [BBVOC]^{inventory} * \frac{ER_{NO_y}^{observed}}{ER_{NO_x}^{inventory}} \qquad \text{E3.3}$$

The NO_x emission ratio observed during the SENEX fire plume intercepts in was 45% and 11% lower than the laboratory-derived NO_x emission ratio for rice straw and ponderosa pine fires respectively. To correctly model the NO_3 oxidation of these fires we reduced our BBVOC emissions by a factor of 55% for rice straw and 89% for ponderosa pine.

In contrast to the method described above for determining initial BBVOCs, model background and initial concentrations of NO_x, CO, and O_3 were taken from the SENEX observations shown in Figure 3.5 later on page 44. We estimate the NO/NO_2 ratio at the fire source using the NO and NO_2 emission ratios from FIREXLab for each fuel. The NO/NO_2 ratios used are 5.3 and 2.8 for rice straw and ponderosa pine, respectively (Selimovic et al., 2017). The background NO_2 mixing ratio was taken to be 0.9 ppbv. The background O_3 mixing ratio, 43.9 ppbv, was used as the starting O_3 mixing ratio and is representative of the background O_3 in the region where BB plumes were intercepted (Figure 3.1).

Chemical mechanisms were adopted from the MCM (v3.3.1, Bloss et al., 2005; Jenkin et al., 1997, 2003, 2012, 2015, via website: http://mcm.york.ac.uk) and published mechanisms for methylguaiacol, syringol, *o*-guaiacol, and 3-methylfuran were added (Table 3.3, Lauraguais et al., 2016; Tapia et al., 2011; Yang et al., 2016). Aerosol uptake reactions were added for N_2O_5 to form $ClNO_2$ and HNO_3. Compounds not included in the above references were modeled as a one-step reaction of BBVOC + NO_3, BBVOC + O_3, or BBVOC + OH to form a single oxidation product. Lastly, mechanisms excluded from the MCM are given in Table 3.4. The species input file used for all reactions outside of the MCM is located at this link: https://esrl.noaa.gov/csd/projects/senex/pubs/.

Reactant 1	**Reactant 2**	**Product 1**	**Product 2**	**Rate coefficient**
GUAIACOL	NO_3	NR1GUAIACOL		0.5×2.69e-11 $^{\beta}$
NR1GUAIACOL	NO_2	NR12GUAIACOL		1e-10 $^{\beta}$
NR12GUAIACOL		HNO3	N6GUAIACOL	1 $^{\alpha}$
GUAIACOL	NO_3	NR1GUAIACOL		0.5×2.69e-11 $^{\beta}$
NR1GUAIACOL	NO_2	NR14GUAIACOL		1e-10 $^{\beta}$
NR14GUAIACOL		HNO3	N4GUAIACOL	1 $^{\alpha}$
MGUAIACOL	NO_3	NR5MGUAIACOL		8.41e-11 $^{\beta}$
NR5MGUAIACOL	NO_2	NR56MGUAIACOL		1e-10 $^{\beta}$
NR56MGUAIACOL		HNO3	N6MGUAIACOL	1 $^{\alpha}$
SYRINGOL	NO_3	NR4SYRINGOL		1.58e-10 $^{\beta}$
NR4SYRINGOL	NO_2	NR34SYRINGOL		1e-10 $^{\beta}$
NR34SYRINGOL		HNO3	N3SYRINGOL	1 $^{\alpha}$
M3F	NO_3	C4MDIAL		0.3401×1.9e-11 $^{\beta}$
M3F	NO_3	FURFUR3AL		0.0036×1.9e-11 $^{\beta}$
M3F	NO_3	PPM3FURAN		0.6563×1.9e-11 $^{\beta}$
C4MDIAL		MMALANHY		0.9288×1e-10

$^{\alpha}$First order (s^{-1})

$^{\beta}$ Second order (cm^3 $molec.^{-1}$ s^{-1})

Table 3.3: Published reactions included in the model. Prefixes of N refer to nitrated products, prefixes of R refer to a radical intermediate, and numeric pre-fixes describe the position on the ring. For example NR12GUAIACOL is 1,2-dinitro-guaiacol radical.

Reactant 1	**Reactant 2**	**Product 1**	**Product 2**	**Rate coefficient (cm^3 $molec.^{-1}$ s^{-1})**
NO_2	NO_3	NO	NO_2	$4.50 \times 10^{-14} \times e^{(-1260/T)}$
HNO_3		NA		6.00×10^{-06}
N_2O_5		NA	NA	4.00×10^{-04}
M3F	NO_3	C4MDIAL	NO_2	1.90×10^{-11}

Table 3.4: MCM reactions excluded from our model.

3.2.2.2 Model and Observation Comparison

Five VOCs (toluene, isoprene + furan, methylvinylketone + methacrolein (MVK+MACR), and methylethylketone (MEK)) as well as acetonitrile (a potential BB tracer) were measured by the PTR-MS during SENEX and overlap with our emissions inventory. We have calculated the normalized excess mixing ratio (NEMR shown in E2.1 on page 11), normalized to acetonitrile, for each intercept shown in Figure 3.5. We use NEMR because the plume age is highly uncertain and therefore cannot define these measurements as emission ratios (Akagi et al., 2011). The NEMR of toluene and MVK+MACR are a factor of 1.2 greater than our inventory. Plume MEK and acetonitrile are factors of 8.3 and 3.8 greater. However, as discussed in section 3.2.1.2, the plume age is highly uncertain and thus the extent of VOC oxidation at the time of sampling is unknown. Furthermore, the time-resolution of the PTR-MS measurements only afford 1-2 data points per plume intercept, and the VOC measurements are not concurrent. Therefore, we neither constrain our emissions, or model results, to match these observations, nor do we use acetonitrile as a BB tracer. Still, on average the above background enhancement of acetonitrile in BB plumes was 1.1 ± 0.1 ppbv.

3.2.2.3 Details on model sensitivity to ambient O_3

In heavily fire impacted areas or polluted urban environments, the ambient O_3 may be larger than that observed during the SENEX nighttime BB intercepts (44 ppbv) and therefore affect the relative NO_3 and O_3 oxidative importance (Jaffe and Wigder, 2012). With sufficient NO_x, an increase in O_3 will increase NO_3 production, as well as O_3 oxidation of BBVOCs. Although, we find that doubling the background O_3 has almost no effect on the relative BBVOC oxidation. BBVOC oxidation by O_3 remains constant for rice straw and decreases from 43% to 39% for

ponderosa pine. Alternatively, reducing the background O_3 by a factor of two increases O_3 oxidation from 25% to 33% for rice straw and from 43% to 55% for ponderosa pine.

We initialized our model with background O_3 observed directly outside of the BB plume shown later in Figure 3.5 (on page 44). While this method likely provides the best estimate of local background O_3 near the BB plume we used to initialize our model, it is also representative of background O_3 levels observed regionally (near the Missouri/Kentucky/Tennessee border) as shown in Figure 3.3. Aircraft observations near the BB plumes, below 1000 m ASL, are shown in yellow in Figure 3.3 and are fit to a line (blue) with an intercept of 42 ppbv O_3. This value is within 5% of the local average of 44 ppbv, and both values are well within the range of O_3 variability at low NO_2.

3.2.2.4 Details on Model Parameters and Sensitivities

All models were run at 298 K, typical conditions for most published rate coefficient experimental conditions. While the ambient temperature during aircraft intercepts of the BB plume was 288 K, we do not expect a 10 K difference to influence model predications outside of the reported error. For the compounds included here with known temperature dependent rate coefficients a 10 K change is equal to a 30% change of the rate coefficient at most, well within the reported error limits. Roughly 90% of compounds used in this study lack published temperature dependent rate coefficients.

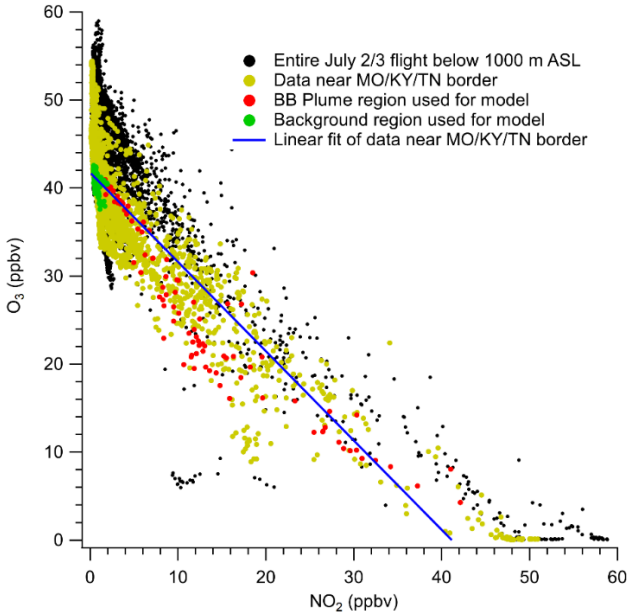

Figure 3.3: Correlation of O_3 and NO_2 for the entire July 2/3 flight (black), observations near the Missouri/Kentucky/Tennessee border (yellow), BB plume intercept (red) and background region data (green) which are aircraft observations used to initialize our model and are also shown in Figure 3.6

In order to account for dilution processes we apply a first order loss of $k_{dil} = 1.16*10^{-5}$ s^{-1}, or a 24 hour lifetime (Edwards et al., 2013b). Varying k_{dil} within a factor of 2, or removing this loss process, did not change BBVOC, NO_3 or N_2O_5 mixing ratios outside of the reported error. The error on NO_2, O_3, and HNO_3 is comparably smaller, and therefore varying k_{dil} does change NO_2, O_3 and HNO_3 concentrations outside of the reported error (Figure 3.4). Our base case model uses the reported/calculated rate coefficients and emissions. We propagate error through our model by running all combinations of upper and lower bound uncertainties on both the rate coefficients and emissions. This results in nine model runs (upper bound rate and upper bound emissions to lower bound rate and lower bound emissions). The base case model result concentrations are then bound by the concentration of the model run that produced the greatest (upper bound) and least (lower bound) concentration at each time step. Margins do not come

from an error statistic, and should therefore not be interpreted as such in further studies since they do not provide information on the error distribution.

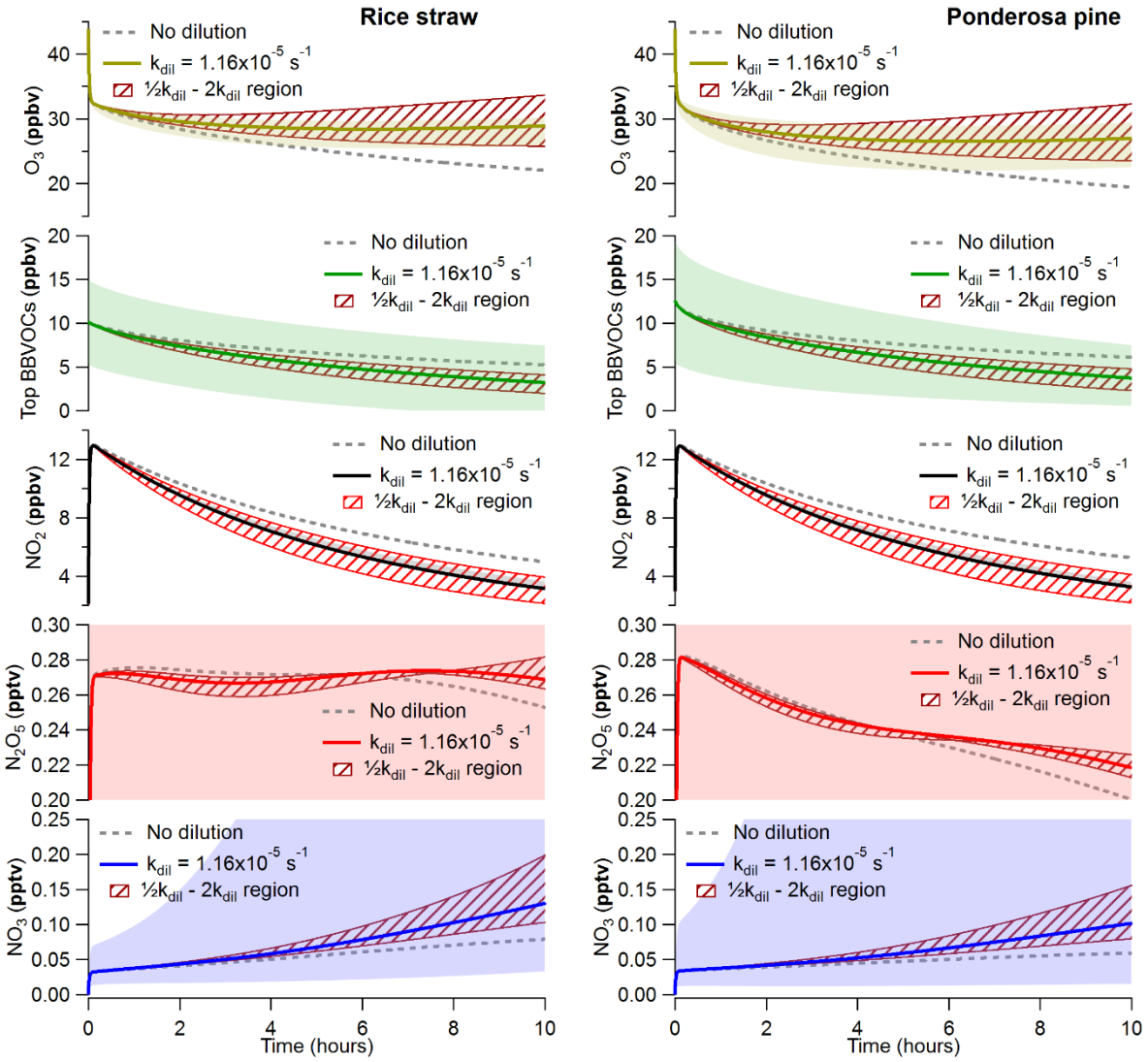

Figure 3.4: Box model time traces of the mixing ratios under different dilution scenarios for O3 (gold), NO2 (black), the BBVOCs accounting for 99% of NO3 reactivity (green), N2O5 (red), and NO3 (blue) for rice straw (left) and ponderosa pine (right) over one night (10 hours). Base case mixing ratio errors are shown by same color shading. Our base dilution case (kdil = 1.16×10-5 s-1 or a 24 hour lifetime) is shown by the solid lines with a factor of two spread encompassed by the patterned area. Scenarios with no dilution are indicated by the dashed grey line.

3.3 Results and Discussion

3.3.1 Description of Plumes Sampled by Aircraft

In panel A of Figure 3.5 the power plant plume intercepts (blue background) are distinguished from the fire plume intercepts (red background) by CO, black carbon, APAN, and glyoxal. Intercepts shown in Figure 3.5 were at an altitude between 700-900 meters. Relative to the BB plume intercepts, the power plant plume intercepts exhibited elevated levels of NO_3 and N_2O_5 (Figure 3.5B). Figure 3.6A shows a flight map of the July 2-3 flight colored red during BB plume intercepts and sized by the APAN mixing ratio. Green dashed boxes indicate sections of data shown in Figure 3.5.

Elevated levels of N_2O_5 and NO_3 might indicate power plant plume influence, but because we expect NO_3 production within BB plumes this is not a definitive tracer. A complete review of all of the July 2/3 flight shows that 3% of data with above background enhancements of our BB identifiers include elevated levels of NO_3 and N_2O_5. Therefore, we argue that the large majority of BB plumes (97%) shown in Figure 3.6 are likely not influenced by power plant plumes.

The flight covered the intersection of Missouri, Kentucky, Tennessee, and Arkansas at the Mississippi river. According to the USDA CropScape database, this land is mainly agricultural and therefore the fire plume is most likely the result of burning crop residue and stubble (CropScape, 2018; Zarzana et al., 2017). Plume intercepts occurred near winter wheat crops, and rice straw crops are situated roughly 70 km northwest. Still, rice straw is the best available fuel proxy for agricultural burning emissions. The wind direction was roughly northwesterly with most BB plume intercepts occurring in the northwest corner of Tennessee.

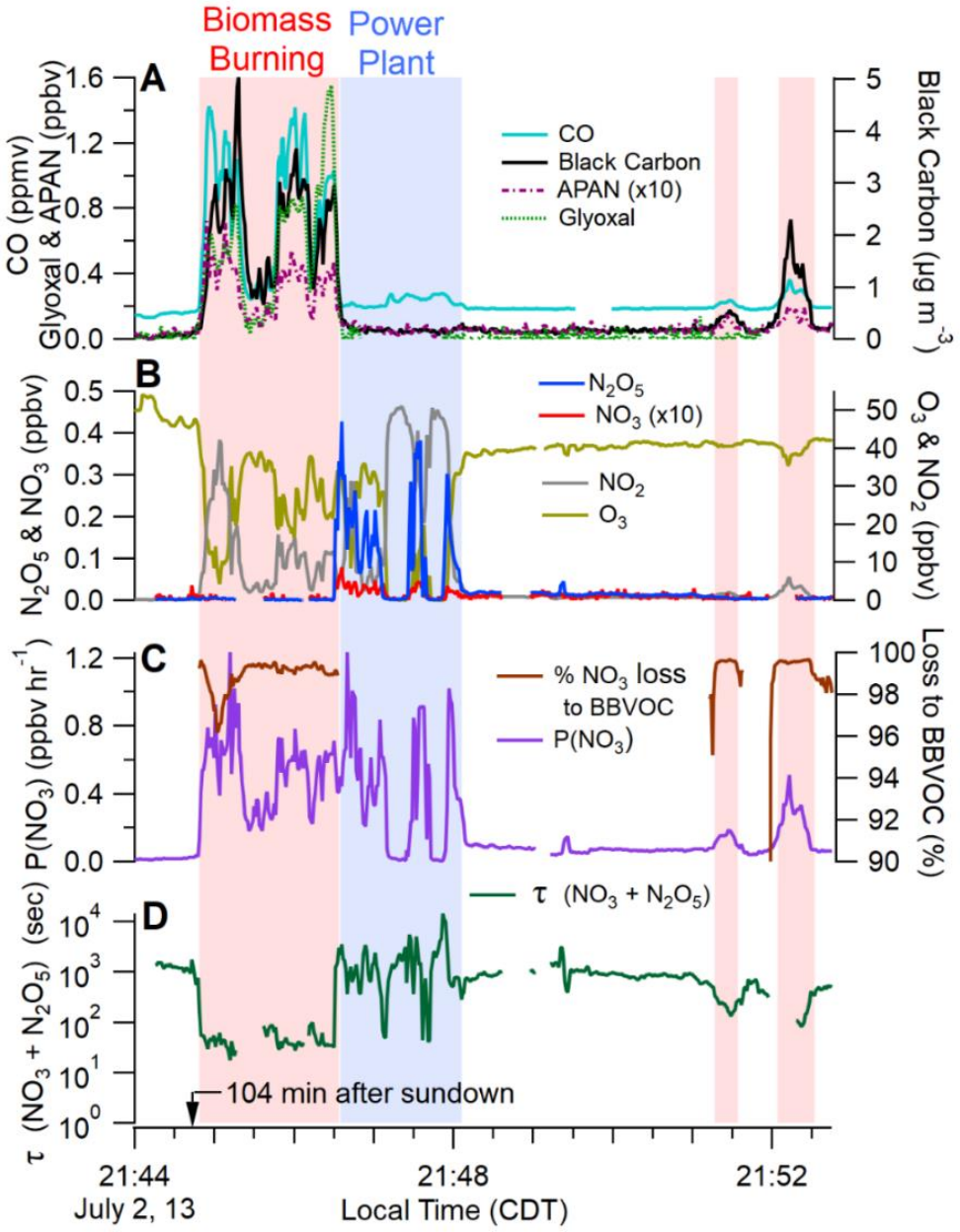

Figure 3.5: Time traces during representative sections of BB (red) and power plant (blue) plume intercepts made 104 minutes after sundown (SZA=90°). A: BB tracers, B: NO_3 N_2O_5, NO_2, and O_3 mixing ratio, C: production rate of NO_3 and the percentage of NO_3 reactivity toward BBVOCs, D: lifetime of NO_3 and N_2O_5.

3.3.2 Analysis of NO_3 and N_2O_5 from Observations

$P(NO_3)$ (given in E2.4 on page 11) was large and of similar magnitude in both the power plant plume and BB plume (Figure 3.5C). Figure 3.6B is colored by $P(NO_3)$ during BB intercepts

only, and shows that large NO_3 production rates, near 1 ppbv hr^{-1}, were observed during multiple BB plume intercepts. Despite the large NO_3 radical production, the NO_3 and N_2O_5 concentrations within the BB plume were below the 3 pptv (Warneke et al., 2016) stated detection limit of the instrument (Figure 3.5B), yielding short $NO_3 + N_2O_5$ lifetimes (τ, given in E2.5). Indeed, as shown in Figure 3.5D, τ is roughly a factor of 100 lower within the BB plume as compared to the power plant plume and background air. Because the NO_3 and N_2O_5 were below stated detection limits in the BB plumes, the corresponding lifetimes shown in Figure 3.5D are upper limits, and the actual lifetimes may be considerably shorter.

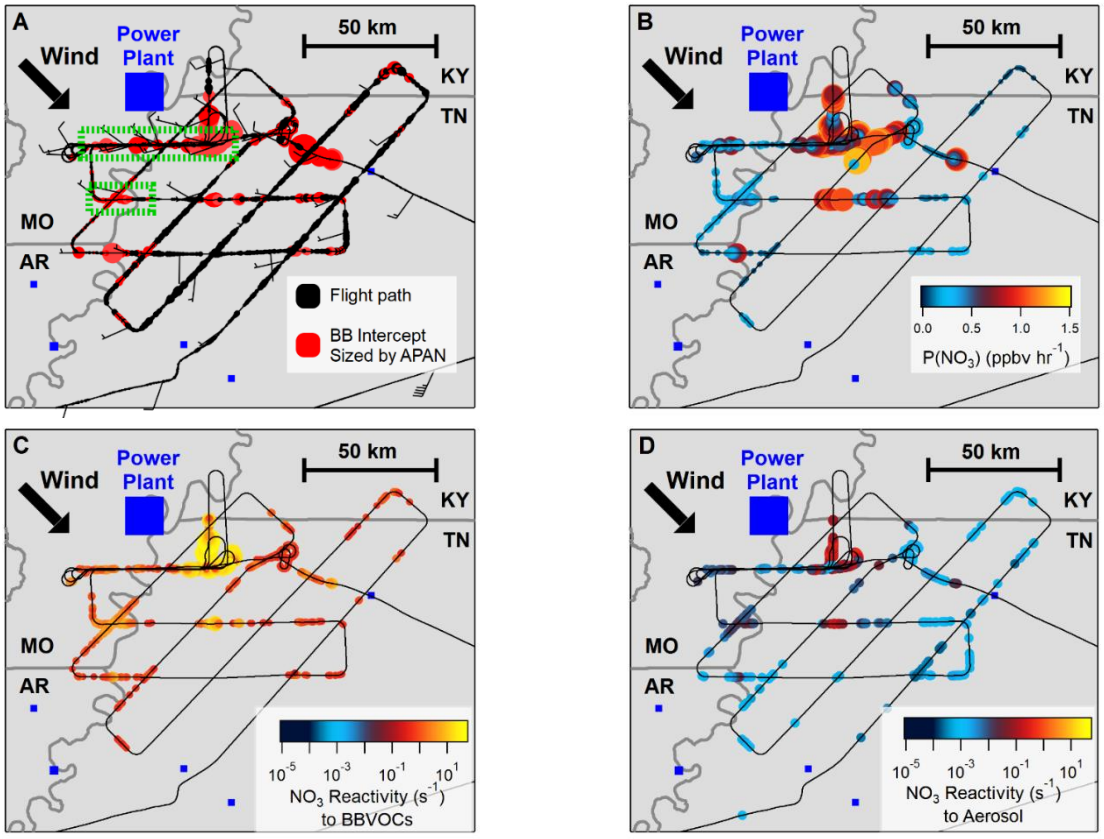

Figure 3.6: Flight maps of the SENEX July 2-3 2013 night flight. A: BB intercepts colored by red markers, sized by APAN (0.01-0.1 ppbv), and green dashes indicate sections shown in Figure 3.5, B: Production rate of NO_3, C: and D: are comparisons of NO_3 reactivity toward BBVOCs (C) and toward aerosol (D) on the same color and log scale.

The high production rate and short lifetime of $NO_3 + N_2O_5$ within the BB plume is evidence for rapid NO_3 or N_2O_5 loss pathways. BB plumes contain large quantities of both aerosol and BBVOCs, which provide two efficient NO_3/N_2O_5 loss pathways. To understand the competition between these loss processes we calculated an instantaneous NO_3 reactivity toward aerosol and toward BBVOCs. The total NO_3 loss to BBVOC is calculated using the sum of BBVOC reactivity normalized to CO (E2.2). The total NO_3 loss to aerosol uptake is given as the sum of both NO_3 and N_2O_5 uptake rate coefficients as seen in E2.6 and E2.7.

Calculations use uptake coefficients of $\gamma_{N_2O_5} = 10^{-2}$ for N_2O_5 (Chang et al., 2011) and $\gamma_{NO_3} = 10^{-3}$ for NO_3. However, γ_{NO_3} values have a wide range (Brown and Stutz, 2012). Using a value of $\gamma_{NO_3} = 1$ the average aerosol reactivity is 0.08 s^{-1} with a median of 0.03 s^{-1}. Using a value of $\gamma_{NO_3} = 10^{-3}$ the average aerosol reactivity is 0.03 s^{-1} with a median of 0.03 s^{-1}. The reactivity toward BBVOCs is on average 4 s^{-1} with a median of 1.4 s^{-1}. Compared to the reactivity of BBVOCs, the choice of NO_3 uptake coefficient γ_{NO_3} has a negligible effect.

As seen in Figure 3.6C & D we compare the NO_3 reactivity toward BBVOCs, and aerosol uptake during BB plume intercepts, respectively. In all BB intercepts, the calculated NO_3 reactivity toward BBVOCs is a factor of 100 - 1000 greater than aerosol uptake. Figure 3.5C shows the percentage of NO_3 reactivity dominated by BBVOC with a median >99%.

3.3.3 Reactivity of NO_3 to BBVOCs

To understand which BBVOCs may be responsible for the rapid initial loss of NO_3 we calculated the relative NO_3 reactivity for 302 compounds in rice straw and ponderosa pine burning emissions. The top panel of Figure 3.7 shows the ranked order of the compounds that account for 99% of the rice straw initial NO_3 reactivity. Eight furan or phenol compounds are responsible for

75% of the initial NO_3 reactivity. Most of, the initial NO_3 reactivity for a rice straw fire is accounted for by phenols (60^{+20}_{-14}%) and furans (23^{+20}_{-6}%), as well as pyrroles and furfurals (8^{+9}_{-3}% combined).

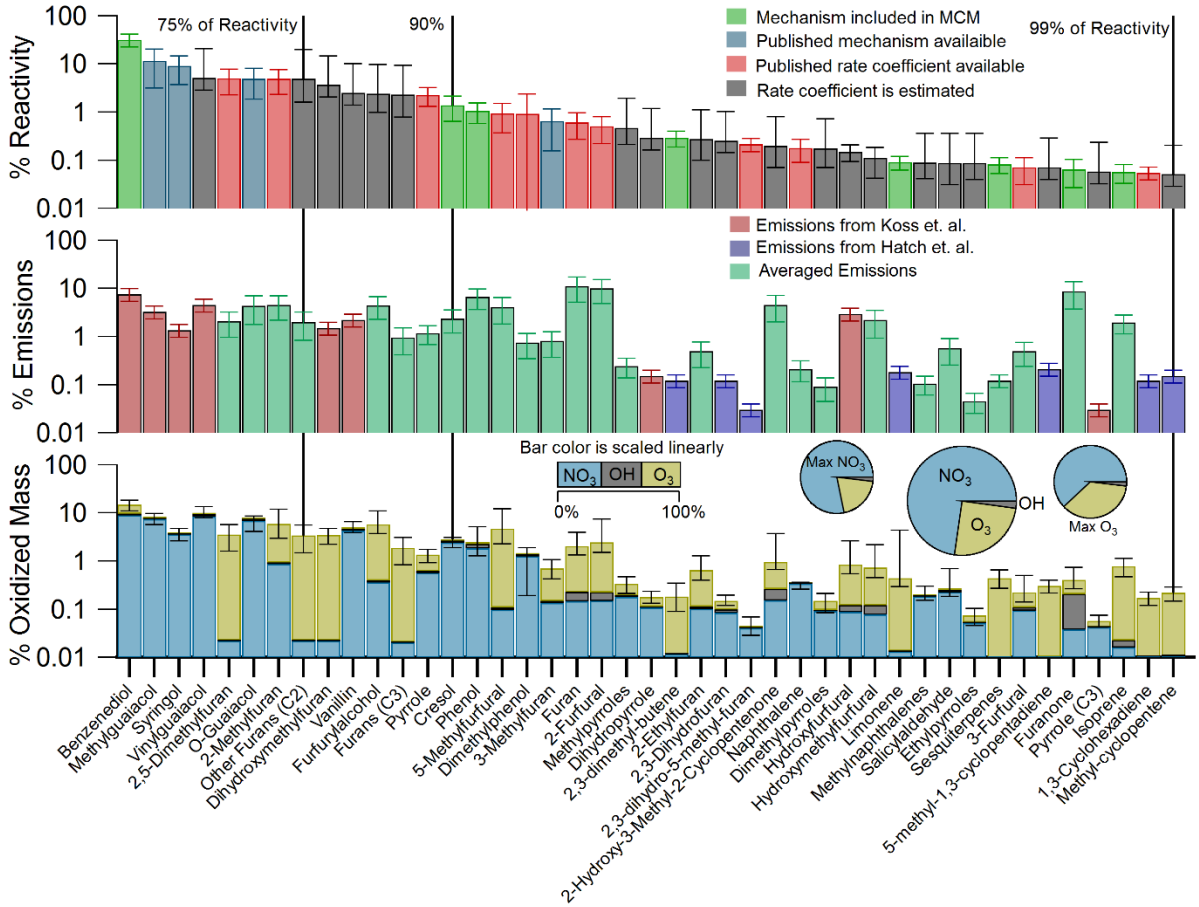

Figure 3.7: Rice Straw fuel. The top panel shows the ranked order of the compounds that account for 99% of the rice straw initial NO_3 reactivity. The color scale describes the origin of the mechanisms or rate coefficient used. The middle panel is the relative BBVOC emission ratio normalized to the total BBVOC emission ratio and the color scale describes the origin of the emissions data. The bottom panel is the relative nighttime reacted mass (10 hours) normalized to total reacted mass. While the bar height is on a log scale, the color scale is linear and indicates the fraction of oxidation by NO_3 (blue), O_3 (gold), and OH (grey). The center pie chart shows the fraction of reacted mass in the base case with the maximum NO_3 oxidation case to the left, and maximum O_3 oxidation case to the right. All panels sum to 100%.

The top panel of Figure 3.8 shows the ranked order of the compounds that account for 97% of the ponderosa pine initial NO_3 reactivity. The top 75% of initial NO_3 reactivity is distributed among 13 compounds with phenols (62^{+27}_{-23}%), furans (18^{+12}_{-4}%), pyrrole and furfural (8^{+8}_{-3}%

combined) again dominating the total reactivity. Unlike rice straw, a ponderosa pine fire plume has significant reactivity towards terpenes (8^{+2}_{-1}%). The initial NO_3 reactivity towards terpenes and unsaturated hydrocarbons in a rice straw plume is <1%. These differences in reactivity are due to differences in emissions between the two fuels as explained below (Hatch et al., 2017).

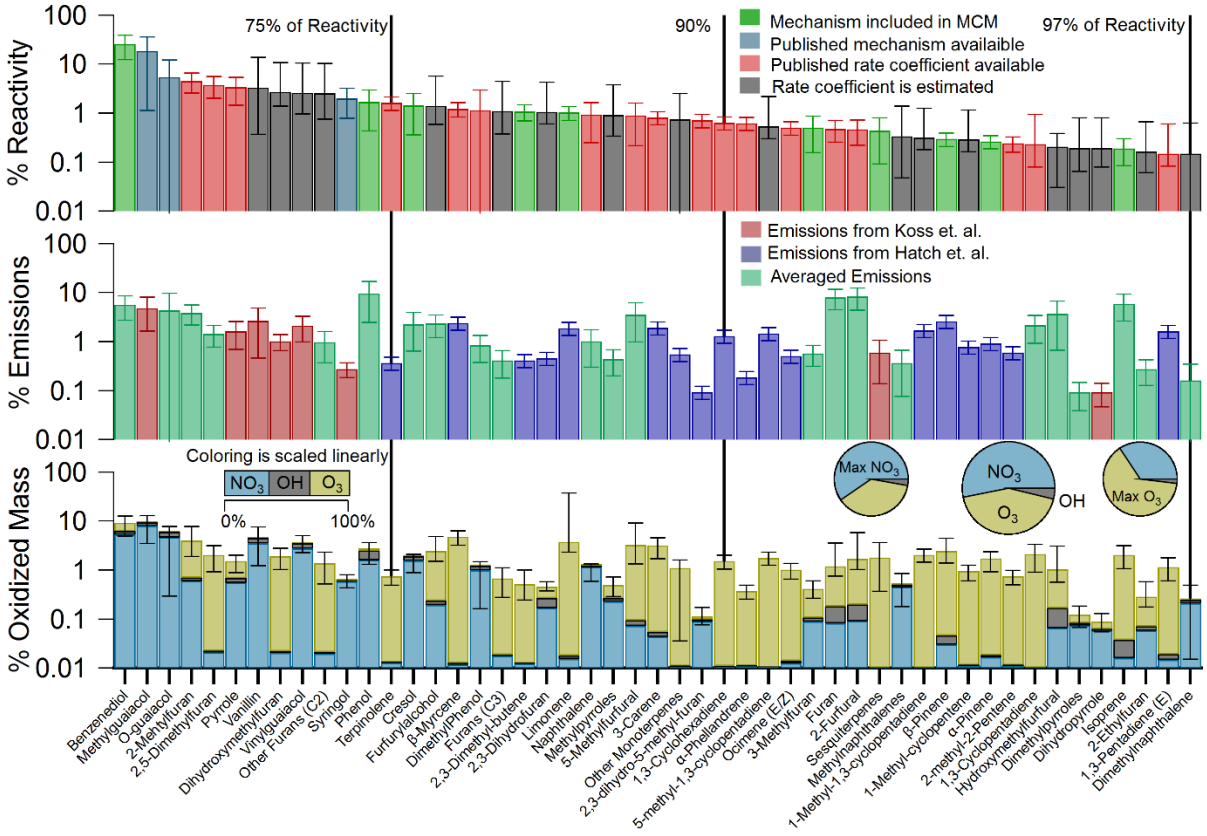

Figure 3.8: Same as Figure 3.7, but for the ponderosa pine fuel. In the bottom panel the bar height is on a log scale, but the color scale is linear and indicates the fraction of oxidation by NO_3 (blue), O_3 (gold), and OH (grey).

The middle panels of Figure 3.7 and Figure 3.8 show the emission ratios for each compound normalized to total emissions. The color indicates the origin of the emission ratio. The rice straw fire emissions for compounds included in Figure 3.7 are mainly furans (33±8%), phenols (27±4%), and furfurals (24±6%), while unsaturated hydrocarbon and terpene emissions account for only 3±1%. In contrast, the ponderosa pine fire emissions have a larger representation

of terpenes (18±4%) and unsaturated hydrocarbons (10±2%), but phenols (33±10%), furans (17±4%) and furfurals (18±6%) are all still significant.

3.3.4 0-D Box Model Analysis

To better understand smoke plume evolution and to determine the amount of BBVOC mass oxidized during one night (10 hours), we ran a 0-D box model for both rice straw and ponderosa pine fire emissions. NO_3 and N_2O_5 remained below 3 pptv (Figure 3.9), consistent with field observations (Figure 3.5B). Figure 3.9 illustrates that the summed concentrations of the most reactive BBVOCs are comparable to NO_2, suggesting there is approximately as much NO_3 precursor available as there is BBVOC to be oxidized. For both fuels, roughly 50-60% of NO_2 and the BBVOC compounds listed in Figure 3.7 and Figure 3.8 are depleted by chemistry (excluding dilution) in one night. Our box-model suggests several abundant BBVOCs survive the night with more than 50% of their initial starting concentration, such as phenol, furan, furfural and hydroxymethylfurfural.

HNO_3 production is complex within the model, and both maximum and minimum uncertainty bounds on HNO_3 concentrations are the result of higher bound BBVOC emissions, but lower and higher bound BBVOC rate coefficients, respectively. HNO_3 is the product of reactions of phenolic compounds with NO_3, which proceeds by H-abstraction. HNO_3 production is dominated by catechol + NO_3 (~60%) within the first few hours, but as the more reactive compounds are depleted, the lesser reactive compounds like methyl guaiacol, guaiacol and syringol react with NO_3 and dominate in the last two hours. HNO_3 may be lost to the particle phase with concurrent NH_3 emission or other nitrogen species, however this loss mechanism is not included in our model.

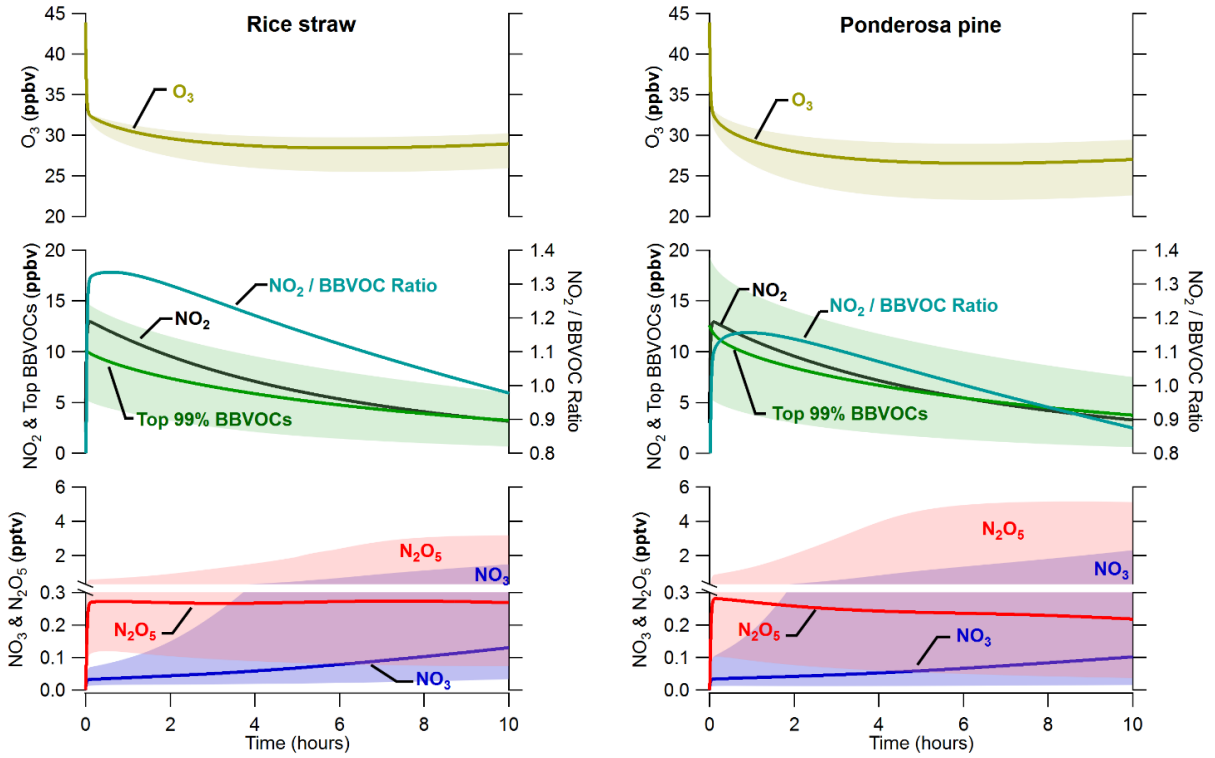

Figure 3.9: Box model time traces of the mixing ratios for O_3 (gold), NO_2 (black), the BBVOCs accounting for 99% of NO_3 reactivity (green), N_2O_5 (red), and NO_3 (blue) for rice straw (left) and ponderosa pine (right) over one night (10 hours). A physical dilution first order loss of $k_{dil} = 1.16*10^{-5}$ s^{-1}, or a 24 hour lifetime is included. Same color shading indicates error. NO_3 and N_2O_5 uncertainty is large and the maximum concentrations are the result of minimal BBVOC emissions causing NO_3 and N_2O_5 to build throughout the night.

For both fuels, catechol is the most reactive compound, and accounts for 32±9% and 26±13% of initial NO_3 reactivity at the start of the simulation for rice straw and ponderosa pine plumes, respectively. However, Koss et al., 2018 were unable to distinguish between catechol and methylfurfural at m/z = 110.1 We assume a 50/50 contribution here, which yields catechol emission ratios of 2.5±0.8 ppbv $ppmv^{-1}$ CO for rice straw and 1.5±0.6 ppbv $ppmv^{-1}$ CO for ponderosa pine. Still, the high reactivity is mainly due to the large catechol rate coefficient ($9.9*10^{-11}$ cm^3 $molecule^{-1}$ s^{-1}, Olariu et al., 2004), which is the third greatest among the emitted compounds.

Catechol is known to react with NO_3 by H-abstraction, with subsequent addition of NO_2 to the aromatic peroxy radical to form 4-nitrocatechol with a near-unity molar yield of 0.91±0.06

(Finewax et al., 2018). Further, 4-nitrocatechol is expected to almost completely (96%) partition to the particle phase (Finewax et al., 2018). Recently, Hartikainen et al., 2018 investigated dark oxidation of residential wood combustion and found strong correlations between the depletion of phenolic compounds and the formation of NO_3-initiated SOA. In wintertime BB events, 4-nitrocatechol and other derivatives have been detected in aerosol and are considered important light-absorbing components of brown carbon (BrC), (Claeys et al., 2012; Desyaterik et al., 2013; Gaston et al., 2016; Hinrichs et al., 2016; Iinuma et al., 2010; Laskin et al., 2015; Lin et al., 2017; Mohr et al., 2013; Xie et al., 2017).

SOA yields are a function of mass loadings (Odum Jay et al., 1996). Using a catechol mass loading of 300 μg m^{-3} from (Finewax et al., 2018) as well as a total observed aerosol plume measurement of 58.7 μg m^{-3} we estimate a 4-nitrocatechol SOA mass yield of 120%. Assuming 0.6 ppbv of catechol in ponderosa pine and 0.8 ppbv in rice straw (initial model conditions) with 44 ppbv O_3, 13 ppbv of NO_x and $k_{dil} = 1.16*10^{-5}$ s^{-1}, we estimate the SOA produced from catechol to be 3.8 ± 1.0 μg m^{-3} in 8 hours and $4.0^{+1.1}_{-1.0}$ μg m^{-3} in 8.5 hours for a rice straw and ponderosa pine plume, respectively. Further, there is evidence to suggest furans and furfurals may also be a source of SOA precursors (Hartikainen et al., 2018; Hatch et al., 2017).

The bottom panel of Figure 3.7 shows the reacted mass per compound normalized to the total reacted mass. The bar height is on a log scale, but the bar color is linearly scaled and indicates the fraction of nighttime oxidation by NO_3 (blue), O_3 (gold), and OH (grey) after 10 hours for each compound. The center pie chart in Figure 3.7 and Figure 3.8 represents the base case fraction of reactant mass oxidized by each oxidant. The left and right pie charts show results for the estimated maximum possible NO_3 and maximum possible O_3 oxidation, respectively. Uncertainty in the

fraction of oxidized mass is calculated from the uncertainties in individual compound emissions and rate coefficients. For the compounds comprising a rice straw BB plume, the majority of mass is oxidized by NO_3 (72^{+6}_{-11}%). This is expected because the rice straw fuel emissions are rich in oxygenated aromatic and hetero-aromatic emissions, which are generally less reactive toward O_3. Terpenes and unsaturated hydrocarbons, which are a small fraction of emissions in Figure 3.7, are relatively more reactive toward O_3. Even so, O_3 still has a significant oxidative impact and is responsible for 26^{+11}_{-6}% of oxidized BBVOC mass.

The relative amount of oxidized mass for ponderosa pine is shown in the bottom panel of Figure 3.8. Almost half of the oxidized mass for compounds included in Figure 3.8 is due to O_3 (43^{+21}_{-6}%) for our base case. The phenolic compounds mainly undergo NO_3 oxidation while terpenes and unsaturated hydrocarbons are mainly oxidized by O_3. Furans and the hetero-aromatics are oxidized approximately evenly by O_3 and NO_3. The increased fraction of O_3 oxidation is the result of the increased fraction of unsaturated hydrocarbon and terpenes in the ponderosa pine emissions when compared to rice straw.

The nighttime chemical evolution and oxidation products of a biomass burning plume will depend on the relative NO_3 and O_3 reactivity. Neglecting the small contribution from OH oxidation, Edwards et al., 2017 show the competition between NO_3 and O_3 oxidation of biogenic VOCs (BVOC) is dependent on the NO_x/BVOC ratio. We scaled our BBVOC emissions to maintain the NO_x/BBVOC ratio expected for rice straw (0.4 ± 0.1) or ponderosa pine (0.3 ± 0.1) emissions. However, because fires are highly variable, the NO_x/BBVOC ratio for any given fuel may vary from fire to fire. For rice straw, a factor of two increase in NO_x increases the fraction of NO_3 oxidation from 72% to 84%, while a factor of two decrease in NO_x decreases relative NO_3

oxidation to 55%. Similarly, for ponderosa pine, doubling NO_x increases the fraction of NO_3 oxidation from 53% to 66%, while halving NO_x decreases relative NO_3 oxidation to 37% and increases O_3 to 57%. Furthermore, we find that a factor of two change in ambient O_3 concentration has little effect on the relative NO_3 and O_3 reactivity as we detail in section 3.2.2.3.

3.3.5 Conclusions

The time of day in which a fire is active will determine the fate of its emissions. This paper presents the first nighttime aircraft intercepts of a BB plume combined with an inventory of 302 BBVOC emissions and an oxidation model to predict the lifetime and fate of BB emissions in the dark. Fire emissions at times near sunset will undergo the chemistry we have detailed here, which suggests a roughly 60% depletion (for both rice straw and ponderosa pine) of fire-derived NO_x. We find that nighttime chemistry is likely to proceed by NO_3, rather than N_2O_5, further slowing the loss of NO_x (R1.8 & R1.11). Our model applies to chemistry at the center of a plume and does not include dispersion. Dispersion mixes NO_x with background O_3 at the edges of the plume leading to faster depletion, and therefore the values we report are likely lower limits. Even so, 18-19% of BBVOC mass, out of the total BBVOC mass that we model, will be oxidized in one night. That is roughly a 55% depletion of the BBVOCs that are reactive toward NO_3. There is evidence that many of these NO_3 reactive compounds can form secondary BrC aerosol (Claeys et al., 2012; Desyaterik et al., 2013; Gaston et al., 2016; Hinrichs et al., 2016; Iinuma et al., 2010; Laskin et al., 2015; Lin et al., 2017; Mohr et al., 2013; Xie et al., 2017), suggesting nighttime oxidation may be a significant source of BB derived BrC. Furthermore, future BB photochemical models should consider that these reactive phenolic-, furan- and furfural-like compounds are not only reactive toward NO_3, but also O_3 and OH, thus affecting next-day BB photochemistry.

3.4 Future Directions

Reactivity calculations and box-model results are limited by a lack of kinetic and mechanistic studies for O_3, NO_3, and OH + BBVOCs reactions. Out of the 302 compounds used in our calculations, only 55 compounds were listed in the MCM with NO_3 reactions and an additional 33 in the MCM without NO_3 reactions. Roughly 23% of the reactivity in Figure 3.7 for rice straw and 19% of the reactivity in Figure 3.8 for ponderosa pine were calculated with estimated NO_3 rate coefficients. In addition, nearly half of the 62 O_3 + BBVOC, and a quarter of the OH + BBVOC, reactions used here have no published rate coefficients.

While pyrrole derivatives have emissions that are less than their furan analogues, it is expected that rate coefficients of pyrroles + NO_3 are greater than furans + NO_3 (Cabañas et al., 2004). Even so, to our knowledge there are no published rate coefficients for any pyrrole derivatives in the emissions inventories. Further, furan type compounds are mainly alkyl-substituted derivatives, but hydro derivatives such as 2,3 dihydrofuran in Figure 3.7 and Figure 3.8, are also emitted. The same is true for pyrroles, for example dihydropyrrole in Figure 3.7 and Figure 3.8. While kinetic studies of hydro-furan/pyrrole compounds are much less available, they likely have rate coefficients greater than their aromatic analogues (Berndt et al., 1996; Martin et al., 2002).

In addition, there are a few alcohol and hydroxyl furans that account for the top 99% of compounds contributing to total BBVOC reactivity. These compounds will likely react via H-abstraction by NO_3 similar to catechol and other phenols and therefore affect the HNO_3 production that is not captured in our box-model without mechanistic information. Lastly, phenol derivatives such as vanillin and vinylguaiacol account for large portions of ponderosa pine and rice straw

reactivity, but we can only estimate their rate coefficients to be similar to guaiacol. More kinetic and mechanistic work is needed in order to understand the importance and role of reactive furan, furfural, phenol, and pyrrole compounds in a nighttime BB plume.

Chapter 4: Nighttime and Daytime Dark Oxidation Chemistry in Wildfire Plumes: An Observation and Model Analysis of FIREX-AQ Aircraft Data

Abstract

Wildfires are increasing in size across the western U.S., leading to increases in human smoke exposure and associated negative health impacts. The impact of biomass burning (BB) smoke, including wildfires, on regional air quality depends on emissions, transport, and chemistry, including oxidation of emitted BB volatile organic compounds (BBVOCs) by the hydroxyl radical (OH), nitrate radical (NO_3), and ozone (O_3). During the daytime, when light penetrates the plumes, BBVOCs are oxidized mainly by O_3 and OH. In contrast, at night, or in optically dense plumes, BBVOCs are oxidized mainly by O_3 and NO_3. This work focuses on the transition between daytime and nighttime oxidation, which has significant implications for the formation of secondary pollutants and loss of nitrogen oxides (NO_x = NO + NO_2), and has been understudied. We present wildfire plume observations made during FIREX-AQ (Fire Influence on Regional to Global Environments and Air Quality), a field campaign involving multiple aircraft, ground, satellite, and mobile platforms that took place in the United States in the summer of 2019 to study both wildfire and agricultural burning emissions and atmospheric chemistry. We use observations from two research aircraft, the NASA DC-8 and the NOAA Twin Otter, with a detailed chemical box model, including updated phenolic mechanisms, to analyze smoke sampled during mid-day, sunset, and nighttime. Aircraft observations suggest a range of NO_3 production rates (0.1 – 1.5 ppbv h^{-1}) in plumes transported both mid-day and after dark. Modeled initial instantaneous reactivity toward BBVOCs for NO_3, OH, and O_3 is 80.1 %, 87.7 %, 99.6 %, respectively. Initial NO_3 reactivity is 10 – 10^4 times greater than typical values in forested or urban environments and reactions with

BBVOCs account for ≥ 98 % of NO_3 loss in sunlit plumes (jNO_2 up to 4×10^{-3} s^{-1}), while conventional photochemical NO_3 loss through reaction with NO and photolysis are minor pathways. Alkenes and furans are mostly oxidized by OH and O_3 (11 – 43%, 54 – 88% for alkenes; 18 – 55 %, 39 – 76 %, for furans, respectively), but phenolic oxidation is split between NO_3, O_3, and OH (26 – 52 %, 22 – 43 %, 16 – 33 %, respectively). Nitrate radical oxidation accounts for 26 – 52 % of phenolic chemical loss in sunset plumes and in an optically thick plume. Nitrocatechol yields varied between 33 % and 45 %, and NO_3 chemistry in BB plumes emitted late in the day is responsible for 72 – 92 % (84 % in an optically thick mid-day plume) of nitrocatechol formation and controls nitrophenolic formation overall. As a result, overnight nitrophenolic formation pathways account for 56 ± 2 % of NO_x loss by sunrise the following day. In all but one overnight plume we model, there is remaining NO_x (13 % – 57 %) and BBVOCs (8 % – 72 %) at sunrise.

4.1 Introduction

Wildfires emit Nitrogen Oxides (NO_x = NO + NO_2), nitrous acid (HONO), biomass burning VOCs (BBVOCs) and particulate matter (PM) that evolve chemically on a range of time scales, from seconds to weeks downwind (Akagi et al., 2011; Andreae and Merlet, 2001b; Decker et al., 2019; Hatch et al., 2015, 2017; Koss et al., 2018; Palm et al., 2020). These emissions and their chemical products influence air quality through ozone (O_3) production, emitted PM, and secondary organic aerosol formation (SOA) (Brey et al., 2018; Jaffe et al., 2020; Jaffe and Wigder, 2012; Lu et al., 2016; Palm et al., 2020; Phuleria et al., 2005). However, the evolution of the smoke downwind is influenced by several variables such as fuel type, burn conditions, moisture content, nitrogen content, meteorology, and time of day.

Like most atmospheric oxidation processes, the oxidation of BBVOCs is influenced by three key atmospheric oxidants: O_3, the hydroxyl radical (OH), and the nitrate radical (NO_3), which are detailed in Chapter 1 on page 2. In the previous chapter, we found that modeled NO_3 reactivity was found to be mostly (>99 %) from reactions with BBVOCs (R1.12) as opposed to heterogeneous reactions with aerosol particles in an agricultural burning plume sampled after sunset. This is the result of elevated concentrations of several highly reactive BBVOCs within the plume. Specifically, directly emitted aromatic alcohols (phenolics) react with NO_3 at near the gas-kinetic limit to form nitrophenolics, a subset of nitroaromatics, and secondary organic aerosol (Finewax et al., 2018; Lauraguais et al., 2014; Liu et al., 2019; Xie et al., 2017). Nitrophenolics absorb strongly in the ultraviolet and visible regions of the solar spectrum, and are expected to significantly contribute to brown carbon (BrC) absorption (Palm et al., 2020; Selimovic et al., 2020). Phenolic reactions with OH in the presence of NO_x also form nitrophenolics, but at one third the yield (Finewax et al., 2018).

Wildfire emissions typically peak in the mid-afternoon to evening, and continue to emit smoke into the night (Giglio, 2007; Li et al., 2019). Furthermore, large smoke plumes can be optically thick, with little photolysis at their center. This means that most smoke plumes will be oxidized in the dark during some, if not all, of their transport. Yet, the vast majority of in-situ field investigations of biomass burning smoke has been conducted under sunlight, and most analyses of daytime smoke plumes have so far focused on plume oxidation by OH and O_3 only (Coggon et al., 2019; Keywood et al., 2015; Liu et al., 2016; Palm et al., 2020).

In the summer of 2019, both the NOAA Twin Otter and the NASA DC-8 aircraft executed a series of research flights sampling smoke plumes as part of the Fire Influence on Regional to

Global Environments and Air Quality (FIREX-AQ) campaign. Here, we present a detailed analysis of smoke plumes from three fires using observations from FIREX-AQ to constrain a detailed zero-dimensional (0-D) chemical box model. We investigate one optically-thick plume emitted mid-day, three smoke plumes emitted near or at sunset, and one theoretical plume emitted after sunset. We discuss the reactivity and competitive oxidation for all oxidants, NO_3, O_3, and OH, toward a suite of BBVOCs. Further, we detail the oxidation pathways of phenolics, discuss the variables that affect the yield of nitrophenolics, and describe how nitrophenolics have a significant impact on NO_x loss and fate.

4.2 Methods

4.2.1 Aircraft Observations

Aircraft Measurements for this analysis are described in detail in section 2.4.2 on page 18. Briefly, this analysis uses NOAA Twin Otter and NASA DC-8 observations of four wildfire plumes. We use observations of CO, NO, NO_2, O_3, HONO, and NO_y (only available on the DC-8) as well as the meteorological conditions temperature, relative humidity, and pressure to constrain the model. We also use a suite of BBVOCs to constrain and/or compare to the model.

4.2.2 Fire Descriptions

Fires used in this analysis are detailed in section 2.5 on page 24 with flight maps in Figure 2.2. Table 2.2 summarizes fire locations, sampling platform, and fuel types (Inciweb, 2019b, 2019c, 2019a). Briefly, this analysis focuses on four semi-Lagrangian experiments from three separate fire complexes: the Castle Fire plume in northern Arizona, the 204 Cow Fire plume in central Oregon (referred to as Cow from here on), and two from the Williams Flats Fire plume in eastern Washington (referred to as WF1 and WF2 from here on).

WF1 contained smoke emitted from about 14:00 – 16:00 local time (PDT), or the early to late afternoon, while WF2 sampled smoke emitted near sunset. The sampled smoke varied in age from 36 min – 4 h. Smoke sampled from the Castle Fire plume varied in age from approximately 2 min – 1.5 h. Smoke sampled from the Cow Fire plume varied in age from approximately 2 – 3 h.

We select the above plume samplings among others because of their data coverage, potential for active chemistry and sunset-like conditions defined as the following: 1) sampled by semi-Lagrangian transects roughly perpendicular to the prevailing wind direction, 2) had available measurements of CO, NO_x, HONO, O_3, photolysis rates, and aerosol surface area, 3) contained either reduced plume-center photolysis ($jNO_2<10^{-3}$ s^{-1}) or plume ages <3 h by sunset, and 4) sampled a plume age range >1 h.

4.2.3 Box Model Description

We modeled smoke plumes from three fires (Castle, Cow, and WF). We present four model cases (Castle, Cow, WF1, WF2) constrained by aircraft observations and one case (Dark) identical to the WF2 case except all modeled photolysis frequencies are set to zero. The Dark case simulates oxidation of the WF2 plume if it was emitted after sunset. The Dark case is used to understand the effect of photolysis on the WF2 model run.

The Cow, WF2, and Dark cases are run from emission until sunrise the following day (about 12 h). The Castle case is run for 2.6 h until all BB emissions are near (<<1%) background levels. We run the WF1 case until the age of the oldest sampled smoke (~4 h) because we do not have any observations of photolysis rates with which to constrain the model past that point.

Box modelling was performed using the Framework for 0-D Atmospheric Modelling (F0AM) (Wolfe et al., 2016), described in 2.2 on page 13, with chemistry and emissions described in the following section. We start the model at the emission time (age = 0) of the earliest smoke transect (the youngest sampled smoke), which occurred between 2 min and 2 h before the first plume transect, depending on the plume. In most cases, we use an iterative method constrained to a subset of observations (described below) to estimate emissions.

While all plumes were sampled by aircraft following a semi-Lagrangian strategy, we model each plume as if it were Lagrangian - i.e., it is assumed that the emissions and fire conditions were constant over the course of sampling. Further, we constrain our model to plume-center observations because we model only the plume-center and represent mixing through a dilution term. Consequently, the model does not represent differences in chemical regimes that may occur between the center and edge of a plume.

4.2.3.1 Chemistry

Our model uses the master chemical mechanism (MCM, v3.3.1 via http://mcm.york.ac.uk), in conjunction with a NOAA biomass burning mechanism included in F0AM v4.0 (Bloss et al., 2005; Coggon et al., 2019; Decker et al., 2019; Jenkin et al., 1997, 2003, 2012, 2015) and updates to OH- and NO_3-initiated oxidation of phenolic compounds described here.

Phenol and cresol oxidation have been studied in greater detail than their oxidation products such as catechols and methylcatechols (Calvert et al., 2011). Thus, in order to update the phenolic chemistry, where literature values are unavailable we extrapolate phenol and cresol branching ratios, rate coefficients, and products for catechol, methylcatechol, and the three isomers of dimethylcatechol. As an example, Figure 4.1 shows our reaction mechanisms involving

catechol. Reactions in black represent reactions already in the MCM, while reactions in brown represent added reactions.

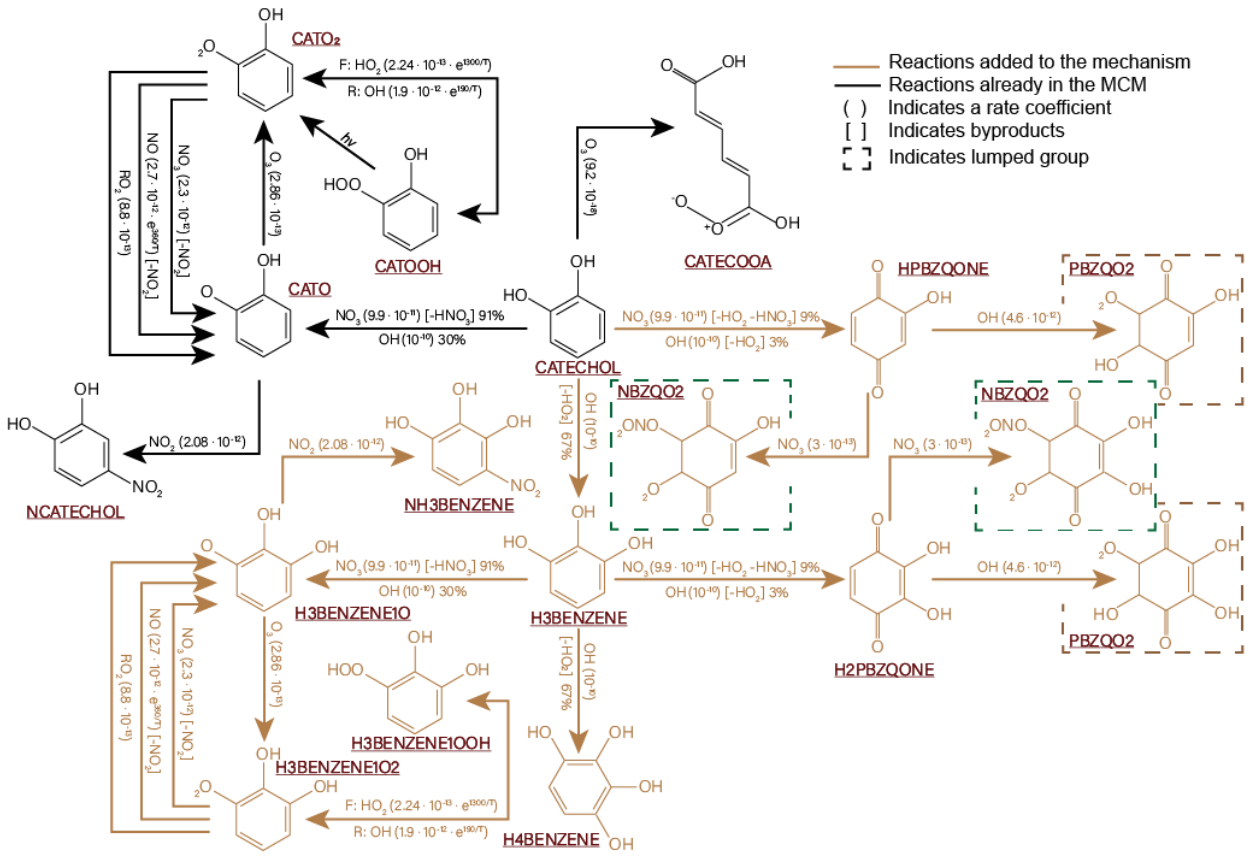

Figure 4.1 : Subset of phenolic mechanism expansion showing catechol related reactions only. Reactions that are in the MCM are shown in black, and added reactions are shown in brown. Compounds that we boxed are lumped in the mechanism. Compound names correspond to the provided FACSIMILE provided in Appendix: Code for Phenolic Mechanism on page 190.

The reaction of phenol and cresol + OH is known to form catechol and methylcatechol, respectively, by OH addition to the ring (Olariu et al., 2002). Similarly, the formation of trihydroxybenzene from catechol was suggested by Nakao et al., 2011 and trihydroxy toluene was identified as an oxidation product from methylcatechol by Schwantes et al., 2017. Further, reactions of phenol and cresol with OH are also known to produce benzoquinones (Olariu et al., 2002) and Schwantes et al., 2017 identified hydroxymethyl benzoquinone from methylcatechol.

Finewax et al., 2018 report the yield of nitrocatechol from OH oxidation of catechol to be 30 ± 3%. Despite these recent studies, MCM v3.3.1 assumes, under high NO_2 conditions, a 100% yield of nitrocatechol and nitromethylcatechol from OH-initiated oxidation of catechol and methylcatechol, respectively.

In the updated phenolic mechanism used here, the rate coefficients and branching ratios are taken from the literature when possible, but estimated from analogous reactions when unavailable. OH-initiated oxidation of catechol, methylcatechol, and dimethylcatechols is assumed to form 30% nitrocatechol, nitromethylcatechol, and nitrodimethylcatechol, respectively, under high NO_2 conditions as extrapolated from Finewax et al., 2018. The remaining 70% of products from OH-initiated catechol, methylcatechol, and dimethylcatechols produce trihydroxybenzene and hydroxybenzoquinone type products consistent with recent work for catechol and methyl catechol oxidation (Nakao et al., 2011 and Schwantes et al., 2017). To calculate the branching ratio between hydroxybenzoquinone and trihydroxybenzene from catechol + OH, we scale the yields found for each type from literature for phenol + OH (Nakao et al., 2011; Olariu et al., 2002). The result is an estimated 3% yield of hydroxybenzoquinone and a 67% yield of trihydroxybenzene. Similarly, for methylcatechol and dimethylcatechol + OH, we scale the yields from literature for each type from *o*-cresol + OH (Nakao et al., 2011; Olariu et al., 2002).

Finewax et al., 2018 report the yield of nitrocatechol from NO_3 oxidation of catechol to be 91±6%. Olariu et al. also found benzoquinone formation from NO_3 + cresol (Olariu et al., 2013). The mechanism by which benzoquinones are formed by NO_3 oxidation of catechol is uncertain. Olariu et al. state that unpublished work finds no evidence for benzoquinone products from phenol + NO_3, while Bolzacchini et al. find evidence for benzoquinone production from NO_3 + phenol if

O_3 is present (Bolzacchini et al., 2001). We assume catechol, methylcatechol, and dimethylcatechols + NO_3 forms 91% nitrocatechol type product and the remaining 9% a benzoquinone type product. For simplification in our box model, we group benzoquinone products.

Referring to Figure 4.1, OH and NO_3 reactions with catechol form a catechol radical (CATO), which can then react with either NO_2 or O_3. Reactions with NO_2 form nitrocatechol (NCATECHOL), while reactions with O_3 form a catechol-peroxy radical ($CATO_2$), which can subsequently react with HO_2 to form a catechol-hydroperoxide (CATOOH). The formation of CATOOH is reversible but our model runs find the lifetime of CATOOH is >100 hours meaning CATOOH acts as a permanent loss of $CATO_2$. While our catechol mechanism does not include heterogeneous reactions, it is likely that CATOOH will be lost through aerosol. We find that CATOOH is responsible for 17 – 26% of net CATO loss. In other words, 17 – 26% of potential nitrocatechol formation is lost to CATOOH. In all model runs, the fraction of potential nitrocatechol lost by O_3 increases as the plume ages.

For updates to both OH- and NO_3- phenolic compound oxidation, we assume similar assumptions for later-generation products and end the oxidation at highly-functionalized products, which will likely form secondary organic aerosol. In the Appendix on page 190, we provide the mechanism in the form of FACSIMILE, which is a standard output format (.fac) from the MCM and is readable in F0AM v4.0.

4.2.3.2 Emissions

We initiate the model using an emissions inventory of 302 BBVOCs in the form of emission ratios (ERs, E2.8) as described in section 2.3 on page 13. Briefly, the ER inventory uses an average of BBVOC emissions studies of ponderosa pine fuel from the Fire Lab at Missoula

Experiment (FLAME-4) (Hatch et al., 2017) and the Fire Influence on Regional and Global Environments Experiment (FIREXLab) (Koss et al., 2018) with rate coefficients taken from literature when available or estimated when unavailable. The model also includes heterogeneous NO_3 and N_2O_5 uptake onto aerosol, calculated for NO_3 heterogeneous reactivity, as shown in E2.6.

4.2.3.3 Model Constraints

Our model is constrained to plume-center and, for some compounds, background measurements of aerosol surface area, photolysis rates, O_3, CO, NO_x, HONO, and total oxidized nitrogen (NO_y). Measurements of NO_y are only available from the DC-8 measurements. We also constrain our models to the meteorological conditions pressure, temperature, and relative humidity. Fire emissions and photolysis conditions can change rapidly, therefore we constrain the model to a subset of plume transects. We chose transects that showed a monotonic decrease of CO with distance from the fire, cover an age range of at least one hour, and have similar emission times as shown in Figure 4.2 and Figure 4.3.

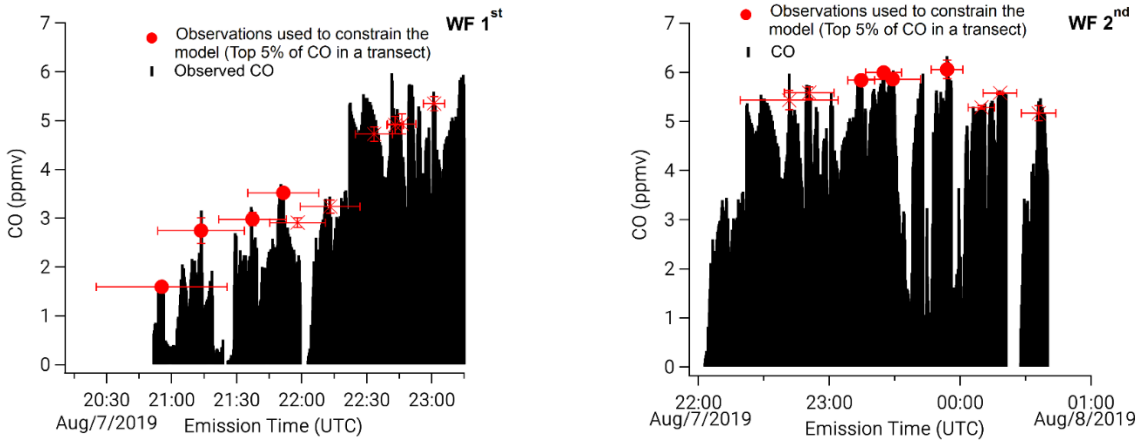

Figure 4.2: Time series of CO (black filled) as a function of emission time. Red markers indicate the top 5 % of CO during a single transect. Filled circles indicate observations chosen to constrain a model run and crosses indicate unused observations. Horizontal error bars indicate error in the plume age estimation.

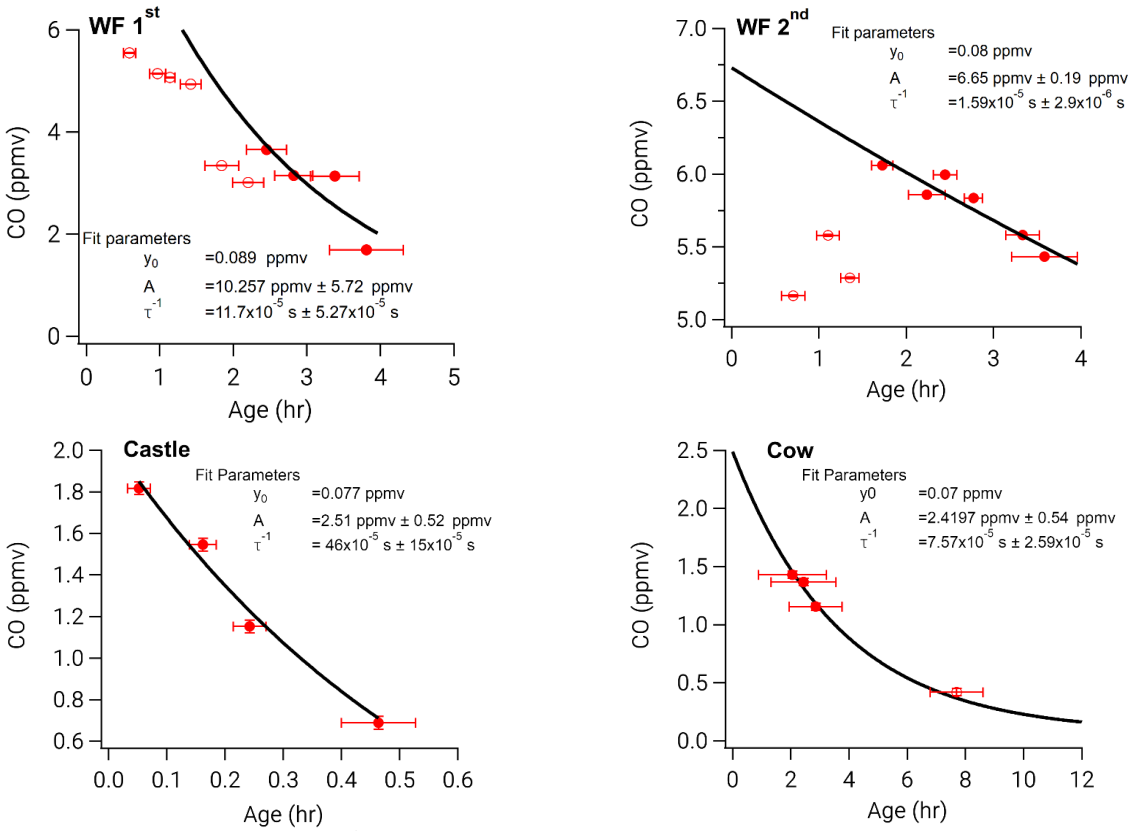

Figure 4.3: Exponential fit ($y = Ae^{x/\tau} + y_0$) to normalized excess mixing ratios (NEMR) of CO used as our best-guess estimate of dilution for each model run. Filled circles indicate observations used to constrain the model run, while open circle indicate observation that are not used.

All model runs included a constant first-order plume dilution rate coefficient (kdil) determined by applying an exponential fit to observed CO as a function of plume age (Figure 4.3). We fit only points used to constrain the model and fixed the exponential fit offset to the observed CO background. We applied k_{dil} to all species in the model. We find values of k_{dil} that range between 4.5 – 60×10^{-5} s^{-1} (Table 4.1), equivalent to a lifetime ($\tau_{dil} = 1/k_{dil}$) of 0.5 – 6.2 h.

Compound	WF1	WF2	Castle	Cow
CO (ppmv)	0.089	0.080	0.124	0.070
NO (ppbv)	0.0	0.0	0.0	0.0
NO_2 (ppbv)	0.0	0.1	0.1	0.06
HONO (ppbv)	0.0	0.0	0.0	0.0
O_3 (ppbv)	96.25	84.2	90	60.7
k_{dil} (×10^{-5} s^{-1})	11.7	1.59	46	7.57

Table 4.1: Table of background mixing ratios of CO, NO, NO_2, HONO, and O_3 for all model runs. The Dark model run has the same conditions as the WF2 model run.

Plume-center observations were determined using a "top 5 %" method as described by Peng et al., 2020. Briefly, within a transect we determine the location of the greatest 5 % of observations for CO and use that location of the plume for analysis of other compounds. This method obtains an average observation for the center, or most concentrated, parts of the plume. Reported uncertainties are the 1-σ variability of the top 5 % region and instrument uncertainties added in quadrature.

Particulate matter in BB plumes attenuates sunlight, and thus photolysis rates, in a process we refer to as plume darkening. In WF plumes we use plume-center observations of 20 photolysis rates (listed in Table 4.2), but for the Castle and Cow plumes only jNO_2 is available due to the limited instrument payload on the NOAA Twin Otter. Average attenuation of jNO_2 within the WF1 and WF2 plumes was 96% (meaning jNO_2 at plume-center was 4 % of jNO_2 outside of the plume). Plume-center attenuation of jNO_2 was 29% for the Castle plume. We sample the Cow plume after sunset and therefore do not have observation of jNO_2 while the smoke was under sunlight (0 – 2 h). We estimate that plume-center jNO_2 attenuation was 34%. This estimate was made by comparing jNO_2 attenuation to plume size (by CO) in the WF and Castle model runs and is consistent with jNO_2 attenuation in plumes emitted from the Cow Fire sampled on other days. All other photolysis rates were estimated using a ratio of the observed jNO_2 to calculated photolysis rates using an MCM trigonometric solar zenith angle (SZA) function below.

$$J = l * \cos(SZA)^m * e^{-n*\sec(SZA)} \quad \text{E4.1}$$

Where l, m, n are derived from least squares fits to j-values from a radiative transfer model and literature cross sections/quantum yields. This calculation is a standard photolysis value method in

F0AM and is described by Jenkin et al., 1997. However, this method does not account for overhead O_3 column, surface albedo, aerosol or other effects.

Photolysis Rates Used to Constrain the WF1 and WF2 Model Runs

$jNO_2 \rightarrow NO + O^3(P)$	$jCH_2O \rightarrow H + HCO$	$jCHOCHO \rightarrow HCO + HCO$
$jO_3 \rightarrow O_2 + O^1(D)$	$jCH_3CHO \rightarrow CH_3 + HCO$	$jCHOCHO \rightarrow CH_2O + CO$
$jH_2O_2 \rightarrow 2OH$	$jpropanal \rightarrow CH_2CH_3 + HCO$	j2,3,butadione
$jNO_3 \rightarrow NO_2 + O^3(P)$	$jMeONO_2 \rightarrow CH_3O + NO_2$	$jMEK \rightarrow CH_3CO + CH_2CH_3$
$jNO_3 \rightarrow NO + O_2$	$jEthONO_2 \rightarrow CH_3CH_2O + NO_2$	$jCH_3COCHO \rightarrow CH_3CO + HCO$
$jHNO_2 \rightarrow OH + NO$	jMVK	$jHNO_3 \rightarrow OH + NO_2$
$jCH_2O \rightarrow H_2 + CO$	$jCHOCHO \rightarrow H_2 + 2CO$	

Table 4.2: List of photolysis rates measured on the DC-8 and used to constrain the WF 1 and WF2 model runs.

In all of the plumes studied here, observed jNO_2 rates are below 10^{-3} s^{-1} excluding the first few minutes of the Castle plume. Values of jNO_2 in the WF2 plume remained low, near 10^{-4} s^{-1} during the sampling time. In contrast, the WF1 plume exhibits increasing jNO_2 rates, which eventually reach 8×10^{-4} s^{-1}. Differences in the photolysis rates between the first and second pass is likely due to the setting sun. Finally, observations of photolysis rates are negligible in the Cow plume as it was sampled after sunset.

4.2.3.4 Model Initiation

In all plumes except the Castle plume, our first transect sampled smoke 36 min – 2 h old and therefore we implemented an iterative method (McDuffie et al., 2018; Wagner et al., 2013) to estimate initial emissions (at age = 0). We began with best-guess estimates of CO, NO, NO_2, HONO and O_3 then systematically changed these initial conditions to minimize the differences between model output and observations downwind. Initial conditions for all cases are shown in Table 4.3. In all cases, backgrounds of NO, NO_2, O_3, CO and HONO were taken as an average outside of the plume and BBVOC backgrounds were assumed to be zero. Background mixing ratios used are shown in Table 4.1.

	WF1		WF2		Castle		Cow	
	ppbv	ppbv $ppmv^{-1}$	ppbv	ppbv $ppmv^{-1}$	ppbv	ppbv $ppmv^{-1}$	ppbv	ppbv $ppmv^{-1}$
CO	8259	-	8329		1954		2618	
NO	28.0	3.4	57.0	6.8	8.4	4.3	16.8	6.4
NO_2	7.0	0.8	0.0	0.0	3.6	1.8	4.2	1.6
HONO	8.0	1.0	30.0	3.6	3.0	1.5	22.5	8.6
O_3	53.9	-	38.3	-	81.3	-	43.2	-

Table 4.3: Table of initial mixing ratios of CO, NO, NO_2, HONO, and O_3 for all model runs. The Dark model run has the same conditions as the WF2 model run.

We determined best-guess estimates of CO and HONO directly from observations of the first transect. To determine a best-guess estimate for NO_x we used the sum of observed NO and NO_2 for the Cow run or NO_y minus HONO (as NO_y will contain HONO) for the WF runs. Best-guess estimates of O_3 were determined using an average of background O_3 observations from a flight leg upwind of the fire and outside of the plume transects, which can vary (see Table 4.4).

We began iteration with CO and k_{dil} by increasing best-guess estimates of CO and varying k_{dil} within the fit errors until we minimized the differences between observed and modeled CO. This in-turn determines the emissions of BBVOCs by E2.8. Next, we iterated NO_x, HONO and the NO/NO_x ratio such that the sum of NO_x and HONO did not exceed the observed NO_y and the initial NO/NO_x ratio remained between 0.6 – 1 (Roberts et al., 2020). Lastly, we iterated the initial and background O_3. As explained below, we were required to iterate on background O_3 in some model runs in order to achieve agreement between model and observations. We repeated the above process to minimize the differences between model and observations. In an attempt to avoid finding a local solution, as opposed to the "best" solution, we reversed the order of iterating O_3, NO_x and HONO when repeating the above process.

Initial condition in the Castle run were taken directly from observations of NO, NO_2, O_3, CO, HONO, phenol, catechol, cresol, and methylcatechol in the first transect where the plume age

was 3 ± 1 min, and therefore was close to age = 0. We initiated the remaining 298 BBVOCs by using CO and E2.8.

	WF1	**WF2**	**Castle**	**Cow**
Average O_3 Upwind (ppbv)	57.8±0.4	48.9 ± 7.5	72 ± 1	-
Average O_3 Outside of transects (ppbv)	53 ± 3	58 ± 8	82 ± 2	53 ± 3

Table 4.4: Table of observed background O_3 during an upwind transect and outside of the plume edges.

4.2.4 Observations and Model Comparison

Accurately modeling the first order loss of CO is critical as it determines the overall plume dilution rate coefficient and initial BBVOC mixing ratios. Median differences in modeled and observed CO range from 39.7 – 307.4 ppbv with a median difference of 2.8 – 11.7 % across all model runs. Percentage and absolute differences between the model runs and observations are detailed in Table 4.5.

Median differences of NO_2 and HONO are 5.1 – 32.2 % and 6.6 – 53.3 %, respectively. There are greater percentage differences in NO_2 and HONO that arise due to lower mixing ratio observations mostly in the WF1 and Castle plumes, with a range of absolute median differences of NO_2 and HONO between 0.4 – 2.0 ppbv and 0.3 – 3.4 ppbv, respectively.

Ozone median differences vary from 0.3 – 6.3 ppbv with a median difference of 0.8 – 27.2 % across all runs. For the WF1 and WF2 plumes we found that a significant increase (38.5 ± 0.4 and 35.3 ± 7.5 ppbv, Table 4.1 and Table 4.4) in model background O_3 compared to the upwind leg was required to capture the observed plume-center O_3. This is due to photochemical O_3 production at the plume edges, where O_3 was as much as a factor of ~2 greater than the background O_3. The increased plume edge O_3 is not captured in our plume-center model, and thus requires an increase in model background O_3.

	Castle				WF1				WF2				Cow			
	(ppbv)		(%)		(ppbv)		(%)		(ppbv)		(%)		(ppbv)		(%)	
	Avg	Med	Avg	Med	Avg	Med	Avg	Med	Avg	Med	Avg	Med	Avg	Med	Avg	Med
CO	80.5	69.9	6.8	6.5	307.4	328.2	13.1	11.7	243.1	243.1	4.1	4.2	37.8	39.7	2.8	2.8
NO_2	0.5	0.4	15.8	6.8	2.0	2.0	126.1	32.2	2.0	2.0	5.0	5.1	1.4	0.9	12.0	8.3
NO	0.3	0.2	54.9	47.6	0.4	0.1	944.6	99.8	1.0	1.0	43.7	40.5	0.1	0.1	100.0	100.0
O_3	1.6	1.7	2.0	2.1	6.1	6.3	6.5	6.2	3.4	3.4	29.7	27.2	0.4	0.3	0.8	0.8
HONO	0.3	0.4	21.6	21.8	0.9	0.8	961.4	53.3	3.4	3.4	16.9	18.8	0.5	0.4	5.5	6.6

Table 4.5: Comparison of model outputs and observations used (as seen in Figure 4.4) as the average (Avg) or median (Med) in absolute (ppbv) and percent difference (%) for all compounds used to iterate the model.

4.2.4.1 Comparisons of Constrained Compounds

The WF fire emissions were significantly greater than the Castle and Cow Fire emissions as is seen in the observed CO (Figure 4.4). Initial plume-center CO was 8.26 and 8.33 ppmv in WF1 and WF2, respectively, but 2.62 and 1.95 ppmv for Cow and Castle, respectively. We report our observations for each species (X) relative to CO in the form of normalized excess missing ratios (NEMR, in E2.1 on page 11) following Yokelson et al., 2013.

Ozone depression and negative NEMRs at the plume-center were observed in all of the sunset, nighttime or darkened fire plumes analyzed here. Observations of $\Delta O_3/\Delta CO$ in the Castle plume remains at just below background levels of O_3 in all observations likely due to the small plume size and large O_3 background (82.5 ± 2.1 ppbv). Generally, $\Delta O_3/\Delta CO$ increases with plume age due to photochemical O_3 production and mixing with background O_3. Ozone in the midday WF1 plume reaches 44.8 ± 3.4 ppbv $ppmv^{-1}$ of CO, or 67.4 ppbv above background, after 3.8 ± 0.5 h of transport.

Referring to Figure 4.5 we find that observed $\Delta NO/\Delta CO$, $\Delta NO_2/\Delta CO$ and $\Delta HONO/\Delta CO$ have variable trends in all plumes. Observations of $\Delta NO/\Delta CO$ are near zero (≤ 0.1 ppbv $ppmv^{-1}$) in the Castle and WF1 plumes, and elevated in the WF2 and Cow plume ($0.21 \pm 0.02 - 1.21 \pm 0.13$ ppbv $ppmv^{-1}$). Observed $\Delta NO/\Delta CO$ in the WF2 plume change sharply between the first four and last five transects suggesting changes in fire emissions or photolysis near emission. In order

to avoid these changes, we use only observations from the latter to constrain our model as discussed in section 4.2.3.3 on page 65.

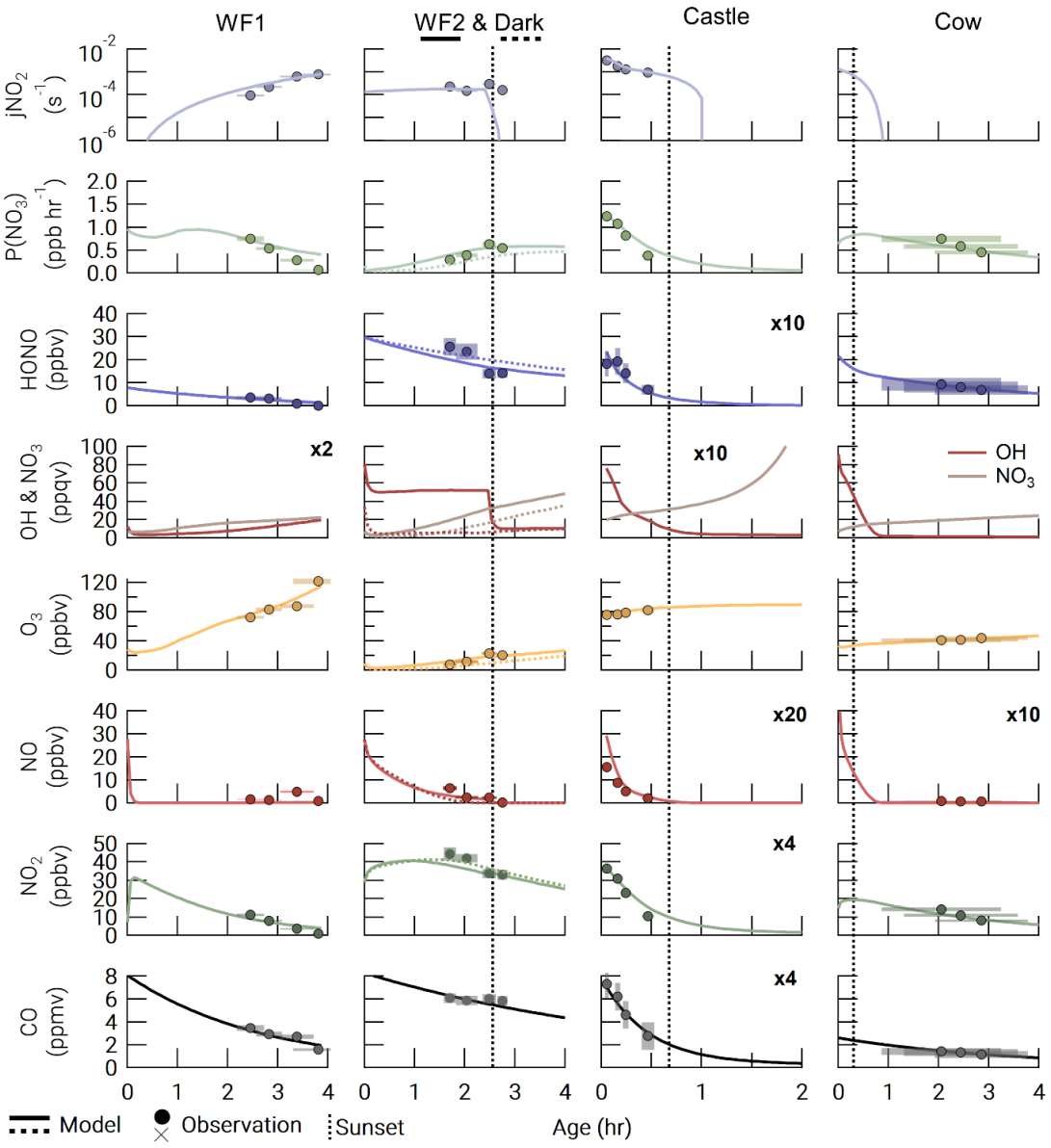

Figure 4.4: Observations (closed circles) and model output (lines) for all model runs. The Dark run is shown as a dashed line in the WF2 column. The time of sunset (defined as when the solar zenith angle reaches 90°) is indicated by a vertical dashed line. Observation errors (y error: variability in the observation at plume-center and instrument uncertainty added in quadrature, x error: uncertainty in plume age determination) are shown as shaded xy boxes.

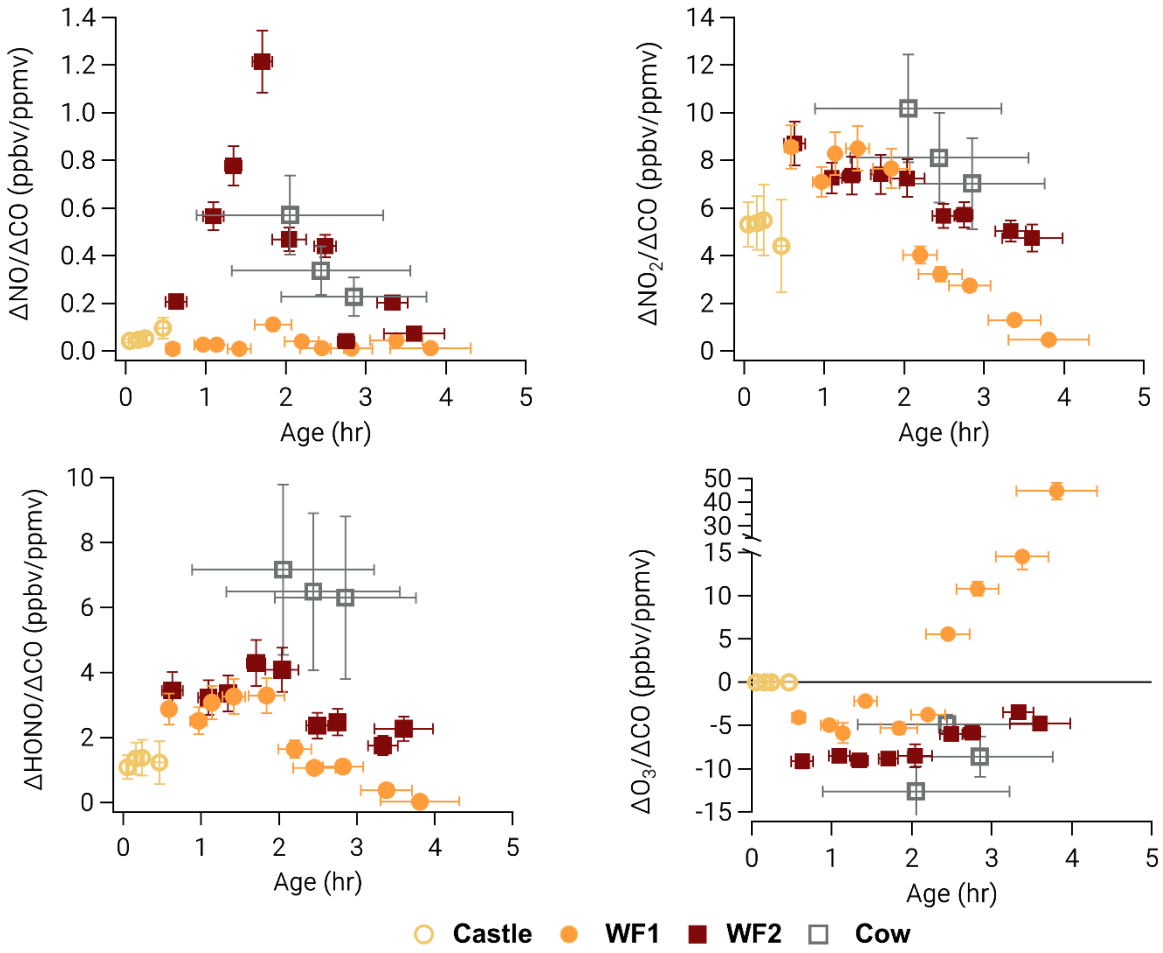

Figure 4.5: Observed normalized excess mixing ratios (NEMRs) of NO, NO_2, HONO, and O_3 for all plumes.

There is a general decrease of $\Delta NO_2/\Delta CO$ and $\Delta HONO/\Delta CO$ over four hours of aging. Observations of $\Delta NO_2/\Delta CO$ in the WF1 plume decrease at a faster rate than those in the WF2 plume, however, both plumes exhibit about 8.6 ppbv $ppmv^{-1}$ in the youngest smoke (35 ± 8 min old).

4.2.4.2 Comparisons of $P(NO_3)$

Emissions of NO_x from biomass burning plumes provide a source of NO_3 suggested to be a major oxidant for BBVOCs (Kodros et al., 2020). The instantaneous NO_3 production rate, $P(NO_3)$, is a common metric of the potential for NO_3 chemistry (Brown and Stutz, 2012) and is

described on page 11 and as E2.4. At the center of the plumes presented in this study, NO_3 production rates were between 0.1 and 1.5 ppbv h^{-1} as seen in Figure 4.4. These NO_3 production rates are consistent with those found in a nighttime agricultural smoke plume measured above a rural area at the border of Missouri and Tennessee during the South East Nexus campaign (SENEX), which varied between 0.2 and 1.2 ppbv h^{-1} as discussed in Chapter 3. These values of $P(NO_3)$ are also similar to those found in urban plumes and forested areas. Production rates of NO_3 in urban plumes typically range within 0 – 3 ppbv h^{-1} at night but can be larger. In forested regions, $P(NO_3)$ is typically below 1 ppbv h^{-1} at night (Brown and Stutz, 2012).

Agreement between the model $P(NO_3)$ and observed $P(NO_3)$ reflects agreement between observed and modeled NO_2 and O_3. The WF1 model run slightly overpredicts NO_2 after 3 hours of aging and therefore overpredicts $P(NO_3)$. Similarly, the Cow model run slightly underpredicts NO_2 compared to observations and therefore the trend in $P(NO_3)$ is slightly underpredicted.

4.2.4.3 Comparison of phenolics

Our work focuses on the role of phenolics in BB plumes and includes updated and expanded phenolic oxidation mechanisms as described in section 4.2.3.1 on page 61. Therefore, capturing the phenolic evolution in our models is critical to understanding the importance of phenolics in BB. In the Castle case, which is initiated with observations of phenolics, we find excellent agreement for catechol, methycatechol, phenol, and cresol (Figure B.1). Further, we find that the model run lies on the upper edges of nitrocatechol errors, and the lower edge of nitrophenol errors. The model run underpredicts nitrocresol by a factor of 60. Note that we do not have available calibrations for nitromethylcatechol, but do provide observations in arbitrary units for the purpose of comparing the time evolution of this compound.

Overall the model recreates the relative time evolution of nitrophenolics well. Disagreement between the model and observed compounds could be caused by many factors including, but not limited to, interfering isomers measured by the UW I^- HR ToF CIMS or the NOAA I^- ToF CIMS, variable fire ERs, and loss or production of nitrophenolics not captured by our mechanism. The MCM includes several gas-phase loss processes of nitrophenolics, but no gas to particle partitioning. Nitrophenolics readily partition to the aerosol phase (Finewax et al., 2018). Further, the MCM does not include photolytic loss of nitrophenolics, despite some evidence to the contrary (Sangwan and Zhu, 2016, 2018). Therefore, when analyzing gas phase nitrophenolic evolution we only consider integrated formation, as discussed in section 4.3.3.2 on page 89.

All other model runs were not initiated to observations of phenolics due to the older age of smoke during the first transect. Even so, in the Cow model run (Figure B.2) we find agreement with catechol and methylcatechol within observation errors. Modeled phenol is about a factor of 3 (Δ1.4 – 2.0 ppbv) greater than the observations. Modeled cresol is about a factor of 10 greater than observations, while its oxidation product, nitrocresol, is 7 times less than the observations. Models are thus able to reproduce some, but not all, phenolic observations in the Cow plume.

Observations of phenolics in the WF plumes are limited to un-calibrated catechol and nitrocatechol observations from the NOAA I^- ToF CIMS (Figure B.3 – Figure B.4). In the WF1 model run, catechol and nitrocatechol appear to deplete faster than the model would suggest. The time evolution of nitrocatechol in the WF2 plume agrees well with the model, and in the WF1 model run the model matches the rough timing of the observed maximum signal.

4.3 Results and Discussion

4.3.1 Reactivity

Reactivity, defined by E2.2 on page 11, is used as a simplified metric to predict the competition of reactions between oxidant and BBVOC. Here, we calculate and detail the reactivity for O_3, NO_3 and OH oxidation of BBVOCs to understand their predicted competition. We also discuss how reactivity of the BB plumes studied here compare to other environments.

At emission, BBVOCs account for the majority of total reactivity for OH (87.7 %), NO_3 (80.1 %), and O_3 (99.6 %) as seen by the bars in Figure 4.6. HCHO and CO account for 5.1 % and 5.3 % of OH reactivity, respectively while NO_2 accounts for a small (0.3 %) fraction. We exclude O_3 reactivity to NO in Figure 4.6 because during the daytime this reaction is in a rapid cycle with NO_2 photolysis and regeneration of O_3 in which odd oxygen, $O_x = NO_2 + O_3$, is conserved. Further reactions of O_3 and NO_2 can lead to loss of O_x. This analysis includes BBVOC oxidation by O_3 but not a detailed budget for O_x.

Underneath each reactivity bar in Figure 4.6 we show the partitioning of the initial BBVOC reactivity. Almost three quarters of OH reactivity is from alkenes (33.0 %), furans (25.0 %) and phenolics (16.4 %). The reactivity of NO_3, by contrast, is controlled by phenolics (64.4 %) and O_3 reactivity is controlled by alkenes (53.8 %) and terpenes (39.2 %). Nitrate radical reactivity toward a smaller fraction of VOCs is consistent with other reactivity analyses of OH, NO_3 and O_3 in forest air (Palm et al., 2017).

Below each pie chart in Figure 4.6 we show reactivity for OH, NO_3, and O_3 toward BBVOCs on an absolute scale. As BBVOCs are oxidized and the plume dilutes the plume reactivity is reduced. Decay of OH and NO_3 reactivity is nearly identical, while that of O_3 is

different (e.g., WF2 and Dark). As a result, fewer BBVOCs, specifically alkenes, are oxidized in the Dark model run keeping reactivity greater when compared to the WF2 model run.

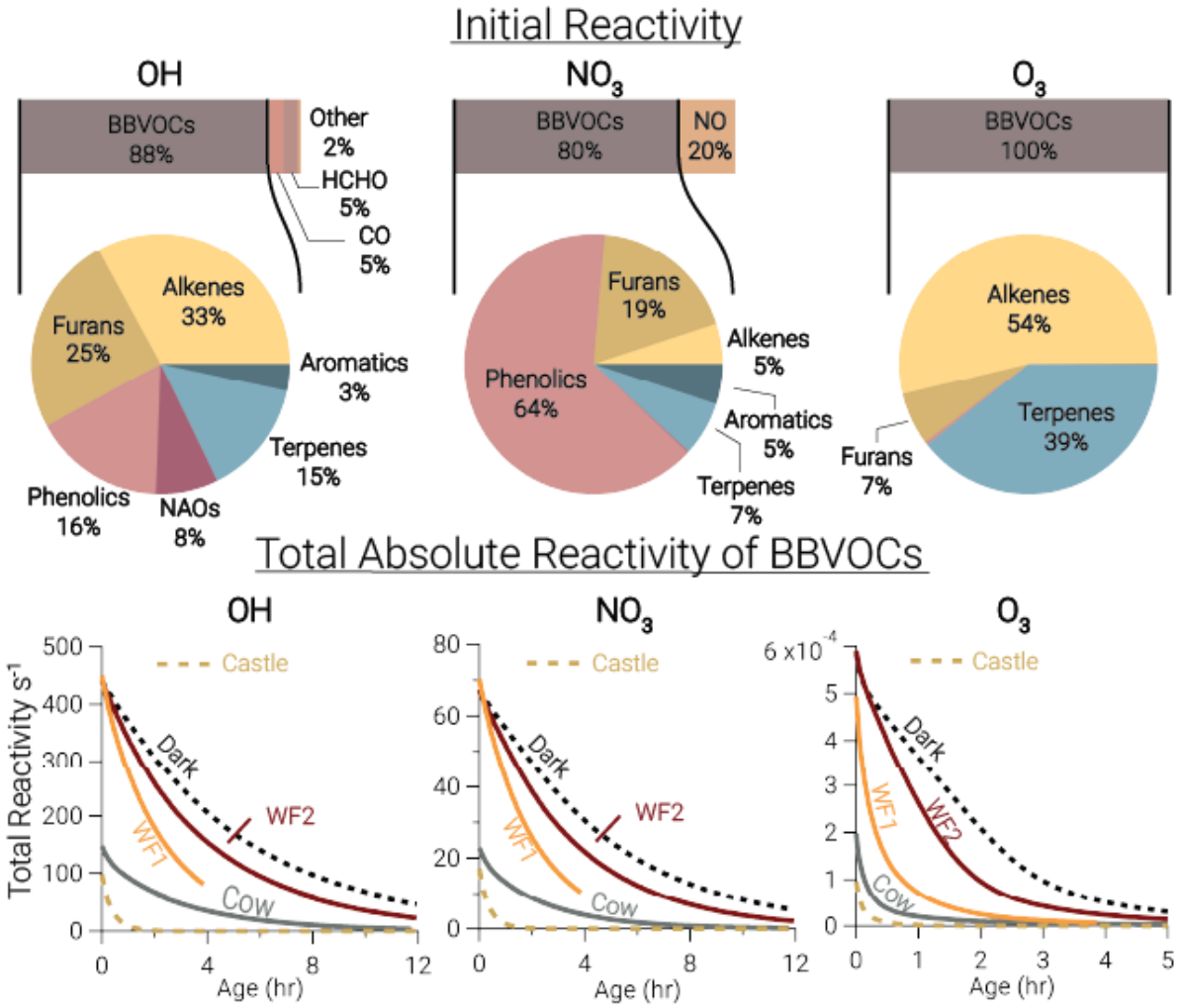

Figure 4.6: Bars: Average (of all model runs) initial relative instantaneous reactivity for all compounds in our model showing that initial reactivity of BBVOCs outweighs all other compounds for all oxidants. Pies: Initial relative reactivity of BBVOCs showing that OH reactivity is controlled by many BBVOC groups, NO_3 reactivity by phenolics, and O_3 reactivity by alkenes and terpenes. Non-aromatic Oxygenates are abreviate by NAOs. Time series: Absolute reactivity of for all model runs showing that reactivity decays at different rates for each model run, and that OH and NO_3 reactivity decay is similar.

Total initial OH reactivity toward BBVOCs ranges from 98.3 – 450.0 s^{-1}. Since the modeled total reactivity is proportional to the plume's initial emission of CO, the largest plumes, WF and Dark, have the greatest total initial total reactivity. Typical OH reactivities range between

$7 – 130\ s^{-1}$ for urban plumes or $1 – 70\ s^{-1}$ in forests (Yang et al., 2016b), demonstrating that wildfire plumes can be similar to urban plumes or significantly more reactive.

Total initial O_3 reactivity toward BBVOCs ranges between $1\times10^{-4}\ s^{-1}$ and $6\times10^{-4}\ s^{-1}$. A recent study of a suburban site in China found O_3 reactivities toward non-methane VOCs between $2.5\times10^{-7} – 1.1\times10^{-6}\ s^{-1}$ (Yang et al., 2020). Reactivity in wildfire plumes exceeds that in urban plumes by a factor of 80 – 3000.

Total initial NO_3 reactivity toward BBVOCs ranges from $17.1 – 70.3\ s^{-1}$. Reactivity of NO_3 is typically reported as a lifetime (τ) as discussed in section 2.1 and given as E2.5. Modeled steady-state lifetimes are predicted to be between 0.5 – 1.2 s. Typical τ in urban plumes range from tens of seconds to tens of minutes and τ in forested regions have been reported between 20 s – 15 min (Brown and Stutz, 2012). The reactivity of NO_3 in wildfire plumes sampled during FIREX-AQ is $10 – 10^4$ times greater than typical values in forested or urban environments. The increased reactivity of NO_3 to BBVOCs within wildfire plumes is greater than the increased reactivity for OH and O_3, highlighting that BB plumes have large overall reactivity that is more pronounced for NO_3 than other oxidants.

In addition to a large suite of reactive BBVOCs that increase NO_3 reactivity, smoke contains concentrations of aerosol and aerosol surface area that are far greater than normally found in urban areas as shown in Chapter 3. When considering NO_3 reactivity we must also consider aerosols, since aerosols present a loss pathway for NO_3 and its equilibrium product N_2O_5 (Brown and Stutz, 2012; Goldberger et al., 2019) as explained in section 2.1.1 on page 11. We calculate the NO_3 heterogeneous reactivity to understand the competition between NO_3 loss to BBVOCs and NO_3/N_2O_5 heterogeneous loss to reaction with aerosol.

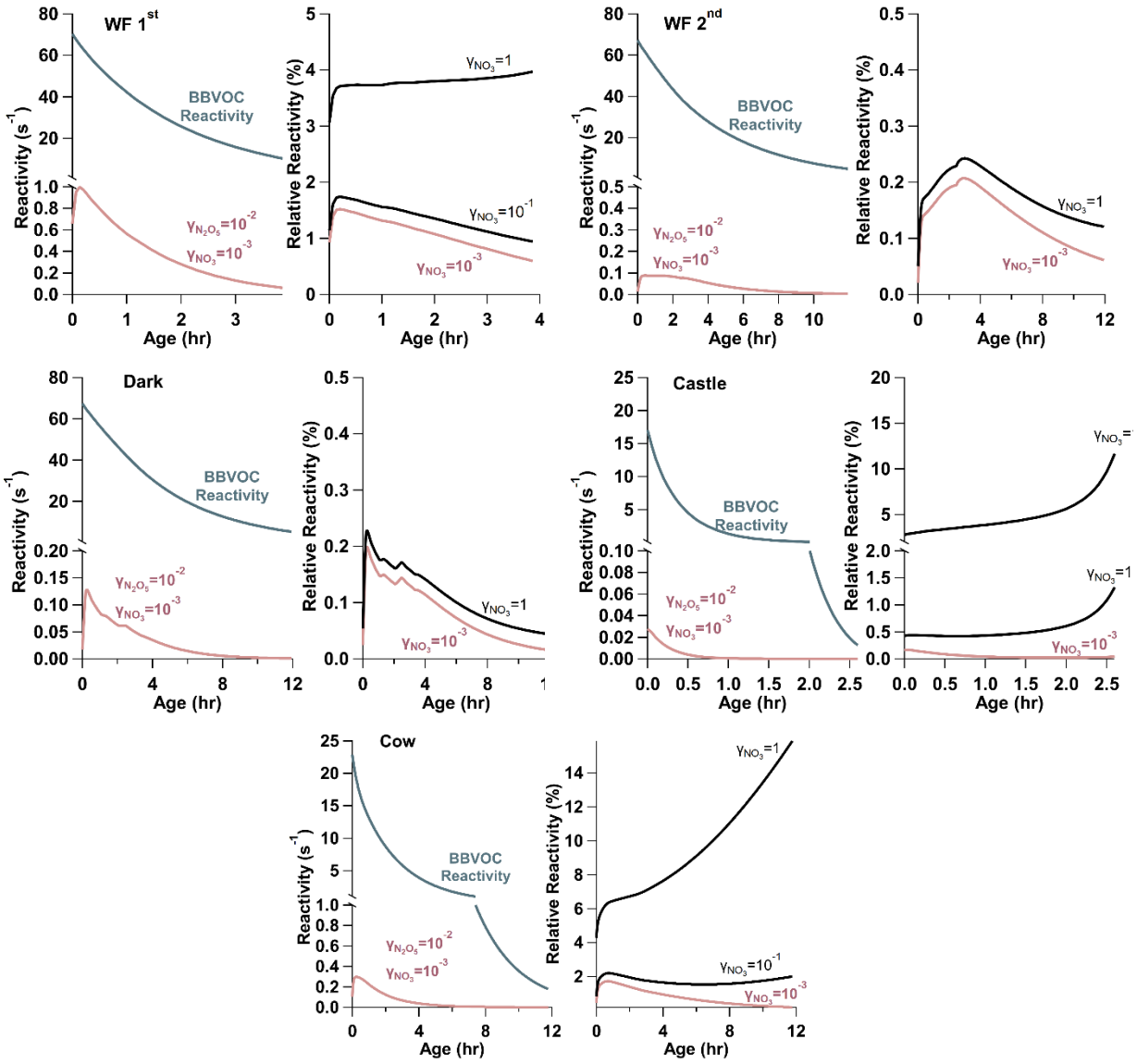

Figure 4.7: Left: total reactivity (s^{-1}) of BBVOCs (blue) and N_2O_5/NO_3 heterogenous uptake reactivity using a $\gamma_{N_2O_5}$ = 10^{-2} and a γ_{NO_3} = 10^{-3} (red). Right: Relative reactivity (%) of N_2O_5/NO_3 heterogenous uptake compared to total reactivity (heterogenous uptake + BBVOCs) for γ_{NO_3} = 1, 10^{-1}, and 10^{-3}. In all model runs, BBVOCs overwhelmingly control NO_3 loss.

As shown in Figure 4.7 heterogeneous losses of NO_3 and N_2O_5 are <2 % of total NO_3 reactivity in all model runs. Further, we find that >90 % of aerosol loss is through N_2O_5 rather than NO_3 uptake. Therefore, heterogeneous losses of NO_3 and N_2O_5 do not appreciably compete with

gas phase BBVOC oxidation, consistent with a similar analysis of nighttime smoke plumes described in Chapter 3.

While our analysis finds that the reactivity in a BB plume is far greater than other environments, it is important to note that our calculations use a large suite of the most reactive VOCs that may not be included in other reactivity studies. Further, our reactivity calculations are based on our BBVOC ER and kinetic database as described in section 2.3 on page 13. While this database includes rate coefficients for the most reactive BBVOCs, it does not include rate coefficients for all 302 BBVOCs with all oxidants. Therefore, our reactivity estimates may be a lower estimate. Our VOC profile does not include alkanes, since FIREX lab studies (Hatch et al., 2015; Koss et al., 2018) and an OH reactivity analysis of FIREX lab emissions found that OH reactivity toward alkanes accounted for 0 – 1 % of total BBVOC reactivity across all fuels (Gilman et al., 2015). Therefore, we expect the absent alkane reactivity in this study to be negligible.

4.3.2 Oxidation Rates

While reactivity is a useful metric to predict the competition between reactions, it does not account for oxidant concentration, which can vary widely depending on photolysis rates, emissions, and competing oxidants. In the following sections we discuss the BBVOC oxidation rate, which is related to reactivity through the oxidant concentration as discussed on page 11 and given as E2.3. In the following sections we compare and contrast reactivity and oxidation budgets and discuss how the initial reactivity changes with plume age for different BBVOC groups. Finally, we discuss the oxidant competition between NO_3, OH, and O_3 for three main groups of BBVOCs: phenolics, furans/furfurals, and alkenes/terpenes.

4.3.2.1 Oxidation of BBVOCs

The integrated oxidation rate, or the oxidation budget (Figure 4.8), is similar to initial reactivity shown in Figure 4.6 for OH oxidation suggesting initial reactivity may be a good indicator for integrated reactivity. However, this does not hold true for NO_3 or O_3.

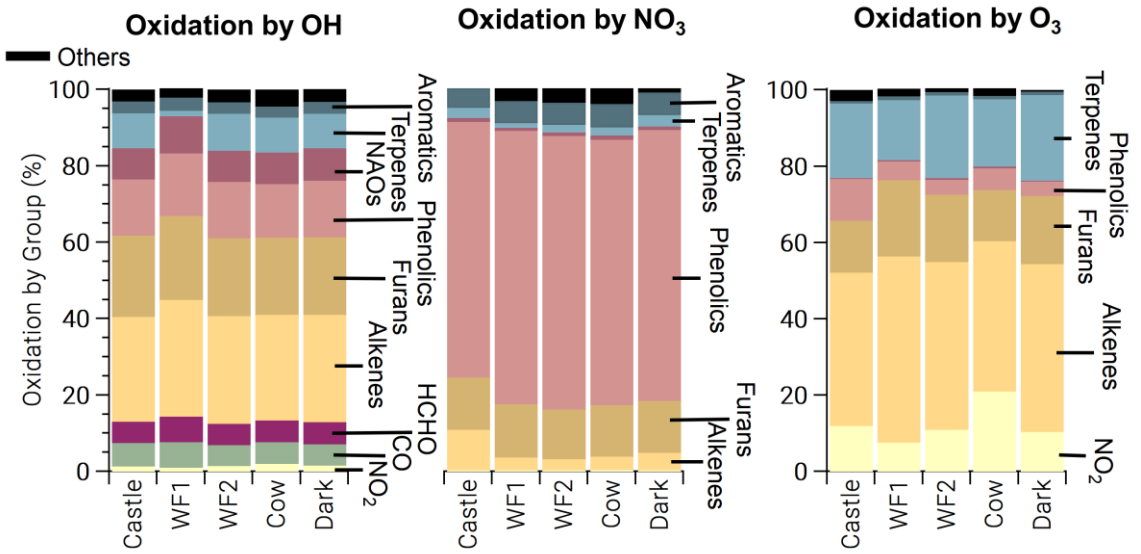

Figure 4.8: Integrated oxidation rate, or oxidation budgets, of BBVOCs by OH (left), NO_3 (center), and O_3 (right) on a relative scale for all five model runs. Oxidation by OH is spread across many BBVOC groups (where NAOs are non-aromatic oxygenates), similar to initial reactivity, but also HCHO, CO, and NO_2. Oxidation by NO_3 is dominated by phenolics, but by a greater fraction than initial reactivity suggests. Oxidation by O_3 is shown without NO and is dominated by alkenes and terpenes as expected from initial reactivity, but unlike initial reactivity it includes large contributions from phenolics and NO_2 (resulting in NO_3 production).

The initial NO_3 reactivity differs substantially from the oxidation budget. For example, 20 % of initial NO_3 reactivity is due to NO, but NO accounts for $\leq$ 1 % of integrated NO_3 loss. Further, photolysis of NO_3 accounts for <1 % of NO_3 loss in all model runs and is greatest in the Castle plume (0.6 %) where measured jNO_2 and calculated jNO_3 reached maximum values of 4×10^{-3} and 0.14 s^{-1}, respectively. Although daytime NO_3 oxidation of reactive VOCs has been found for heavily polluted urban air (Brown et al., 2005; Geyer et al., 2003; Osthoff et al., 2006), the dominant NO_3 loss processes in urban plumes is NO reaction and photolysis (Brown and Stutz,

2012; Wayne et al., 1991). The different controlling NO_3 loss pathway here highlights the unique and highly reactive environment of BB plumes. Further, 67 – 70 % of integrated NO_3 reaction is due to phenolics, which is larger than initial total NO_3 reactivity (56 %). Integrated alkene, terpene, and furan oxidation by NO_3 are all lower than their initial reactivities.

The production of NO_3 and subsequent loss to BBVOCs is a significant (8 – 21 %) loss of O_3, and much greater than the initial O_3 reactivity to NO_2 of 0.4 %. Similarly, integrated loss of O_3 to alkenes (40 – 49 %) and terpenes (16 – 23 %) is much less than initial reactivity would suggest (54 % and 39 %, respectively). Conversely, phenolics and furans account for 4 – 11 % and 13 – 20 % of O_3 loss, respectively, even though their relative initial reactivity is < 1 % and 7 %, respectively. Overall, the differences between initial reactivity and integrated oxidation rate are explained by changing reactivity as BBVOC are oxidized with plume age.

An example is seen in Figure 4.9 for O_3 in the Castle model run, which has a large O_3 background (72 $\pm$ 1 – 82 $\pm$ 2 ppbv), is a relatively small plume, and is sunlit at emission. As a result, alkenes and terpenes are depleted quickly through oxidation by O_3 and OH. The combined O_3 reactivity of alkenes and terpenes reduces from 82 % to 44 % after two hours, during which time phenolic reactivity increases from < 1 % to ~40 %. In other words, as BBVOCs are depleted the reactivity profile of each oxidant will change and can result in significant differences between the initial reactivity and oxidant budget.

In contrast to NO_3 and O_3, loss of OH by each BBVOC group is within 1 % of that predicted by the initial reactivity, except for terpenes. Initial reactivity of terpenes is about 13 %, while actual destruction of OH by terpenes averaged to 8 %. While terpene oxidation by OH is lower than its

reactivity in all model runs, it is especially low (2 %) in the WF1 model run, which is likely due to the large concentration of O_3 from photochemical production.

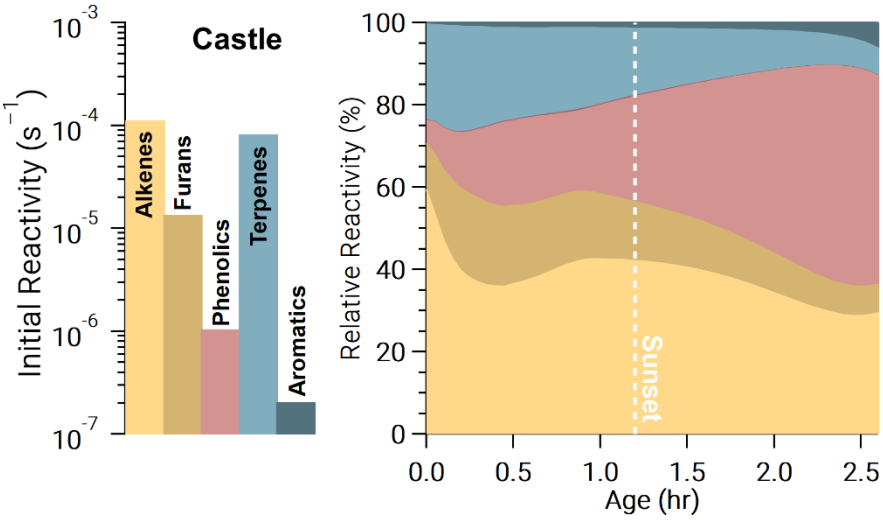

Figure 4.9: Ozone reactivity from the Castle model run in the form of absolute initial reactivity (bars, log scale) and relative BBVOC reactivity as a function of plume age (stacked, linear scale). As the plume ages, O_3 reactivity toward each BBVOC group changes significantly.

Losses of OH are not only due to highly reactive BBVOCs. HCHO, CO, and NO_2 are responsible for 12 – 14 % of OH destruction. This is consistent with an OH reactivity analysis from North American fuels burned during the FIREX laboratory study, which found 13 $\pm$ 1 % of OH reactivity was due to HCHO, CO, and NO_2 (Gilman et al., 2015). The fraction of OH reactivity toward CO and NO_2 are similar to those found in a tropical rainforest (Fuchs et al., 2017), but much smaller than the fraction of OH reactivity toward CO (7 %) and NO_2 (18 %) found at an urban site (Gilman et al., 2009) and the fraction of OH reactivity toward CO (20 – 25 %) and NO_x (12 – 22 %) at a rural site (Edwards et al., 2013a).

4.3.2.2 Oxidant Competition

To study the competition between all oxidants, we focus on three main BBVOC groups: phenolics, furans/furfurals, and alkenes/terpenes. Generally, furans/furfurals and alkenes/terpenes

groups are mainly oxidized by OH and O_3, while NO_3 plays a small role (Figure 4.10). Oxidation of furans/furfurals and alkenes/terpenes by OH (18 – 55 %, 11 – 43 %, respectively) and O_3 (39 – 76 %, 54 – 88 %, respectively) can vary widely depending on the plume. We find this is due to the variability of actinic flux. In model runs with less photolysis at emission, OH oxidation is low compared to model runs that are more optically thin. This reduction of oxidation by OH appears to be replaced by O_3 rather than NO_3. For example, relative furan/furfural oxidation by OH in the WF1 model run (relatively large integrated jNO_2) is 31 % less than that in the Cow model run (comparatively lower integrated jNO_2), yet O_3 oxidation is 32 % greater.

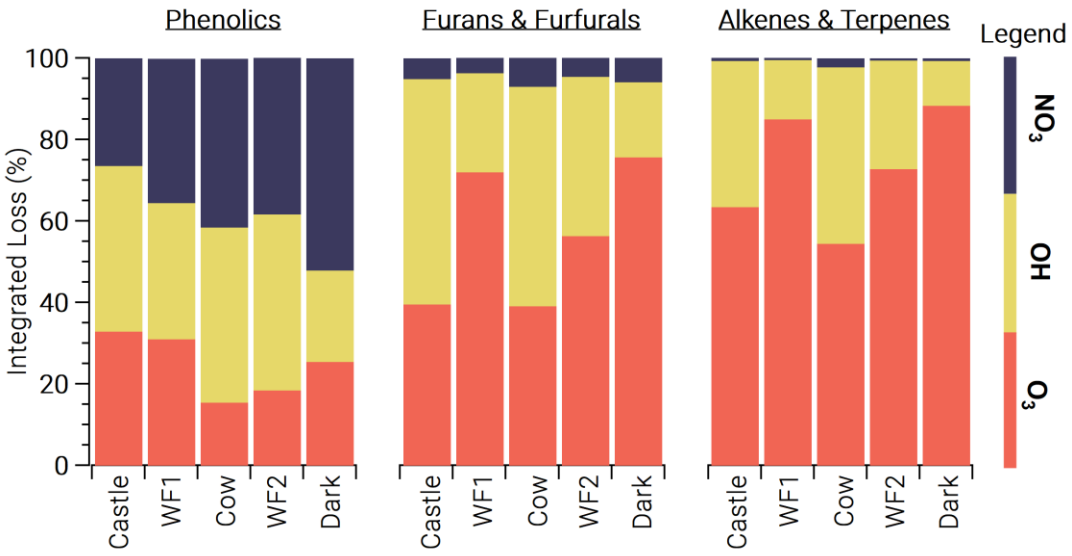

Figure 4.10: Integrated loss of phenolics (left), furans & furfurals (middle) and alkenes & terpenes (right) reacting with NO_3 (blue), OH (yellow) and O_3 (orange). The model runs are ordered from left to right by decreasing integrated jNO_2. Generally, furan/furfurals and alkenes/terpenes are oxidized primarily by O_3 and OH. In contrast, phenolic oxidation is split across all oxidants.

This relationship does not hold for phenolics, which are subject to significant NO_3 oxidation (26 – 52 %) (Figure 4.10). Phenolic oxidation by OH (22 – 43 %) and O_3 (16 – 33 %) are slightly less than NO_3. As a result, phenolic oxidation by NO_3 dominates in the WF1 and Dark

model runs, while OH dominates in the Castle model run. In the WF2 and Cow model runs, NO_3 and OH oxidation is roughly equal.

Generally, NO_3 oxidation of phenolics increases with O_3 availability and decreases with available actinic flux, but these relationships are coupled and complex. One example is seen in the WF2 model run, which has the second lowest integrated jNO_2 value, and large emissions of NO that keep O_3 low during sunlit hours. Therefore, $P(NO_3)$ is reduced, NO_3 is present at lower mixing ratios within the first hour of oxidation, and phenolics are less subject to NO_3 oxidation when compared to the other model runs.

As actinic flux increases so does OH and O_3 production, and therefore oxidant competition. One example is shown by the Castle model run where OH leads phenolic oxidation (41 %) with O_3 second (33 %). The Castle model run demonstrates the greatest observed background O_3 (90 ppbv). Further, the Castle model run has significantly smaller total emissions (based on CO) than the other model runs and the greatest integrated jNO_2. Due to the increased background O_3 and photochemical production of OH, NO_3 plays a smaller role in the oxidation of phenolics.

4.3.3 Phenolic Oxidation and Nitrophenolic Production

The importance of phenolic oxidation for BB is evidenced by the rapidly growing literature (Bertrand et al., 2018; Chen et al., 2019; Coggon et al., 2019; Decker et al., 2019; Finewax et al., 2018; Gaston et al., 2016; Hartikainen et al., 2018; Iinuma et al., 2010; Lauraguais et al., 2014; Lin et al., 2015; Liu et al., 2019; Meng et al., 2020; Mohr et al., 2013; Palm et al., 2020; Selimovic et al., 2020; Wang and Li, 2021; Xie et al., 2017). Both OH and NO_3 oxidation of phenolics leads to nitrophenolics, which have been shown to significantly contribute to SOA production (Palm et al., 2020). However, not all nitrophenolics are created equal. Understanding the competition

between phenolic oxidation by NO_3 and OH is critical because their oxidation pathways have significantly different implications for nitrogen budgets and total nitrophenolic yield. Nitrophenolics formed by OH requires one NO_2 molecule with a nitrophenolic yield between 27 – 33 %. In contrast nitrophenolics formed by NO_3 require two molecules of NO_2, have a yield of 85 – 97 % and produce HNO_3 as a byproduct (see Figure 4.1 and Finewax et al., 2018).

Yet, current phenolic mechanisms are extremely limited. For example, in the MCM nitrophenolics are the only oxidation products of phenolics + NO_3 or OH and the yields are assumed to be 100%. Phenolic oxidation studies are typically limited to final products without detailed examination of intermediates. Phenol and cresol reactions are well studied in comparison to catechol, methylcatechol, and higher order phenolics. For that reason, we use studies of phenol and cresol oxidation to extrapolate analogous branching ratios, rate coefficients, and products for catechol, methylcatechol, and three isomers of dimethylcatechol. All of these compounds are included in the MCM, but for the purpose of the following analysis we have expanded the phenolic reaction pathways in our model as explained in section 4.2.3.1 on page 61 and shown in Figure 4.1.

In the remaining sections, we detail how the competition for phenolic oxidation changes as the plume evolves over time. We then discuss the factors that cause differences in nitrophenolic production rate as well as how differences in OH and NO_3 phenolic oxidation lead to substantial differences in nitrocatechol yield. Finally, in the following section, we explore how nitrophenolics significantly impact the nitrogen budget.

4.3.3.1 Evolution of Phenolic Oxidation

Generally, the modeled total phenolic oxidation rate varies between 1-10 ppbv hr^{-1} at emission Figure 4.11A – D), but the change in oxidation rate is not constant and trends with available actinic flux. Model runs with active initial photochemistry (Castle, WF2, and Cow) exhibit decreasing total oxidation rates, while model runs with little to no photolysis (WF1 and Dark) reach a local maximum rate after ~2 h and ~5 h, respectively. These increases in oxidation rate are due to increases in O_3 and NO_3 oxidation once NO is depleted.

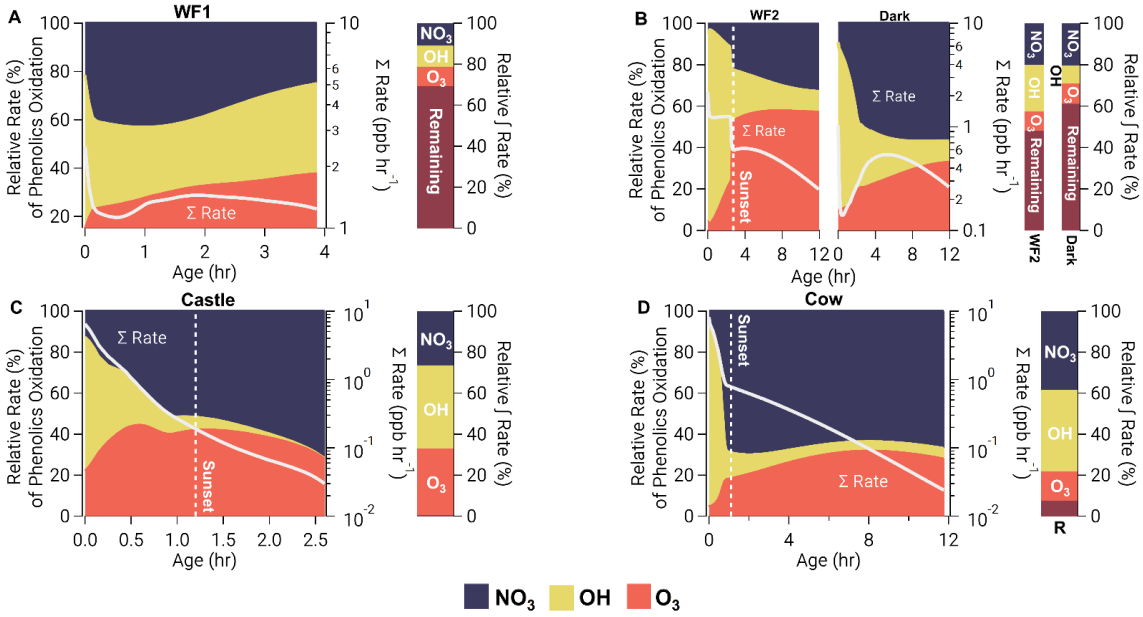

Figure 4.11: Oxidation metrics of all phenolic compounds for WF1 model run (A), WF2 and dark model runs (B), Castle model run (C), and Cow model run (D). Left axis: relative oxidation of phenolics for NO_3 (blue), OH (yellow), and O_3 (orange). Right log axis: absolute total oxidation (white line). Bar: Relative integrated rate of oxidation of phenolics for NO_3 (blue), OH (yellow), O_3 (orange) and the remaining phenolics at the model end (red).

Before sunset and in early stages of plume oxidation, the major channel of phenolic oxidation is via OH. However, in the WF1 model run NO_3 oxidation dominates after only 12 minutes (Figure 4.11A). As the WF1 model run dilutes, photolysis rates increase and O_3 is entrained promoting NO_3 production. This increase in oxidant concentration keeps phenolic oxidation > 1 ppbv h^{-1} for at least four hours before the end of the model, unlike other model runs

that drop below 1 ppbv h^{-1} of total phenolic oxidation within 0.5 - 3 h. After 2.6 h, in the WF1 model run, all oxidants contribute equally to phenolic oxidation and thereafter, OH and O_3 equally split oxidation while the influence of NO_3 decreases. At the end of the WF1 model run, 69% of initial phenolics remain unoxidized.

As the sun sets in our sunset model runs (WF2, Castle, and Cow) a transition from OH controlled to a mixture of NO_3 and O_3 controlled oxidation occurs when OH production, and total oxidation rate decrease rapidly. Interestingly, OH dominates phenolic oxidation in the Dark model run (initiated after sunset) for the first 1.8 h before NO_3 oxidation takes over. During this time, OH is produced by decomposition of Criegee intermediates formed through ozonolysis of unsaturated hydrocarbons, primarily catechol (Figure 4.1), methylcatechol and limonene. In other sunset model runs, OH plays a smaller role after sunset. Even so, this suggests that all BBVOC oxidation after sunset is driven by O_3 chemistry, either through direct oxidation by O_3, $NO_2 + O_3$ to form NO_3, or by formation and decomposition of Criegee intermediates to form OH.

The WF2, Dark, and Cow model runs all contain unreacted phenolic emissions at sunrise the following day (48%, 61%, and 8%, respectively, Figure 4.11). The WF2 and Dark model runs have significantly more phenolics that remain at sunrise because of their larger (~×3) emissions compared to the Cow model run. Further, the WF2 and Dark model run conditions differ only by the presence of photolysis and therefore the difference in remaining phenolics between the WF2 and Dark is due to the time of day the smoke was emitted. In contrast to these three model runs, the emissions in Castle are depleted within 2.6 h due to its small size.

4.3.3.2 Total Nitrophenolic Formation

Nitrophenolic formation increases with O_3 and photolysis, which promotes formation of NO_3 and OH. For example, the Castle and Cow model runs have relatively large O_3 and jNO_2 at emission and therefore form nitrophenolics rapidly (0.6 – 1.4 ppbv h^{-1} within the first 15 min). In contrast, the WF and Dark model runs have near zero O_3 due to large emissions of NO and relatively low or zero jNO_2 and therefore form nitrophenolics more slowly (<0.1 – 0.7 ppbv h^{-1} within the first 15 min).

Despite the rapid formation of nitrophenolics in the Castle model run, it has the least (excluding WF1) total nitrophenolic formation relative to total emissions as seen in Figure 4.12.

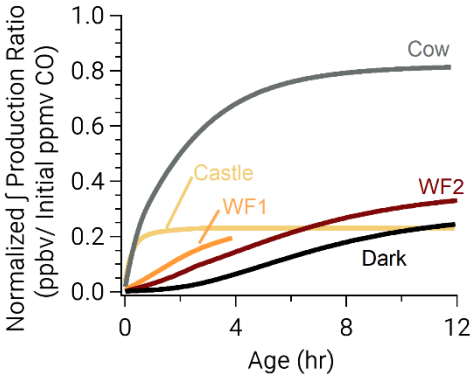

Figure 4.12: Integrated nitrophenolic production normalized to initial CO to compare nitrophenolic production across varying amounts of initial emissions. The simulated Castle and Cow plumes form nitrophenolics quickly. Even so, the Castle plume forms less nitrophenolics than other runs.

Figure 4.12 shows integrated nitrophenolic formation per emitted ppmv of CO, which allows us to compare total nitrophenolic formation across varying plume sizes. In contrast to the Castle model run, the Cow model run has the greatest nitrophenolic formation. These differences are the result of differing phenolic oxidation pathways. The Castle model run has a large (90 ppbv) O_3 background, which results in O_3 accounting for ~40% of phenolic oxidation between 30 min – 2 h of age (Figure 4.11C). At the end of the Castle model run (2.6 h) O_3 oxidation accounts for

33% of total phenolic loss, the largest of any model run (Figure 4.10). This is markedly different than the Cow model run where OH and NO_3 chemistry control phenolic oxidation before sunset, and NO_3 after. While O_3 accounts for only 16 % of phenolic loss at the end of the model run (~12 h). In our model, the reaction of O_3 + phenolics forms a ring opening product (Figure 4.1), but the rate coefficients and mechanisms are largely uncertain as discussed in the following section.

We include 157 phenolics in our above analysis, but only a few phenolics account for large fractions of nitrophenolic formation. At the end of our model runs, catechol and methylguaiacol account for the largest fraction of phenolic oxidation. Both compounds are mostly oxidized by NO_3. Catechol + NO_3 alone accounts for 10 – 16 % of total phenolic oxidation rate or 30 – 32 % of NO_3 + phenolic oxidation. Similarly, methylguaiacol accounts for 22 – 26 % of NO_3 + phenolic rates and is the largest fraction of phenolic oxidation by OH (17 – 18 % of OH + phenolic rates). However, to our knowledge, oxidation products of methylguaiacol by OH and NO_3 are unknown, but likely lead to nitrophenolics and therefore our nitrophenolic formation rates are likely underestimated.

4.3.3.3 Nitrocatechol Yield

The reaction of OH and NO_3 with catechol to form nitrocatechol accounts for the largest fraction (32 – 33 %) of total nitrophenolic formation. Therefore, here, we focus on nitrocatechol and detail the nitrocatechol yield from NO_3 and OH + catechol. Understanding nitrocatechol yield and its sensitivities is important to understanding the fate of NO_x and NO_x lifetime discussed in section 4.3.4 on page 94. However, the nitrocatechol yield depends on many variables such as the concentrations of NO_x, BBVOC, O_3 and the NO_x/BBVOC ratio as well as the certainty in our

chemical mechanisms. Therefore, we discuss the sensitivity of all of these factors on nitrocatechol yield below.

Yields of nitrocatechol vary between 33 – 45 % depending on the model run, where NO_3 is responsible for the 72 – 92 % of nitrocatechol Figure 4.13A). Figure 4.13 explores factors that govern nitrocatechol yield, defined as the molar ratio of nitrocatechol production to catechol destruction. Yields of nitrocatechol from OH are low relative to NO_3 yield due to the formation of trihydroxybenzene and benzoquinones (Figure 4.1), which account for 10 – 32 % and 4 – 5 % of total catechol loss, respectively.

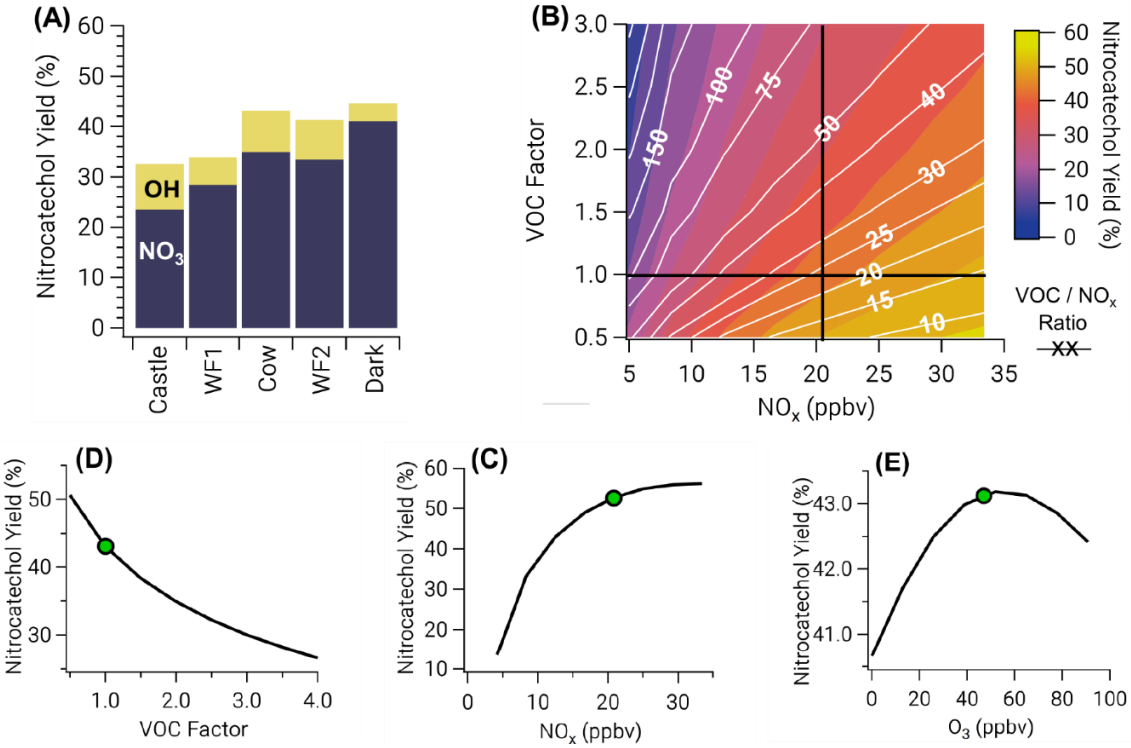

Figure 4.13: Panel A: nitrocatechol yield for all model runs colored by the fraction of nitrocatechol formed from NO_3 and OH oxidation of catechol. Panels B–E are shown for the Cow model run, which is representative of all other runs. B: two overlaid contour plots of VOC/NO_x ratio (white lines and white text) and nitrocatechol yield (color scale), with black cross sections that intersect at the observed Cow conditions. C: a cross section of B for nitrocatechol yield as a function of NO_x (horizontal black line). D: a cross section of B for nitrocatechol yield as a function of VOC factor, a multiple of the initial VOC emissions (vertical black line). E: nitrocatechol yield as a function of initial O_3. Green dots in C-E indicate observed conditions used for the model run. Nitrocatechol is primarily formed from NO_3 and the yield increases with increasing NO_x, but decreases with increasing BBVOC and BBVOC/NO_x ration. Ozone has little effect on nitrocatechol yield.

The largest yield (45 %) is from the Dark model run, where NO_3 oxidation accounts for more than 52 % of phenolic oxidation. In contrast, the lowest yield of nitrocatechol is from the Castle model run (33 %), which has the lowest emissions of NO_x compared to the other model runs. A similar yield (34 %) is found in the WF1 model run, however this model ends after only 4 h when 69 % of phenolics still remain. In short, nitrocatechol yield increases with increasing fraction of phenolic oxidation by NO_3.

To understand the dependence of nitrocatechol formation on O_3, NO_x, total BBVOC emissions (defined by the sum of ERs in our BBVOC inventory) and BBVOC/NO_x, we ran a sensitivity analysis on the nitrocatechol yield (Figure 4.13 B – E). Based on emitted NO_x and CO, BBVOC/NO_x ratios in plumes we sample range from 11 – 35. However, due to fire variability, BBVOC emissions can vary by at least a factor of two and for many BBVOCs by more than a factor of 10 from our emission ratios as shown in Figure 2.1 on page 16. Furthermore, we only account for BBVOCs that are most reactive to O_3, OH, and NO_3, which is smaller than total emitted BBVOCs.

The nitrocatechol yield generally decreases with increasing BBVOC/NO_x (color scale and white lines in Figure 4.13B). As expected, nitrocatechol yields increase with increasing NO_x (Figure 4.13C). Across all model runs, the nitrocatechol yield increases to 43 % – 57 % over a NO_x range of 4.2 – 91.2 ppbv. Further, the nitrocatechol yield changes to 27 % – 50 % (Figure 4.13D) when varying total BBVOC emissions by a factor 0.5 – 4. Finally, we investigate the sensitivity of nitrocatechol yield to initial O_3 and find that all model runs have little sensitivity to O_3 (Figure 4.13E) with an absolute change in nitrocatechol yield <3 % for all model runs when varying initial O_3 over a range of 0 – 113 ppbv.

The low sensitivity of nitrocatechol yield to O_3 may be partially explained by competition between O_3 and NO_3 + phenolic reactions after sunset. To explore this, we use framework developed by Edwards et al., 2017. Briefly, as stated in section 4.3.2.1 on page 81, BBVOCs are the main sink for NO_3 and therefore NO_3 loss rate is controlled by the NO_3 formation rate. As a result, NO_3 can be considered to be in approximate steady state between production by NO_2 + O_3 and loss by NO_3 + BBVOC. Further, according to Figure 4.8, the majority of NO_3 is lost to phenolics. As a result, the rate of phenolic oxidation after sunset (when OH oxidation of phenolics is minimized) can be approximated as

$$-\frac{d[\text{phenolics}]}{dt} \approx (k_{O_3}[\text{phenolics}] + k_{NO_2+O_3}[NO_2])[O_3] \qquad \text{E4.2}$$

which shows that the dominant oxidant is determined by the ratio of NO_2 and phenolics. We find that the ratio of phenolics to NO_2 at which NO_3 and O_3 oxidation is equal to be ~10 (at 298 K, using an ER weighted average k_{O_3} = 2.6×10^{-18} cm^3 $molecule^{-1}$ s^{-1}) with NO_3 oxidation more important below this ratio, and O_3 oxidation more important above it. Modeled phenolics/NO_2 ratios at sunset range between 0.7 – 1.2 and in all model runs, except the Castle model run, the ratio decreases with age. This suggests that in all model runs NO_3 oxidation is expected to control phenolic oxidation after sunset.

The phenolic oxidation analysis above relies on phenolic mechanisms and rate coefficients that are highly uncertain. For example, the above calculated ratio could be much lower in cold lofted plumes, but knowledge of temperature dependent O_3 + phenolic rate coefficients are unavailable. Using temperatures observed in the WF2 plume (~268 K) for $k_{NO_2+O_3}$the phenolics to NO_2 ratio at which NO_3 and O_3 oxidation is equal would be ~ 4.

The rate coefficient and products for the reaction of catechol + O_3 that we use are generated using MCM mechanism methodology (Jenkin et al., 2003; Saunders et al., 2003). An experimental study on the gas-phase reaction of catechol + O_3 finds an RH dependent rate coefficient that decreases non-linearly from 1.3×10^{-17} to 1.2×10^{-19} cm^3 $molecule^{-1}$ s^{-1} with increasing RH (El Zein et al., 2015). The MCM uses a rate coefficient of 9.2×10^{-18} cm^3 $molecule^{-1}$ s^{-1}. Further, to our knowledge there are no experimental kinetic or mechanistic studies of phenol + O_3. In the plumes we investigate, RH varied between roughly 20 – 60 %. Using an RH dependent rate coefficient for O_3 + catechol we find that the nitrocatechol yields range between 31 – 58 % with little change in yield for the Castle model run (–2 %) and larger change for the Dark model run (+13 %).

4.3.4 Fate of NO_x in Dark BB Plumes

Fire emissions are concentrated sources of NO_x, but as a result of photochemistry and oxidation the loss processes and lifetime of plume NO_x are variable. Photochemical NO_x loss pathways include reaction with OH (R4.1), net formation of peroxy acyl nitrates (PANs) (R4.2), and formation of organic nitrates (R4.3).

$NO_2 + OH + M \rightarrow HNO_3 + M$ R4.1

$NO_2 + R(O)O_2 + M \rightarrow PAN + M$ R4.2

$NO + RO_2 + M \rightarrow RONO_2 + M$ R4.3

The NO_x rate consumption is further influenced by the formation and the subsequent fate of NO_3 (R1.9, R1.11 – R1.14). Heterogeneous uptake of N_2O_5 (R1.9) and production of nitrophenolics double the NO_x consumption rate since in both cases subsequent chemistry consumes one additional NO_2 molecule, with the rate limiting step being $NO_2 + O_3$. Below, we focus on the products of NO_x oxidation, determined as $NO_z = NO_y - NO_x$.

Results are similar for all model runs, and we discuss the WF2 model run as a case study. While a complete NO_z budget analysis constrained to observations is beyond the scope of this work, we compare our model results of PAN, (peroxy acetyl nitrate, a component of PANs) to observations (Figure B.4). PAN accounts for ~65% of PANs, and PANs account for the largest fraction of NO_z in our model runs during sunlit hours. Our model reproduces PAN well in one transect, but underpredicts PAN by a factor of ~2.5 in others. Similar to O_3, PAN is enhanced on plume edges and the enhancement likely mixes into the center, which is not captured by our model runs. Therefore, we constrain our model to PAN observations, present an average result (Figure 4.14), and consider our model unconstrained to PAN to be a lower-bound PAN estimate and our model constrained to PAN to be an upper-bound PAN estimate.

4.3.4.1 NO_z Budgets

The late day emitted plumes modeled in this paper exhibit photochemical loss of NO_x initially. In the period prior to sunset, PANs and PNA (peroxynitric acid, HO_2NO_2) dominate NO_z and PANs alone accounts for 51 ± 6 % of NO_z by sunset. The WF2 plume is lofted, and therefore cold (~267 K), which results in a long PAN and PNA lifetime (~150 h, and ~0.4 h respectively). Even so, as these plumes continue to age, PANs and PNA decompose slowly (Figure 4.14) to provide NO_2 that promotes nitrophenolic formation and increases nitrophenolic yield (see section 4.3.3.3 on page 90). The increase in NO_2 after sunset promotes $CH_3O_2NO_2$ as well as NO_3 chemistry products, which grow steadily overnight. The contribution of PANs and PNA to NO_z decreases from 71 ± 6 % at sunset to 17 ± 2 % at sunrise. Relative NO_x loss to PANs and PNA is mostly replaced by the formation of nitrophenolics (Δ 19 ± 1 %), HNO_3 by NO_3 chemistry (Δ 22 %), and other or unknown NO_3 products (Δ 11 %) overnight.

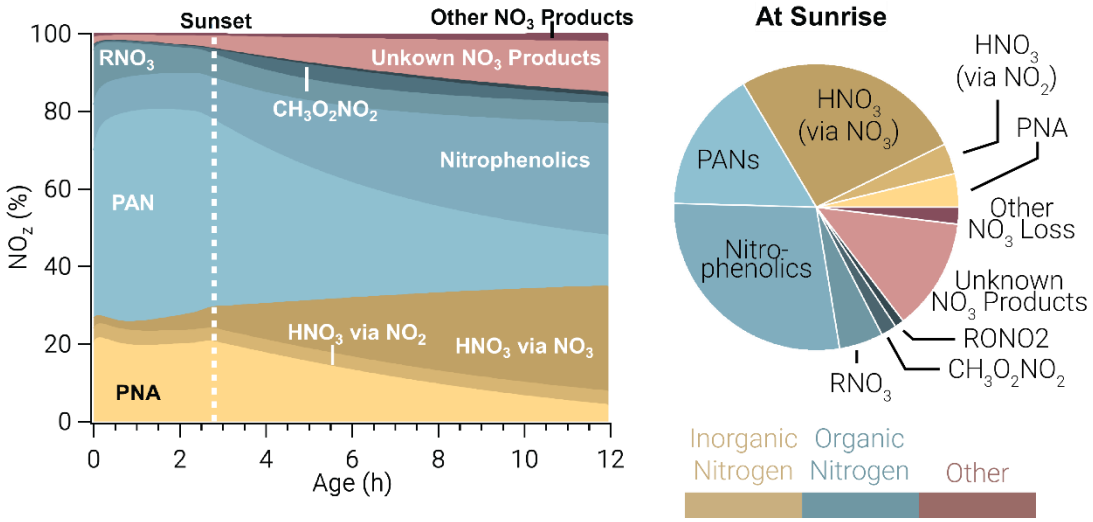

Figure 4.14: Relative integrated NO_x reservoirs and sinks for the WF2 model run as a function of plume age (left) and at sunrise (right). This result is the average between a WF2 model run constrained and unconstrained to PAN observations as explained in the main text. Gold colors indicate inorganic nitrogen, blue colors indicate organic nitrogen, and red colors indicate other forms of NO_z. In this analysis we consider HONO to be a member of NO_x, rather than NO_z. PAN and PNA dominate NO_z during the daytime, but after sunset these decompose to provide NO_2 that is subsequently lost to nitrophenolics and other NO_3 products overnight.

After sunset NO_3 chemistry takes over and by sunrise NO_3 chemistry products lead the (66 ± 2 %) NO_z budget. Nitrophenolic formation accounts for 56 ± 2 % of NO_z in the form of HNO_3 and nitrophenolics where nitrophenolics alone account for 29 ± 1 % of NO_z. Total HNO_3 formation accounts for 31 ± 1 % of NO_z, however most (88 %) of HNO_3 results from NO_3 chemistry. Despite accounting for only 9% (by mole) of initial emissions in our model runs, phenolics have a large and disproportionate effect on NO_x loss at night.

A similar example is seen in the Dark model run (Figure 4.15), where PANs and PNA dominate NO_z budget for 2.3 h until NO is depleted. At this time, PNA and PANs steadily decrease while NO_3 products steadily increase throughout the night. By sunrise the next day, NO_3 chemistry products (including unknown products) account for 80 % of NO_z. In all model runs there is a significant (12 – 16 %) NO_z formed through NO_3 chemistry that leads to unknown products. These

unknown products are primarily the result of NO_3 + heterocycles such as furans and pyrroles, which have published rate coefficients but little mechanistic work in the literature.

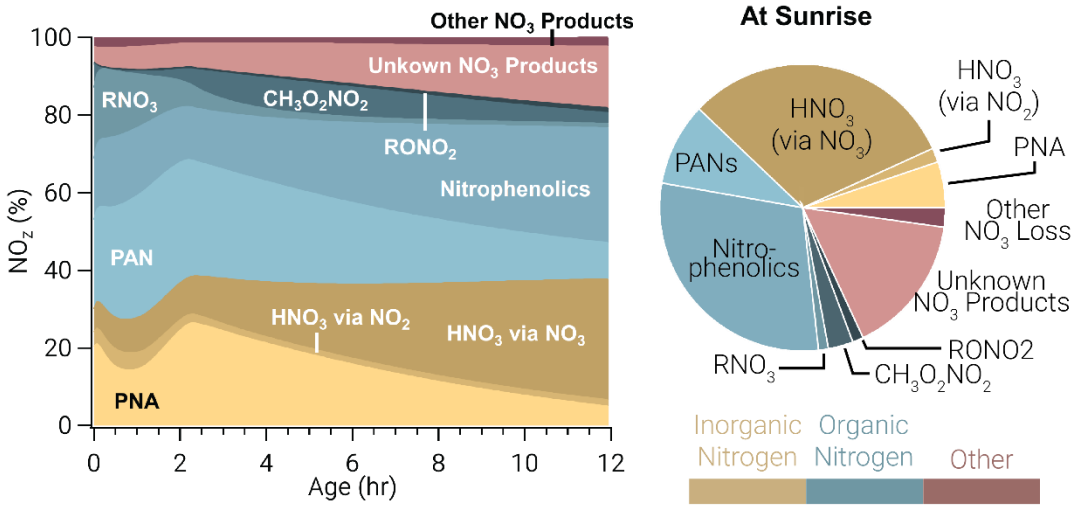

Figure 4.15: Similar to Figure 4.14, but for the Dark model run.

4.3.4.2 NO_x Lifetime

The availability of O_3 and sunlight at emission strongly affects NO_x lifetime (τ_{NO_x}, Figure 4.16) defined below

$$\tau_{NO_x} = \frac{1}{\sum_i k_i} \qquad \text{E4.3}$$

where k_i is a unimolecular rate coefficient for (R1.8, R4.1 – R4.3). Model runs with relatively large photolysis and O_3 at emission (Castle, Cow, and WF1) have near emission τ_{NO_x} that range from 1 – 3 h (Figure 4.16), which are accompanied by larger total oxidation rates for all BBVOCs Figure B.5 – Figure B.6). These model runs also exhibit the fastest nitrophenolic formation rates (Figure 4.12 on page 89). In contrast model runs with low or zero photolysis and near zero O_3 (WF2 and Dark) exhibit near emission τ_{NO_x} = ~10 – 16 h and τ_{NO_x} = 20 – 150 h, respectively. The absence of photolysis in the Dark model run explains the large difference in τ_{NO_x}between the WF2 and

Dark model runs as the WF2 model run has greater O_3 and $P(NO_3)$ that promotes NO_3 chemistry as well as OH radical that promotes PANs formation.

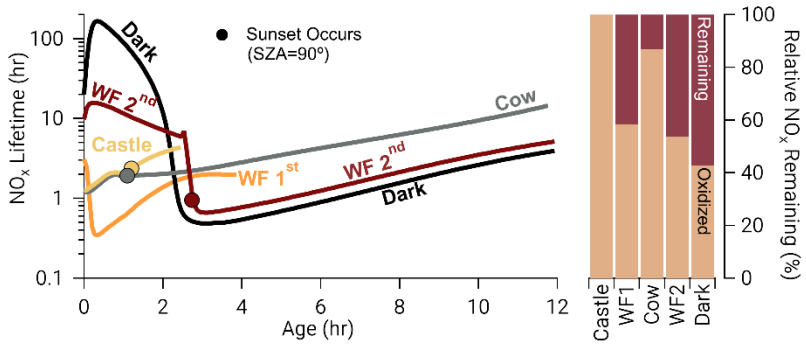

Figure 4.16: Time series: NO_x lifetime in hours on a log scale for all model runs where closed circles indicate the time of sunset (solar zenith angle = 90°). Bars: the relative NO_x remaining calculated as the fraction of NO_x remaining at the end of our model divided by the amount of NO_x that was reacted, excluding dilution. After the depletion of NO, NO_x chemistry changes dramatically in the WF2 and Dark model runs, reducing NO_x lifetime rapidly. A significant amount of NO_x remains in the WF2 and Dark model runs at sunrise, providing potential for significant morning chemistry to occur.

Once NO is depleted in both model runs NO_x chemistry changes. The BBVOCs oxidation rate rapidly increases (Figure B.5 – Figure B.6) and NO_x loss switches from primarily PAN and PNA to nitrophenolic production as the sun sets (Figure 4.14) and O_3 is entrained from the background. As such, τ_{NO_x}decreases markedly to ~ 0.5 h.

Due to their reduced oxidation rates at emission, the WF2 and Dark model runs retain about half (46% and 57 %, respectively) of the emitted NO_x by sunrise the next day. Here, we calculate remaining NO_x as the fraction of NO_x remaining at the end of our model divided by the amount of NO_x that was reacted, excluding dilution. This is about a $\Delta NO_x/\Delta CO$ of ~4 ppbv ppmv^{-1} at sunrise, which is similar to the initial emissions of Castle (~6 ppbv ppmv^{-1}) and WF1 (~5 ppbv ppmv^{-1}). Further, at sunrise, we expect the WF2 and Dark plumes to be more optically transparent and free of NO, and thus oxidation rates to increase rapidly as they both still contain NO_x. An increase in oxidation at sunrise will likely be more important for the Dark model run, as it retains 61% of the

emitted phenolics as opposed to 48 % in the WF2 model run. Plumes emitted after sunset have slower oxidation rates compared to daytime plumes (see section 4.3.2 on page 80), but undergo additional oxidation from evening to morning. However, outside of the plume-center, where O_3 is less effected by reaction with NO and is more likely to be generated by photochemical production, NO_x loss rates may be much larger. Therefore, NO_x away from the plume-center will likely be depleted more rapidly.

4.4 Conclusions

This chapter details the competitive oxidation of BBVOCs in four near-sunset, or low-photolysis, smoke plumes sampled by the NOAA Twin Otter or the NASA DC-8 aircraft during the FIREX-AQ 2019 field campaign. We model these plumes, as well as a theoretical dark plume, using an observationally constrained 0-D chemical box model. Our model suggests OH is reactive to most BBVOCs, while NO_3 is most reactive to phenolics, and O_3 to alkenes and terpenes. We find that initial reactivity is a good indicator for subsequent oxidation by OH, but not for NO_3 and O_3. For example, unlike urban plumes, we find that NO_3 loss to NO, photolysis and heterogeneous uptake are negligible loss pathways, and that most ($\geq$98 %) of NO_3 loss occurs through BBVOC oxidation.

Phenolics are the only BBVOC group for which oxidation by NO_3, OH, and O_3 is competitive. Specifically, NO_3 is responsible for 26 – 52 % of phenolic loss and leads (36%) phenolic oxidation in an optically thick mid-day plume. In addition, all phenolic oxidation after sunset is dependent on O_3, whether through direct oxidation by O_3, production of NO_3 by NO_2 + O_3, or ozonolysis of unsaturated hydrocarbons and subsequent decomposition to OH radicals.

We find NO_3 chemistry is responsible for 72 – 92 % (84 % in an optically thick mid-day plume) of nitrocatechol formation and controls nitrophenolic formation overall. Ultimately, nitrophenolic formation pathways account for 58 – 66 % of NO_x loss by sunrise the following day. Formation of nitrophenolics by NO_3, as opposed to OH, is the largest NO_x sink and accounts for most of the inorganic and organic nitrogen at the end of the night. While both PANs and PNA account for most of the NO_x loss shortly after emission, they decompose overnight providing a NO_x source for nitrophenolic formation and increase nitrocatechol yield. In short, NO_3 chemistry should be considered, even during the daytime, when investigating BB plume oxidation as we find it is the main source of nitrophenolic formation in plumes studied here and thus may be a dominant pathway to SOA formation.

4.5 Future Directions

We show above that the formation of nitrophenolics is likely dominated by the NO_3 radical at plume center. Outside of the plume center photolysis rates are expected to be larger, which may increase the loss of NO_3. Further, O_3 and OH production is expected to be greater on plume edges, thus increasing the competition for phenolic oxidation. Our 0-D box model is unable to explore these regions and therefore further studies are required to understand how the oxidation of BB plumes proceeds outside of the plume center.

Chapter 5: A Novel Analysis to Quantify Plume Crosswind Heterogeneity Applied to Biomass Burning Smoke

Abstract

We present a novel method, the Gaussian Observational Model for Edge to Center Heterogeneity (GOMECH), to quantify the horizontal chemical structure of plumes. GOMECH is a function of a long-lived tracer (such as CO) and fits observations of short-lived emissions and secondary products to provide metrics for plume width and center. To validate this approach, we use GOMECH to investigate several chemical processes related to OH and NO_3 oxidation of phenolics in fire plumes sampled during FIREX-AQ (Fire Influence on Regional to Global Environments and Air Quality, a 2019 wildfire smoke study). A GOMECH analysis of 430 crosswind transects suggests HONO is 16 – 27 ± 1% narrower than CO depending on age and emission time. Maleic anhydride, an indicator for OH chemistry, is 6 – 12 ± 1% wider than CO depending on age. NO_3 radical production is 0 – 9 ± 1% narrower than CO depending on emission time. Phenol, and methylcatechol are narrower than CO (4 ± 3% and 16 ± 1%, respectively), and catechol is 3 – 19 ± 1% narrower than CO depending on age and emission time. Nitrophenolic aerosol is 5 ± 2% narrower than CO. Lastly, we corroborate GOMECH results with a large eddy simulation model in a case study of nitrocatechol aerosol production in large wildfire plumes.

5.1 Introduction

Similar to plumes from urban and electric power generation sources, (Brown et al., 2012; Jones et al., 2005; Meidan et al., 2019) BB plume chemistry varies in the crosswind dimension during plume advection (Peng et al., 2020). BB plumes are unique because they emit large amounts of aerosols, which amplify chemical differences between plume center and edge through plume

darkening, or the attenuation of sunlight, concentrated at the plume center (Decker et al., 2021; Peng et al., 2020).

Differences in sunlight between the center and edge of BB plumes may result in differences in the amount and reactivity of atmospheric oxidants such as ozone (O_3), the hydroxyl radical (OH) and the nitrate radical (NO_3). For example, Peng et al. showed that in wildfire plumes the photolysis of nitrous acid (HONO) (R1.1) can be the dominant source of OH and that it occurs at greater rates on plume edges relative to the center (Peng et al., 2020). Further, OH concentrations are expected to depend non-linearly with NO_x, which can vary in concentration in the crosswind dimension (de Gouw et al., 2019).

Entrainment of background O_3, as well as photochemical production, can provide O_3 for plume oxidation near plume edges (Trentmann et al., 2003). Further, NO can depress O_3 at the plume center in freshly emitted plumes.

The role of NO_3 in daytime BB plumes has generally been neglected, or expected to occur primarily at the plume center where photolysis rates are depressed (Decker et al., 2019; Keywood et al., 2015; Kodros et al., 2020; Palm et al., 2020). The NO_3 radical is formed by the gas-phase reaction of O_3 and NO_2 (R1.8). In urban plumes during daytime, the NO_3 radical is rapidly destroyed by photolysis and by reaction with NO (τ<10 s) (Brown and Stutz, 2012; Wayne et al., 1991). The nitrate radical is also a precursor for N_2O_5, which undergoes heterogeneous uptake to produce $ClNO_2$ and HNO_3 (Brown and Stutz, 2012; Chang et al., 2011; McDuffie et al., 2018).

Despite these potential loss pathways, plume center models suggest most of the NO_3 is expected to be lost to BBVOCs (Decker et al., 2019, 2021). This is due, in part, to phenolics that react with NO_3 at near the gas-kinetic limit to form nitrophenolics and secondary organic aerosol (SOA) (Decker et al., 2019; Finewax et al., 2018; Lauraguais et al., 2014; Liu et al., 2019; Palm et al., 2020; Xie et al., 2017). Nitrophenolics absorb strongly in the ultraviolet and visible regions of the solar spectrum and are expected to significantly contribute to brown carbon (BrC) absorption (Kodros et al., 2020; Palm et al., 2020; Selimovic et al., 2020). Phenolic reactions with OH in the presence of NO_x also form nitrophenolics, but at a lower yield (Finewax et al., 2018).

Plume sampling by research aircraft is often conducted perpendicular to the direction of transport, the crosswind dimension, which reveals complex structures that reflect the heterogeneity in emission and chemistry (Palm et al., 2020; White et al., 1976). While plume structures vary in the crosswind vertical dimension as well, we focus only on the horizontal dimension in this work. Analysis of chemical evolution in plumes often avoid an analysis of plume heterogeneity and mixing by integrating the observations across the plume horizontally, or only considering plume center observations (Brock et al., 2003; Decker et al., 2019, 2021; Jost et al., 2003; Müller et al., 2016; Neuman et al., 2016; Peng et al., 2020; Trentmann et al., 2005). Plume-dispersion models represent one approach to quantify the spatial variation of plumes (Wang et al., 2017). Another includes high resolution Eulerian models (Alvarado and Prinn, 2009; Trentmann et al., 2002, 2003) or turbulence-resolving models (large eddy simulation, LES) (Wang et al., 2021), however these are computationally expensive and therefore include limited chemistry. When the crosswind plume structure is considered, it is often studied as a function of distance from the plume center (e.g.

Figure 5.1A), which makes the task of comparing plume heterogeneity as a function of age difficult because plumes tend to grow in size with age downwind of the source.

We describe a novel method, the Gaussian Observational Model for Edge to Center Heterogeneity (GOMECH), that quantitatively describes plume structures in the crosswind horizontal relative to a long-lived tracer. GOMECH is capable of separating differential crosswind plume oxidation rates. We present GOMECH and use it investigate several major chemical processes related to OH and NO_3 oxidation, with an emphasis on phenolic compounds, in fire plumes observed by both the NOAA Twin Otter and NASA DC-8 aircraft during the Fire Influence on Regional to Global Environments and Air Quality (FIREX-AQ), described below. First, we use GOMECH to model the plume structure of OH and NO_3, using the chemical proxies HONO, maleic anhydride (MA), PAN, O_3, and NO_3 production rate as well as phenolics and nitrophenolics in a bulk analysis of 430 crosswind transects. Finally, we consider a case study of a large wildfire to elucidate the relationships of OH, NO_3, and aerosol nitrocatechol plume structures by GOMECH and an LES model.

5.2 Methods

5.2.1 Aircraft Measurements

Aircraft Measurements for this analysis are described in detail in section 2.4.2 on page 18. Briefly, this analysis uses NOAA Twin Otter and NASA DC-8 observations of four wildfire plumes from the Williams Flats Fire sampled on 3 Aug and 7 Aug (panels A, B, E, F in Figure 2.2). We use observations of CO, NO, NO_2, O_3, HONO, PAN, furan (measured as $C_4H_2O_3$),

nitrophenolic aerosol ($C_6H_5NO_3$ + $C_6H_5NO_4$ + $C_7H_7NO_3$ + $C_7H_7NO_4$), and nitrocatechol aerosol (measured as $C_6H_5NO_4$).

5.2.2 LES Model

We analyze model results from a Large Eddy Simulation (LES) of the Williams Flats Fire that were previously described by Wang et al., 2021 with the addition of catechol oxidation mechanisms for NO_3, OH and O_3. The fire plume is driven by surface fluxes of sensible heat and chemicals, both approximated from GOES-16 satellite (Li et al., 2020) measurements. This LES model is coupled with a representative chemical mechanism, consisting of 44 transported tracers and 84 chemical reactions, covering major tropospheric chemical reactions involving NO_x - VOCs - O_3 chemistry in addition to a phenolic mechanism below. The photolysis frequencies are calculated using the Fast Tropospheric Ultraviolet-Visible scheme (Tie et al., 2003). Two inert aerosol tracers, black carbon and organic carbon, are included to account for the aerosol impacts on radiation. The LES model domain is 70 km x 30 km x 6 km (height), with a horizontal resolution of 100 m and a vertical resolution ranging from 78 m (at the surface) to 138 m (near the top). The LES model is run in an idealized configuration, initialized using vertical profiles of potential temperature, specific humidity, wind, chemical species from a mesoscale (12 km) WRF-Chem simulation. This idealized configuration does not consider terrain.

Reactant 1	Reactant 2	Rate Coefficients	Product Yield	Product
Catechol	OH	1.00-10	0.30	CatecholO
Catechol	NO_3	9.90-11	0.91	CatecholO
Catechol	O_3	9.20-18	1.00	--
CatecholO	NO_2	2.80-12	1.00	Nitroaromatic

Table 5.1: Simplified catechol mechanism added to the LES model to model nitrocatechol formation. Rate coefficients are in units of cm^3 $molec.^{-1}$ s^{-1}. Product yields are taken from Finewax et al. 2018.

5.2.3 Derivation of the Gaussian Observational Model for Edge to Center Heterogeneity

Section C.1 provides a detailed derivation of GOMECH, which is briefly outlined below. Dispersion of a point source emission leads to a Gaussian shape as a function of crosswind distance (y) that is symmetric about the plume center (y = 0) (Turner, 1970). We define the plume center as the location of the maximum observed CO, a long-lived BB emission. The crosswind structure of CO is thus

$$CO = A_{CO} e^{\frac{-y^2}{w_{CO}^2}} \quad \text{(E5.1)}$$

Here, A_{CO} is the maximum of CO and w_{CO} is the plume width of CO. The plume width is defined as the distance from plume center to the location where CO = $A_{CO} e^{-1}$.

Similarly, for a species i the crosswind structure is

$$i = A_i e^{\frac{-(y-b)^2}{w_i^2}} \quad \text{(E5.2)}$$

where A_i is the maximum of i, w_i is the plume width of i , and b is the location of maximum i relative to the plume center of CO. The variable b accounts for measurements where the maximum of i is shifted relative to CO (e.g. j_{HONO} in Figure 5.1A).

However, fires typically consist of a series of hot spots or a fire front that creates complex crosswind plume structures that often do not appear Gaussian when considered as a function of distance from the plume center. Under the assumption that all emissions sampled in the crosswind are 1) affected by mixing equally, 2) were co-located, and 3) did not vary with fire conditions, then any change in the crosswind structure of i, relative to CO, will be due to chemistry or photolysis. To resolve plume structure effects from chemistry or photolysis, we rederive i as a function of CO by eliminating y in both (E5.1) and (E5.2) (See section C.1) shown below, which is the full form of GOMECH.

$$i = A_i \times A_{CO}^{-\frac{w_{CO}^2}{w_i^2}} \times CO^{\frac{w_{CO}^2}{w_i^2}} \exp\left[\frac{2b\left[\sqrt{w_{CO}^2 \ln(Q_{CO}) - w_{CO}^2 \ln(A_{CO})}\right]}{w_i^2} - \frac{b^2}{w_i^2}\right] \quad \text{(E5.3)}$$

Here, both b and w_i are relative to w_{CO}. To simplify E5.3, we define w_{CO} as 1 and normalize i and CO to a maximum of 1, which are denoted as the unitless Q_i and Q_{CO}, respectively. For measurements that are enhanced in the crosswind transect (e.g. HONO in Figure 5.1A) we define the ambient background signal (a 10 s average before and after the plume) as 0. For measurements depleted in the crosswind transect (e.g. j_{HONO} in Figure 5.1A) we define 0 as the minimum observed signal in the plume. After doing so, Q_i is

$$Q_i = Q_{CO}^{\frac{1}{w_i^2}} \exp\left[\frac{2b\left[\sqrt{\ln(Q_{CO})}\right]}{w_i^2} - \frac{b^2}{w_i^2}\right] \quad \text{(E5.4)}$$

We use E5.4 to perform a least-squares fit of Q_i as a function of Q_{CO} to determine both w_i and b relative to w_{CO} for observed crosswind transects. While our analysis uses normalized

observations, non-normalized observations can be used with E5.3 to find equivalent, yet unitless, w_i and b relative to w_{CO}.

The concepts surrounding GOMECH are detailed, with examples (Figure 5.1 – Figure 5.8). Briefly, differences in plume structures of Q_i relative to Q_{CO} include 1) enhanced loss of Q_i on plume edges relative to plume center, or enhanced formation of Q_i at plume center relative to plume edge (termed narrowing, see HONO in Figure 5.1A), or 2) enhanced formation of Q_i at plume edges relative to plume center or enhanced loss of Q_i at plume center relative to plume edge (termed widening) where either may lead to a plume edge Q_i greater than plume center (b>0, see j_{HONO} in Figure 5.1A).

The relationships above are empirical, but as described below they fit the differential gradients of an array of short-lived species relative to CO. The text provides uncertainty metrics to quantify the validity of this empirical approach. Briefly, reported errors for w and b are the estimated standard deviation of the fit. Shading on GOMECH plume shapes are residuals of the fitted observations averaged per normalized CO bins of 0.004. GOMECH cannot accurately approximate the plume center of measurements that exhibit strong plume asymmetry (Figure 5.4). Inlet effects (such as hysteresis) can bias plume shapes (Figure 5.5). Lastly, low signal to noise can result in plume widths that are likely lower limits (for narrow plumes) or upper limits (for wide plumes). Therefore, in bulk analyses (discussed below) we exclude plumes based on signal thresholds (Table 5.2).

Measurement	Threshold for each plume
HONO (Twin Otter)	Median signal> 5×background
HONO (DC-8)	Median signal> 3×background
Maleic anhydride	Median signal> 3×background
Phenol	Median signal > 500 pptv
Catechol	None
Methylcatechol	Median signal > 10 pptv
Nitrophenolic aerosol	> 10 μg sm^{-3}

Table 5.2: Thresholds used to filter plumes for each compound in the campaign-wide analysis. Only plumes with sufficient signal to noise can be used in GOMECH to minimize bias to noise.

5.2.3.1 Introduction to GOMECH by Example of HONO and jHONO

Here, we explain how recreated structures from GOMECH relate to physical plume structures. Plume narrowing, widening, or plume center shifts result from differences in production or loss rate between the compound of interest and the tracer compound (CO). A narrow plume occurs when a compound decreases in concentration at a faster rate, relative to CO, on the plume edges or when a compound increases in concentration at a faster rate, relative to CO, at the plume center. Plume widening is similar. A wide plume occurs when a compound increases in concentration at a faster rate, relative to CO, at plume edges, or decreases in concentration at a faster rate, relative to CO, at the plume center. Plume center shifts are related to plume widening, but occur when a compound is sufficiently lost at plume center, or sufficiently produced on the plume edge, such that the maximum concentration is no longer located at the plume center, or aligned with CO. We show examples of the above plumes throughout the text, but here we detail and explain one plume transect shown in Figure 5.1 and Figure 5.2 for CO, HONO, and j_{HONO}.

As shown in Figure 5.1A, HONO and j_{HONO} have plume structures that appear roughly anti-correlated as a function of distance from the plume center. Plotting normalized HONO and j_{HONO} vs normalized CO results in a scatter of data points that are indeed roughly anti-correlated

Figure 5.1B). Using GOMECH, we find that both j_{HONO} and HONO can be fit to a Gaussian shape relative to CO (lines in Figure 5.1B). This empirically suggests that the attenuation of j_{HONO} can be approximated by a Gaussian shape. Further, as HONO loss is likely dominated by photolysis, the HONO plume structure can be expected to be Gaussian as well. Figure 5.1C shows the recreated plume shapes of both HONO and j_{HONO}. The recreated plume shapes generally reflect the anti-correlation seen in Figure 5.1A.

There are three marked intersections of HONO and j_{HONO} with the normalized values of HONO, j_{HONO}, and CO indicated on the right of Figure 5.1A. We use these markings to understand how well the recreated plume shapes relate to the physical plume and to each other. As seen in Figure 5.1C, the recreated plume shapes intersect at a HONO and j_{HONO} value of 0.24 ± 0.02 and a CO value of 0.64 ± 0.10. This can be interpreted to mean that whenever normalized CO is 0.64, we expect HONO and j_{HONO} to intersect at a value of 0.24. Our plume structure approximations assume a plume is symmetric, and therefore one may expect there to be only two intersections in Figure 5.1A, yet we see three intersections. This does not necessarily mean the plume is asymmetric, but instead is the result of plume variability in CO and j_{HONO}, and thus HONO.

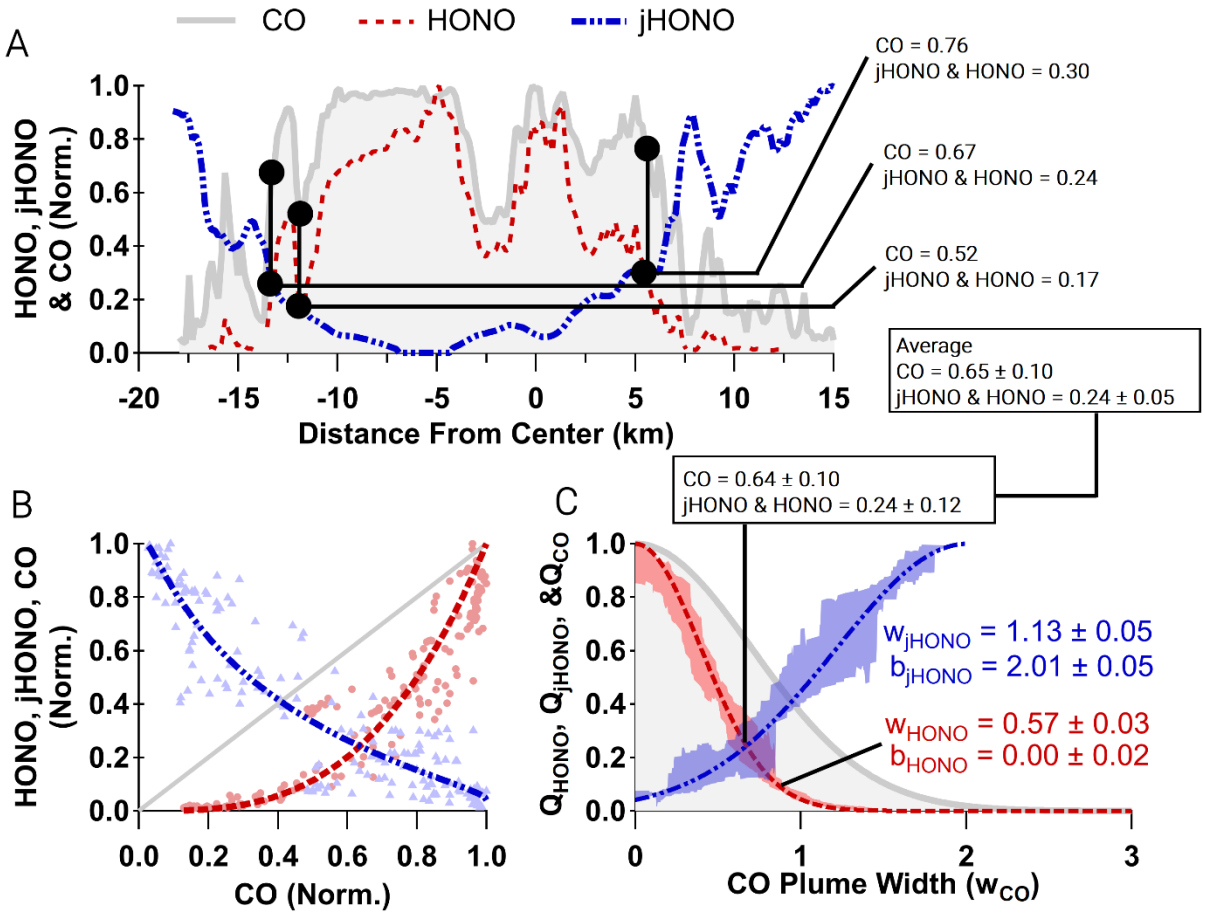

Figure 5.1 Panel A: example of normalized observations of HONO (red), j_{HONO} (blue) and CO (filled grey trace) plotted against distance from plume center for the Williams Flats Fire sampled by the DC-8. The plume was sampled at 01:29 UTC on Aug 7 2019. Average plume age was 1.4 h, but varied between 1.25 – 1.50 h within the transect. Intersections of HONO and j_{HONO}, with the corresponding value of CO, are indicated. Panel B: normalized observations of HONO (red circles), j_{HONO} (blue triangles), and CO (black line) plotted against normalized CO with fits (using GOMECH) shown as lines. Panel C: recreated plume shapes using GOMECH of j_{HONO} (blue) and HONO (red) with fitting parameters indicated. Shading indicates the estimated standard deviation of the fit.

The three marked intersections vary in values of CO between 0.76 – 0.52 and j_{HONO} and HONO values of 0.30 – 0.17. Even so, we show in the boxes of Figure 5.1 that the average of the marked intersections agree with the recreated plume shape. This would suggest that GOMECH recreates the average intersection of normalized HONO and j_{HONO}. This result is similar across all of our recreated plume shapes. As we discuss below, GOMECH can be used to estimate the physical plume typically within 20% of the average observed values.

Figure 5.2 shows HONO from Figure 5.1, and illustrates a plume width of 0.57 (w_{HONO} = 0.57). The plume width is defined as the horizontal distance between plume center and edge at a value of e^{-1}, or an approximate value of 0.37 as seen in Figure 5.1B. To understand how the modeled plume structure relates to the physical plume, we have marked five locations in Figure 5.1A that correspond to normalized HONO values of 0.5. The normalized CO value at these five locations averages to 0.80 $\pm$ 0.08 (error is standard deviation of the average). The corresponding location in the approximated plume shape results in a normalized CO value of 0.80 $\pm$ 0.06 (error is the average residual for normalized CO binds of 0.004). In this example, the approximated plume shape reproduces the average value of HONO relative to CO at a normalized HONO value of 0.5. Further, the approximated plume shape has no offset (b_{HONO} = 0), meaning the HONO maximum is aligned with the CO maximum. However, as shown in Figure 5.1A, the HONO maximum (HONO = 1.0) corresponds to a CO value of 0.96. This discrepancy is not captured by the model, and may be due to difficulty fitting small offset values. Further, the difference in plume center location is not captured within the fit errors.

The color scale at the top of Figure 5.2A indicates the fit residuals, and shows that agreement between the approximated plume shape and real plume can vary between 0.0 – 0.4. The average $\pm$ 1σ fit residual is 0.09 $\pm$ 0.09, which suggests that, generally, the approximated plume shape agrees with the physical plume structure within 9 $\pm$ 9% for this example.

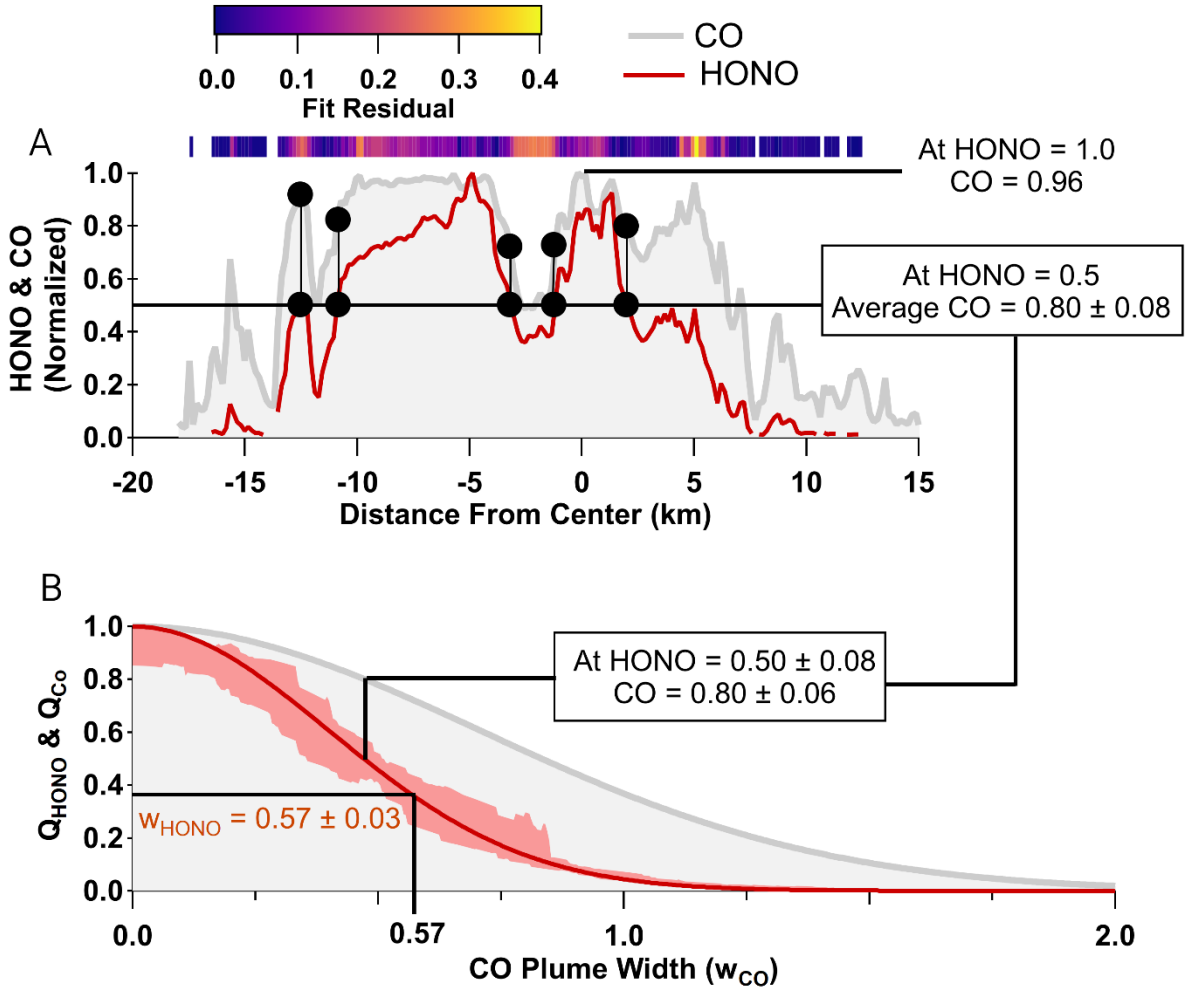

Figure 5.2 Panel A: normalized observations of HONO (red), also shown in Figure 5.1, and CO (filled grey trace) plotted against distance from plume center. Values of normalized CO that correspond to a normalized HONO value of 0.5 as well as the normalized CO value corresponding to maximum HONO are indicated. The fit residuals are shown on a color scale and the fit is shown in Figure 5.1B. Panel B: The recreated plume shape using GOMECH where shading indicates the estimated standard deviation of the fit. The HONO plume width as well as the CO values corresponding to a recreated normalized HONO value of 0.5 are indicated.

Figure 5.3 is analogous to Figure 5.2, but for j_{HONO}, and shows a plume width of w_{jHONO} = 1.13 with a plume center shift of b_{jHONO} = 2.01. The plume center shift is defined as the location of the plume center relative to CO plume width. To understand how the approximated plume structure relates to the physical plume, we have marked four locations in Figure 5.3A that correspond to normalized j_{HONO} values of 0.5. The average value of CO for these marked points is

0.36 ± 0.09. The corresponding value (j_{HONO} = 0.50 ± 0.11) in the recreated plume shape gives a CO value of 0.31 ± 0.17 meaning the recreated plume shape agrees with the physical plume shape at a j_{HONO} value of 0.50. We have also indicated the j_{HONO} plume maximum (j_{HONO} = 1). However, the j_{HONO} max corresponds to a CO value of 0.09, while the recreated plume shape maximum corresponds to a CO value of 0.02. These discrepancies are outside of the fit errors, but are within the fit residual average of 0.09 ± 0.08 suggesting that the recreated plume shape generally agrees with the physical plume values within 9 ± 8%.

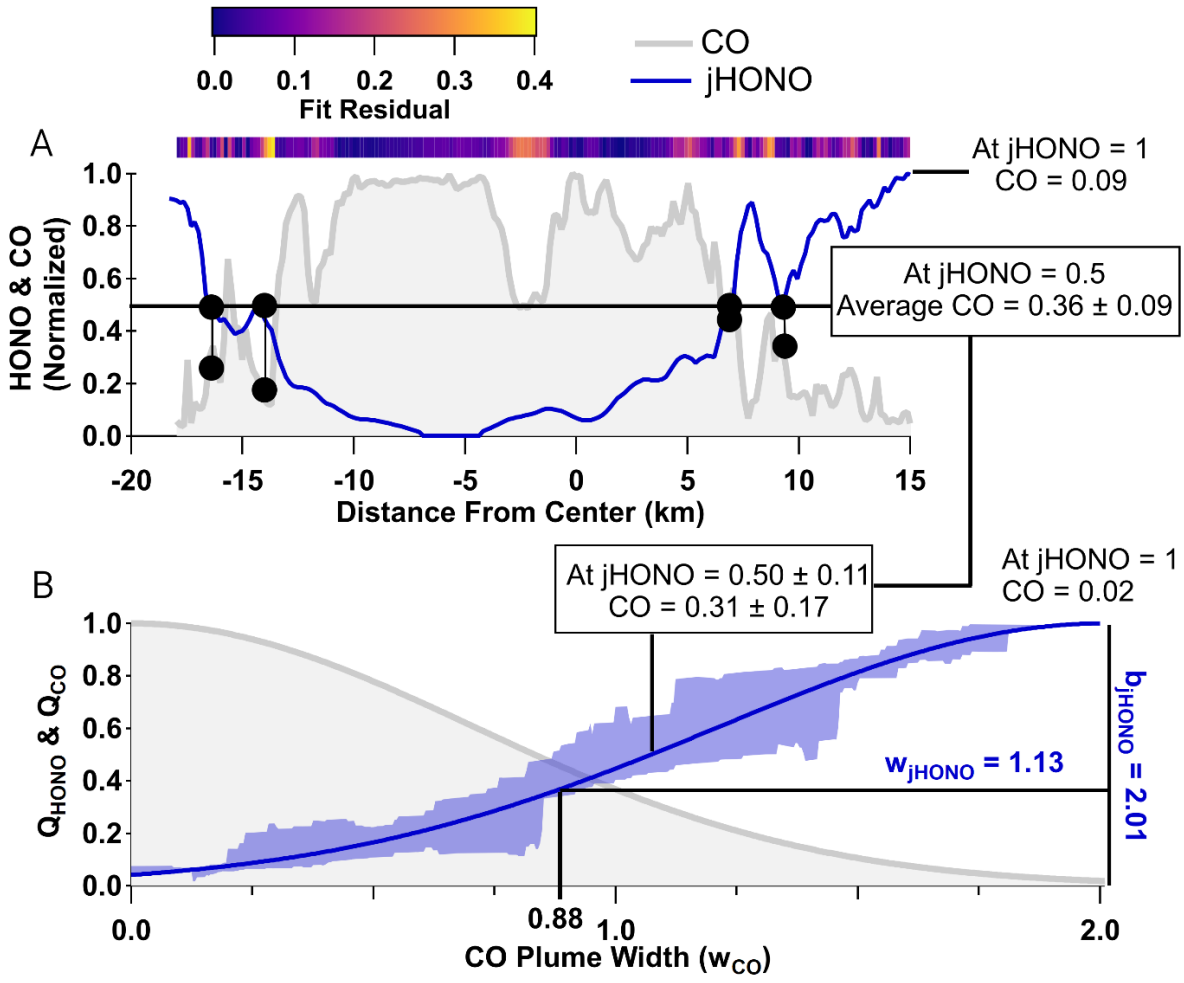

Figure 5.3: Similar to Figure 5.2, but for jHONO.

5.2.3.2 Discussion on Uncertainties and Model Limitations

There are a number of metrics that can be used to understand how well the model captures the plume structure. To illustrate these, we present a plume transect of MA, (maleic anhydride, measured as $C_4H_2O_3$), in Figure 5.4.

To gain an overall understanding of how well the model captures the plume structure, we show the fit residuals, with the average $\pm$ standard deviation and median residual indicated as a colored bar. Further, the model plume structure in Figure 5.4B shows three metrics for uncertainty: 1) Fit error, or the estimated standard deviation of the fit, as vertical hashes bounding the plume shape, 2) the average of residuals for a corresponding CO binned value (bin width = 0.004) as a dark shading, and 3) the maximum residual for a corresponding CO binned value as a light shading.

The range of residuals shown in Figure 5.4A is larger than the examples shown in Figure 5.2 and Figure 5.3 for HONO and j_{HONO}. Further, the plume center is poorly captured. These could be caused by a number of reasons that include, but are not limited to, 1) asymmetry in the plume structure, 2) a discontinuity at $w_{CO} = 0$ as explained below, and 3) low signal to noise ratios.

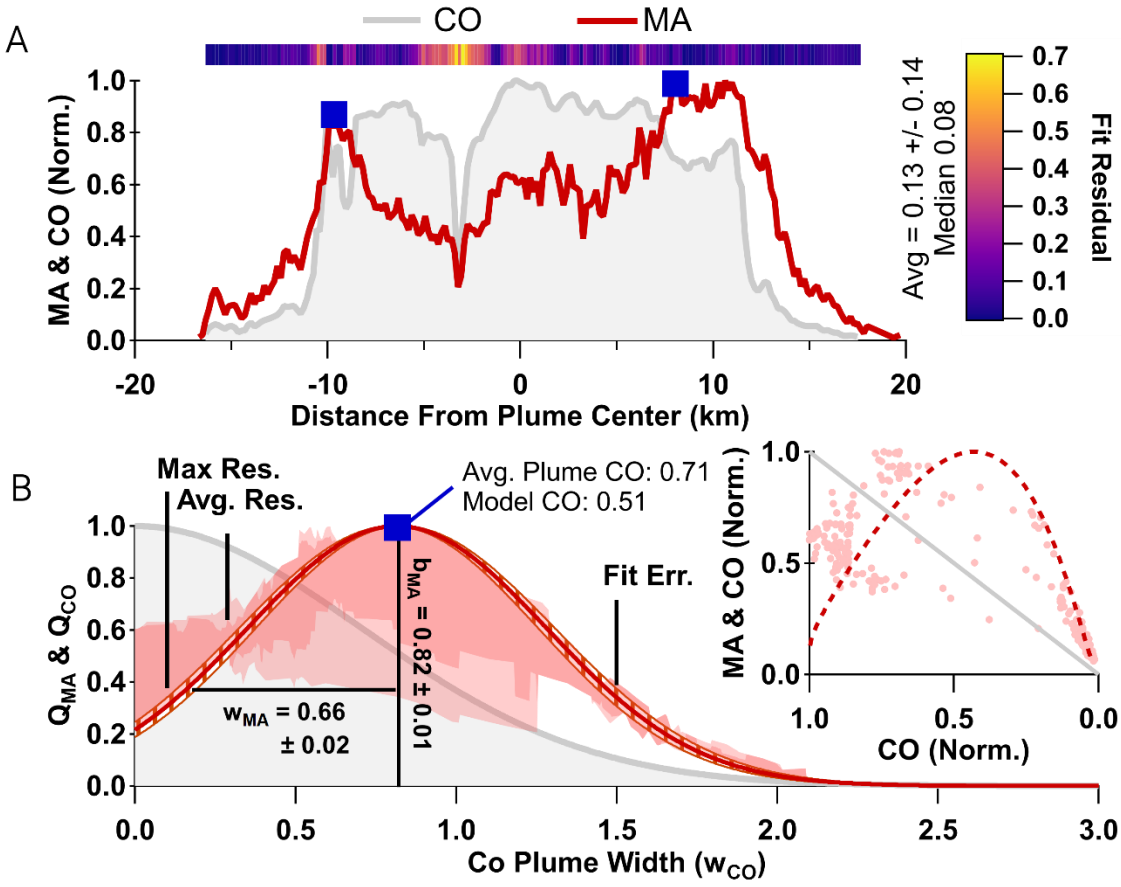

Figure 5.4 Panel A: normalized observations of maleic anhydride (MA, measured as $C_4H_2O_3$) and CO plotted against distance from plume center from the Williams Flats Fire sampled by the DC-8 at 01:50 UTC on Aug 7 2019. Average plume age was 2.5 h, but varied between 2.4 – 2.9 h within the transect. Fit residuals are shown as a color scale with the average ± standard deviation and median indicated. Blue squares indicate the two maxima of normalized MA and correspond to the maxium plume shape in panel B. Panel B: recreated plume shape of MA using GOMECH with the estimated standard deviation of the fit indicated by vertical red bars bounding the plume shape, the average of binned residuals (CO bin width = 0.004) as darker shading and the max residuals as lighter shading. Inset shows normalized MA (red circles) plotted against normalized CO (on a reversed axis) with the fit shown as a dashed line.

5.2.3.3 Limitations in assuming plume symmetry

Potential reasons 1 and 2 are related because GOMECH assumes that a plume is symmetric and can therefore be approximated by a single Gaussian. For plumes with a center shift (b) > 0, this assumption results in a point of discontinuity located at a CO plume width of zero. In other

words, if the recreated plume shapes in Figure 5.4B were mirrored about the vertical axis, the junction between the two resulting Gaussians would be discontinuous. Indeed, in Figure 5.4B there are large residuals that lie exclusively above the model at plume widths near $w_{CO} = 0$, suggesting that a single Gaussian does not capture this region of the plume structure well. One solution would be to derive a fitting equation using the sum of two off-center Gaussians with equal, but opposite sign, center shifts ($\pm$ b). The result is shown below.

$$Q_X = Q_{CO}^{\frac{1}{w_i^2}} e^{\left[\frac{2b\left[\sqrt{\ln(Q_{CO})}\right]}{w_i^2} - \frac{b^2}{w_i^2}\right]} + Q_{CO}^{\frac{1}{w_i^2}} e^{\left[\frac{-2b\left[\sqrt{\ln(Q_{CO})}\right]}{w_i^2} - \frac{b^2}{w_i^2}\right]} \quad \text{(E5.5)}$$

Using E5.5 to fit the transects in Figure 5.4 we find an improvement in fitting residuals, however negligible change in the values of w_{MA} and b_{MA}. Generally, we find similar results for other compounds and transects and therefore we choose to use the simpler form shown in E5.4

5.2.3.4 Limitations caused by low signal to noise

GOMECH requires the fit to return the maximum observed signal, which is a value of 1 for our normalized observations. As a result, the fit residuals are typically concentrated below the recreated plume shape as seen in Figure 5.4B. If the signal to noise is sufficiently low, it can result in an inaccurate identification of the plume center, or plumes that are narrower than reality. Therefore, we filter transects used in our bulk-analysis to remove low signal to noise data.

Measurement	Threshold for each plume
HONO (Twin Otter)	Median signal> 5×background
HONO (DC-8)	Median signal> 3×background
Maleic anhydride	Median signal> 3×background
Phenol	Median signal > 500 pptv
Catechol	None
Methylcatechol	Median signal > 10 pptv
Nitrophenolic aerosol	> 10 μg sm^{-3}

Table 5.3: Thresholds used to filter plumes for each compound in the campaign-wide analysis. Only plumes with sufficient signal to noise can be used in GOMECH to minimize bias to noise.

To determine thresholds, we binned normalized observations by normalized CO bins of 0.05 and then applied GOMECH to the bin median. This provides 20 points for a GOMECH fit. We then compared this result to a GOMECH global fit (without binning) of the same data. We increased the threshold value until both methods agree within fitting errors. This method removes crosswind plume transects with low signal that biases the GOMECH fit.

5.2.3.5 Inlet Effects

When applying GOMECH, care must be taken to ensure that inlet effects do not bias the result. Generally, we find that inlet effects widen a plume due to hysteresis in the measurement when the aircraft exits a plume. See, for example, Figure 5.5, which shows observations of C_4H_4O (likely furan, an isomer or a proton-transfer fragment as measured by NOAA-PTR-ToF-MS). GOMECH suggests the width of C_4H_4O is 106% of CO. Further, by all uncertainty metrics, the fit appears to accurately capture the shape of C_4H_4O relative to CO with a median residual of 0.03. Even so, the observations are likely biased by hysteresis caused by the low volatility of C_4H_4O. Therefore, any physical interpretation of the fit is restricted to an upper-limit width.

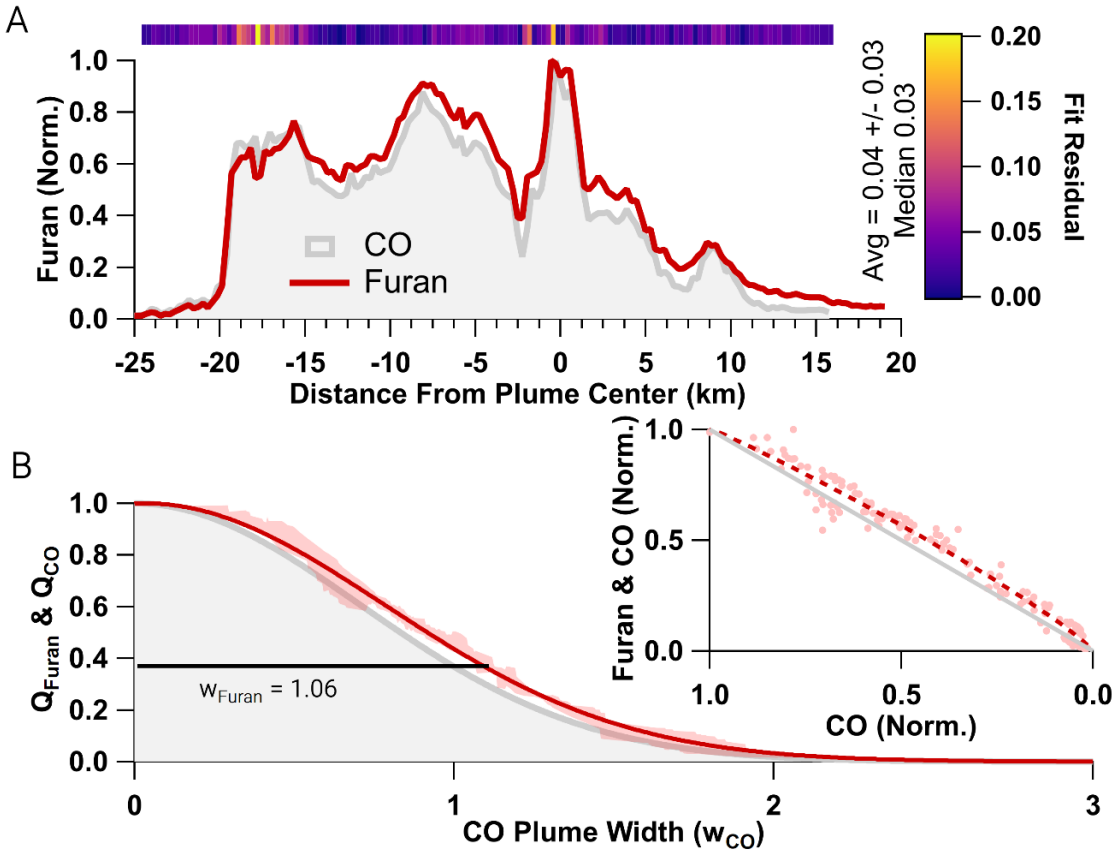

Figure 5.5: Similar to Figure 5.2, but for C_4H_4O (likely the sum of furan and other proton-transfer products), which shows how inlet effects can result in wide plume structures.

5.3 Results and Discussion

5.3.1 Quantification of Photochemical Plume Structure

Nitrous acid, HONO, is a major biomass burning emission that undergoes rapid photolysis to produce OH radicals (R1.1). The HONO photolytic lifetime (i.e., j_{HONO}^{-1}) on the edge of a plume is of order tens of minutes (Figure 5.1A), typically more rapid than mixing time scales that reduce its differential gradient relative to CO. As such HONO is depleted relative to CO on plume edges creating a narrow HONO plume structure, consistent with results by Peng et al. 2020. GOMECH analysis provides a quantitative measure of these gradients and their implications for plume photochemistry. The GOMECH fit in Figure 5.6B–C shows quantitatively that HONO is 33 ± 2%

narrower (w_{HONO} = 0.67±0.02) than CO. Therefore, we expect that OH has been produced on the plume edges.

Indeed, we see plume edge enhancements of OH oxidation products, namely maleic anhydride (MA, Figure 5.6A) and peroxy acetyl nitrate (PAN, Figure 5.7A) on plume edges. MA is an oxidation product that results from OH oxidation of furans (see section C.3 on page 195, Aschmann et al., 2011, 2014; Coggon et al., 2019; Tapia et al., 2011; Yuan et al., 2017). While we find similarity in plume structure between PAN and MA, we primarily use MA as an indicator for OH chemistry (Chattopadhyay et al., 2020).

GOMECH demonstrates that MA is 38 ± 2% narrower than CO and the maximum of MA is shifted to a CO plume width of b_{MA} = 0.92 ± 0.02. The greatest depletion of HONO relative to CO is located at ~0.81 w_{CO} (Figure 5.6C). This is near the greatest enhancement of MA, consistent with a chemical regime in which loss of HONO and production of MA are spatially similar. Additional examples are shown for HONO, PAN, O_3 and j_{HONO} in Figure 5.6 – Figure 5.8.

As we demonstrate further below, GOMECH provides a measure of plume structure that is qualitatively consistent with expected chemistry, trends in plume age and trends in photolysis history. Further, the model produces consistent results for individual compounds regardless of research platform and measurement technique.

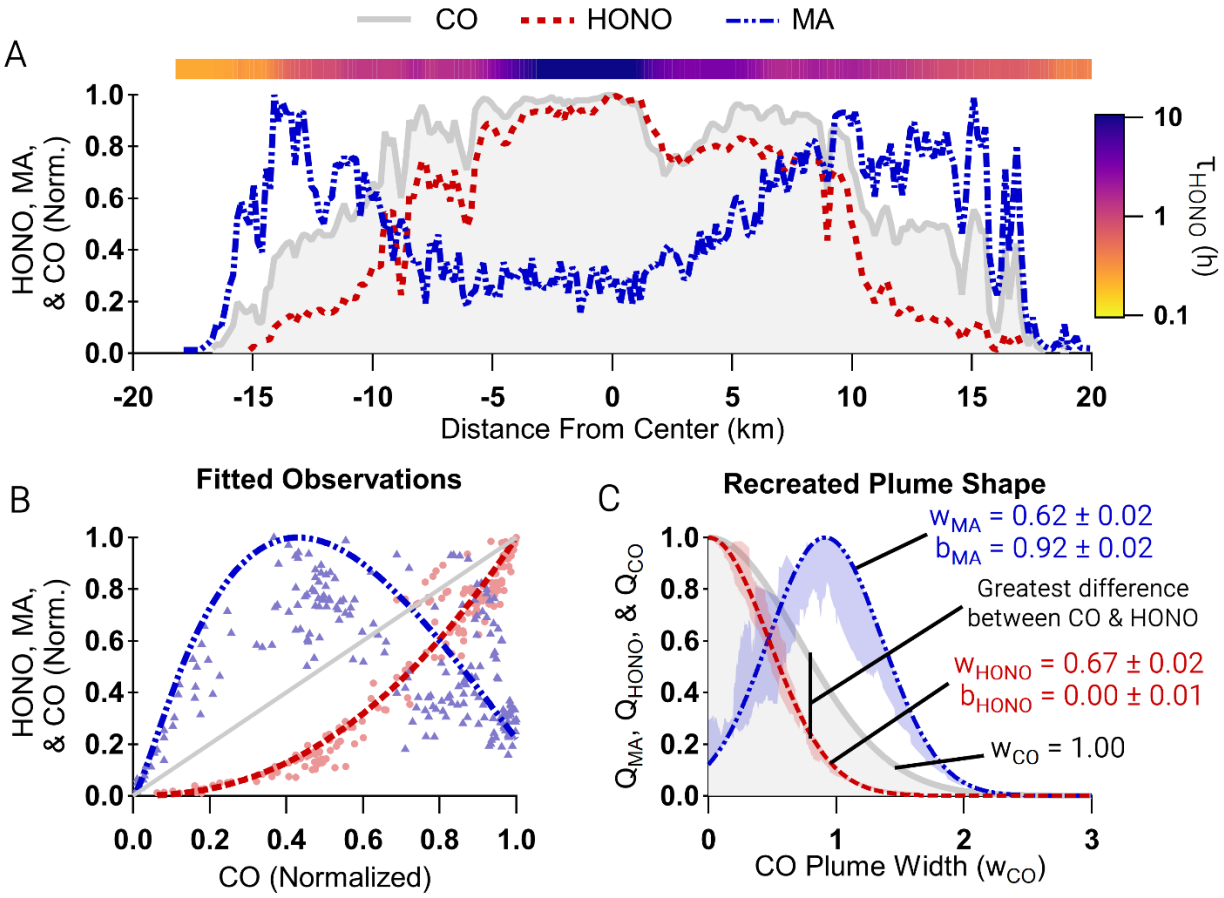

Figure 5.6 Panel A: Panel A: normalized observations of HONO (red), maleic anhydride (MA, measured as $C_4H_2O_3$) (blue), and CO (grey outline and fill) as well as HONO photolytic lifetime in hours (τ_{HONO}, color scale), plotted against distance from plume center (maximum CO) from a plume transect of the Williams Flats Fire sampled by the DC-8 at 01:22 UTC on Aug 8 2019. Average plume age was 1.2 h, but varied between 1 – 1.25 h within the transect. Panel B: normalized observations of HONO (red circles), MA (blue triangles), and CO (grey line) plotted against normalized CO with fits (using Eq. 4) of MA (blue) and HONO (red). Panel C: recreated plumes shapes of HONO (red) and MA (blue) using the fit parameters derived in Panel B as well as shading indicating fit residuals averaged by normalized CO bins of 0.004. The recreated plume shapes suggest HONO is 33±2% narrower than CO and MA is 38±2% narrower than CO, but the maximum MA is shifted to a CO plume width of 0.92±0.02.

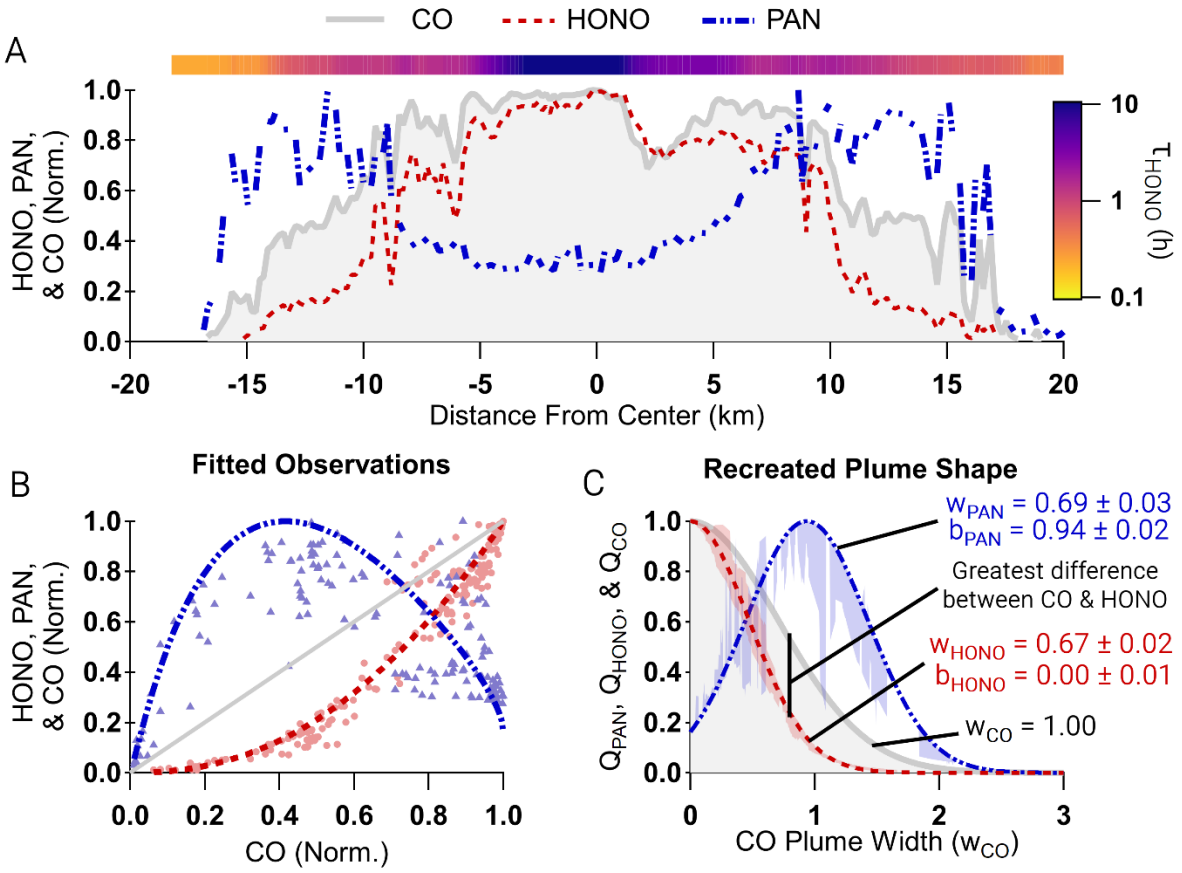

Figure 5.7 Similar to Figure 5.6, but for HONO and O_3. The plume is from a transect from the Williams Flats Fire sampled by the DC-8 at 01:22 UTC on Aug 7 2019. Average plume age was 1.2 h, but varied between 1 – 1.25 h within the transect.

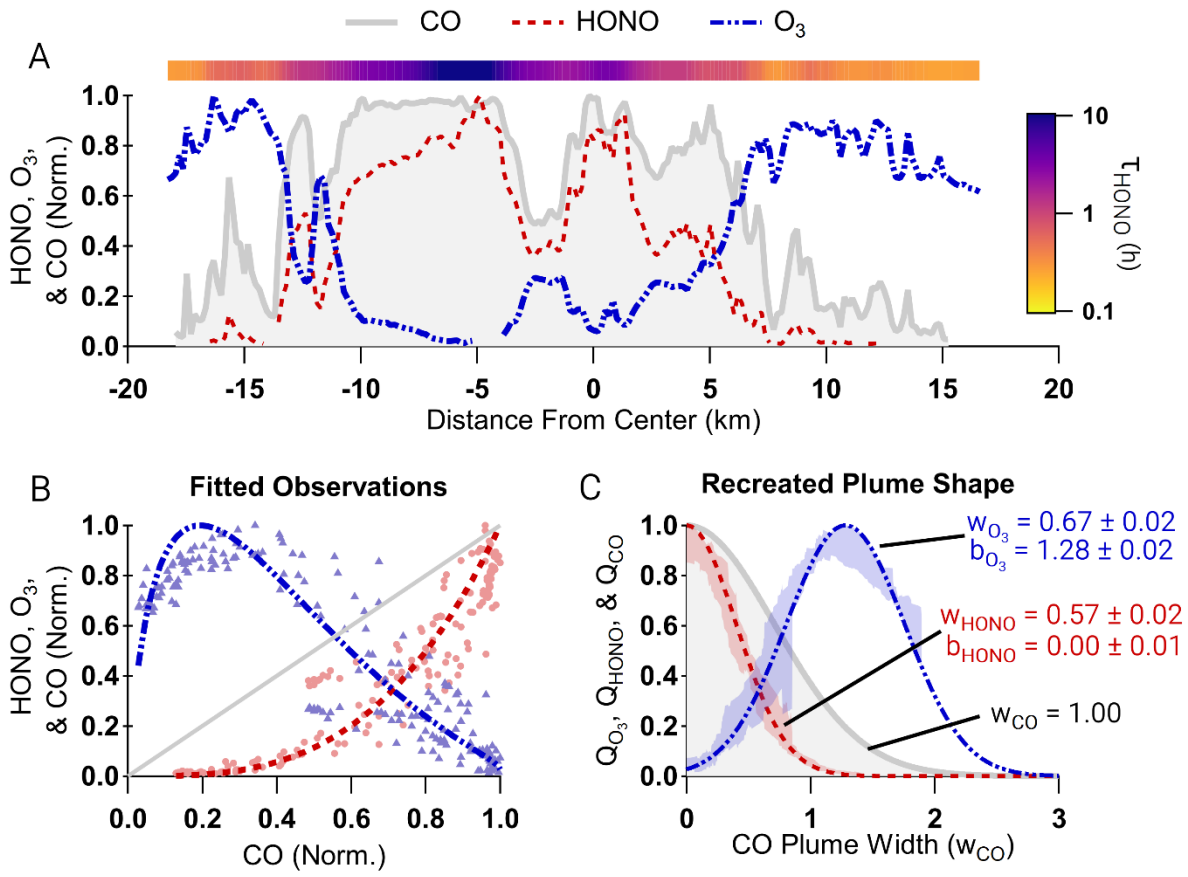

Figure 5.8: Similar to Figure 5.6, but for HONO and O_3. The plume was sampled at 01:29 UTC on Aug 7 2019 by the DC-8. Average plume age was 1.4 h, but varied between 1.25 – 1.50 h within the transect.

5.3.2 Bulk Analysis of Photochemical Plume Structures

Conclusions from Figure 5.6 apply to the majority of the observations. A bulk analysis of HONO measured from the DC-8 (210 crosswind transects) and NOAA Twin Otter (220 crosswind transects) finds average plume widths that are 24 ± 1% and 20 ± 1% narrower than CO, respectively. Average plume ages with ± 1σ variabilities were 2.2 ± 1.1 h and 2.3 ± 1.3 h, respectively. Thus, HONO plume structures were consistently narrower than CO across research platform and plume. Indeed, as shown by the example crosswind transects in Figure 5.9A, HONO plume structures appear complex, but generally depleted on plume edges.

Despite this complexity, GOMECH is able to identify trends in HONO plume width as a function of smoke age and the solar zenith angle at the time of emission, or emitted solar zenith angle (ESZA, where 0° is solar noon and 90° is sunset). ESZA provides insight into the photolysis history of the sampled smoke.

HONO plumes narrow with increasing age (Figure 5.9B–C and Table 5.4). Specifically, for smoke age < 1 h $w_{HONO} = 0.83 \pm 0.01$, and for smoke age > 1 h $w_{HONO} = 0.73 \pm 0.01$, consistent with previous results (Peng et al., 2020). Similarly, the HONO plume width is narrower for smoke emitted earlier in the day. Specifically, for smoke emitted before late afternoon (ESZA < 60°) $w_{HONO} = 0.71 \pm 0.01$, and for smoke emitted in the evening or later (ESZA > 60°) $w_{HONO} = 0.84 \pm 0.01$. These results are explained by decreasing j_{HONO} with increasing ESZA. Median j_{HONO}^{-1} values were 0.45 h before late afternoon and 2.34 h in the evening or later. Replacing CO with methane, benzene, or toluene as a long-lived tracer produces similar trends (Figure 5.9). The w_{HONO} dependence on ESZA further reveals that HONO photolysis, and thus OH production, is larger earlier in the day.

	ESZA < 40°				**40° < ESZA < 60°**				**ESZA > 60°**			
Long-lived tracer	***w***	**b**	**Med. Res.**	**Avg. Res.**	***w***	**b**	**Med. Res.**	**Avg. Res**	***w***	**b**	**Med. Res.**	**Avg. Res**
CO	0.74 ± 0.01	0.00 ± 0.01	0.07	0.12 ± 0.13	0.71 ± 0.01	0.00 ± 0.01	0.10	0.13 ± 0.12	0.84 ± 0.01	0.00 ± 0.01	0.06	0.10 ± 0.10
Methane	0.71 ± 0.02	0.00 ± 0.01	0.07	0.12 ± 0.13	0.70 ± 0.01	0.00 ± 0.01	0.09	0.13 ± 0.12	0.78 ± 0.01	0.00 ± 0.01	0.08	0.11 ± 0.10
Benzene	0.79 ± 0.02	0.00 ± 0.01	0.07	0.11 ± 0.13	0.81 ± 0.01	0.00 ± 0.01	0.09	0.11 ± 0.11	0.86 ± 0.01	0.00 ± 0.01	0.06	0.11 ± 0.12
Toluene	0.79 ± 0.02	0.00 ± 0.01	0.07	0.11 ± 0.13	0.81 + 0.01	0.00 ± 0.01	0.09	0.11 ± 0.10	0.87 ± 0.02	0.00 ± 0.01	0.07	0.11 ± 0.12
	Age < 1 h				**1 h < Age < 2 h**				**Age > 2 h**			
CO	0.83± 0.01	0.00 ± 0.01	0.07	0.10 ± 0.11	0.73± 0.01	0.00 ± 0.01	0.09	0.12 ± 0.12	0.74± 0.01	0.00 ± 0.01	0.09	0.13 ± 0.12
Methane	0.82 ± 0.02	0.00 ± 0.01	0.06	0.10 ± 0.11	0.72 ± 0.01	0.00 ± 0.01	0.08	0.11 ± 0.11	0.70 ± 0.01	0.00 ± 0.01	0.08	0.12 ± 0.13
Benzene	0.87 ± 0.02	0.00 ± 0.01	0.06	0.10 ± 0.12	0.80 ± 0.02	0.00 ± 0.01	0.08	0.12 ± 0.12	0.81 ± 0.01	0.00 ± 0.01	0.08	0.10 ± 0.11
Toluene	0.87 ± 0.02	0.00 ± 0.01	0.06	0.11 ± 0.12	0.80 ± 0.02	0.00 ± 0.01	0.08	0.12 ± 0.12	0.82 ± 0.01	0.00 ± 0.01	0.08	0.11 ± 0.11
DC-8 (Campaign-wide)	w: 0.0.76 ± 0.01 b = 0.00 ± 0.01 Median ESZA = 44 °; Median Age = 2.7 h											
Twin Otter (Campaign-wide)	w = 0.80 ± 0.01 b = 0.00 ± 0.01 Median ESZA = 76°; Median Age = 2.6 h											

Table 5.4: Plume widths of HONO as a function of age and emitted solar zenith angle (ESZA) with median and average (± standard deviation) residuals.

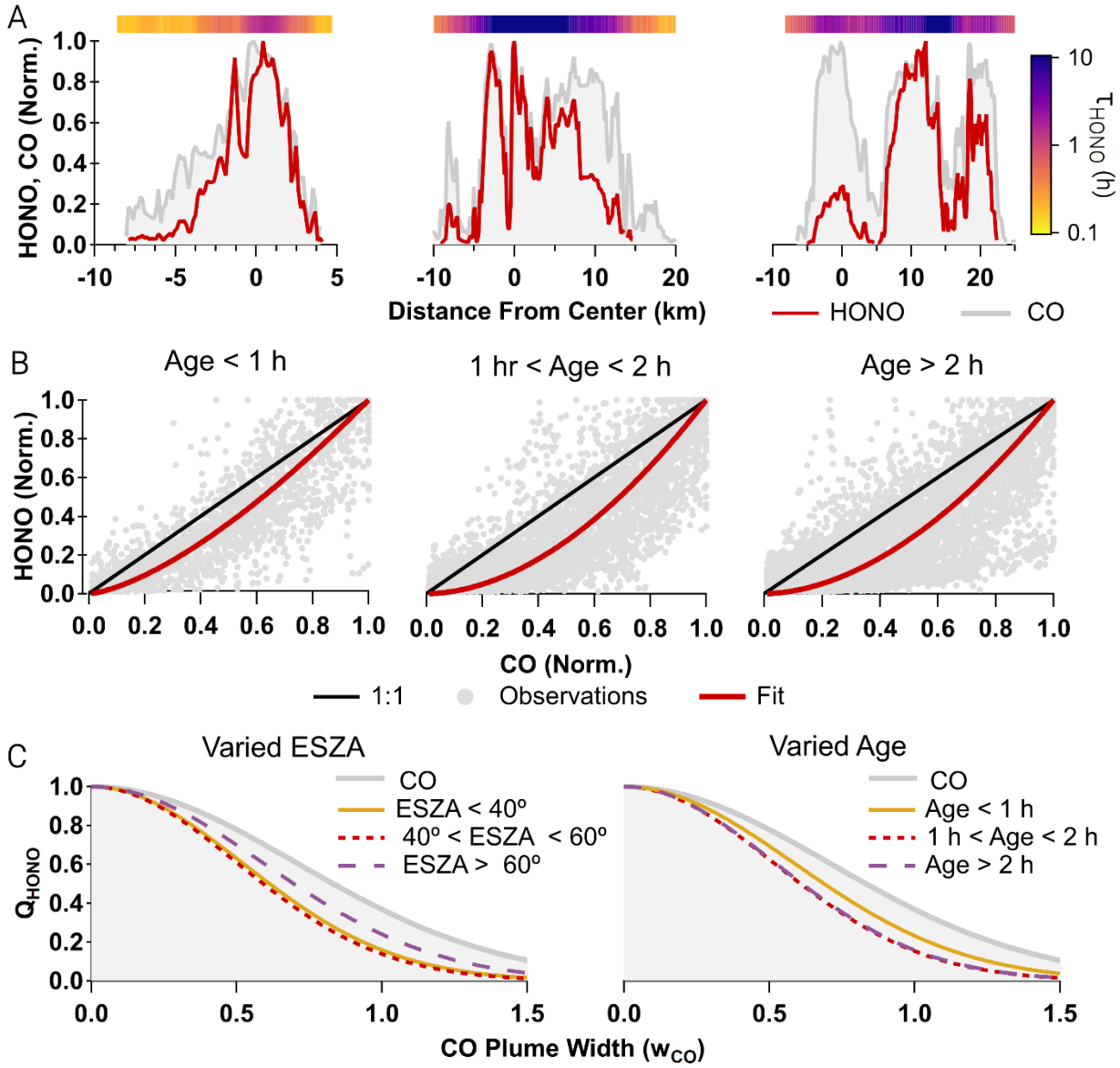

Figure 5.9 Panel A: all data shown is from the DC-8 dataset. Panel A: examples of normalized observations of HONO (red), CO (grey fill) and HONO photolytic lifetime (color scale) plotted against distance from plume center from three separate crosswind transects. Panel B: bulk analysis examples of normalized crosswind transects of HONO (grey markers) and CO (black) plotted against normalized CO with fits shown in red. Panel C: recreated plume shapes of HONO binned by emitted solar zenith angles and plume ages, which show that the HONO plume shape is consistently narrower than CO.

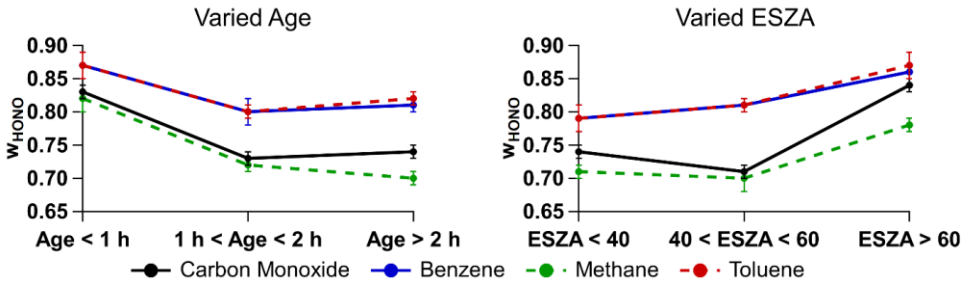

Figure 5.10: HONO widths calculated by GOMECH for plumes binned by age and emitted solar zentih angle (ESZA) using carbon monoxide, benzene, methane, and toluene as chemical tracers.

Indeed, the MA plume width (w_{MA}) is consistently >1, (Figure 5.11and Table 5.5). The plume center of MA generally aligns with CO (b = 0), unlike the example in Figure 5.6 (discussed in the following section). The w_{MA} varies between 1.06±0.01 and 1.12±0.04 across plume age. There is not a clear trend in w_{MA} with ESZA, but w_{MA} appears to decrease with age. The consistently wider plume structure of MA is indicative of enhanced OH oxidation of furans on the plume edges.

ESZA < 40°				**40° < ESZA < 60°**				**ESZA > 60°**			
w	b	Med. Res.	Avg. Res	*w*	b	Med. Res.	Avg. Res	*w*	b	Med. Res.	Avg. Res
1.07 ± 0.01	0.00 ± 0.01	0.05	0.07 ± 0.07	1.08 ± 0.01	0.00 ± 0.01	0.05	0.07 ± 0.07	1.08 ± 0.01	0.00 ± 0.01	0.05	0.06 ± 0.05
Age < 1 h				**1 h < Age < 2 h**				**Age > 2 h**			
1.12 ± 0.04	0.00 ± 0.03	0.10	0.13 ± 0.11	1.11 ± 0.01	0.00 ± 0.01	0.05	0.07 ± 0.07	1.06 ± 0.01	0.00 ± 0.01	0.04	0.06 ± 0.06

Table 5.5: Plume widths of maleic anhydride as a function of age and emitted solar zenith angle (ESZA) with median and average (± standard deviation) residuals.

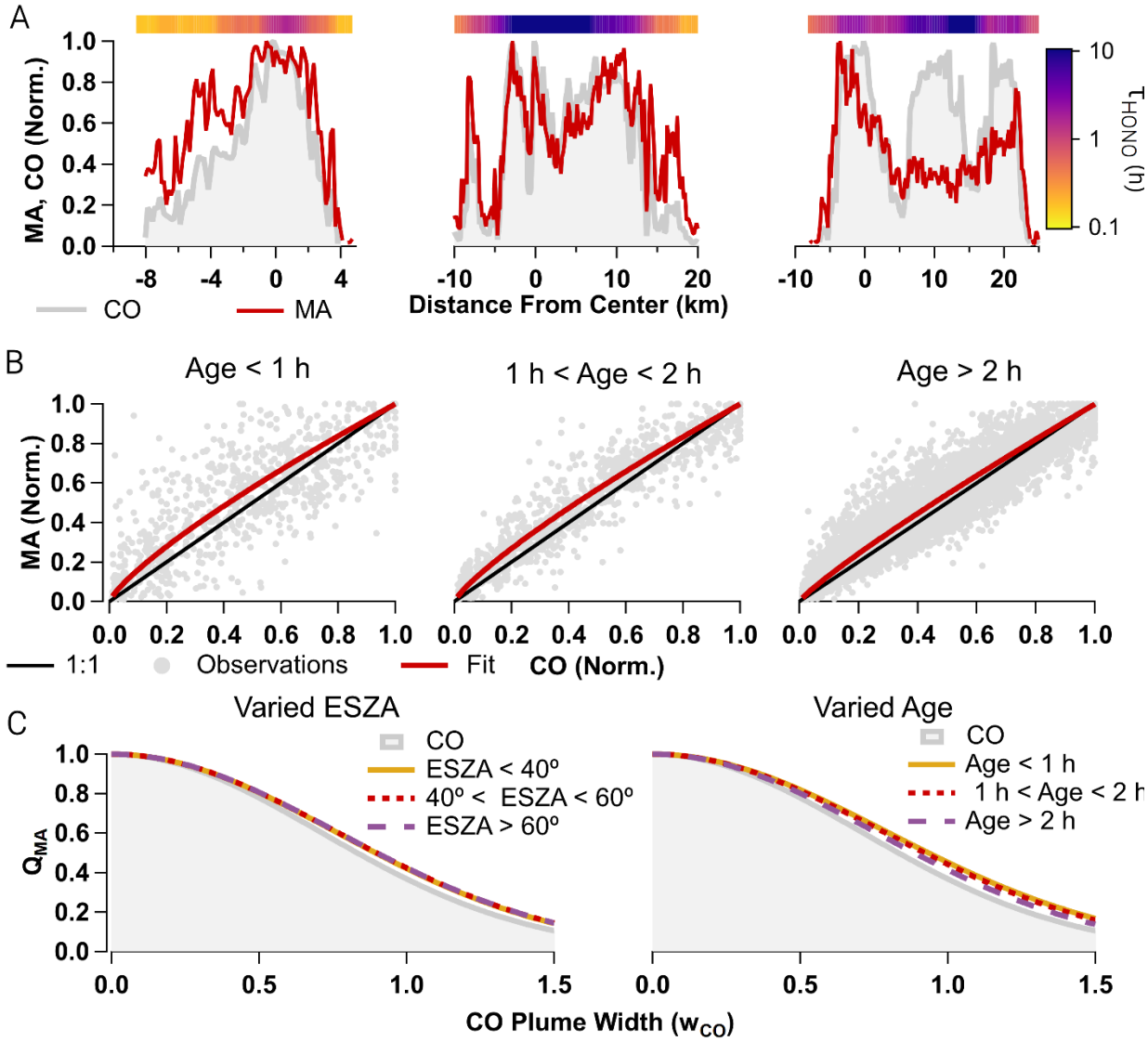

Figure 5.11 Panel A: examples of normalized observations of maleic anhydride (MA, measured as $C_4H_2O_3$, blue fill) and CO (black) as well as plume age (red dashed line) and HONO photolytic lifetime (color scale) plotted against distance from plume center from crosswind transects sampled by the DC-8. Panel B: examples of normalized observations of MA (grey markers) and CO (black) plotted against normalized CO with fits shown in red. Panel C: recreated plume shapes using GOMECH of MA for varying emitted solar zenith angles and plume ages.

5.3.3 Bulk analysis of NO_3 plume structure

To investigate NO_3 chemistry, we perform a GOMECH bulk analysis on the instantaneous NO_3 production rate, $P(NO_3)$ (E2.4). There is a clear trend in $P(NO_3)$ plume width ($w_{P(NO_3)}$) as a function of ESZA that is consistent across research aircraft (Figure 5.12 and Table 5.6). For smoke

emitted in the afternoon (ESZA < 40° from the DC-8 and ESZA < 50° on the Twin Otter, data bins differ due to differences in targeted smoke emission times by each aircraft) $w_{P(NO_3)}$ = 0.92±0.01 and 0.91±0.01, respectively. Smoke emitted in the evening or later (ESZA > 60° from the DC-8 and ESZA > 75° on the Twin Otter) generally aligned with CO ($w_{P(NO_3)}$ = 1.00±0.02 and 1.00±0.02, respectively). This suggests that the greatest enhancements of NO_3 are likely at the plume center earlier in the day. Even so, the majority of plume width (91 – 100%), and thus emissions, will be in a region where $P(NO_3)$ > background levels.

	ESZA < 40°				40° < ESZA < 60°				ESZA > 60°			
DC-8	***w***	**b**	**Med. Res.**	**Avg. Res**	***w***	**b**	**Med. Res.**	**Avg. Res**	***w***	**b**	**Med. Res.**	**Avg. Res**
All ages	0.92 ± 0.01	0.00 ± 0.01	0.08	0.13 ± 0.13	0.97 ± 0.01	0.00 ± 0.01	0.08	0.12 ± 0.12	1.00 ± 0.02	0.0 ± 0.02	0.09	0.12 ± 0.12
	Age < 1 h				**1 h < Age < 2 h**				**Age > 2 h**			
All ESZA	1.01 ± 0.02	0.00 ± 0.02	0.10	0.13 ± 0.12	0.94 ± 0.01	0.00 ± 0.01	0.08	0.13 ± 0.14	0.95 ± 0.01	0.00 ± 0.01	0.08	0.12 ± 0.13
	ESZA < 50°				**50° < ESZA < 75°**				**ESZA > 75°**			
Twin Otter	***w***	**b**	**Med. Res.**	**Avg. Res**	***w***	**b**	**Med. Res.**	**Avg. Res**	***w***	**b**	**Med. Res.**	**Avg. Res**
All ages	0.91 ± 0.01	0.00 ± 0.01	0.09	0.12 ± 0.12	0.98 ± 0.01	0.00 ± 0.01	0.06	0.09 ± 0.08	1.00 ± 0.02	0.00 ± 0.01	0.06	0.07 ± 0.07
	Age < 1 h				**1 h < Age < 1.5 h**				**Age > 1.5 h**			
All ESZA	0.93 ± 0.01	0.00 ± 0.01	0.07	0.11 ± 0.12	0.98 ± 0.01	0.00 ± 0.01	0.08	0.11 ± 0.11	0.98 ± 0.01	0.00 ± 0.01	0.07	0.09 ± 0.09

Table 5.6: Plume widths of $P(NO_3)$ as a function of age and emitted solar zenith angle (ESZA) with median and average (± standard deviation) residuals.

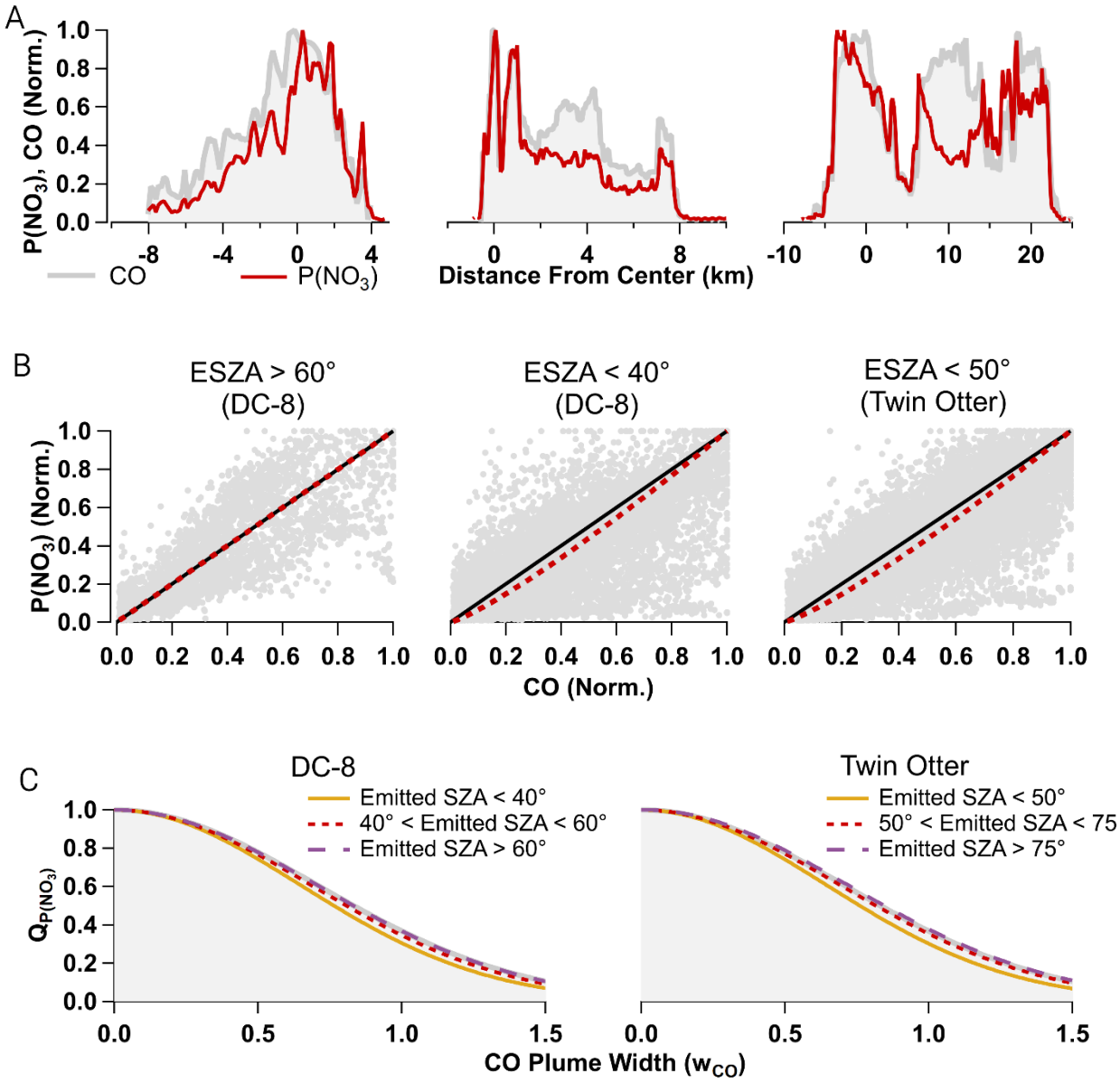

Figure 5.12 Panel A: examples of normalized calculated $P(NO_3)$ (blue fill) and CO (black) plotted against distance from plume center from wildfire plume transects sampled by both the NASA DC-8 and NOAA Twin Otter. Panel B: examples of campaign-wide normalized calculated $P(NO_3)$ (grey markers) and CO (black) plotted against normalized CO with fits (using Eq. S8) shown in red. Panel C: recreated plume shapes using GOMECH of $P(NO_3)$ for varying emitted solar zenith angles and plume ages.

5.3.4 Bulk analysis of phenolic plume structure

Phenolic compounds are uniquely enhanced in biomass burning emissions and are short lived, exhibiting high reactivity to both OH and NO_3 (Decker et al., 2019; Finewax et al., 2018; Mellouki et al., 2021). We investigate three masses which can be attributed to phenolics reported by the I^- CIMS aboard the Twin Otter: C_6H_6O (likely phenol), $C_6H_6O_2$ (likely catechol), and $C_7H_8O_2$ (likely methylcatechol) (Palm et al., 2020). In a bulk GOMECH analysis the average plume widths of phenol ($w_{phenol} = 0.96 \pm 0.03$), catechol ($w_{catechol} = 0.91 \pm 0.01$), and methylcatechol ($w_{methylcatechol} = 0.84 \pm 0.01$) are narrower than CO (Figure 5.13 and Table 5.7). These widths decrease with increasing bimolecular rate coefficient (Mellouki et al., 2021) between the phenolic and NO_3 or OH. As we show above, OH is expected to be enhanced at plume edges and NO_3 will sometimes be present on plume edges; therefore, it is likely that the narrow phenolics plume structure is caused by enhanced oxidation by both NO_3 and OH on the plume edges.

	Catechol								
	ESZA < 50			**50 < ESZA < 75**			**ESZA > 75**		
	w	**Med. Res.**	**Avg. Res**	***w***	**Med. Res.**	**Avg. Res**	***w***	**Med. Res.**	**Avg. Res**
Age < 1.5 h	0..89 ± 0.01	0.11	0.14 ± 0.13	0.97 ± 0.01	0.10	0.14 ± 0.12	--	--	--
Age > 1.5 h	0.81 ± 0.01	0.11	0.14 ± 0.13	0.89 ± 0.01	0.08	0.13 ± 0.13	0.90 ± 0.01	0.08	0.13 ± 0.14
	Phenol			**Catechol**			**Methylcatechol**		
	w	**Med. Res.**	**Avg. Res**	***w***	**Med. Res.**	**Avg. Res**	***w***	**Med. Res.**	**Avg. Res**
All ages	0.96 ± 0.03	0.06	0.08 ± 0.08	0.91 ± 0.01	0.09	0.13 ± 0.12	0.84 ± 0.01	0.04	0.07 ± 0.08

Table 5.7: Plume widths of catechol as a function of age and emitted solar zenith angle (ESZA) as well as average widths for phenol, catechol, and methyl catechol with median and average (± standard deviation) residuals.

Further, GOMECH shows that the catechol plume is narrower for aged smoke and for smoke emitted earlier in the day (Figure 5.13B–C and Table 5.7). For example, in aged smoke (> 1.5 h) emitted early in the day (ESZA < 50°) catechol is 19±1% narrower than CO. In contrast, catechol in young smoke (age < 1.5 h) emitted later in the day (ESZA between 50° – 75°) is only 3±1% narrower than CO. As shown above, GOMECH suggests that OH production is enhanced on plume edges earlier in the day, while $P(NO_3)$ is enhanced at plume center earlier in the day.

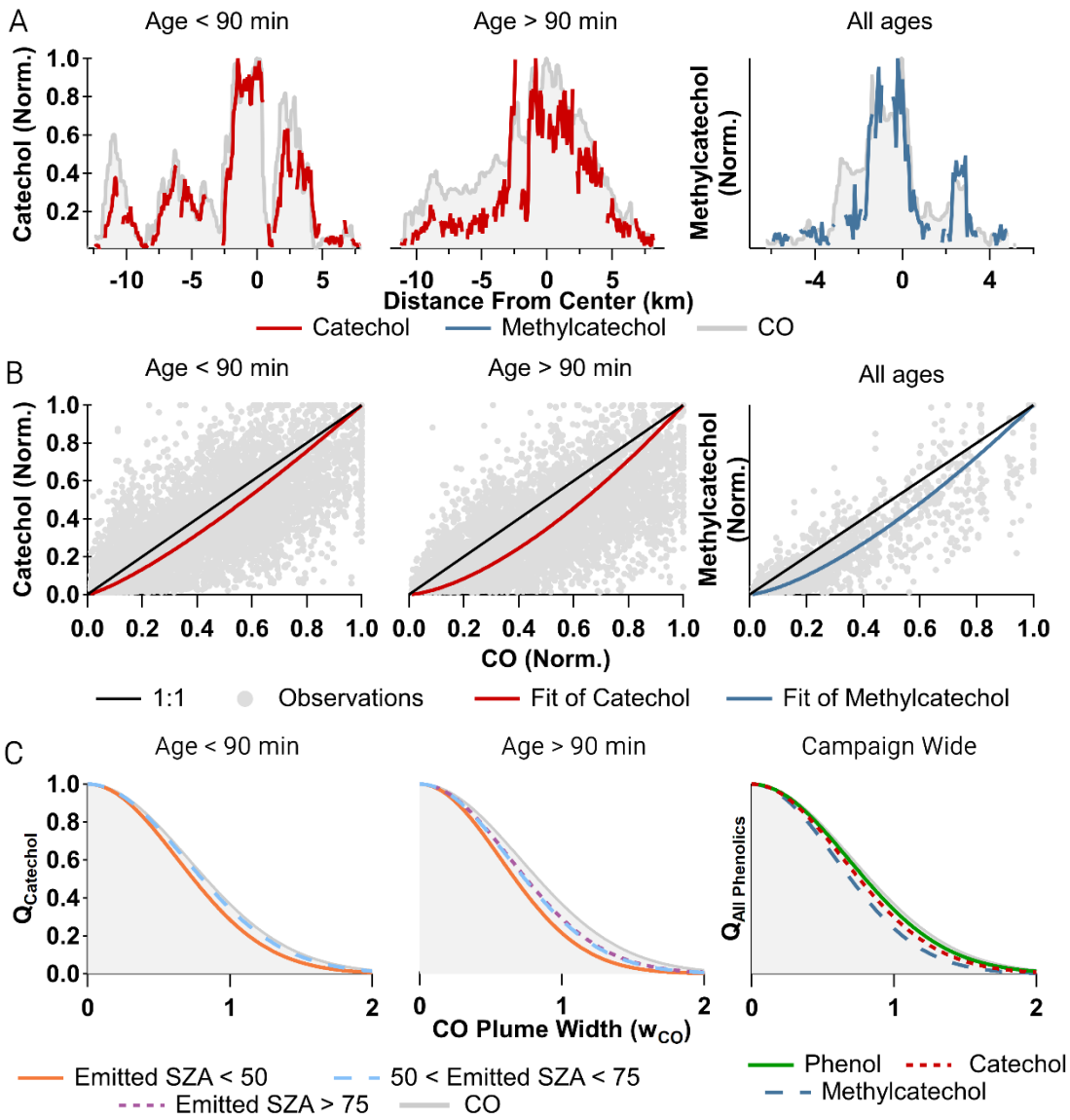

Figure 5.13 Panel A: examples of normalized observations of catechol (measured as $C_6H_6O_2$, red) and methylcatechol (measured as $C_7H_8O_2$, blue) and CO (grey fill) plotted against distance from plume center from wildfire plume transects sampled by the NOAA Twin Otter. Panel B: bulk analysis examples of normalized crosswind transects of catechol, methylcatechol (grey markers) and CO (black) plotted against normalized CO with fits (using Eq. 4) shown by solid colored lines. Panel C: recreated plume shapes of phenol (measured as C_6H_6O, green), catechol (red dash) and methylcatechol (blue dash) as well as of catechol colored by emitted solar zenith angle and separated by age. Data gaps in Panel A are from instrument zeros.

Therefore, it is likely that the apparent narrowing trend with ESZA is due to OH oxidation of catechol.

Both NO_3 and OH oxidation of phenolics results in formation of nitrophenolic SOA. Running a GOMECH bulk analysis of Twin Otter AMS nitrophenolic signals (Palm et al., 2020) suggests the average nitrophenolic aerosol is 5±2% narrower than CO (Figure 5.14 and Table 5.8). A narrow plume may be the result of nitrophenolic photolysis (Sangwan and Zhu, 2016, 2018) on plume edges. However, enhanced formation at plume center would be consistent with enhanced plume center NO_3, which is known to form nitrophenolics at a greater yield than OH (Finewax et al., 2018) and was shown to produce the majority of nitrophenolics at the center of daytime BB plumes sampled during FIREX-AQ (Decker et al., 2021).

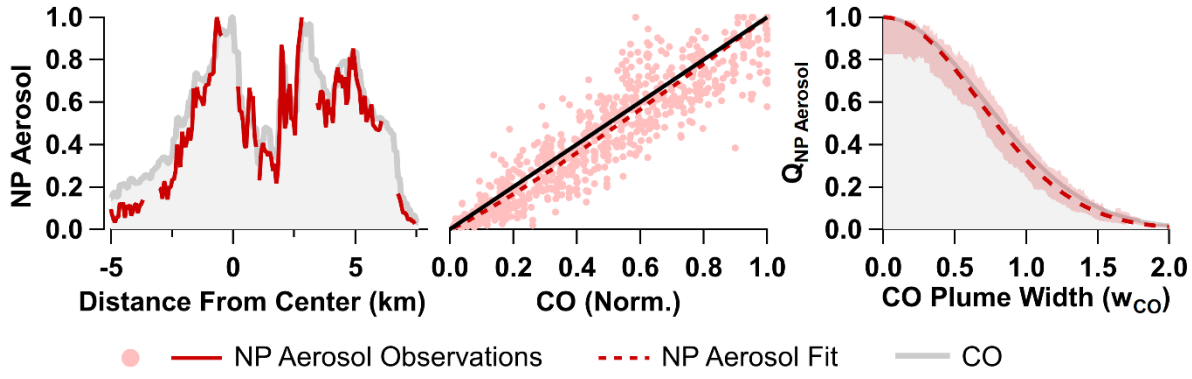

Figure 5.14 left: an example of nitrophenolic ions (NP aerosol, red fill) and CO (black) plotted against distance from plume center from a wildfire plume transects sampled by the NOAA Twin Otter. Middle: normalized calculated $P(NO_3)$ (markers) and CO (black) plotted against normalized CO with fit (red dashed line) Right: recreated plume shape using GOMECH of NP aerosol.

AMS Nitrophenolic signals			
w	**b**	**Med. Res.**	**Avg. Res**
0..95 ± 0.02	0.00 ± 0.02	0.07	0.08 ± 0.07

Table 5.8: GOMECH results for AMS nitrophenolic mass signals

5.3.5 Williams Flats Fire Case Study

The Williams Flats (WF) fire produced the largest wildfire plume sampled by the DC-8 and was larger than any plume sampled by the Twin Otter (as determined by CO emissions, Figure 5.15). We consider four sampling patterns of the WF fire: two on 3 Aug and two on 7 Aug 2019

(Figure 2.2 Panels B,C,F,G on page 25). These plumes are chosen because they had significant plume darkening at their center (90-99% attenuation of j_{HONO}), which results in clear center-edge effects that help to differentiate the influence of OH and NO_3 chemistry on the formation of nitrophenolics.

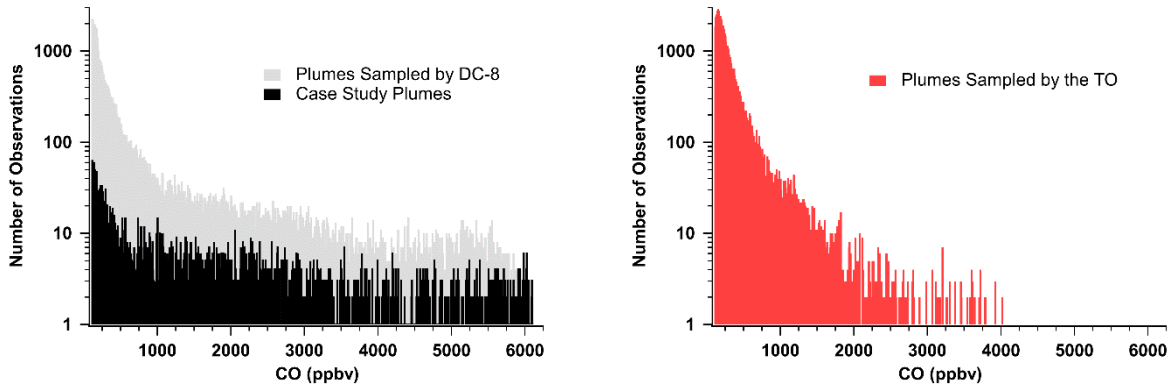

Figure 5.15: Histogram of CO observations within smoke plumes considered in this study from the Twin Otter (TO, red) and NASA DC-8 (grey) and from the Aug 3 and Aug 7 first and second passes of the Williams Flats Fire plume sampled by the DC-8 (black). Bin widths are 10 ppbv of CO.

Figure 5.16 shows that MA, aerosol $C_6H_5NO_4$ (attributed to nitrocatechol ,Pagonis et al., 2020) and calculated $P(NO_3)$ are depressed at the plume center, and have maxima near the plume edge for the 7 Aug plume. This is the result of significantly reduced actinic flux at plume center reducing photolytic OH production as well as emissions of NO titrating O_3 and thus $P(NO_3)$. We apply GOMECH to these observations as seen in Figure 5.16B-C (fits shown in Figure 5.17 and Table 5.9). We show only three young plume transects (age: 1–2 h) because GOMECH was unable to reliably locate the plume center of MA in smoke 2 – 3 h old (e.g., Figure 5.4).

GOMECH reveals that the plume center of nitrocatechol aerosol is most similar to MA ($\Delta b = 0.08 \pm 0.03$ and $\Delta w = 0.09 \pm 0.03$) as opposed to $P(NO_3)$ ($\Delta b = 0.25 \pm 0.02$ and $\Delta w = 0.15 \pm 0.02$) in the youngest transect (left in Figure 5.16C). The nitrocatechol aerosol shifts toward the CO plume

center and becomes narrower with age until it is closely aligned with P(NO_3) in the second (Δb = 0.05±0.02 and Δw = 0.08±0.02) and third (Δb = 0.02±0.01 and Δw = 0.04±0.01) transects. Our LES model suggests similar results.

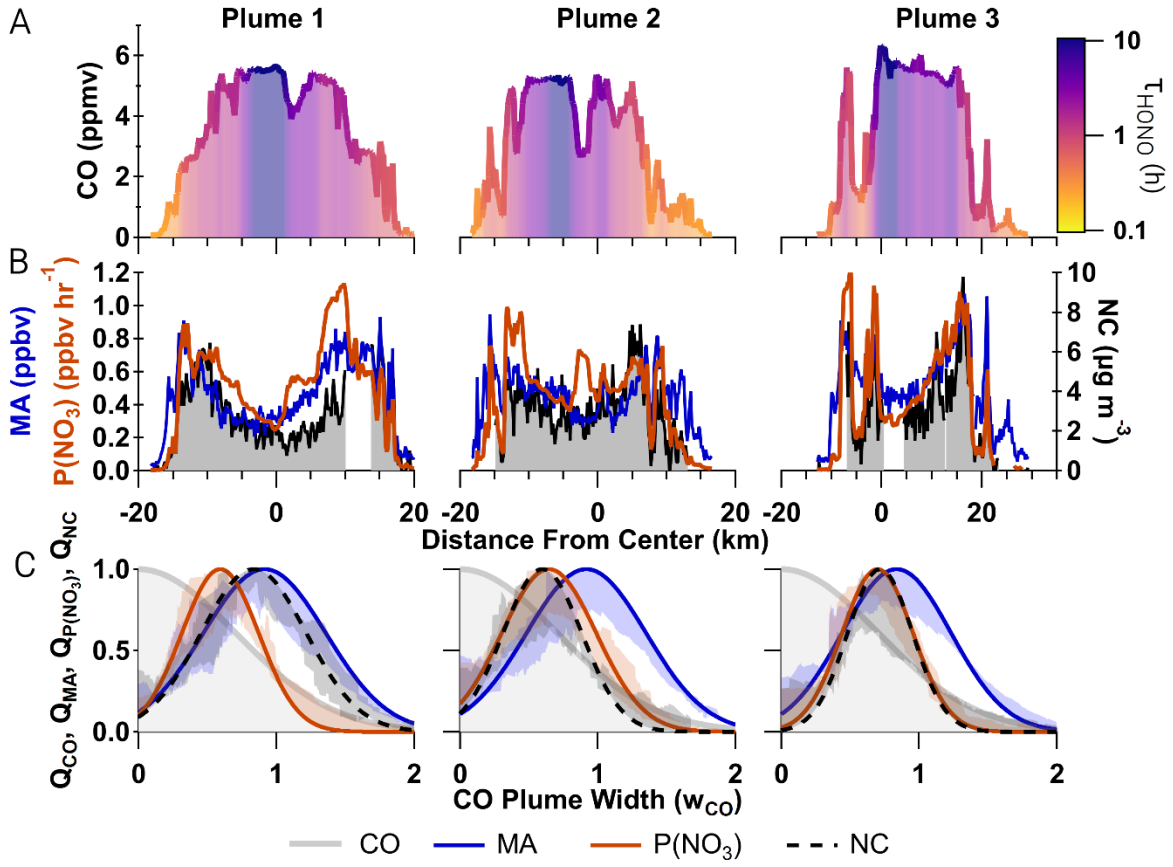

Figure 5.16 Panel A: observations of CO colored by HONO photolytic lifetime plotted against distance from plume center from plume transects of the Williams Flats Fire sampled by the NASA DC-8. Panel B: observations of maleic anhydride (MA, measured as C4H2O3, blue) and aerosol nitrocatechol (NC, measured as C6H5NO4, black outline and fill) as well as calculated P(NO3) (red). Panel C: recreated plume shapes of MA (blue), NC (black), and P(NO3) (red) from fit parameters shown in Figure 5.17 as well as shading indicating fit residuals averaged by normalized CO bins of 0.004. Data gaps for NC are due to instrument zeros. Plume ages for plumes 1, 2, and 3 are 1 – 1.25 h, 1.25 – 1.50 h, and 1.65 – 1.95 h.

Plume	Observation	w	b	Med. Res.	Avg. Res
1	P(NO_3)	0.39 ± 0.01	0.59 ± 0.01	0.13	0.17 ± 0.14
	MA (NOAA)	0.63 ± 0.02	0.92 ± 0.02	0.16	0.18 ± 0.13
	MA (UIBK)	0.64 ± 0.02	0.90 ± 0.02	0.16	0.19 ± 0.13
	NC	0.54 ± 0.02	0.84 ± 0.02	0.14	0.17 ± 0.13
2	P(NO_3)	0.49 ± 0.01	0.65 ± 0.01	0.12	0.16 ± 0.13
	MA (NOAA)	0.61 ± 0.02	0.92 ± 0.02	0.18	0.21 ± 0.17
	MA (UIBK)	0.58 ± 0.02	0.89 ± 0.02	0.21	0.22 ± 0.17

	NC	0.41 ± 0.02	0.60 ± 0.02	0.19	0.22 ± 0.16
3	$P(NO_3)$	0.37 ± 0.01	0.70 ± 0.01	0.09	0.11 ± 0.10
	MA (NOAA)	0.56 ± 0.01	0.84 ± 0.01	0.08	0.10 ± 0.08
	MA (UIBK)	0.55 ± 0.01	0.82 ± 0.01	0.09	0.10 ± 0.09
	NC	0.33 ± 0.01	0.72 ± 0.01	0.11	0.14 ± 0.12

Table 5.9: Plume widths and plume centers for the 7 Aug Williams Flats second pass case study. Median and average (± standard deviation) residuals are also shown. Observations include $P(NO_3)$, maleic anhydride (MA, measured as $C_4H_2O_3$) by both the NOAA and University of Innsbruck PTR-ToF-MS and aerosol nitrocatechol.

We apply our LES model to the 3 Aug second pass sampling of the WF fire where we find agreement between model results and observations of nitrocatechol aerosol (Figure 5.18). We are unable to run the LES model on the 7 Aug sampling due to complex plume dynamics.

Even so, LES model results show similar plume structures to those observed in Figure 5.16. Modeled nitrocatechol aerosol, MA, and $P(NO_3)$ are enhanced on plume edges while modeled catechol narrows downwind of the fire (Figure 5.19A and D). Further, LES model result show that nitrocatechol formation is controlled by NO_3 chemistry on the plume edges, similar to GOMECH results in Figure 5.16C.

Applying GOMECH to crosswind transects of the LES model (Figure 5.19D Table 5.10) shows that the catechol plume width narrows between 10 to 20 km downwind of the fire ($w_{catechol}$ = 0.81±0.01 and $w_{catechol}$ = 0.56±0.02, respectively). The LES model reveals that catechol loss on plume edges is mostly due to OH oxidation. Enhanced OH oxidation on the plume edge is consistent with the plume edge enhancements of MA shown by GOMECH in Figure 5.16C.

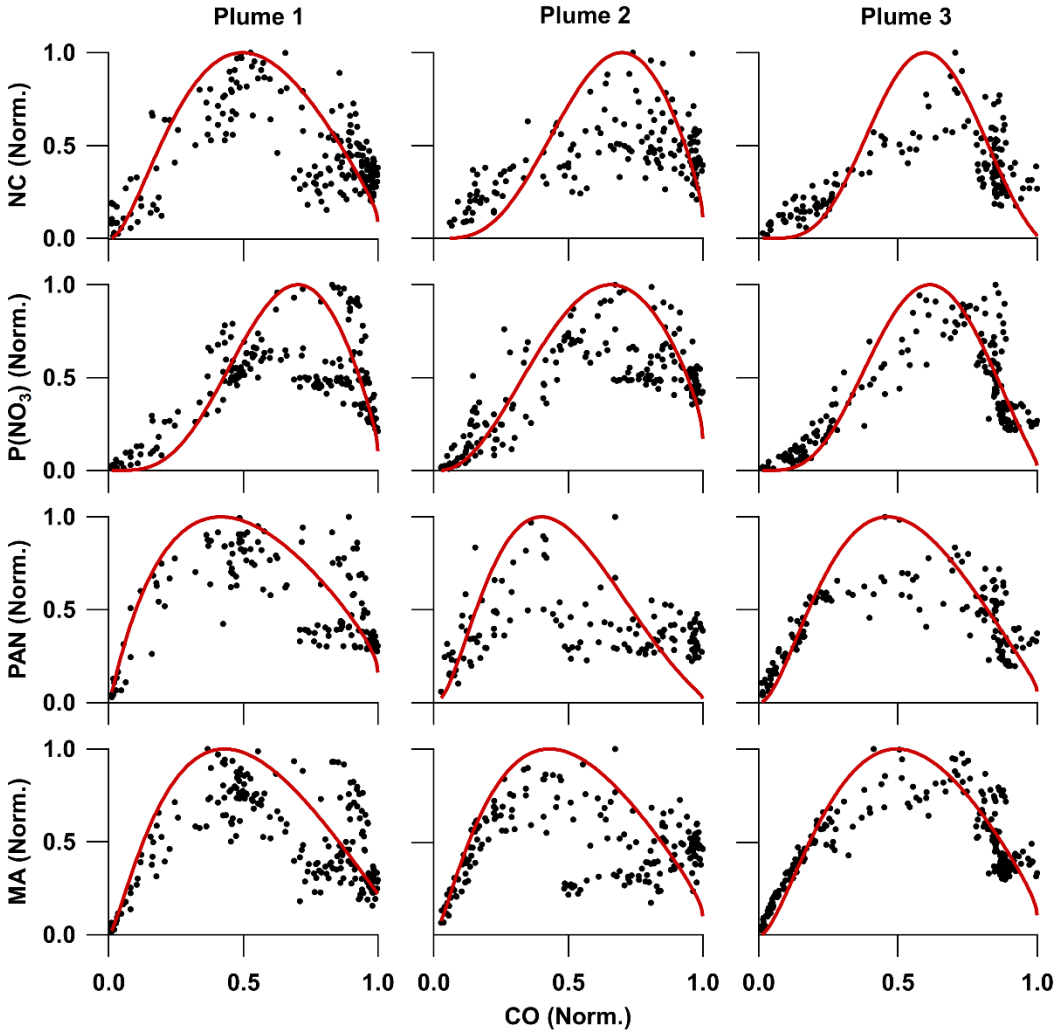

Figure 5.17: observations of maleic anhydride (MA, measured as C4H2O3), PAN, and nitrocatechol aerosol (NC, measured as aerosol C6H5NO4) as well as calculated P(NO3) (all as black markers) plotted against normalized CO, which correspond to plumes shown in Figure 5.16. GOMECH fits are shown as red solid lines.

While most of the catechol loss is due to OH, the cumulative production of nitrocatechol aerosol is mostly (55%) from NO_3 chemistry (Figure 5.20). This is consistent with a plume center model of the Williams Flats plumes and is due to differences in nitrocatechol yield from NO_3 and OH oxidation pathways (Decker et al., 2021). Indeed, the GOMECH structure of $P(NO_3)$ and aerosol nitrocatechol are closely aligned ($\Delta b = 0.03 \pm 0.01$ and $\Delta w = 0.04 \pm 0.03$) compared to MA ($\Delta b = 0.19 \pm 0.03$ and $\Delta w = 0.05 \pm 0.03$) at 10 km downwind of the fire source (Figure 5.19D). As

the plume is transported to 15 and 20 km downwind, there is significantly more overlap between the GOMECH structure of $P(NO_3)$ and aerosol nitrocatechol (71%, 78% respectively) compared to MA (48%, 56%, respectively). Eventually, the plume center of aerosol nitrocatechol determined by GOMECH aligns with CO, similar to GOMECH results seen in the 7 Aug case for smoke sampled with an age > 3 h (Figure 5.21).

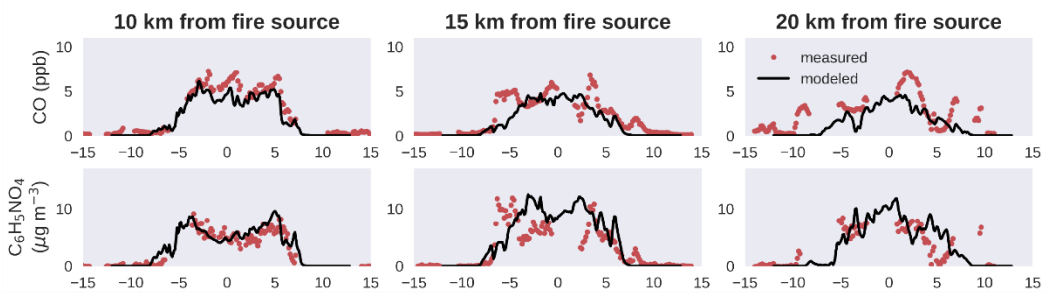

Figure 5.18: Results from an observationally constrained LES model of the 3 Aug second pass sampling of the Williams Flats Fire sampled by the DC-8 at three distances (10, 15, 20 km) downwind of the fire source. Observations of CO (top) and $C_6H_5NO_4$ aerosol (bottom) are compared to model transects used to constrain the model. Flight transects were conducted at an average $\pm$ 1-σ altitude above sea level of 2813 $\pm$ 3 m.

Distance Downwind	Compound	w	b	Med. Res.	Avg. Res
10 km	NO_3	0.51 $\pm$ 0.01	1.25 $\pm$ 0.01	0.09	0.11 $\pm$ 0.08
	$P(NO_3)$	0.47 $\pm$ 0.02	0.81 $\pm$ 0.01	0.14	0.16 $\pm$ 0.13
	MA	0.56 $\pm$ 0.02	1.03 $\pm$ 0.02	0.13	0.18 $\pm$ 0.15
	NC	0.51 $\pm$ 0.02	0.84 $\pm$ 0.01	0.14	0.18 $\pm$ 0.16
	Catechol	0.81 $\pm$ 0.01	0.00 $\pm$ 0.01	0.06	0.07 $\pm$ 0.05
15 km	NO_3	0.57 $\pm$ 0.02	0.98 $\pm$ 0.01	0.11	0.13 $\pm$ 0.09
	$P(NO_3)$	0.55 $\pm$ 0.02	0.48 $\pm$ 0.01	0.08	0.11 $\pm$ 0.09
	MA	0.61 $\pm$ 0.02	0.76 $\pm$ 0.01	0.12	0.13$\pm$ 0.11
	NC	1.11 $\pm$ 0.04	0.00 $\pm$ 0.03	0.04	0.07 $\pm$ 0.07
	Catechol	0.59 $\pm$ 0.03	0.00 $\pm$ 0.02	0.03	0.07 $\pm$ 0.08
20 km	NO_3	0.59 $\pm$ 0.01	0.88 $\pm$ 0.01	0.06	0.08 $\pm$ 0.08
	$P(NO_3)$	0.63 $\pm$ 0.01	0.42 $\pm$ 0.01	0.05	0.06 $\pm$ 0.05
	MA	0.59 $\pm$ 0.01	0.70 $\pm$ 0.01	0.06	0.09 $\pm$ 0.08
	NC	1.13 $\pm$ 0.01	0.00 $\pm$ 0.01	0.02	0.03 $\pm$ 0.03
	Catechol	0.56 $\pm$ 0.02	0.00 $\pm$ 0.02	0.03	0.04 $\pm$ 0.03

Table 5.10: GOMECH fitting results for LES model transects for NO_3, $P(NO_3)$, maleic anhydride (MA), nitrocatechol (NC), and catechol. Transects of CO and NC from the LES model are shown in Figure 5.19.

The above conclusions are further supported by correlations of nitrocatechol aerosol with integrated $P(NO_3)$ or MA (see Figure 5.22), which shows nitrocatechol aerosol is best correlated

with integrated $P(NO_3)$ (R^2 = 0.72 – 0.92) when compared to MA (R^2 = 0.35 – 0.76) in all four Williams Flats plumes we study.

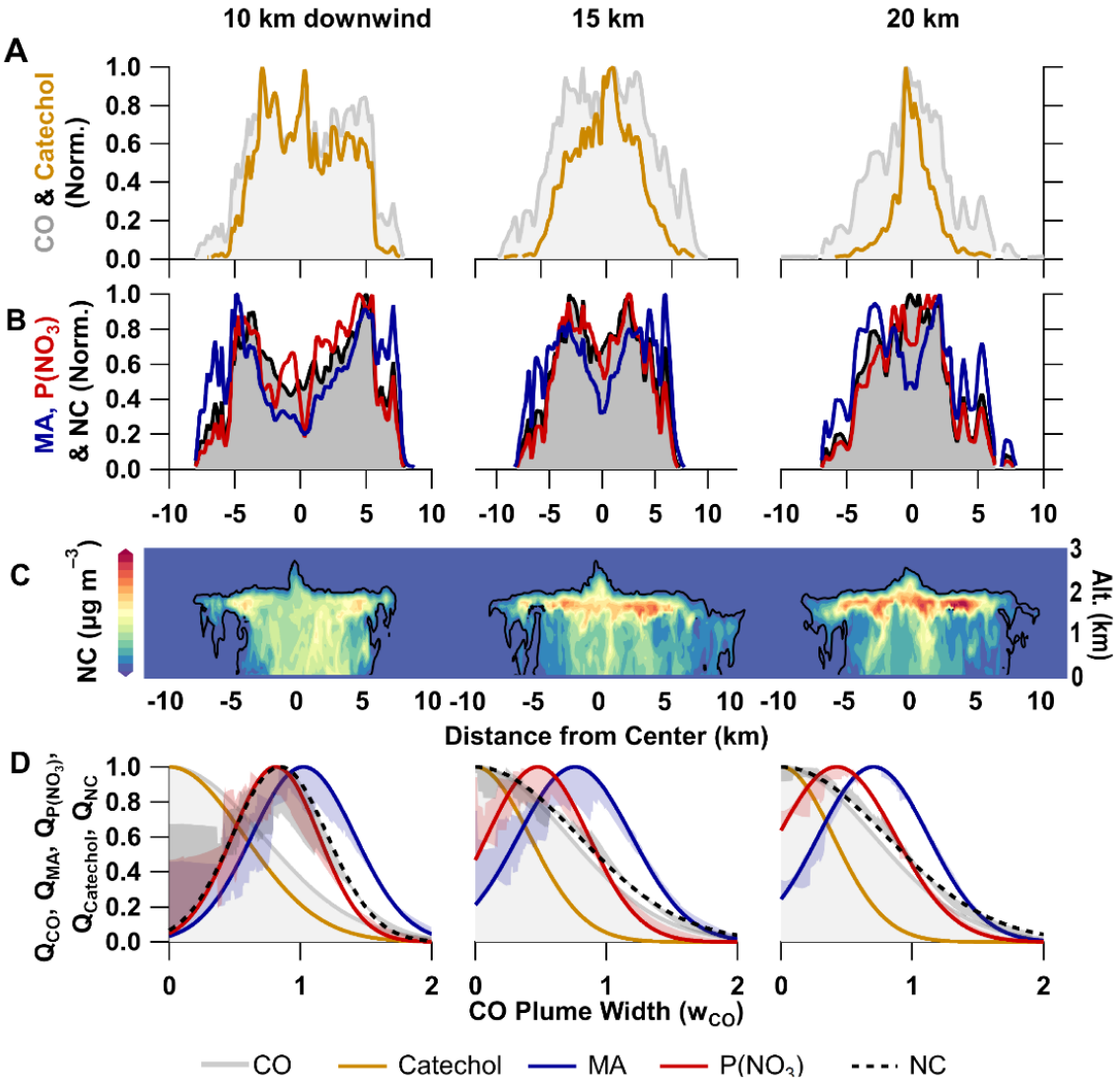

Figure 5.19 Panel A: LES model results of CO (grey) and catechol (brown) for three crosswind transects 10, 15, and 20 km downwind of the Williams Flats Fire sampled on 3 Aug 2019 by the NASA DC-8. Panel B: LES model results for maleic anhydride (MA, blue), $P(NO_3)$ (red), and aerosol nitrocatechol (black). Panel C: LES model curtains of aerosol nitrocatechol (color scale). Panel D: GOMECH plume shapes of MA (blue), NC (black), and $P(NO_3)$ (red). Shading indicates fit residuals averaged by normalized CO bins of 0.004.

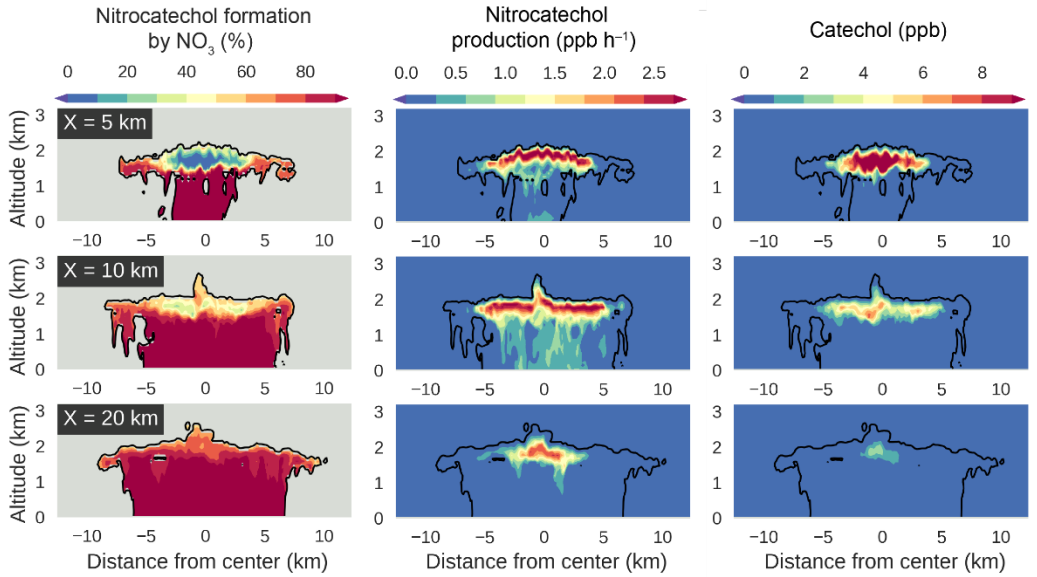

Figure 5.20: Results from an observationally constrained LES model of the 3 Aug second pass sampling of the Williams Flats Fire sampled by the DC-8 at three distances (X = 5, 10, 20 km) downwind of the fire source. First column: percent formation of nitrocatechol by NO_3 are indicated by the color scale. Second column: nitrocatechol production (ppb h^{-1}) from both OH and NO_3. Third column: catechol mixing ratio (ppb).

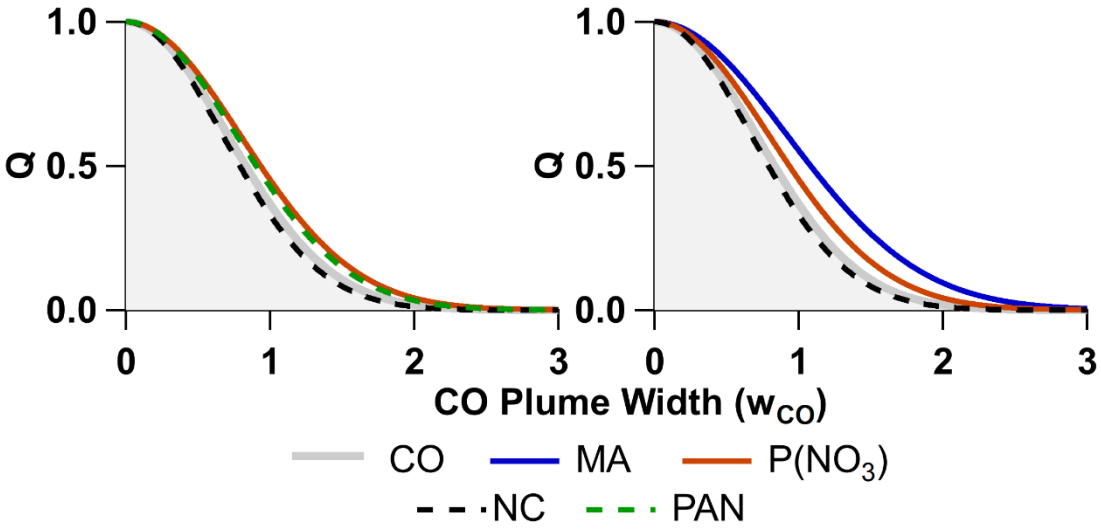

Figure 5.21: GOMECH recreated plume shapes for maleic anhydride (blue, MA), $P(NO_3)$ (red), aerosol nitrocatechol (NC, dashed black), and PAN (dashed green) for 7 Aug Williams Flats second pass plumes with ages > 3 h. Average residual shading is omitted for clarity, but does overlap across each measurement.

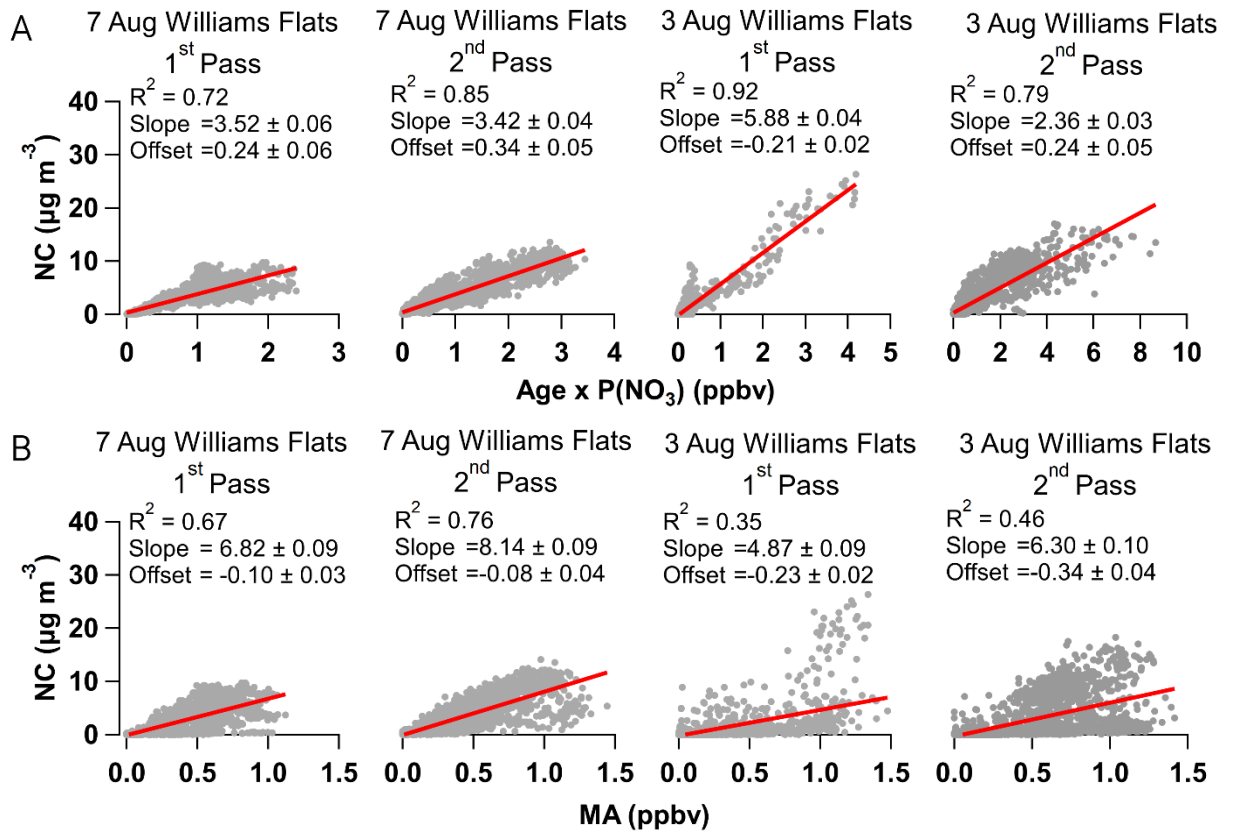

Figure 5.22 Panel A: correlations of NC (nitrocatechol aerosol measured as $C_6H_5NO_4$) plotted against calculated $P(NO_3)$ multiplied by plume age, as an estimate of total NO_3 radical produced, for four samplings of the Williams Flats plume by the DC-8 with fit parameters and R^2 indicated. Panel B: similar to Panel A but for NC plotted against MA (maleic anhydride measured as $C_4H_2O_3$).

5.3.5.1 Correlations of $P(NO_3)$ and maleic anhydride with nitrocatechol

We integrate $P(NO_3)$ to estimate the total production of NO_3 by multiplying $P(NO_3)$ with plume age. This method provides a lower limit of NO_3 because it is a rectangular approximation of an exponential decay. Doing so produces an improvement in the correlation and more accurately compares a mixing ratio of NO_3 to MA as opposed to comparing a rate of production to a mixing ratio.

The slopes shown in Figure 5.22 represent the nitrocatechol aerosol yield per NO_3 produced, though, as mentioned above, the NO_3 produced is a lower limit. Interestingly, the slope

of nitrocatechol aerosol vs integrated $P(NO_3)$ is consistent between the first and second pass of the 7 Aug WF plume, but not for 3 Aug WF plumes or any of nitrocatechol aerosol vs MA. The stronger correlation of nitrocatechol aerosol with integrated $P(NO_3)$ further suggests that nitrocatechol production is better associated with NO_3 chemistry when compared to OH chemistry.

5.4 Conclusions

The oxidation of phenolics and formation of nitrophenolics are known to contribute to SOA and BrC formation in BB plumes (Palm et al., 2020). Further, NO_3 chemistry has been suggested to contribute to most of the organic aerosol from BB in at least one analysis (Kodros et al., 2020). Our analysis suggests that NO_3 chemistry may be a major source of nitrophenolics, even on plume edges, in daytime BB plumes studied during FIREX-AQ, and a dominant (55%) source in our case study.

As shown above, GOMECH is able to resolve spatial heterogeneity in NO_3 and OH chemistry by recreating plume structures within 20% of the observations. Narrower or wider plumes (such as HONO or MA) are better approximated with GOMECH and have lower fit residuals when compared to more complex plume structures with plume center shifts ($b \neq 0$, such as MA, PAN or O_3). GOMECH is a simple, empirical model that can be fit to aircraft data from discrete emission sources. GOMECH provides a method for studying the spatial heterogeneity of plumes by providing quantitative measures of differential gradients in short lived species relative to long lived tracers, and as such, can quantify chemical regimes in chemically evolving plumes. GOMECH is general and therefore may find application in urban plumes, or plumes from power

generation sources. If so, it would provide insights into chemical processes contributing to the evolution of short-lived emissions and their oxidation products.

Chapter 6: Summary and Conclusions

BB is a large source of reactive compounds to the atmosphere. Wildfires in particular are increasing in size across the western U.S., leading to increases in human smoke exposure and associated negative health impacts, and the trend is expected to continue. The daytime photochemistry of BB emissions has been studied in some detail, and continues to be a focus of further study. However, there has been little focus on nighttime reactions despite the potential for substantial oxidative and heterogeneous chemistry. In this thesis, we present three seminal studies that investigate the dark oxidation of daytime and nighttime BB plumes sampled by aircraft.

We used a combination of field observations and modeling to investigate the oxidation of BB plumes. Chapter 2 describes these methodologies, including 1) a detailed emissions and kinetics inventory built from laboratory investigations of controlled burns, 2) late day and nighttime aircraft observations of agricultural burning and wildfire smoke plumes, 3) a detailed 0-D chemical box model, and 4) a novel observation-based center to edge chemical heterogeneity plume model.

In Chapter 3, we present the first analysis of nighttime aircraft observations of BB plumes. The analysis from the SENEX 2013 campaign investigated the formation and fate of oxidants (NO_3, N_2O_5, O_3, and OH) and BBVOCs in nighttime smoke of a representative agricultural burn (rice straw fuel) and western wildfire (ponderosa pine fuel). Chapter 3 describes the development of an emissions database derived by combining databases from Koss et al., 2018 and Hatch et al., 2017 in the form of emission ratios. We combine these emission ratios with bimolecular rate coefficients of 302 BBVOCs for NO_3, OH, and O_3. With our emissions database, we use a

chemically detailed 0-D box model with observations from BB smoke sampled over the southeastern U.S. to model the chemical evolution of BB plumes overnight. Field observations suggest NO_3 production was approximately 1 ppbv hr^{-1}, while NO_3 and N_2O_5 were at or below 3 pptv, indicating rapid NO_3/N_2O_5 reactivity. Our model analysis shows that >99% of NO_3/N_2O_5 loss is due to BBVOC + NO_3 reactions rather than aerosol uptake of N_2O_5. The nighttime BBVOC oxidation for rice straw and ponderosa pine fires is dominated by NO_3 (72, 53%, respectively) but O_3 oxidation is significant (25, 43%) leading to roughly 55% overnight depletion of the most reactive BBVOCs and NO_2. Our analysis is the first to highlight the importance of NO_3 oxidation, and identifies phenolics as an important reactant for NO_3 in BB plumes.

Chapter 4 expands on the findings in Chapter 3 with new observations of western U.S. wildfire plumes sampled during FIREX-AQ. We use observations from two research aircraft, the NASA DC-8 and the NOAA Twin Otter, of four wildfire plumes. We constrain the detailed chemical box model used in Chapter 3, but with updated phenolic mechanisms, to aircraft observations to analyze smoke sampled during mid-day, sunset, and nighttime. Aircraft observations suggest a range of NO_3 production rates (0.1 – 1.5 ppbv h^{-1}) in plumes transported both mid-day and after dark. Modeled initial instantaneous reactivity toward BBVOCs for NO_3, OH, and O_3 is 80.1 %, 87.7 %, 99.6 %, respectively. Initial NO_3 reactivity is $10 – 10^4$ times greater than typical values in forested or urban environments, and reactions with BBVOCs account for ≥ 98 % of NO_3 loss in sunlit plumes (jNO_2 up to 4×10^{-3} s^{-1}), while conventional photochemical NO_3 loss through reaction with NO and photolysis are minor pathways. This is the result of highly reactive phenolic compounds, which are oxidized by NO_3, O_3, and OH (26 – 52 %, 22 – 43 %, 16

– 33 %, respectively). Even so, NO_3 oxidation accounts for 26 – 52 % of phenolic chemical loss in sunset plumes and in an optically thick daytime plume.

Nitrocatechol is a product of phenolic oxidation by NO_3 or OH. Its yields varied between 33 % and 45 %. NO_3 chemistry in BB plumes emitted late in the day is responsible for 72 – 92 % (84 % in an optically thick mid-day plume) of nitrocatechol formation. The NO_3 reaction pathways controls nitrophenolic formation overall. As a result, overnight nitrophenolic formation pathways account for 56 $\pm$ 2 % of NO_x loss by sunrise the following day. These findings emphasize the importance of NO_3 oxidation. In short, all 3 major oxidants contribute to daytime and nighttime BB oxidation due to the extreme reactivity in these plumes.

Both Chapter 3 and 4 study only the center of a BB plume. In Chapter 5 we present a novel methodology, the Gaussian Observational Model for Edge to Center Heterogeneity (GOMECH), to quantitatively describe the aircraft observed horizontal chemical structure of plumes as a function of a conserved tracer, in this case CO. GOMECH can be used to fit observations and provides metrics for plume width and center. We demonstrate GOMECH with an analysis of plumes sampled during FIREX-AQ. We investigate the oxidation of phenolics by OH, through an analysis of HONO and maleic anhydride, and NO_3, through an analysis of $P(NO_3)$. We also investigate the formation of nitrophenolics. The plume structure of $P(NO_3)$ suggests that NO_3 may be concentrated at plume center, but that 91 – 100% of emissions will be in a region where $P(NO_3)$ is greater than background levels. The plume width of HONO in smoke emitted in the afternoon was up to 30 % narrower than CO while the plume width for smoke emitted in the evening was up to 22 % narrower than CO, suggesting OH is enhanced on plume edges. Similarly plume widths of maleic anhydride were as large as 13 % wider than CO for smoke emitted in the afternoon, but

only as large as 6 % wider for plumes emitted in the evening. As a result, the plume width of phenol (4%), catechol (9%), and methylcatechol (16%) are consistently narrower than CO. The plume width of nitrophenolic aerosol is up to 5% narrower than CO, suggesting nitrophenolics may be produced at a greater rate at plume center.

In a case study of four exceptionally large wildfire plumes, GOMECH suggests NO_3 and OH are concentrated in plume edges and that nitrocatechol aerosol plume structure is closely aligned with that of $P(NO_3)$. Further, nitrocatechol aerosol is best correlated with integrated $P(NO_3)$ ($R^2 = 0.72 – 0.92$) when compared to MA ($R^2 = 0.35 – 0.76$), suggesting NO_3 chemistry controls nitrocatechol production. These results are further corroborated by an LES model of an observed large plume, indicating the majority of nitrocatechol is formed via NO_3 on plume edges while OH controls formation at plume center. Generally, our analysis suggests that NO_3 chemistry may be a major source of nitrophenolics in daytime BB plumes studied during FIREX-AQ, and a dominant source in our case study plumes. Therefore, NO_3 chemistry should be considered, even during the daytime and on plume edges, when considering phenolic oxidation and nitrophenolic formation in BB plumes.

We also show in Chapter 5 that GOMECH is able to recreate crosswind plume structures within 20% of the observations. Narrow or wide plumes are better approximated with our model and have lower fit residuals when compared to more complex plume structures with plume center shifts. There are examples in which the model fails to capture the physical plume structure, and this may be due to plume asymmetry. Despite these caveats, GOMECH provides a simple and

general method for studying the spatial heterogeneity of plumes and could be applied to, for example, urban plumes, or plumes from power generation sources.

Overall, the analyses in this thesis underline the importance of NO_3 chemistry in BB plumes. We find the counterintuitive results that NO_3 chemistry occurs in only the darkest plume centers, or after dark. We show that the oxidation of phenolics by NO_3 may be a dominant source of nitrophenolics in BB smoke, regardless of time of day or location within the plume, which is suggests NO_3 chemistry may be a significant source of BB SOA. After sunset, these reactions have a significant impact on NO_x loss overnight, which removes NO_x for photochemical O_3 production at sunrise the following day. The results we present here further the understanding of BB oxidation chemistry, a subject of growing importance as the impacts of BB smoke on North American air quality continue to grow.

Bibliography

Abatzoglou, J. T. and Williams, A. P.: Impact of anthropogenic climate change on wildfire across western US forests, Proc. Natl. Acad. Sci., 113(42), 11770–11775, doi:10.1073/pnas.1607171113, 2016.

Ahern, A., Goldberger, L., Jahl, L., Thornton, J. and Sullivan, R. C.: Production of N2O5 and ClNO2 through nocturnal processing of biomass-burning aerosol, Environ. Sci. Technol., 52(2), 550–559, doi:10.1021/acs.est.7b04386, 2018.

Akagi, S. K., Yokelson, R. J., Wiedinmyer, C., Alvarado, M. J., Reid, J. S., Karl, T., Crounse, J. D. and Wennberg, P. O.: Emission factors for open and domestic biomass burning for use in atmospheric models, Atmos. Chem. Phys., 11(9), 4039–4072, doi:10.5194/acp-11-4039-2011, 2011.

Alvarado, M. J. and Prinn, R. G.: Formation of ozone and growth of aerosols in young smoke plumes from biomass burning: 1. Lagrangian parcel studies, J. Geophys. Res. Atmos., 114(9), 1–19, doi:10.1029/2008JD011144, 2009.

Andreae, M. O. and Merlet, P.: Emission of trace gases and aerosols from biomass burning, Global Biogeochem. Cycles, 15(4), 955–966, doi:10.1029/2000GB001382, 2001a.

Andreae, M. O. and Merlet, P.: Emissions of trace gases and aerosols from biomass burning, Biogeochemistry, 15(4), 955–966, 2001b.

Aschmann, S. M., Nishino, N., Arey, J. and Atkinson, R.: Kinetics of the reactions of OH radicals with 2-and 3-methylfuran, 2,3-and 2,5-dimethylfuran, and e -and Z -3-hexene-2,5-dione, and products of OH + 2,5-dimethylfuran, Environ. Sci. Technol., 45(5), 1859–1865, doi:10.1021/es103207k, 2011.

Aschmann, S. M., Nishino, N., Arey, J. and Atkinson, R.: Products of the OH Radical-Initiated Reactions of Furan, 2- and 3-Methylfuran, and 2,3- and 2,5-Dimethylfuran in the Presence of NO, J. Phys. Chem. A, 118(2), 457–466, doi:10.1021/jp410345k, 2014.

Atkinson, R.: Kinetics and Mechanisms of the Gas-Phase Reactions of the NO3 Radical with Organic Compounds, J. Phys. Chem. Ref. Data, 20(3), 459–507, doi:10.1063/1.555887, 1991.

Atkinson, R. and Arey, J.: Atmospheric Degradation of Volatile Organic Compounds, Chem. Rev., 103(3), 4605–4638, doi:10.1021/cr0206420, 2003a.

Atkinson, R. and Arey, J.: Gas-phase tropospheric chemistry of biogenic volatile organic compounds: A review, in Atmospheric Environment, vol. 37, pp. 197–219, Pergamon., 2003b.

Avnery, S., Mauzerall, D. L., Liu, J. and Horowitz, L. W.: Global crop yield reductions due to surface ozone exposure: 1. Year 2000 crop production losses and economic damage, Atmos. Environ., 45(13), 2284–2296, doi:10.1016/j.atmosenv.2010.11.045, 2011.

Balch, J. K., Bradley, B. A., Abatzoglou, J. T., Chelsea Nagy, R., Fusco, E. J. and Mahood, A. L.: Human-started wildfires expand the fire niche across the United States, Proc. Natl. Acad. Sci. U. S. A., 114(11), 2946–2951, doi:10.1073/pnas.1617394114, 2017.

Barbero, R., Abatzoglou, J. T., Larkin, A. N., Kolden, C. A. and B., S.: Climate change presents increased potential for very large fires in the contiguous United States, Int. J. Wildl. Fire, 24(7), 892–899, doi:dx.doi.org/10.1071/WF15083, 2015.

Bell, M. L., Peng, R. D. and Dominici, F.: The exposure-response curve for ozone and risk of mortality and the adequacy of current ozone regulations, Environ. Health Perspect., 114(4), 532–536, doi:10.1289/ehp.8816, 2006.

Berndt, T., Böge, O., Kind, I. and Rolle, W.: Reaction of NO3 Radicals with 1,3-

Cyclohexadiene, α-Terpinene, and α-Phellandrene: Kinetics and Products, Berichte der Bunsengesellschaft für Phys. Chemie, 100(4), 462–469, doi:10.1002/bbpc.19961000410, 1996.

Bertrand, A., Stefenelli, G., Jen, C. N., Pieber, S. M., Bruns, E. A., Ni, H., Temime-Roussel, B., Slowik, J. G., Goldstein, A. H., El Haddad, I., Baltensperger, U., Prévôt, A. S. H., Wortham, H. and Marchand, N.: Evolution of the chemical fingerprint of biomass burning organic aerosol during aging, Atmos. Chem. Phys., 18(10), 7607–7624, doi:10.5194/acp-18-7607-2018, 2018.

Bierbach, A., Barnes, I., Becker, K. H. and Wiesen, E.: Atmospheric Chemistry of Unsaturated Carbonyls: Butenedial, 4-Oxo-2-pentenal, 3-Hexene-2,5-dione, Maleic Anhydride, 3H-Furan-2-one, and 5-Methyl-3H-furan-2-one, Environ. Sci. Technol., 28(4), 715–729, doi:10.1021/es00053a028, 1994.

Bishop, G. A. and Haugen, M. J.: The Story of Ever Diminishing Vehicle Tailpipe Emissions as Observed in the Chicago, Illinois Area, Environ. Sci. Technol., 52(13), 7587–7593, doi:10.1021/acs.est.8b00926, 2018.

Bloss, C., Wagner, V., Jenkin, M. E., Volkamer, R., Bloss, W. J., Lee, J. D., Heard, D. E., Wirtz, K., Martin-Reviejo, M., Rea, G., Wenger, J. C. and Pilling, M. J.: Development of a detailed chemical mechanism (MCMv3.1) for the atmospheric oxidation of aromatic hydrocarbons, Atmos. Chem. Phys., 5(3), 641–664, doi:10.5194/acp-5-641-2005, 2005.

Bolzacchini, E., Bruschi, M., Hjorth, J., Meinardi, S., Orlandi, M., Rindone, B. and Rosenbohm, E.: Gas-Phase Reaction of Phenol with NO3, Environ. Sci. Technol., 35, 1791–1797, 2001.

Bond, T. C., Doherty, S. J., Fahey, D. W., Forster, P. M., Berntsen, T., Deangelo, B. J.,

Flanner, M. G., Ghan, S., Kärcher, B., Koch, D., Kinne, S., Kondo, Y., Quinn, P. K., Sarofim, M. C., Schultz, M. G., Schulz, M., Venkataraman, C., Zhang, H., Zhang, S., Bellouin, N., Guttikunda, S. K., Hopke, P. K., Jacobson, M. Z., Kaiser, J. W., Klimont, Z., Lohmann, U., Schwarz, J. P., Shindell, D., Storelvmo, T., Warren, S. G. and Zender, C. S.: Bounding the role of black carbon in the climate system: A scientific assessment, J. Geophys. Res. Atmos., 118(11), 5380–5552, doi:10.1002/jgrd.50171, 2013.

Brey, S. J. and Fischer, E. V.: Smoke in the City: How Often and Where Does Smoke Impact Summertime Ozone in the United States?, Environ. Sci. Technol., 50(3), 1288–1294, doi:10.1021/acs.est.5b05218, 2016.

Brey, S. J., Barnes, E. A., Pierce, J. R., Wiedinmyer, C. and Fischer, E. V.: Environmental Conditions, Ignition Type, and Air Quality Impacts of Wildfires in the Southeastern and Western United States, Earth's Futur., 6(10), 1442–1456, doi:10.1029/2018EF000972, 2018.

Brock, C. A., Schröder, F., Kärcher, B., Petzold, A., Busen, R. and Fiebig, M.: Ultrafine particle size distribution measured in aircraft exhaust plumes, J. Geophys. Res., 105(Vi), 26555–26567, 2000.

Brock, C. A., Trainer, M., Ryerson, T. B., Neuman, J. A., Parrish, D. D., Holloway, J. S., Nicks, D. K., Frost, G. J., Hübler, G., Fehsenfeld, F. C., Wilson, J. C., Reeves, J. M., Lafleur, B. G., Hilbert, H., Atlas, E. L., Donnelly, S. G., Schauffler, S. M., Stroud, V. R. and Wiedinmyer, C.: Particle growth in urban and industrial plumes in Texas, J. Geophys. Res. Atmos., 108(3), 1–12, doi:10.1029/2002jd002746, 2003.

Brock, C. A., Cozic, J., Bahreini, R., Froyd, K. D., Middlebrook, A. M., McComiskey, A., Brioude, J., Cooper, O. R., Stohl, A., Aikin, K. C., De Gouw, J. A., Fahey, D. W., Ferrare, R. A.,

Gao, R. S., Gore, W., Holloway, J. S., Hübler, G., Jefferson, A., Lack, D. A., Lance, S., Moore, R. H., Murphy, D. M., Nenes, A., Novelli, P. C., Nowak, J. B., Ogren, J. A., Peischl, J., Pierce, R. B., Pilewskie, P., Quinn, P. K., Ryerson, T. B., Schmidt, K. S., Schwarz, J. P., Sodemann, H., Spackman, J. R., Stark, H., Thomson, D. S., Thornberry, T., Veres, P., Watts, L. A., Warneke, C. and Wollny, A. G.: Characteristics, sources, and transport of aerosols measured in spring 2008 during the aerosol, radiation, and cloud processes affecting Arctic Climate (ARCPAC) Project, Atmos. Chem. Phys., 11(6), 2423–2453, doi:10.5194/acp-11-2423-2011, 2011.

Brown, S.: Absorption spectroscopy in high finesse cavities for atmospheric studies, Chem. Rev., 103, 5219, 2003.

Brown, S. S. and Stutz, J.: Nighttime radical observations and chemistry, Chem. Soc. Rev., 41, 6405–6447, doi:10.1039/c2cs35181a, 2012.

Brown, S. S., Stark, H. and Ravishankara, A. R.: Cavity ring-down spectroscopy for atmospheric trace gas detection: Application to the nitrate radical (NO3), Appl. Phys. B Lasers Opt., 75(2–3), 173–182, doi:10.1007/s00340-002-0980-y, 2002.

Brown, S. S., Stark, H. and Ravishankara, A. R.: Applicability of the steady state approximation to the interpretation of atmospheric observations of NO3 and N2O5, J. Geophys. Res., 108(D17), 4539, doi:10.1029/2003JD003407, 2003.

Brown, S. S., Osthoff, H. D., Stark, H., Dubé, W. P., Ryerson, T. B., Warneke, C., de Gouw, J. A., Wollny, A. G., Parrish, D. D., Fehsenfeld, F. C. and Ravishankara, A. R.: Aircraft observations of daytime NO3 and N2 O5 and their implications for tropospheric chemistry, J. Photochem. Photobiol. A Chem., 176(1-3 SPEC. ISS.), 270–278, doi:10.1016/j.jphotochem.2005.10.004, 2005.

Brown, S. S., Dubé, W. P., Karamchandani, P., Yarwood, G., Peischl, J., Ryerson, T. B., Neuman, J. A., Nowak, J. B., Holloway, J. S., Washenfelder, R. A., Brock, C. A., Frost, G. J., Trainer, M., Parrish, D. D., Fehsenfeld, F. C. and Ravishankara, A. R.: Effects of NOx control and plume mixing on nighttime chemical processing of plumes from coal-fired power plants, J. Geophys. Res. Atmos., 117(7), 1–14, doi:10.1029/2011JD016954, 2012.

Brown, S. S., An, H., Lee, M., Park, J.-H., Lee, S.-D., Fibiger, D. L., McDuffie, E. E., Dubé, W. P., Wagner, N. L. and Min, K.-E.: Cavity enhanced spectroscopy for measurement of nitrogen oxides in the Anthropocene: results from the Seoul tower during MAPS 2015, Faraday Discuss., 200(529), 529–557, doi:10.1039/C7FD00001D, 2017.

Bruns, E. A., El Haddad, I., Keller, A., Klein, F., Kumar, N. K., Pieber, S. M., Corbin, J. C., Slowik, J. G., Brune, W. H., Baltensperger, U. and Prévôt, A. S. H.: Inter-comparison of laboratory smog chamber and flow reactor systems on organic aerosol yield and composition, Atmos. Meas. Tech., 8(6), 2315–2332, doi:10.5194/amt-8-2315-2015, 2015.

Bruns, E. A., El Haddad, I., Slowik, J. G., Kilic, D., Klein, F., Baltensperger, U. and Prévôt, A. S. H.: Identification of significant precursor gases of secondary organic aerosols from residential wood combustion, Sci. Rep., 6(June), 1–9, doi:10.1038/srep27881, 2016.

Cabañas, B., Baeza, M. T., Salgado, S., Martín, P., Taccone, R. and Martínez, E.: Oxidation of heterocycles in the atmosphere: Kinetic study of their reactions with NO3 radical, J. Phys. Chem. A, 108(49), 10818–10823, doi:10.1021/jp046524t, 2004.

Calvert, J. G., Mellouki, A., Orlando, J. J., Pilling, M. J. and Wallington, T. J.: Mechanisms of Atmospheric Oxidation of the Oxygenate., 2011.

Chang, W. L., Bhave, P. V., Brown, S. S., Riemer, N., Stutz, J. and Dabdub, D.:

Heterogeneous atmospheric chemistry, ambient measurements, and model calculations of N2O5: A review, Aerosol Sci. Technol., 45(6), 655–685, doi:10.1080/02786826.2010.551672, 2011.

Chattopadhyay, A., Burkholder, J. B., Papadimitriou, V. C. and Marshall, P.: Temperature-dependent rate coefficients for the gas-phase OH + furan-2 , 5-dione (C 4 H 2 O 3 , maleic anhydride) reaction, , (May), 623–631, doi:10.1002/kin.21387, 2020.

Chen, X., Sun, Y., Qi, Y., Liu, L., Xu, F. and Zhao, Y.: Mechanistic and kinetic investigations on the ozonolysis of biomass burning products: Guaiacol, syringol and creosol, Int. J. Mol. Sci., 20(18), doi:10.3390/ijms20184492, 2019.

Claeys, M., Vermeylen, R., Yasmeen, F., Gómez-González, Y., Chi, X., Maenhaut, W., Mészáros, T. and Salma, I.: Chemical characterisation of humic-like substances from urban, rural and tropical biomass burning environments using liquid chromatography with UV/vis photodiode array detection and electrospray ionisation mass spectrometry, Environ. Chem., 9(3), 273–284, doi:10.1071/EN11163, 2012.

Coggon, M. M., Lim, C. Y., Koss, A. R., Sekimoto, K., Yuan, B., Gilman, J. B., Hagan, D. H., Selimovic, V., Zarzana, K. J., Brown, S. S., M Roberts, J., Müller, M., Yokelson, R., Wisthaler, A., Krechmer, J. E., Jimenez, J. L., Cappa, C., Kroll, J. H., De Gouw, J. and Warneke, C.: OH chemistry of non-methane organic gases (NMOGs) emitted from laboratory and ambient biomass burning smoke: Evaluating the influence of furans and oxygenated aromatics on ozone and secondary NMOG formation, Atmos. Chem. Phys., 19(23), 14875–14899, doi:10.5194/acp-19-14875-2019, 2019.

CropScape: CropScape - NASS CDL Program, [online] Available from: https://nassgeodata.gmu.edu/CropScape/ (Accessed 6 August 2018), 2018.

Crosson, E. R.: A cavity ring-down analyzer for measuring atmospheric levels of methane, carbon dioxide, and water vapor, Appl. Phys. B Lasers Opt., 92(3 SPECIAL ISSUE), 403–408, doi:10.1007/s00340-008-3135-y, 2008.

Decarlo, P. F., Kimmel, J. R., Trimborn, A., Northway, M. J., Jayne, J. T., Aiken, A. C., Gonin, M., Fuhrer, K., Horvath, T., Docherty, K. S., Worsnop, D. R. and Jimenez, J. L.: Field-Deployable, High-Resolution, Time-of-Flight Aerosol Mass Spectrometer, Anal. Chem., 78(24), 8281–8289, doi:8410.1029/2001JD001213.Analytical, 2006.

Decker, Z. C. J., Zarzana, K. J., Coggon, M., Min, K.-E., Pollack, I., Ryerson, T. B., Peischl, J., Edwards, P., Dubé, W. P., Markovic, M. Z., Roberts, J. M., Veres, P. R., Graus, M., Warneke, C., de Gouw, J., Hatch, L. E., Barsanti, K. C. and Brown, S. S.: Nighttime Chemical Transformation in Biomass Burning Plumes: A Box Model Analysis Initialized with Aircraft Observations, Environ. Sci. Technol., 53(5), 2529–2538, doi:10.1021/acs.est.8b05359, 2019.

Decker, Z. C. J., Robinson, M. A., Barsanti, K. C., Bourgeois, I., Matthew, M., Digangi, J. P., Diskin, G. S., Flocke, F. M., Franchin, A., Carley, D., Hall, S. R., Halliday, H., Holmes, C. D., Huey, L. G., Lee, R., Lindaas, J., Middlebrook, A. M., Montzka, D. D., Moore, R., Andrew, J., Nowak, J. B., Palm, B. B., Peischl, J., Rickly, P. S., Rollins, A. W., Ryerson, T. B., Schwantes, R. H., Thornhill, L., Thornton, J. A., Geoffrey, S., Ullmann, K., Rooy, P. Van, Veres, P. R., Weinheimer, A. J., Winstead, E., Womack, C. and Brown, S. S.: Nighttime and Daytime Dark Oxidation Chemistry in Wildfire Plumes : An Observation and Model Analysis of FIREX-AQ Aircraft Data, Atmos. Chem. Phys. Discuss., 1–45, doi:doi.org/10.5194/acp-2021-267, 2021.

Dennison, P. E., Brewer, S. C., Arnold, J. D. and Moritz, M. A.: Large wildfire trends in the western United States, 1984-2011, Geophys. Res. Lett., 41, 2014GL059576,

doi:10.1002/2014gl059576, 2014.

Dentener, F. J. and Crutzen, P. J.: Reaction of N 2 O 5 on tropospheric aerosols: Impact on the global distributions of NO x , O 3 , and OH, J. Geophys. Res. Atmos., 98(D4), 7149–7163, doi:10.1029/92JD02979, 1993.

Desyaterik, Y., Sun, Y., Shen, X., Lee, T., Wang, X., Wang, T. and Collett, J. L.: Speciation of "brown" carbon in cloud water impacted by agricultural biomass burning in eastern China, J. Geophys. Res. Atmos., 118(13), 7389–7399, doi:10.1002/jgrd.50561, 2013.

Dubé, W. P., Brown, S. S., Osthoff, H. D., Nunley, M. R., Ciciora, S. J., Paris, M. W., McLaughlin, R. J. and Ravishankara, A. R.: Aircraft instrument for simultaneous, *in situ* measurement of NO3 and N2O5 via pulsed cavity ring-down spectroscopy, Rev. Sci. Instrum., 77(3), 034101, doi:10.1063/1.2176058, 2006.

Edwards, P. M., Evans, M. J., Furneaux, K. L., Hopkins, J., Ingham, T., Jones, C., Lee, J. D., Lewis, A. C., Moller, S. J., Stone, D., Whalley, L. K. and Heard, D. E.: OH reactivity in a South East Asian tropical rainforest during the oxidant and particle photochemical processes (OP3) project, Atmos. Chem. Phys., 13(18), 9497–9514, doi:10.5194/acp-13-9497-2013, 2013a.

Edwards, P. M., Young, C. J., Aikin, K., DeGouw, J., Dubé, W. P., Geiger, F., Gilman, J., Helmig, D., Holloway, J. S., Kercher, J., Lerner, B., Martin, R., McLaren, R., Parrish, D. D., Peischl, J., Roberts, J. M., Ryerson, T. B., Thornton, J., Warneke, C., Williams, E. J. and Brown, S. S.: Ozone photochemistry in an oil and natural gas extraction region during winter: Simulations of a snow-free season in the Uintah Basin, Utah, Atmos. Chem. Phys., 13(17), 8955–8971, doi:10.5194/acp-13-8955-2013, 2013b.

Edwards, P. M., Aikin, K. C., Dube, W. P., Fry, J. L., Gilman, J. B., De Gouw, J. A., Graus,

M. G., Hanisco, T. F., Holloway, J., Hübler, G., Kaiser, J., Keutsch, F. N., Lerner, B. M., Neuman, J. A., Parrish, D. D., Peischl, J., Pollack, I. B., Ravishankara, A. R., Roberts, J. M., Ryerson, T. B., Trainer, M., Veres, P. R., Wolfe, G. M. and Warneke, C.: Transition from high- to low-NOx control of night-time oxidation in the southeastern US, Nat. Geosci., 10(7), 490–495, doi:10.1038/ngeo2976, 2017.

Eilerman, S. J., Peischl, J., Neuman, J. A., Ryerson, T. B., Aikin, K. C., Holloway, M. W., Zondlo, M. A., Golston, L. M., Pan, D., Floerchinger, C. and Herndon, S.: Characterization of Ammonia, Methane, and Nitrous Oxide Emissions from Concentrated Animal Feeding Operations in Northeastern Colorado, Environ. Sci. Technol., 50(20), 10885–10893, doi:10.1021/acs.est.6b02851, 2016.

EPA, U. S.: Ground-level Ozone Pollution | US EPA, [online] Available from: https://www.epa.gov/ground-level-ozone-pollution (Accessed 4 April 2021), 2021.

Finewax, Z., De Gouw, J. A. and Ziemann, P. J.: Identification and Quantification of 4-Nitrocatechol Formed from OH and NO3 Radical-Initiated Reactions of Catechol in Air in the Presence of NOx: Implications for Secondary Organic Aerosol Formation from Biomass Burning, Environ. Sci. Technol., 52(4), 1981–1989, doi:10.1021/acs.est.7b05864, 2018.

Fuchs, H., Dubé, W. P., Ciciora, S. J. and Brown, S. S.: Determination of inlet transmission and conversion efficiencies for in situ measurements of the nocturnal nitrogen oxides, NO3, N 2O5 and NO2, via pulsed cavity ring-down spectroscopy, Anal. Chem., 80(15), 6010–6017, doi:10.1021/ac8007253, 2008.

Fuchs, H., Tan, Z., Lu, K., Bohn, B., Broch, S., Brown, S. S., Dong, H., Gomm, S., Häseler, R., He, L., Hofzumahaus, A., Holland, F., Li, X., Liu, Y., Lu, S., Min, K. E., Rohrer, F., Shao, M.,

Wang, B., Wang, M., Wu, Y., Zeng, L., Zhang, Y., Wahner, A. and Zhang, Y.: OH reactivity at a rural site (Wangdu) in the North China Plain: Contributions from OH reactants and experimental OH budget, Atmos. Chem. Phys., 17(1), 645–661, doi:10.5194/acp-17-645-2017, 2017.

Gaston, C. J., Lopez-Hilfiker, F. D., Whybrew, L. E., Hadley, O., McNair, F., Gao, H., Jaffe, D. A. and Thornton, J. A.: Online molecular characterization of fine particulate matter in Port Angeles, WA: Evidence for a major impact from residential wood smoke, Atmos. Environ., 138, 99–107, doi:10.1016/j.atmosenv.2016.05.013, 2016.

Geyer, A., Alicke, B., Ackermann, R., Martinez, M., Harder, H., Brune, W., Di Carlo, P., Williams, E., Jobson, T., Hall, S., Shetter, R. and Stutz, J.: Direct observations of daytime NO3: Implications for urban boundary layer chemistry, J. Geophys. Res. Atmos., 108(12), 1–11, doi:10.1029/2002jd002967, 2003.

Giglio, L.: Characterization of the tropical diurnal fire cycle using VIRS and MODIS observations, Remote Sens. Environ., 108(4), 407–421, doi:10.1016/j.rse.2006.11.018, 2007.

Gilman, J. B., Kuster, W. C., Goldan, P. D., Herndon, S. C., Zahniser, M. S., Tucker, S. C., Brewer, W. A., Lerner, B. M., Williams, E. J., Harley, R. A., Fehsenfeld, F. C., Warneke, C. and De Gouw, J. A.: Measurements of volatile organic compounds during the 2006 TexAQS/GoMACCS campaign: Industrial influences, regional characteristics, and diurnal dependencies of the OH reactivity, J. Geophys. Res. Atmos., 114(7), 1–17, doi:10.1029/2008JD011525, 2009.

Gilman, J. B., Lerner, B. M., Kuster, W. C., Goldan, P. D., Warneke, C., Veres, P. R., Roberts, J. M., De Gouw, J. A., Burling, I. R. and Yokelson, R. J.: Biomass burning emissions and potential air quality impacts of volatile organic compounds and other trace gases from fuels

common in the US, Atmos. Chem. Phys., 15(24), 13915–13938, doi:10.5194/acp-15-13915-2015, 2015.

Goldberger, L. A., Jahl, L. G., Thornton, J. A. and Sullivan, R. C.: N2O5 reactive uptake kinetics and chlorine activation on authentic biomass-burning aerosol, Environ. Sci. Process. Impacts, 21(10), 1684–1698, doi:10.1039/c9em00330d, 2019.

de Gouw, J. A., Parrish, D. D., Brown, S. S., Edwards, P., Gilman, J. B., Graus, M., Hanisco, T. F., Kaiser, J., Keutsch, F. N., Kim, S. W., Lerner, B. M., Neuman, J. A., Nowak, J. B., Pollack, I. B., Roberts, J. M., Ryerson, T. B., Veres, P. R., Warneke, C. and Wolfe, G. M.: Hydrocarbon Removal in Power Plant Plumes Shows Nitrogen Oxide Dependence of Hydroxyl Radicals, Geophys. Res. Lett., 46(13), 7752–7760, doi:10.1029/2019GL083044, 2019.

De Gouw, J. and Warneke, C.: Measurements of volatile organic compounds in the earth's atmosphere using proton-transfer-reaction mass spectrometry, Mass Spectrom. Rev., 26(2), 223–257, doi:10.1002/mas.20119, 2007.

Grosjean, D. and Williams, E. L.: Environmental persistence of organic compounds estimated from structure-reactivity and linear free-energy relationships. Unsaturated aliphatics, Atmos. Environ. Part A, Gen. Top., 26(8), 1395–1405, doi:10.1016/0960-1686(92)90124-4, 1992.

Harrison, M. A. J., Barra, S., Borghesi, D., Vione, D., Arsene, C. and Iulian Olariu, R.: Nitrated phenols in the atmosphere: A review, Atmos. Environ., 39(2), 231–248, doi:10.1016/j.atmosenv.2004.09.044, 2005.

Hartikainen, A., Yli-Pirilä, P., Tiitta, P., Leskinen, A., Kortelainen, M., Orasche, J., Schnelle-Kreis, J., Lehtinen, K., Zimmermann, R., Jokiniemi, J. and Sippula, O.: Volatile organic compounds from logwood combustion: Emissions and transformation under dark and

photochemical aging conditions in a smog chamber, Environ. Sci. Technol., 52(4979–4988), acs.est.7b06269, doi:10.1021/acs.est.7b06269, 2018.

Hatch, L. E., Luo, W., Pankow, J. F., Yokelson, R. J., Stockwell, C. E. and Barsanti, K. C.: Identification and quantification of gaseous organic compounds emitted from biomass burning using two-dimensional gas chromatography–time-of-flight mass spectrometry, Atmos. Chem. Phys., 15(4), 1865–1899, doi:10.5194/acp-15-1865-2015, 2015.

Hatch, L. E., Yokelson, R. J., Stockwell, C. E., Veres, P. R., Simpson, I. J., Blake, D. R., Orlando, J. J. and Barsanti, K. C.: Multi-instrument comparison and compilation of non-methane organic gas emissions from biomass burning and implications for smoke-derived secondary organic aerosol precursors, Atmos. Chem. Phys., 17(2), 1471–1489, doi:10.5194/acp-17-1471-2017, 2017.

Hatch, L. E., Rivas-ubach, A., Jen, C. N., Lipton, M., Goldstein, A. H. and Barsanti, K. C.: Measurements of I / SVOCs in biomass-burning smoke using solid-phase extraction disks and two-dimensional gas chromatography, Atmos. Chem. Phys., 18, 17801–17817, doi:10.5194/acp-18-17801-2018, 2018.

Hennigan, C. J., Sullivan, A. P., Collett, J. L. and Robinson, A. L.: Levoglucosan stability in biomass burning particles exposed to hydroxyl radicals, Geophys. Res. Lett., 37(9), 1–4, doi:10.1029/2010GL043088, 2010.

Hennigan, C. J., Miracolo, M. A., Engelhart, G. J., May, A. A., Presto, A. A., Lee, T., Sullivan, A. P., McMeeking, G. R., Coe, H., Wold, C. E., Hao, W. M., Gilman, J. B., Kuster, W. C., De Gouw, J., Schichtel, B. A., Collett, J. L., Kreidenweis, S. M. and Robinson, A. L.: Chemical and physical transformations of organic aerosol from the photo-oxidation of open biomass burning

emissions in an environmental chamber, Atmos. Chem. Phys., 11(15), 7669–7686, doi:10.5194/acp-11-7669-2011, 2011.

Higuera, P. E., Abatzoglou, J. T., Littell, J. S. and Morgan, P.: The changing strength and nature of fire-climate relationships in the northern Rocky Mountains, U.S.A., 1902-2008, PLoS One, 10(6), 1–21, doi:10.1371/journal.pone.0127563, 2015.

Hinrichs, R. Z., Buczek, P. and Trivedi, J. J.: Solar Absorption by Aerosol-Bound Nitrophenols Compared to Aqueous and Gaseous Nitrophenols, Environ. Sci. Technol., 50(11), 5661–5667, doi:10.1021/acs.est.6b00302, 2016.

Holloway, J. S., Jakoubek, R. O., Parrish, D. D., Gerbig, C., Volz-Thomas, A., Schmitgen, S., Fried, A., Wert, B., Henry, B. and Drummond, J. R.: Airborne intercomparison of vacuum ultraviolet fluorescence and tunable diode laser absorption measurements of tropospheric carbon monoxide, J. Geophys. Res. Atmos., 105(D19), 24251–24261, doi:10.1029/2000JD900237, 2000.

Holmes, C. D., Fite, C. H., Agastra, A., Schwarz, Joshua, P., Yokelson, R. J., Bui, T. P., Kondragunta, S. and Peterson, D. A.: Critical evaluation of smoke age inferred from different methods during FIREX-AQ, in AGU Fall Meeting 2020., 2020.

Iinuma, Y., Boge, O., Grade, R. and Herrmann, H.: Methyl-Nitrocatechols : Atmospheric Tracer Compounds for Biomass Burning Secondary Organic Aerosols, Environ. Sci. Technol., 44, 8453–8459, 2010.

Inciweb: 204 Cow Fire - InciWeb the Incident Information System, [online] Available from: https://inciweb.nwcg.gov/incident/maps/6526/ (Accessed 27 December 2020a), 2019.

Inciweb: Castle Fire - InciWeb the Incident Information System, [online] Available from: https://inciweb.nwcg.gov/incident/article/7048/53693/ (Accessed 27 December 2020b), 2019.

Inciweb: Williams Flats Fire - InciWeb the Incident Information System, [online] Available from: https://inciweb.nwcg.gov/incident/6493/ (Accessed 27 December 2020c), 2019.

Jaffe, D. A. and Wigder, N. L.: Ozone production from wildfires: A critical review, Atmos. Environ., 51, 1–10, doi:http://dx.doi.org/10.1016/j.atmosenv.2011.11.063, 2012.

Jaffe, D. A., O'Neill, S. M., Larkin, N. K., Holder, A. L., Peterson, D. L., Halofsky, J. E. and Rappold, A. G.: Wildfire and prescribed burning impacts on air quality in the United States, J. Air Waste Manag. Assoc., 70(6), 583–615, doi:10.1080/10962247.2020.1749731, 2020.

Jenkin, M. E., Saunders, S. M. and Pilling, M. J.: The tropospheric degradation of volatile organic compounds: a protocol for mechanism development, Atmos. Environ., 31(1), 81–104, doi:10.1016/S1352-2310(96)00105-7, 1997.

Jenkin, M. E., Saunders, S. M., Wagner, V. and Pilling, M. J.: Protocol for the development of the Master Chemical Mechanism, MCM v3 (Part B): Tropospheric degradation of aromatic volatile organic compounds, Atmos. Chem. Phys., 3(1), 181–193, doi:10.5194/acp-3-181-2003, 2003.

Jenkin, M. E., Wyche, K. P., Evans, C. J., Carr, T., Monks, P. S., Alfarra, M. R., Barley, M. H., McFiggans, G. B., Young, J. C. and Rickard, A. R.: Development and chamber evaluation of the MCM v3.2 degradation scheme for β-caryophyllene, Atmos. Chem. Phys., 12(11), 5275–5308, doi:10.5194/acp-12-5275-2012, 2012.

Jenkin, M. E., Young, J. C. and Rickard, A. R.: The MCM v3.3.1 degradation scheme for isoprene, Atmos. Chem. Phys., 15(20), 11433–11459, doi:10.5194/acp-15-11433-2015, 2015.

Jones, R. L., Ball, S. M. and Shallcross, D. E.: Small scale structure in the atmosphere: Implications for chemical composition and observational methods, Faraday Discuss., 130(x), 165–

179, doi:10.1039/b502633b, 2005.

Jost, C., Trentmann, J., Sprung, D., Andrea, M. O., Quaid, J. B. and Barjat, H.: Trace gas chemistry in a young biomass burning plume over Namibia: Observations and model simulations, J. Geophys. Res. Atmos., 108(13), doi:10.1029/2002jd002431, 2003.

Kerdouci, J., Picquet-Varrault, B. and Doussin, J. F.: Prediction of rate constants for gas-phase reactions of nitrate radical with organic compounds: A new structure-activity relationship, ChemPhysChem, 11(18), 3909–3920, doi:10.1002/cphc.201000673, 2010.

Kerdouci, J., Picquet-Varrault, B. and Doussin, J. F.: Structure-activity relationship for the gas-phase reactions of NO3radical with organic compounds: Update and extension to aldehydes, Atmos. Environ., 84(3), 363–372, doi:10.1016/j.atmosenv.2013.11.024, 2014.

Keywood, M., Cope, M., Meyer, C. P. P. M., Iinuma, Y. and Emmerson, K.: When smoke comes to town: The impact of biomass burning smoke on air quality, Atmos. Environ., 121, 13–21, doi:10.1016/j.atmosenv.2015.03.050, 2015.

Khan, M. A. H., Percival, C. J., Caravan, R. L., Taatjes, C. A. and Shallcross, D. E.: Criegee intermediates and their impacts on the troposphere, Environ. Sci. Process. Impacts, 20(3), 437–453, doi:10.1039/c7em00585g, 2018.

Kodros, J., Papanastasiou, D., Paglione, M., Masiol, M. and Squizzato, S.: The oxidizing power of the dark side : Rapid nocturnal aging of biomass burning as an overlooked source of oxidized organic aerosol, , 7382, doi:10.1073/pnas.2010365117, 2020.

Koss, A. R., Sekimoto, K., Gilman, J. B., Selimovic, V., Coggon, M. M., Zarzana, K. J., Yuan, B., Lerner, B. M., Brown, S. S., Jimenez, J. L., Krechmer, J., Roberts, J. M., Warneke, C., Yokelson, R. J. and de Gouw, J.: Non-methane organic gas emissions from biomass burning:

identification, quantification, and emission factors from PTR-ToF during the FIREX 2016 laboratory experiment, Atmos. Chem. Phys., 18(October), 3299–3319, doi:10.5194/acp-2017-924, 2018.

Kupc, A., Williamson, C., Wagner, N. L., Richardson, M. and Brock, C. A.: Modification, calibration, and performance of the Ultra-High Sensitivity Aerosol Spectrometer for particle size distribution and volatility measurements during the Atmospheric Tomography Mission (ATom) airborne campaign, Atmos. Meas. Tech., 11(1), 369–383, doi:10.5194/amt-11-369-2018, 2018.

LAS: Laser Aerosol Spectrometer 3340A -, [online] Available from: https://www.tsi.com/products/particle-sizers/particle-size-spectrometers/laser-aerosol-spectrometer-3340a/ (Accessed 18 March 2021), n.d.

Laskin, A., Laskin, J. and Nizkorodov, S. A.: Chemistry of Atmospheric Brown Carbon, Chem. Rev., 115(10), 4335–4382, doi:10.1021/cr5006167, 2015.

Lauraguais, A., Coeur-Tourneur, C., Cassez, A., Deboudt, K., Fourmentin, M. and Choël, M.: Atmospheric reactivity of hydroxyl radicals with guaiacol (2-methoxyphenol), a biomass burning emitted compound: Secondary organic aerosol formation and gas-phase oxidation products, Atmos. Environ., 86, 155–163, doi:10.1016/j.atmosenv.2013.11.074, 2014.

Lauraguais, A., El Zein, A., Coeur, C., Obeid, E., Cassez, A., Rayez, M.-T. and Rayez, J.-C.: Kinetic Study of the Gas-Phase Reactions of Nitrate Radicals with Methoxyphenol Compounds: Experimental and Theoretical Approaches, J. Phys. Chem. A, 120(17), 2691–2699, doi:10.1021/acs.jpca.6b02729, 2016.

Lee, B. H., Lopez-Hilfiker, F. D., Mohr, C., Kurtén, T., Worsnop, D. R. and Thornton, J. A.: An iodide-adduct high-resolution time-of-flight chemical-ionization mass spectrometer:

Application to atmospheric inorganic and organic compounds, Environ. Sci. Technol., 48(11), 6309–6317, doi:10.1021/es500362a, 2014.

Li, F., Zhang, X., Roy, D. P. and Kondragunta, S.: Estimation of biomass-burning emissions by fusing the fire radiative power retrievals from polar-orbiting and geostationary satellites across the conterminous United States, Atmos. Environ., 211(November 2018), 274–287, doi:10.1016/j.atmosenv.2019.05.017, 2019.

Li, F., Zhang, X., Kondragunta, S., Schmidt, C. C. and Holmes, C. D.: A preliminary evaluation of GOES-16 active fire product using Landsat-8 and VIIRS active fire data, and ground-based prescribed fire records, Remote Sens. Environ., 237(December 2019), 111600, doi:10.1016/j.rse.2019.111600, 2020.

Liggio, J., Li, S. M., Hayden, K., Taha, Y. M., Stroud, C., Darlington, A., Drollette, B. D., Gordon, M., Lee, P., Liu, P., Leithead, A., Moussa, S. G., Wang, D., O'Brien, J., Mittermeier, R. L., Brook, J. R., Lu, G., Staebler, R. M., Han, Y., Tokarek, T. W., Osthoff, H. D., Makar, P. A., Zhang, J., Plata, D. L. and Gentner, D. R.: Oil sands operations as a large source of secondary organic aerosols, Nature, 534(7605), 91–94, doi:10.1038/nature17646, 2016.

Lin, P., Liu, J., Shilling, J. E., Kathmann, S. M., Laskin, J. and Laskin, A.: Molecular characterization of brown carbon (BrC) chromophores in secondary organic aerosol generated from photo-oxidation of toluene, Phys. Chem. Chem. Phys., 17(36), 23312–23325, doi:10.1039/C5CP02563J, 2015.

Lin, P., Bluvshtein, N., Rudich, Y., Nizkorodov, S. A., Laskin, J. and Laskin, A.: Molecular Chemistry of Atmospheric Brown Carbon Inferred from a Nationwide Biomass Burning Event, Environ. Sci. Technol., 51(20), 11561–11570, doi:10.1021/acs.est.7b02276, 2017.

Liu, C., Liu, J., Liu, Y., Chen, T. and He, H.: Secondary organic aerosol formation from the OH-initiated oxidation of guaiacol under different experimental conditions, Atmos. Environ., 207, 30–37, doi:10.1016/j.atmosenv.2019.03.021, 2019.

Liu, J. C., Pereira, G., Uhl, S. A., Bravo, M. A. and Bell, M. L.: A systematic review of the physical health impacts from non-occupational exposure to wildfire smoke, Environ. Res., 136, 120–132, doi:10.1016/j.envres.2014.10.015, 2015.

Liu, X., Zhang, Y., Huey, L. G., Yokelson, R. J., Wang, Y., Jimenez, J. L., Campuzano-Jost, P., Beyersdorf, A. J., Blake, D. R., Choi, Y., St. Clair, J. M., Crounse, J. D., Day, D. A., Diskin, G. S., Fried, A., Hall, S. R., Hanisco, T. F., King, L. E., Meinardi, S., Mikoviny, T., Palm, B. B., Peischl, J., Perring, A. E., Pollack, I. B., Ryerson, T. B., Sachse, G., Schwarz, J. P., Simpson, I. J., Tanner, D. J., Thornhill, K. L., Ullmann, K., Weber, R. J., Wennberg, P. O., Wisthaler, A., Wolfe, G. M. and Ziemba, L. D.: Agricultural fires in the southeastern U.S. during SEAC4RS: Emissions of trace gases and particles and evolution of ozone, reactive nitrogen, and organic aerosol, J. Geophys. Res. Atmos., 121(12), 7383–7414, doi:10.1002/2016JD025040, 2016.

Lu, X., Zhang, L., Yue, X., Zhang, J., Jaffe, D. A., Stohl, A., Zhao, Y. and Shao, J.: Wildfire influences on the variability and trend of summer surface ozone in the mountainous western United States, Atmos. Chem. Phys., 16(22), 14687–14702, doi:10.5194/acp-16-14687-2016, 2016.

Marlon, J. R., Bartlein, P. J., Gavin, D. G., Long, C. J., Anderson, R. S., Briles, C. E., Brown, K. J., Colombaroli, D., Hallett, D. J., Power, M. J., Scharf, E. A. and Walsh, M. K.: Long-term perspective on wildfires in the western USA, Proc. Natl. Acad. Sci. U. S. A., 109(9), 535–543, doi:10.1073/pnas.1112839109, 2012.

Martin, P., Tuazon, E. C., Aschmann, S. M., Arey, J. and Atkinson, R.: Formation and

atmospheric reactions of 4,5-dihydro-2-methylfuran, J. Phys. Chem. A, 106(47), 11492–11501, doi:10.1021/jp021499h, 2002.

Martínez, E., Cabañas, B., Aranda, A., Martín, P. and Salgado, S.: Absolute Rate Coefficients for the Gas-Phase Reactions of NO3 Radical with a Series of Monoterpenes at T = 298 to 433 K, J. Atmos. Chem., 33(3), 265–282, doi:10.1023/A:1006178530211, 1999.

McClure, C. D. and Jaffe, D. A.: US particulate matter air quality improves except in wildfire-prone areas, Proc. Natl. Acad. Sci., 201804353, doi:10.1073/pnas.1804353115, 2018.

McDuffie, E. E., Fibiger, D. L., Dubé, W. P., Lopez-Hilfiker, F., Lee, B. H., Thornton, J. A., Shah, V., Jaeglé, L., Guo, H., Weber, R. J., Michael Reeves, J., Weinheimer, A. J., Schroder, J. C., Campuzano-Jost, P., Jimenez, J. L., Dibb, J. E., Veres, P., Ebben, C., Sparks, T. L., Wooldridge, P. J., Cohen, R. C., Hornbrook, R. S., Apel, E. C., Campos, T., Hall, S. R., Ullmann, K. and Brown, S. S.: Heterogeneous N2O5 Uptake During Winter: Aircraft Measurements During the 2015 WINTER Campaign and Critical Evaluation of Current Parameterizations, J. Geophys. Res. Atmos., 123(8), 4345–4372, doi:10.1002/2018JD028336, 2018.

Meidan, D., Holloway, J. S., Edwards, P. M., Dubé, W. P., Middlebrook, A. M., Liao, J., Welti, A., Graus, M., Warneke, C., Ryerson, T. B., Pollack, I. B., Brown, S. S. and Rudich, Y.: Role of Criegee Intermediates in Secondary Sulfate Aerosol Formation in Nocturnal Power Plant Plumes in the Southeast US, ACS Earth Sp. Chem., 3(5), 748–759, doi:10.1021/acsearthspacechem.8b00215, 2019.

Mellouki, A., Ammann, M., Cox, R. A., Crowley, J. N., Herrmann, H., Jenkin, M. E., Mcneill, V. F., Troe, J. and Wallington, T. J.: Evaluated kinetic and photochemical photochemical data for atmospheric chemistry: Volume VIII - Gas-phase reactions of organic species with four,

or more, carbon atoms (= C4), Atmos. Chem. Phys., 21(6), 4797–4808, doi:10.5194/acp-21-4797-2021, 2021.

Meng, L., Coeur, C., Fayad, L., Houzel, N., Genevray, P., Bouzidi, H., Tomas, A. and Chen, W.: Secondary organic aerosol formation from the gas-phase reaction of guaiacol (2-methoxyphenol) with NO3 radicals, Atmos. Environ., 240, 117740, doi:10.1016/j.atmosenv.2020.117740, 2020.

Min, K.-E., Washenfelder, R. a., Dubé, W. P., Langford, a. O., Edwards, P. M., Zarzana, K. J., Stutz, J., Lu, K., Rohrer, F., Zhang, Y. and Brown, S. S.: A broadband cavity enhanced absorption spectrometer for aircraft measurements of glyoxal, methylglyoxal, nitrous acid, nitrogen dioxide, and water vapor, Atmos. Meas. Tech. Discuss., 9(10), 423–440, doi:10.5194/amtd-8-11209-2015, 2016.

Mohr, C., Lopez-Hilfiker, F. D., Zotter, P., Prévoît, A. S. H., Xu, L., Ng, N. L., Herndon, S. C., Williams, L. R., Franklin, J. P., Zahniser, M. S., Worsnop, D. R., Knighton, W. B., Aiken, A. C., Gorkowski, K. J., Dubey, M. K., Allan, J. D. and Thornton, J. A.: Contribution of Nitrated Phenols to Wood Burning Brown Carbon Light Absorption in Detling, United Kingdom During Winter Time, Environ. Sci. Technol., 47(12), 6316–6324, doi:10.1021/es400683v, 2013.

Mondello, L., Tranchida, P. Q., Dugo, P. and Dugo, G.: Comprehensive two-dimensional gas chromatography-mass spectrometry: A review, Mass Spectrom. Rev., 27(2), 101–124, doi:10.1002/mas.20158, 2008.

Moore, R. H., Wiggins, E. B., Ahern, A. T., Zimmerman, S., Jost, P. C., Robinson, C. E., Ziemba, L. D., Winstead, E. L., Anderson, B. E., Brock, C. A., Brown, M. D., Chen, G., Crosbie, E. C., Jimenez, J. L., Jordan, C. E., Lyu, M., Nault, B. A., Rothfuss, N. E., Sanchez, K. J.,

Schueneman, M., Shingler, T. J., Shook, M. A., Kenneth, L., Wagner, N. L. and Wang, J.: Sizing Response of the Ultra-High Sensitivity Aerosol Size Spectrometer (UHSAS) and Laser Aerosol Spectrometer (LAS) to Changes in Submicron Aerosol Composition and Refractive Index, Atmos. Meas. Tech., doi:10.5194/amt-2021-21, 2021.

Müller, M., Mikoviny, T., Feil, S., Haidacher, S., Hanel, G., Hartungen, E., Jordan, A., Märk, L., Mutschlechner, P., Schottkowsky, R., Sulzer, P., Crawford, J. H. and Wisthaler, A.: A compact PTR-ToF-MS instrument for airborne measurements of volatile organic compounds at high spatiotemporal resolution, Atmos. Meas. Tech., 7(11), 3763–3772, doi:10.5194/amt-7-3763-2014, 2014.

Müller, M., Anderson, B. E., Beyersdorf, A. J., Crawford, J. H., Diskin, G. S., Eichler, P., Fried, A., Keutsch, F. N., Mikoviny, T., Thornhill, K. L., Walega, J. G., Weinheimer, A. J., Yang, M., Yokelson, R. J. and Wisthaler, A.: In situ measurements and modeling of reactive trace gases in a small biomass burning plume, Atmos. Chem. Phys., 16(6), 3813–3824, doi:10.5194/acp-16-3813-2016, 2016.

Nakao, S., Clark, C., Tang, P., Sato, K. and Cocker, D.: Secondary organic aerosol formation from phenolic compounds in the absence of NOx, Atmos. Chem. Phys., 11(20), 10649–10660, doi:10.5194/acp-11-10649-2011, 2011.

Navarro, K. M., Clark, K. A., Hardt, D. J., Reid, C. E., Lahm, P. W., Domitrovich, J. W., Butler, C. R. and Balmes, J. R.: Science of the Total Environment Wildland fire fighter exposure to smoke and COVID-19 : A new risk on the fire line, Sci. Total Environ., 760, 144296, doi:10.1016/j.scitotenv.2020.144296, 2021.

Neuman, J. A., Trainer, M., Brown, S. S., Min, K. E., Nowak, J. B., Parrish, D. D., Peischl,

J., Pollack, I. B., Roberts, J. M., Ryerson, T. B. and Veres, P. R.: HONO emission and production determined from airborne measurements over the Southeast U.S., J. Geophys. Res., 121(15), 9237–9250, doi:10.1002/2016JD025197, 2016.

NIFC: NIFC 2019 Statistics and Summary, [online] Available from: https://www.predictiveservices.nifc.gov/intelligence/2019_statssumm/2019Stats&Summ.html (Accessed 8 January 2021), 2019.

O'Dell, K., Ford, B., Fischer, E. V. and Pierce, J. R.: Contribution of Wildland-Fire Smoke to US PM 2.5 and Its Influence on Recent Trends, Environ. Sci. Technol., doi:10.1021/acs.est.8b05430, 2019.

Odum Jay, R., Hoffmann, T., Bowman, F., Collins, D., Flagan Richard, C. and Seinfeld John, H.: Gas particle partitioning and secondary organic aerosol yields, Environ. Sci. Technol., 30(8), 2580–2585, doi:10.1021/es950943+, 1996.

Olariu, R., Klotz, B., Barnes, I., Becker, K. and Mocanu, R.: FT – IR study of the ring-retaining products from the reaction of OH radicals with phenol , o - , m - , and p -cresol, Atmos. Environ., 36(22), 3685–3697, doi:https://doi.org/10.1016/S1352-2310(02)00202-9, 2002.

Olariu, R. I., Bejan, I., Barnes, I., Klotz, B., Becker, K. H. and Wirtz, K.: Rate coefficients for the gas-phase reaction of NO3 radicals with selected dihydroxybenzenes, Int. J. Chem. Kinet., 36(11), 577–583, doi:10.1002/kin.20029, 2004.

Olariu, R. I., Barnes, I., Bejan, I., Arsene, C., Vione, D., Klotz, B. and Becker, K. H.: FT-IR Product Study of the Reactions of NO3 Radicals With ortho-, meta-, and para-Cresol, Environ. Sci. Technol., 47(14), 7729–7738, doi:10.1021/es401096w, 2013.

Ortega, A. M., Day, D. A., Cubison, M. J., Brune, W. H., Bon, D., De Gouw, J. A. and

Jimenez, J. L.: Secondary organic aerosol formation and primary organic aerosol oxidation from biomass-burning smoke in a flow reactor during FLAME-3, Atmos. Chem. Phys., 13(22), 11551–11571, doi:10.5194/acp-13-11551-2013, 2013.

Osthoff, H. D., Sommariva, R., Baynard, T., Pettersson, A., Williams, E. J., Lerner, B. M., Roberts, J. M., Stark, H., Goldan, P. D., Kuster, W. C., Bates, T. S., Coffman, D., Ravishankara, A. R. and Brown, S. S.: Observation of daytime N2O5 in the marine boundary layer during New England Air Quality Study - Intercontinental Transport and Chemical Transformation 2004, J. Geophys. Res. Atmos., 111(23), doi:10.1029/2006JD007593, 2006.

Osthoff, H. D., Roberts, J. M., Ravishankara, A. R., Williams, E. J., Lerner, B. M., Sommariva, R., Bates, T. S., Coffman, D., Quinn, P. K., Dibb, J. E., Stark, H., Burkholder, J. B., Talukdar, R. K., Meagher, J., Fehsenfeld, F. C. and Brown, S. S.: High levels of nitryl chloride in the polluted subtropical marine boundary layer, Nat. Geosci., 1(5), 324–328, doi:10.1038/ngeo177, 2008.

Pagonis, D., Campuzano-Jost, P., Guo, H., Day, D., Schueneman, M., Brown, W., Nault, B., Stark, H., Siemens, K., Laskin, A., Piel, F., Tomsche, L., Wisthaler, A., Coggon, M., Gkatzelis, G., Halliday, H., Krechmer, J., Moore, R., Thomson, D., Warneke, C., Wiggins, E. and Jimenez, J.: Airborne Extractive Electrospray Mass Spectrometry Measurements of the Chemical Composition of Organic Aerosol, Atmos. Meas. Tech. Discuss., (October), 1–23, doi:10.5194/amt-2020-395, 2020.

Palm, B. B., Campuzano-Jost, P., Day, D. A., Ortega, A. M., Fry, J. L., Brown, S. S., Zarzana, K. J., Dube, W., Wagner, N. L., Draper, D. C., Kaser, L., Jud, W., Karl, T., Hansel, A., Gutiérrez-Montes, C. and Jimenez, J. L.: Secondary organic aerosol formation from in situ OH,

O3, and NO3 oxidation of ambient forest air in an oxidation flow reactor, Atmos. Chem. Phys., 17(8), 5331–5354, doi:10.5194/acp-17-5331-2017, 2017.

Palm, B. B., Peng, Q., Fredrickson, C. D., Lee, B. H., Garofalo, L. A., Pothier, M. A., Kreidenweis, S. M., Farmer, D. K., Pokhrel, R. P., Shen, Y., Murphy, S. M., Permar, W., Hu, L., Campos, T. L., Hall, S. R., Ullmann, K., Zhang, X., Flocke, F., Fischer, E. V. and Thornton, J. A.: Quantification of organic aerosol and brown carbon evolution in fresh wildfire plumes, Proc. Natl. Acad. Sci. U. S. A., 117(47), 29469–29477, doi:10.1073/pnas.2012218117, 2020.

Parks, S. A., Miller, C., Parisien, M. A., Holsinger, L. M., Dobrowski, S. Z. and Abatzoglou, J.: Wildland fire deficit and surplus in the western United States, 1984-2012, Ecosphere, 6(12), 1–13, doi:10.1890/ES15-00294.1, 2015.

Peng, Q., Palm, B. B., Melander, K. E., Lee, B. H., Hall, S. R., Ullmann, K., Campos, T., Weinheimer, A. J., Apel, E. C., Hornbrook, R. S., Hills, A. J., Montzka, D. D., Flocke, F., Hu, L., Permar, W., Wielgasz, C., Lindaas, J., Pollack, I. B., Fischer, E. V., Bertram, T. H. and Thornton, J. A.: HONO Emissions from Western U.S. Wildfires Provide Dominant Radical Source in Fresh Wildfire Smoke, Environ. Sci. Technol., 54(10), 5954–5963, doi:10.1021/acs.est.0c00126, 2020.

Phuleria, H. C., Fine, P. M., Zhu, Y. and Sioutas, C.: Air quality impacts of the October 2003 Southern California wildfires, J. Geophys. Res. Atmos., 110(7), 1–11, doi:10.1029/2004JD004626, 2005.

Piel, F., Müller, M., Mikoviny, T., Pusede, S. E. and Wisthaler, A.: Airborne measurements of particulate organic matter by proton-transfer-reaction mass spectrometry (PTR-MS): A pilot study, Atmos. Meas. Tech., 12(11), 5947–5958, doi:10.5194/amt-12-5947-2019, 2019.

Piel, F., Müller, M., Winkler, K., Skytte Af Sätra, J. and Wisthaler, A.: Introducing the

extended volatility range proton-Transfer-reaction mass spectrometer (EVR PTR-MS), Atmos. Meas. Tech., 14(2), 1355–1363, doi:10.5194/amt-14-1355-2021, 2021.

Pollack, I. B., Lerner, B. M. and Ryerson, T. B.: Evaluation of ultraviolet light-emitting diodes for detection of atmospheric NO2 by photolysis - Chemiluminescence, J. Atmos. Chem., 65(2–3), 111–125, doi:10.1007/s10874-011-9184-3, 2010.

Pope, C. A. and Dockery, D. W.: Health effects of fine particulate air pollution: Lines that connect, J. Air Waste Manag. Assoc., 56(6), 709–742, doi:10.1080/10473289.2006.10464485, 2006.

Ridley, B. A., Grahek, F. E. and Walega, J. G.: A Small High-Sensitivity, Medium-Response Ozone Detector Suitable for Measurements from Light Aircraft, J. Atmos. Ocean. Technol., 9(2), 142–148, doi:10.1175/1520-0426(1992)009<0142:ASHSMR>2.0.CO;2, 1992.

Ro Lee, Y., Ji, Y., Tanner, D. J. and Gregory Huey, L.: A low-activity ion source for measurement of atmospheric gases by chemical ionization mass spectrometry, Atmos. Meas. Tech., 13(5), 2473–2480, doi:10.5194/amt-13-2473-2020, 2020.

Roberts, J. M., Jobson, B. T., Kuster, W., Goldan, P., Murphy, P., Williams, E., Frost, G., Riemer, D., Apel, E., Stroud, C. and others: An examination of the chemistry of peroxycarboxylic nitric anhydrides and related volatile organic compounds during Texas Air Quality Study 2000 using ground-based measurements, J. Geophys. Res., 108(D16), 4495, doi:10.1029/2003JD003383, 2003.

Roberts, J. M., Stockwell, C. E., Yokelson, R. J., De Gouw, J., Liu, Y., Selimovic, V., Koss, A. R., Sekimoto, K., Coggon, M. M., Yuan, B., Zarzana, K. J., Brown, S. S., Santin, C., Doerr, S. H. and Warneke, C.: The nitrogen budget of laboratory-simulated western US wildfires

during the FIREX 2016 Fire Lab study, Atmos. Chem. Phys., 20(14), 8807–8826, doi:10.5194/acp-20-8807-2020, 2020.

Roberts, M., Jobson, T., Fehsenfeld, C., Min, M. and N, A. M.: Observations of APAN during TexAQS 2000 s , Eric Atlas i ’ i i :, Geophys. Res. Lett., 28(22), 4195–4198, 2001.

Rollins, A. W., Rickly, P. S., Gao, R. S., Ryerson, T. B., Brown, S. S., Peischl, J. and Bourgeois, I.: Single-photon laser-induced fluorescence detection of nitric oxide at sub-parts-per-trillion mixing ratios, Atmos. Meas. Tech., 13(5), 2425–2439, doi:10.5194/amt-13-2425-2020, 2020.

Rotstayn, L. D. and Penner, J. E.: Indirect aerosol forcing, quasi forcing, and climate response, J. Clim., 14(13), 2960–2975, doi:10.1175/1520-0442(2001)014<2960:IAFQFA>2.0.CO;2, 2001.

Ryerson, T. B., Huey, L. G., Knapp, K., Nueman, J. A., Parrish, D. D., Sueper, D. T. and Fehsenfeld, F. C.: Design and initial characterization of an inlet for gas-phase NOy measurements from aircraf, J. Geophys. Res. Atmos., 104(D5), 5483–5492, 1999.

Sachse, G. W., Collins Jr, J. E., Hill, G. F., Wade, L. O., Lewis, B. G. and Ritter, J. A.: Airborne tunable diode laser sensor for high-precision concentration and flux measurements of carbon monoxide and methane, Proc. SPIE, 1433, 157–166, doi:10.1117/12.46162, 1991.

Sangwan, M. and Zhu, L.: Absorption cross sections of 2-Nitrophenol in the 295−400 nm region and photolysis of 2-Nitrophenol at 308 and 351 nm, J. Phys. Chem. A, 120(50), 9958–9967, doi:10.1021/acs.jpca.6b08961, 2016.

Sangwan, M. and Zhu, L.: Role of Methyl-2-nitrophenol Photolysis as a Potential Source of OH Radicals in the Polluted Atmosphere: Implications from Laboratory Investigation, J. Phys.

Chem. A, 122(7), 1861–1872, doi:10.1021/acs.jpca.7b11235, 2018.

Saunders, S. M., Pascoe, S., Johnson, A. P., Pilling, M. J. and Jenkin, M. E.: Development and preliminary test results of an expert system for the automatic generation of tropospheric VOC degradation mechanisms, Atmos. Environ., 37(13), 1723–1735, doi:10.1016/S1352-2310(03)00072-4, 2003.

Schwantes, R. H., Schilling, K. A., McVay, R. C., Lignell, H., Coggon, M. M., Zhang, X., Wennberg, P. O. and Seinfeld, J. H.: Formation of highly oxygenated low-volatility products from cresol oxidation, Atmos. Chem. Phys., 17(5), 3453–3474, doi:10.5194/acp-17-3453-2017, 2017.

Schwarz, J. P., Gao, R. S., Fahey, D. W., Thomson, D. S., Watts, L. A., Wilson, J. C., Reeves, J. M., Darbeheshti, M., Baumgardner, D. G., Kok, G. L., Chung, S. H., Schulz, M., Hendricks, J., Lauer, A., Kärcher, B., Slowik, J. G., Rosenlof, K. H., Thompson, T. L., Langford, A. O., Loewenstein, M. and Aikin, K. C.: Single-particle measurements of midlatitude black carbon and light-scattering aerosols from the boundary layer to the lower stratosphere, J. Geophys. Res. Atmos., 111(16), 1–15, doi:10.1029/2006JD007076, 2006.

Sekimoto, K., Koss, A. R., Gilman, J. B., Selimovic, V., Coggon, M. M., Zarzana, K. J., Yuan, B., Lerner, B. M., Brown, S. S., Warneke, C., Yokelson, R. J., Roberts, J. M. and de Gouw, J.: High- and low-temperature pyrolysis profiles describe volatile organic compound emissions from western US wildfire fuels, Atmos. Chem. Phys., 18, 9263–9281, doi:10.5194/acp-18-9263-2018, 2018.

Selimovic, V., Yokelson, R. J., Warneke, C., Roberts, J. M., de Gouw, J. A. and Griffith, D. W. T.: Aerosol optical properties and trace gas emissions from laboratory-simulated western US wildfires during FIREX, Atmos. Chem. Phys., 18, 2929–2948, doi:10.5194/acp-18-2929-2018,

2017.

Selimovic, V., Yokelson, R. J., McMeeking, G. R. and Coefield, S.: Aerosol Mass and Optical Properties, Smoke Influence on O3, and High NO3 Production Rates in a Western U.S. City Impacted by Wildfires, J. Geophys. Res. Atmos., 125(16), 1–22, doi:10.1029/2020JD032791, 2020.

Shetter, R. E. and Müller, M.: Photolysis frequency measurements using actinic flux spectroradiometry during the PEM-Tropics mission: Instrumentation description and some results, J. Geophys. Res. Atmos., 104(D5), 5647–5661, doi:10.1029/98JD01381, 1999.

Silvern, R. F., Jacob, D. J., Mickley, L. J., Sulprizio, M. P., Travis, K. R., Marais, E. A., Cohen, R. C., Laughner, J. L., Choi, S., Joiner, J. and Lamsal, L. N.: Using satellite observations of tropospheric NO2 columns to infer long-term trends in US NOx emissions: The importance of accounting for the free tropospheric NO2 background, Atmos. Chem. Phys., 19(13), 8863–8878, doi:10.5194/acp-19-8863-2019, 2019.

SMPS: Scanning Mobility Particle Sizer Spectrometer 3936 -, [online] Available from: https://tsi.com/discontinued-products/scanning-mobility-particle-sizer-spectrometer-3936/ (Accessed 18 March 2021), n.d.

Sparks, T. L., Ebben, C. J., Wooldridge, P. J., Lopez-Hilfiker, F. D., Lee, B. H., Thornton, J. A., McDuffie, E. E., Fibiger, D. L., Brown, S. S., Montzka, D. D., Weinheimer, A. J., Schroder, J. C., Campuzano-Jost, P., Jimenez, J. L. and Cohen, R. C.: Comparison of Airborne Reactive Nitrogen Measurements During WINTER, J. Geophys. Res. Atmos., 124(19), 10483–10502, doi:10.1029/2019JD030700, 2019.

Stedman, D. H., Daby, E. E., Stuhl, F. and Niki, H.: Analysis of ozone and nitric oxide by

a chemiluminescent method in laboratory and atmospheric studies of photochemical smog, J. Air Pollut. Control Assoc., 22(4), 260–263, doi:10.1080/00022470.1972.10469635, 1972.

Stockwell, C. E., Yokelson, R. J., Kreidenweis, S. M., Robinson, A. L., Demott, P. J., Sullivan, R. C., Reardon, J., Ryan, K. C., Griffith, D. W. T. and Stevens, L.: Trace gas emissions from combustion of peat, crop residue, domestic biofuels, grasses, and other fuels: Configuration and Fourier transform infrared (FTIR) component of the fourth Fire Lab at Missoula Experiment (FLAME-4), Atmos. Chem. Phys., 14(18), 9727–9754, doi:10.5194/acp-14-9727-2014, 2014.

Stockwell, C. E., Veres, P. R., Williams, J. and Yokelson, R. J.: Characterization of biomass burning emissions from cooking fires, peat, crop residue, and other fuels with high-resolution proton-transfer-reaction time-of-flight mass spectrometry, Atmos. Chem. Phys., 15(2), 845–865, doi:10.5194/acp-15-845-2015, 2015.

Tanimoto, H.: A new peroxycarboxylic nitric anhydride identified in the atmosphere: CH2=CHC(O)OONO2 (APAN), Geophys. Res. Lett., 28(14), 2831–2834, 2001.

Tanimoto, H., Furutani, H., Kato, S., Matsumoto, J., Makide, Y. and Akimoto, H.: Seasonal cycles of ozone and oxidized nitrogen species in northeast Asia 1. Impact of regional climatology and photochemistry observed during RISOTTO 1999-2000, J. Geophys. Res. Atmos., 107(24), doi:10.1029/2001JD001496, 2002.

Tapia, A., Villanueva, F., Salgado, M. S., Cabañas, B., Martínez, E. and Martín, P.: Atmospheric degradation of 3-methylfuran: Kinetic and products study, Atmos. Chem. Phys., 11(7), 3227–3241, doi:10.5194/acp-11-3227-2011, 2011.

Thornton, J. A., Kercher, J. P., Riedel, T. P., Wagner, N. L., Cozic, J., Holloway, J. S., Dubé, W. P., Wolfe, G. M., Quinn, P. K., Middlebrook, A. M., Alexander, B. and Brown, S. S.: A

large atomic chlorine source inferred from mid-continental reactive nitrogen chemistry., Nature, 464(7286), 271–4, doi:10.1038/nature08905, 2010.

Tie, X., Madronich, S., Walters, S., Zhang, R., Rasch, P. and Collins, W.: Effect of clouds on photolysis and oxidants in the troposphere, J. Geophys. Res., 108(D20), 4642, doi:10.1029/2003JD003659, 2003.

Trentmann, J., Andreae, M. O., Graf, H. F., Hobbs, P. V., Ottmar, R. D. and Trautmann, T.: Simulation of a biomass-burning plume: Comparison of model results with observations, J. Geophys. Res. Atmos., 107(1–2), 1–15, doi:10.1029/2001jd000410, 2002.

Trentmann, J., Andreae, M. O. and Graf, H. F.: Chemical processes in a young biomass-burning plume, J. Geophys. Res. Atmos., 108(22), doi:10.1029/2003jd003732, 2003.

Trentmann, J., Yokelson, R. J., Hobbs, P. V, Winterrath, T., Christian, T. J., Andreae, M. O. and Mason, S. A.: An analysis of the chemical processes in the smoke plume from a savanna fire, J. Geophys. Res. Atmos., 110(D12), n/a-n/a, doi:10.1029/2004JD005628, 2005.

Turner, D. B.: Workbook of Atmospheric Dispersion Estimates : An Introduction to Dispersion Modeling, Second Edition, 2nd ed., Public Health Services, Cincinnati., 1970.

Veres, P., Roberts, J. M., Burling, I. R., Warneke, C., de Gouw, J. and Yokelson, R. J.: Measurements of gas-phase inorganic and organic acids from biomass fires by negative-ion proton-transfer chemical-ionization mass spectrometry, J. Geophys. Res. Atmos., 115(D23), n/a-n/a, doi:10.1029/2010JD014033, 2010.

Veres, P. R., Andrew Neuman, J., Bertram, T. H., Assaf, E., Wolfe, G. M., Williamson, C. J., Weinzierl, B., Tilmes, S., Thompson, C. R., Thames, A. B., Schroder, J. C., Saiz-Lopez, A., Rollins, A. W., Roberts, J. M., Price, D., Peischl, J., Nault, B. A., Møller, K. H., Miller, D. O.,

Meinardi, S., Li, Q., Lamarque, J. F., Kupc, A., Kjaergaard, H. G., Kinnison, D., Jimenez, J. L., Jernigan, C. M., Hornbrook, R. S., Hills, A., Dollner, M., Day, D. A., Cuevas, C. A., Campuzano-Jost, P., Burkholder, J., Paul Bui, T., Brune, W. H., Brown, S. S., Brock, C. A., Bourgeois, I., Blake, D. R., Apel, E. C. and Ryerson, T. B.: Global airborne sampling reveals a previously unobserved dimethyl sulfide oxidation mechanism in the marine atmosphere, Proc. Natl. Acad. Sci. U. S. A., 117(9), 4505–4510, doi:10.1073/pnas.1919344117, 2020.

Wagner, N. L., Riedel, T. P., Young, C. J., Bahreini, R., Brock, C. A., Dubé, W. P., Kim, S., Middlebrook, A. M., Öztürk, F., Roberts, J. M., Russo, R., Sive, B., Swarthout, R., Thornton, J. A., VandenBoer, T. C., Zhou, Y. and Brown, S. S.: N2O5 uptake coefficients and nocturnal NO2 removal rates determined from ambient wintertime measurements, J. Geophys. Res. Atmos., 118(16), 9331–9350, doi:10.1002/jgrd.50653, 2013.

Wang, S. and Li, H.: NO3·-Initiated Gas-Phase Formation of Nitrated Phenolic Compounds in Polluted Atmosphere, Environ. Sci. Technol., (3), doi:10.1021/acs.est.0c08041, 2021.

Wang, S., Coggon, M. M., Gkatzelis, G. I., Warneke, C., Bourgeois, I., Ryerson, T. B., Peischl, J., Veres, P. R., Neuman, J. A., Hair, J., Shingler, T., Fenn, M. A., Diskin, G. S., Huey, L. G., Lee, Y. R., Apel, E. C., Hornbrook, R. S., Hills, A. J., Hall, S. R., Ullmann, K., Bela, M. M., Trainer, M. K., Kumar, R., Orlando, J., Flocke, F. and Emmons, L. K.: Chemical Tomography in a Fresh Wildland Fire Plume: a Large Eddy Simulation (LES) Study, , doi:10.1002/ESSOAR.10507041.1, 2021.

Wang, Y. J., Hu, M., Lin, P., Guo, Q. F., Wu, Z. J., Li, M. R., Zeng, L. M., Song, Y., Zeng, L. W., Wu, Y. S., Guo, S., Huang, X. F. and He, L. Y.: Molecular Characterization of Nitrogen-

Containing Organic Compounds in Humic-like Substances Emitted from Straw Residue Burning, Environ. Sci. Technol., 51(11), 5951–5961, doi:10.1021/acs.est7b00248, 2017.

Warneke, C., De Gouw, J. A., Holloway, J. S., Peischl, J., Ryerson, T. B., Atlas, E., Blake, D., Trainer, M. and Parrish, D. D.: Multiyear trends in volatile organic compounds in Los Angeles, California: Five decades of decreasing emissions, J. Geophys. Res. Atmos., 117(17), 1–10, doi:10.1029/2012JD017899, 2012.

Warneke, C., Trainer, M., De Gouw, J. A., Parrish, D. D., Fahey, D. W., Ravishankara, A. R., Middlebrook, A. M., Brock, C. A., Roberts, J. M., Brown, S. S., Neuman, J. A., Lerner, B. M., Lack, D., Law, D., Hübler, G., Pollack, I., Sjostedt, S., Ryerson, T. B., Gilman, J. B., Liao, J., Holloway, J., Peischl, J., Nowak, J. B., Aikin, K. C., Min, K. E., Washenfelder, R. A., Graus, M. G., Richardson, M., Markovic, M. Z., Wagner, N. L., Welti, A., Veres, P. R., Edwards, P., Schwarz, J. P., Gordon, T., Dube, W. P., McKeen, S. A., Brioude, J., Ahmadov, R., Bougiatioti, A., Lin, J. J., Nenes, A., Wolfe, G. M., Hanisco, T. F., Lee, B. H., Lopez-Hilfiker, F. D., Thornton, J. A., Keutsch, F. N., Kaiser, J., Mao, J. and Hatch, C. D.: Instrumentation and measurement strategy for the NOAA SENEX aircraft campaign as part of the Southeast Atmosphere Study 2013, Atmos. Meas. Tech., 9(7), 3063–3093, doi:10.5194/amt-9-3063-2016, 2016.

Wayne, R. ., Barnes, I., Biggs, P., Burrows, J. ., Canosa-Mas, C. ., Hjorth, J., Le Bras, G., Moortgat, G. ., Perner, D., Poulet, G., Restelli, G. and Sidebottom, H.: The nitrate radical: Physics, chemistry, and the atmosphere, Atmos. Environ. Part A. Gen. Top., 25(1), 1–203, doi:10.1016/0960-1686(91)90192-A, 1991.

Westerling, A. L., Hidalgo, H. G., Cayan, D. R. and Swetnam, T. W.: Warming and Earlier Spring Increase Western U.S. Forest Wildfire Activity, Science (80-.)., 313(5789), 940–943

[online] Available from: http://www.sciencemag.org/content/313/5789/940.abstract, 2006.

Westerling, A. L. R.: Increasing western US forest wildfire activity: Sensitivity to changes in the timing of spring, Philos. Trans. R. Soc. B Biol. Sci., 371(1696), doi:10.1098/rstb.2015.0178, 2016.

White, W., Anderson, J., Blumenthal, D., Husar, R., Gillani, N., Husar, J. and Wilson, W.: Formation and transport of secondary air pollutants: ozone and aerosols in the St. Louis urban plume, Science (80-.)., 194(4261), 187–189, doi:10.1126/science.959846, 1976.

Wild, R. J., Edwards, P. M., Dube, W. P., Baumann, K., Edgerton, E. S., Quinn, P. K., Roberts, J. M., Rollins, A. W., Veres, P. R., Warneke, C., Williams, E. J., Yuan, B., Brown, S. S., Dubé, W. P., Baumann, K., Edgerton, E. S., Quinn, P. K., Roberts, J. M., Rollins, A. W., Veres, P. R., Warneke, C., Williams, E. J., Yuan, B. and Brown, S. S.: A measurement of total reactive nitrogen, NOy, together with NO2, NO, and O3 via cavity ring-down spectroscopy, Environ. Sci. Technol., 48(16), 9609–9615, doi:10.1021/es501896w, 2014.

Williams, A. P., Abatzoglou, J. T., Gershunov, A., Guzman-Morales, J., Bishop, D. A., Balch, J. K. and Lettenmaier, D. P.: Observed Impacts of Anthropogenic Climate Change on Wildfire in California, Earth's Futur., 7(8), 892–910, doi:10.1029/2019EF001210, 2019.

Wolfe, G. M., Thornton, J. A., McNeill, V. F., Jaffe, D. A., Reidmiller, D., Chand, D., Smith, J., Swartzendruber, P., Flocke, F. and Zheng, W.: Influence of trans-Pacific pollution transport on acyl peroxy nitrate abundances and speciation at Mount Bachelor Observatory during INTEX-B, Atmos. Chem. Phys., 7(20), 5309–5325, doi:10.5194/acp-7-5309-2007, 2007.

Wolfe, G. M., Marvin, M. R., Roberts, S. J., Travis, K. R. and Liao, J.: The framework for 0-D atmospheric modeling (F0AM) v3.1, Geosci. Model Dev., 9(9), 3309–3319,

doi:10.5194/gmd-9-3309-2016, 2016.

Xie, M., Chen, X., Hays, M. D., Lewandowski, M., Offenberg, J., Kleindienst, T. E. and Holder, A. L.: Light Absorption of Secondary Organic Aerosol: Composition and Contribution of Nitroaromatic Compounds, Environ. Sci. Technol., 51(20), 11607–11616, doi:10.1021/acs.est.7b03263, 2017.

Xing, J., Mathur, R., Pleim, J., Hogrefe, C., Gan, C. M., Wong, D. C., Wei, C., Gilliam, R. and Pouliot, G.: Observations and modeling of air quality trends over 1990-2010 across the Northern Hemisphere: China, the United States and Europe, Atmos. Chem. Phys., 15(5), 2723–2747, doi:10.5194/acp-15-2723-2015, 2015.

Yang, B., Zhang, H., Wang, Y., Zhang, P., Shu, J., Sun, W. and Ma, P.: Experimental and theoretical studies on gas-phase reactions of NO3 radicals with three methoxyphenols: Guaiacol, creosol, and syringol, Atmos. Environ., 125(3), 243–251, doi:10.1016/j.atmosenv.2015.11.028, 2016a.

Yang, Y., Shao, M., Wang, X., Nölscher, A. C., Kessel, S., Guenther, A. and Williams, J.: Towards a quantitative understanding of total OH reactivity: A review, Atmos. Environ., 134(2), 147–161, doi:10.1016/j.atmosenv.2016.03.010, 2016b.

Yang, Y., Wang, Y., Zhou, P., Yao, D., Ji, D., Sun, J., Wang, Y., Zhao, S., Huang, W., Yang, S., Chen, D., Gao, W., Liu, Z., Hu, B., Zhang, R., Zeng, L., Ge, M., Petäjä, T., Kerminen, V. M., Kulmala, M. and Wang, Y.: Atmospheric reactivity and oxidation capacity during summer at a suburban site between Beijing and Tianjin, Atmos. Chem. Phys., 20(13), 8181–8200, doi:10.5194/acp-20-8181-2020, 2020.

Yokelson, R. J., Crounse, J. D., DeCarlo, P. F., Karl, T., Urbanski, S., Atlas, E., Campos,

T., Shinozuka, Y., Kapustin, V., Clarke, A. D., Weinheimer, A., Knapp, D. J., Montzka, D. D., Holloway, J., Weibring, P., Flocke, F., Zheng, W., Toohey, D., Wennberg, P. O., Wiedinmyer, C., Mauldin, L., Fried, A., Richter, D., Walega, J., Jimenez, J. L., Adachi, K., Buseck, P. R., Hall, S. R. and Shetter, R.: Emissions from biomass burning in the Yucatan, Atmos. Chem. Phys., 9(15), 5785–5812, doi:10.5194/acp-9-5785-2009, 2009.

Yokelson, R. J., Andreae, M. O. and Akagi, S. K.: Pitfalls with the use of enhancement ratios or normalized excess mixing ratios measured in plumes to characterize pollution sources and aging, Atmos. Meas. Tech., 6(8), 2155–2158, doi:10.5194/amt-6-2155-2013, 2013.

Yuan, Y., Zhao, X., Wang, S. and Wang, L.: Atmospheric Oxidation of Furan and Methyl-Substituted Furans Initiated by Hydroxyl Radicals, J. Phys. Chem. A, 121(48), 9306–9319, doi:10.1021/acs.jpca.7b09741, 2017.

Zarzana, K. J., Min, K. E., Washenfelder, R. A., Kaiser, J., Krawiec-Thayer, M., Peischl, J., Neuman, J. A., Nowak, J. B., Wagner, N. L., Dubè, W. P., Clair, J. M. S., Wolfe, G. M., Hanisco, T. F., Keutsch, F. N., Ryerson, T. B. and Brown, S. S.: Emissions of Glyoxal and Other Carbonyl Compounds from Agricultural Biomass Burning Plumes Sampled by Aircraft, Environ. Sci. Technol., 51(20), 11761–11770, doi:10.1021/acs.est.7b03517, 2017.

El Zein, A., Coeur, C., Obeid, E., Lauraguais, A. and Fagniez, T.: Reaction Kinetics of Catechol (1,2-Benzenediol) and Guaiacol (2-Methoxyphenol) with Ozone, J. Phys. Chem. A, 119(26), 6759–6765, doi:10.1021/acs.jpca.5b00174, 2015.

Zheng, W., Flocke, F. M., Tyndall, G. S., Swanson, A., Orlando, J. J., Roberts, J. M., Huey, L. G. and Tanner, D. J.: Characterization of a thermal decomposition chemical ionization mass spectrometer for the measurement of peroxy acyl nitrates (PANs) in the atmosphere, Atmos.

Chem. Phys., 11(13), 6529–6547, doi:10.5194/acp-11-6529-2011, 2011.

Appendix A

Glossary of Terms

- 0-D: Zero dimensional
- ACES: Airborne Cavity Enhanced Spectrometer
- AMS: Aerosol Mass Spectrometer
- APAN: acryloyl peroxynitrate
- APN: acyl peroxy nitrates
- BB: Biomass Burning
- BC: Black carbon
- BrC: Brown carbon
- CAFS: Charged-coupled device Actinic Flux Spectroradiometer
- CES: Cavity Enhanced Spectrometer
- CIMS: Chemical Ionization Mass Spectrometry
- CL: Chemiluminescence
- Cow: 204 Cow Fire
- CRDS: Cavity Ring-down Spectrometer
- EPA: Environmental Protection Agency
- ER: Emission Ratio
- ESZA: Emitted Solar Zenith Angle
- F0AM: Framework for 0-D Atmospheric Modeling
- FIREX-AQ: Fire Influence on Regional and Global Environments Experiment and Air Quality – NASA and NOAA multi-platform campaign.
- FIREXLab: Fire Influence on Regional and Global Environments Experiment – NOAA laboratory investigation
- FLAME-4: Fire Lab at Missoula Experiment
- GCxGC: Two-dimensional gas chromatography
- GOMECH: Gaussian Observational Model for Edge to Center Heterogeneity
- HO_x: OH + HO_2
- HRRR: High-Resolution Rapid Refresh
- HYSPLIT: Hybrid Single-Particle Lagrangian Integrated Trajectory
- LAS: Laser Aerosol Spectrometer
- LES: Large Eddy Simulation
- MACR: methacrolein
- MCM: Master Chemical Mechanism
- MDT: Mountain Daylight Time
- MEK: Methyl ethyl ketone
- MS: Mass Spectrometer
- MST: Mountain Standard Time
- MVK: Methyl vinyl ketone
- NAM CONUS: North American Mesoscale Continental United States
- NASA: National Aeronautics and Space Administration
- NCAR: National Center for Atmospheric Research

- NEMR: Normalized Excess Mixing Ratio
- NIFC: National Interagency Fire Center
- NOAA: National Oceanic and Atmosphere Administration
- NO_x: NO + NO_2, nitrogen oxides
- O_x: NO_2 + O_3
- P(NO_3): NO_3 radical production rate
- PAN: Peroxy Acyl Nitrate
- pCl: particle chloride
- PDT Pacific Daylight Time
- PM: Particulate Matter
- ppbv: parts per billion by volume
- ppmv: parts per million by volume
- ppqv: parts per quadrillion by volume
- pptv: parts per trillion by volume
- PST: Pacific Standard Time
- PTR: Proton Transfer Reaction
- SAR: Structure Activity Relationship
- SENEX: Southeast Nexus
- SMPS: Scanning mobility particle sizer
- SP2: single particle soot photometer
- SZA: Solar Zenith Angle
- ToF: Time of Flight
- TUV: Tropospheric Ultraviolet and Visible radiation model
- UHSAS: Ultra-high sensitivity aerosol spectrometer
- UTC: Coordinated Universal Time
- VOC: Volatile Organic Compound
- WF1/WF2: First and second pass of the Williams Flats Fire, respectively.

Appendix B

Additional Information for Chapter 4: Nighttime and Daytime Dark Oxidation Chemistry in Wildfire Plumes: An Observation and Model Analysis of FIREX-AQ Aircraft Data

B.1 Observation and Model Comparison

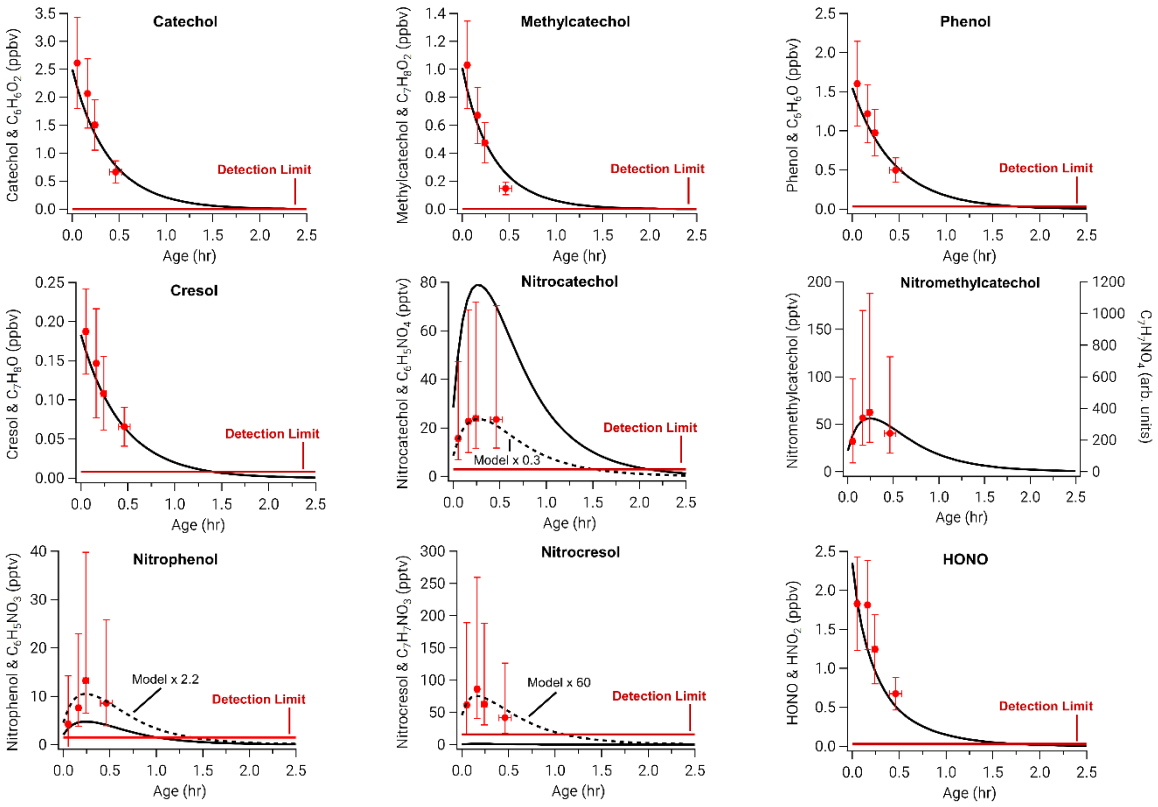

Figure B.1: Model outputs (black line) and observations (red circles) of the Castle plume where model compounds are indicated by the name and observations by chemical formula. Observations are made by the University of Washington I^- HR ToF CIMS. Detection limits for calibrated compounds are shown as horizontal red lines. For compounds without calibrations we report arbitrary units on the right axis for the purpose of comparing time evolution.

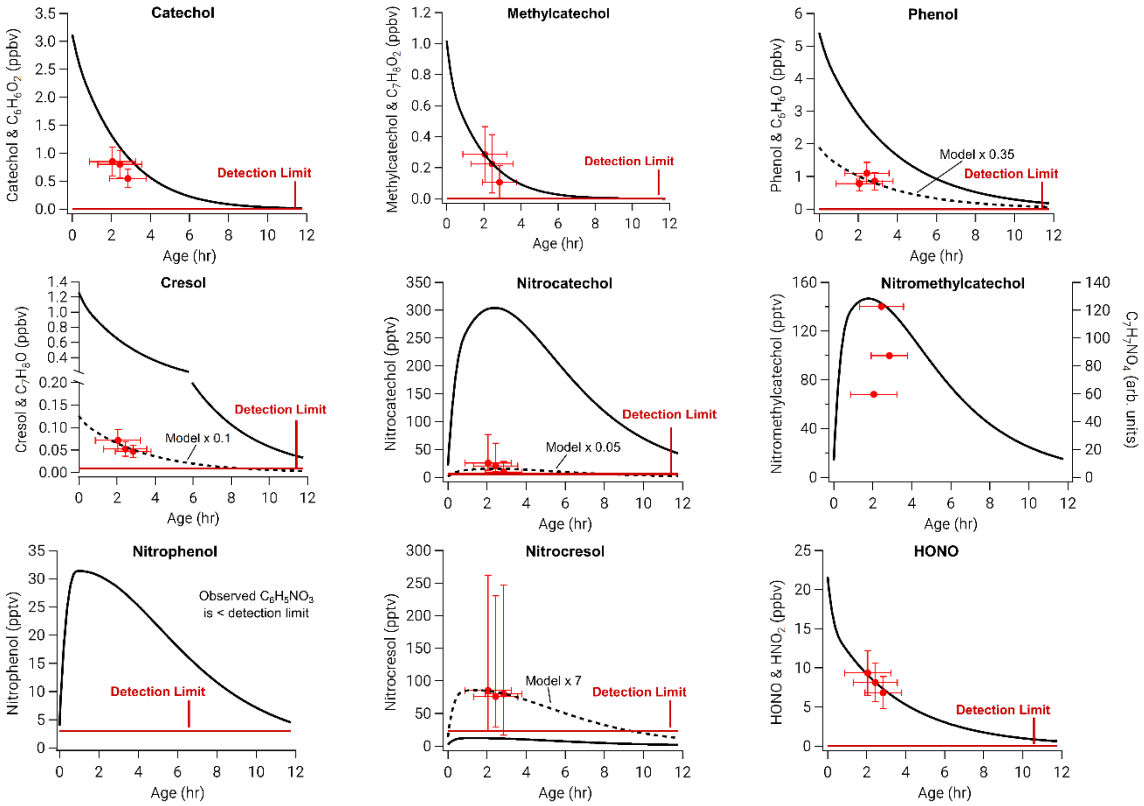

Figure B.2: Similar to Figure B.1, but for the Cow plume.

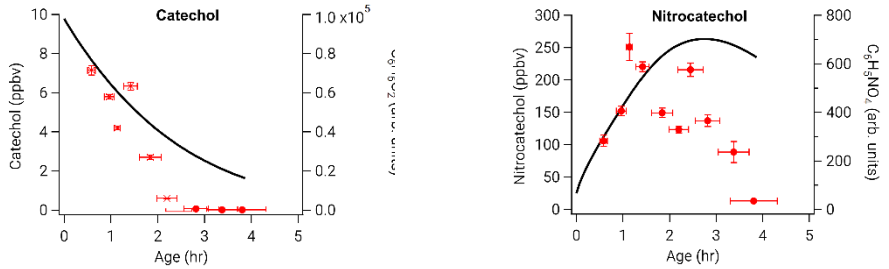

Figure B.3: Model outputs (black line) and observations (red circles) of the WF1 plume where model compounds are indicated by the name and observations by chemical formula. Observations are made by the NOAA I^- CIMS. We report arbitrary units on the right axis for the purpose of comparing time evolution.

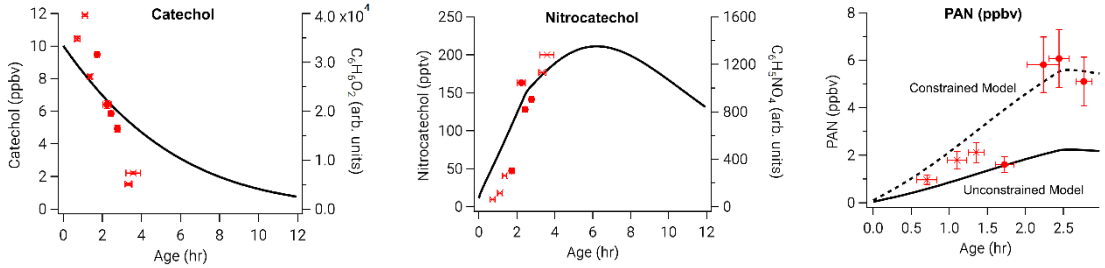

Figure B.4: Model outputs (black line) and observations (red circles) of the WF2 plume where model compounds are indicated by the name and observations by chemical formula. Observations are made by the NOAA I^- CIMS for $C_6H_6O_2$ and $C_6H_5NO_4$ and by the GT CIMS. For uncalibrated compounds, we report arbitrary units on the right axis for the purpose of comparing time evolution.

B.2 Oxidation Rate and Competition of Furans/Furfurals and Alkenes/Terpenes

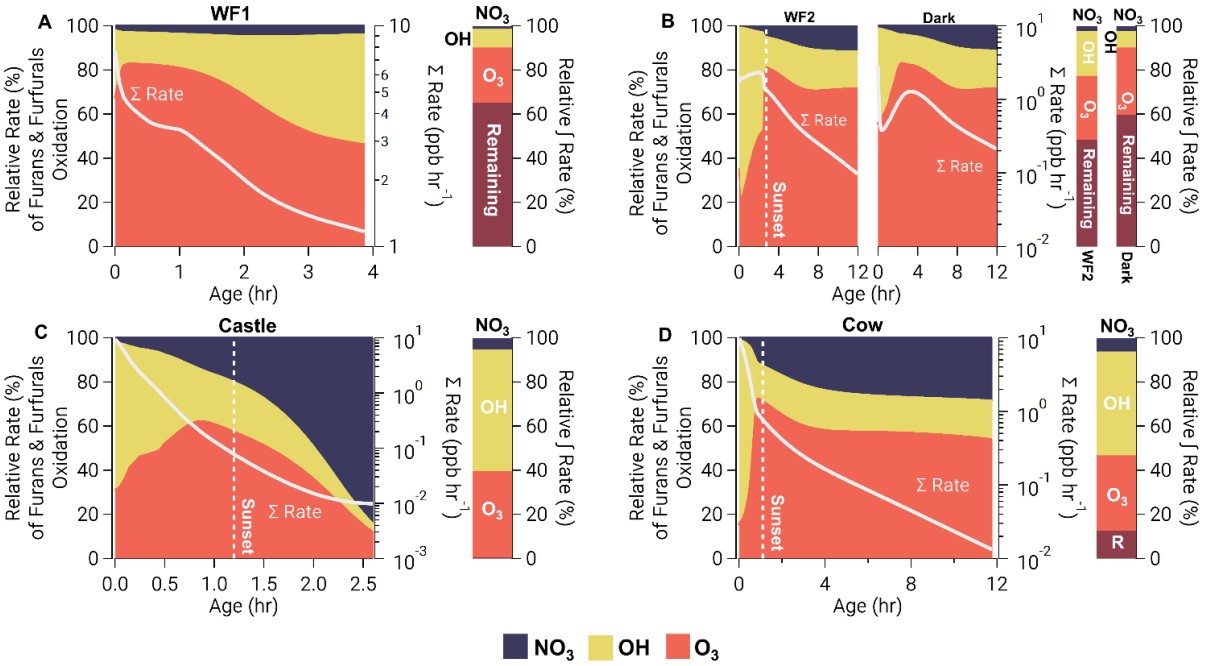

Figure B.5: Similar to Figure 4.10, but for furans and furfurals.

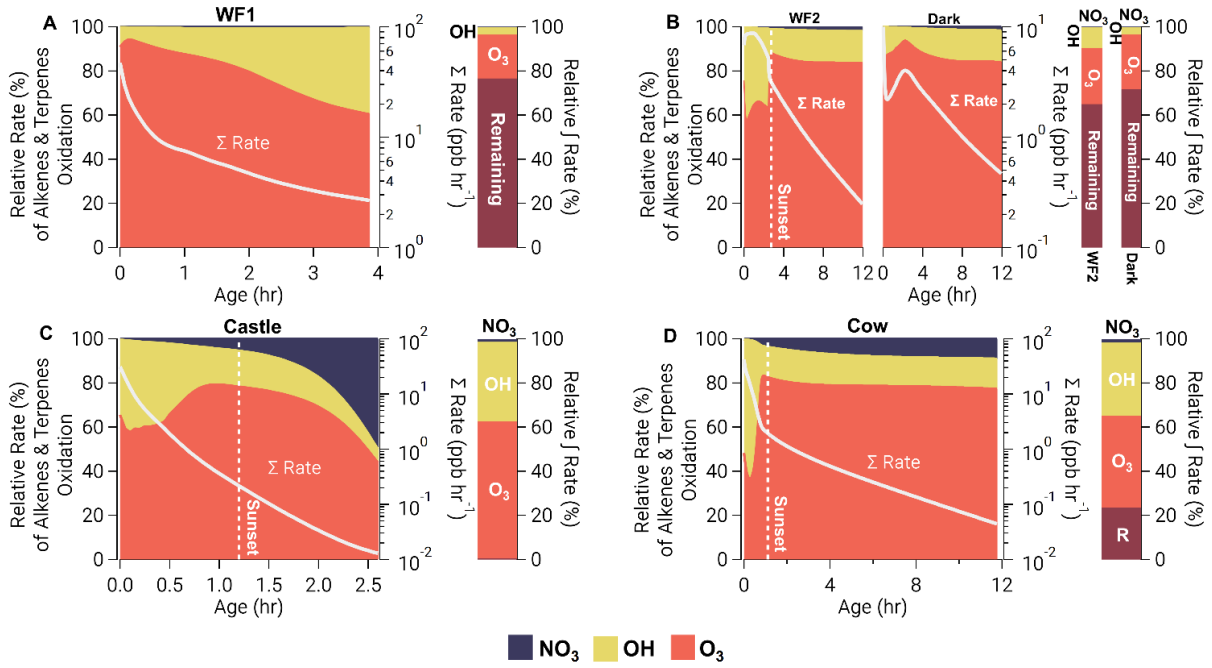

Figure B.6: Similar to Figure 4.10, but for alkenes.

B.3 Code for Phenolic Mechanism

Note: reactions in red are already in the MCM and will need to be replaced when used in conjunction with an MCM mechanism.

Catechols

% 1.0D-10*0.3 : CATECHOL + OH = CATEC1O ;
% 1.0D-10*0.67 : CATECHOL + OH = H3BENZENE + HO2 ;
% 1.0D-10*0.03 : CATECHOL + OH = HPBZQONE + HO2;
% 3.00D-13 : HPBZQONE + NO3 = NBZQO2 ;
% 4.6D-12 : HPBZQONE + OH = PBZQO2 ;
% 1.0D-10*0.3 : H3BENZENE + OH = H3BENZENE1O ;
% 1.0D-10*0.67 : H3BENZENE + OH = H4BENZENE + HO2;
% 1.0D-10*0.03 : H3BENZENE + OH = H2PBZQONE + HO2;
% 3.00D-13 : H2PBZQONE + NO3 = NBZQO2 ;
% 4.6D-12 : H2PBZQONE + OH = PBZQO2 ;
% 2.08D-12 : H3BENZENE1O + NO2 = NH3BENZENE ;
% 2.86D-13 : H3BENZENE1O + O3 = H3BENZENE1O2 ;
% KRO2HO2*0.770 : H3BENZENE1O2 + HO2 = HCATEC1OOH ;
% KRO2NO : H3BENZENE1O2 + NO = H3BENZENE1O + NO2 ;
% KRO2NO3 : H3BENZENE1O2 + NO3 = H3BENZENE1O + NO2 ;
% 8.80D-13*RO2 : H3BENZENE1O2 = H3BENZENE1O ;
% 9.9D-11*0.91 : CATECHOL + NO3 = CATEC1O + HNO3 ;
% 9.9D-11*0.09 : CATECHOL + NO3 = HPBZQONE + HO2 + HNO3 ;
% 9.9D-11*0.91 : H3BENZENE + NO3 = H3BENZENE1O + HNO3 ;

% 9.9D-11*0.09 : H3BENZENE + NO3 = H2PBZQONE + HO2 + HNO3 ;

Methylcatechols

% 2.0D-10*0.3 : MCATECHOL + OH = MCATEC1O ;
% 2.0D-10*0.64 : MCATECHOL + OH = H3TOLUENE + HO2;
% 2.0D-10*0.06 : MCATECHOL + OH = HPTLQONE + HO2;
% 1.00D-12 : HPTLQONE + NO3 = NPTLQO2 ;
% 2.3D-11 : HPTLQONE + OH = PTLQO2 ;
% 2.0D-10*0.3 : H3TOLUENE + OH = H3TOLUENE1O ;
% 2.0D-10*0.64 : H3TOLUENE + OH = H4TOLUENE + HO2;
% 2.0D-10*0.06 : H3TOLUENE + OH = H2PTLQONE + HO2;
% 1.00D-12 : H2PTLQONE + NO3 = NPTLQO2 ;
% 2.3D-11 : H2PTLQONE + OH = PTLQO2 ;
% 2.08D-12 : H3TOLUENE1O + NO2 = NH3TOLUENE ;
% 2.86D-13 : H3TOLUENE1O + O3 = H3TOLUENE1O2 ;
% KRO2HO2*0.820 : H3TOLUENE1O2 + HO2 = HMCATEC1OOH ;
% KRO2NO : H3TOLUENE1O2 + NO = H3TOLUENE1O + NO2 ;
% KRO2NO3 : H3TOLUENE1O2 + NO3 = H3TOLUENE1O + NO2 ;
% 8.80D-13*RO2 : H3TOLUENE1O2 = H3TOLUENE1O ;
% 1.7D-10*0.91 : MCATECHOL + NO3 = MCATEC1O + HNO3 ;
% 1.7D-10*0.09 : MCATECHOL + NO3 = HPTLQONE + HO2 + HNO3 ;
% 1.7D-10*0.91 : H3TOLUENE + NO3 = H3TOLUENE1O + HNO3 ;
% 1.7D-10*0.09 : H3TOLUENE + NO3 = H2PTLQONE + HO2 + HNO3 ;

Dimethylcatechols

% 2.05D-10*0.3 : OXYCATECH + OH = OXCATEC1O ;
% 2.05D-10*0.64 : OXYCATECH + OH = H3OXYLENE + HO2;
% 2.05D-10*0.06 : OXYCATECH + OH = HOXYQONE + HO2;
% 1.00D-12 : HOXYQONE + NO3 = NOXYQO2 ;
% 2.35D-10 : HOXYQONE + OH = OXYQO2 ;
% 2.05D-10*0.3 : H3OXYLENE + OH = H3OXYLENE1O ;
% 2.05D-10*0.64 : H3OXYLENE + OH = H4OXYLENE + HO2;
% 2.05D-10*0.06 : H3OXYLENE + OH = H2OXYQONE + HO2;
% 1.00D-12 : H2OXYQONE + NO3 = NOXYQO2 ;
% 2.35D-10 : H2OXYQONE + OH = OXYQO2 ;
% 2.08D-12 : H3OXYLENE1O + NO2 = NH3OXYLENE ;
% 2.86D-13 : H3OXYLENE1O + O3 = H3OXYLENE1O2 ;
% KRO2HO2*0.859 : H3OXYLENE1O2 + HO2 = HOCATEC1OOH ;
% KRO2NO : H3OXYLENE1O2 + NO = H3OXYLENE1O + NO2 ;
% KRO2NO3 : H3OXYLENE1O2 + NO3 = H3OXYLENE1O + NO2 ;
% 8.80D-13*RO2 : H3OXYLENE1O2 = H3OXYLENE1O ;
% 2.01D-10*0.91 : OXYCATECH + NO3 = OXCATEC1O + HNO3 ;
% 2.01D-10*0.09 : OXYCATECH + NO3 = HOXYQONE + HO2 + HNO3 ;
% 2.01D-10*0.91 : H3OXYLENE + NO3 = H3OXYLENE1O + HNO3 ;
% 2.01D-10*0.09 : H3OXYLENE + NO3 = H2OXYQONE + HO2 + HNO3 ;

% 2.05D-10*0.3 : PXYCATECH + OH = PXCATEC1O ;
% 2.05D-10*0.64 : PXYCATECH + OH = H3PXYLENE + HO2;
% 2.05D-10*0.06 : PXYCATECH + OH = HPXYQONE + HO2;
% 1.00D-12 : HPXYQONE + NO3 = NPXYQO2 ;
% 2.35D-11 : HPXYQONE + OH = PXYQO2 ;
% 2.05D-10*0.3 : H3PXYLENE + OH = H3PXYLENE1O ;
% 2.05D-10*0.64 : H3PXYLENE + OH = H4PXYLENE + HO2;
% 2.05D-10*0.06 : H3PXYLENE + OH = H2PXYQONE + HO2;
% 1.00D-12 : H2PXYQONE + NO3 = NPXYQO2 ;
% 2.35D-11 : H2PXYQONE + OH = PXYQO2 ;
% 2.08D-12 : H3PXYLENE1O + NO2 = NH3PXYLENE ;
% 2.86D-13 : H3PXYLENE1O + O3 = H3PXYLENE1O2 ;
% KRO2HO2*0.859 : H3PXYLENE1O2 + HO2 = HPCATEC1OOH ;
% KRO2NO : H3PXYLENE1O2 + NO = H3PXYLENE1O + NO2 ;
% KRO2NO3 : H3PXYLENE1O2 + NO3 = H3PXYLENE1O + NO2 ;
% 8.80D-13*RO2 : H3PXYLENE1O2 = H3PXYLENE1O ;
% 2.01D-10*0.91 : PXYCATECH + NO3 = PXCATEC1O + HNO3 ;
% 2.01D-10*0.09 : PXYCATECH + NO3 = HPXYQONE + HO2 + HNO3 ;
% 2.01D-10*0.91 : H3PXYLENE + NO3 = H3PXYLENE1O + HNO3 ;
% 2.01D-10*0.09 : H3PXYLENE + NO3 = H2PXYQONE + HO2 + HNO3 ;

% 2.05D-10*0.3 : MXYCATECH + OH = MXCATEC1O ;
% 2.05D-10*0.64 : MXYCATECH + OH = H3MXYLENE + HO2;
% 2.05D-10*0.06 : MXYCATECH + OH = HMXYQONE + HO2;
% 1.00D-12 : HMXYQONE + NO3 = NMXYQO2 ;
% 2.35D-11 : HMXYQONE + OH = MXYQO2 ;
% 2.05D-10*0.3 : H3MXYLENE + OH = H3MXYLENE1O ;
% 2.05D-10*0.64 : H3MXYLENE + OH = H4MXYLENE + HO2;
% 2.05D-10*0.06 : H3MXYLENE + OH = H2MXYQONE + HO2 ;
% 1.00D-12 : H2MXYQONE + NO3 = NMXYQO2 ;
% 2.35D-11 : H2MXYQONE + OH = MXYQO2 ;
% 2.08D-12 : H3MXYLENE1O + NO2 = NH3MXYLENE ;
% 2.86D-13 : H3MXYLENE1O + O3 = H3MXYLENE1O2 ;
% KRO2HO2*0.859 : H3MXYLENE1O2 + HO2 = HMXCTEC1OOH ;
% KRO2NO : H3MXYLENE1O2 + NO = H3MXYLENE1O + NO2 ;
% KRO2NO3 : H3MXYLENE1O2 + NO3 = H3MXYLENE1O + NO2 ;
% 8.80D-13*RO2 : H3MXYLENE1O2 = H3MXYLENE1O ;
% 2.01D-10*0.91 : MXYCATECH + NO3 = MXCATEC1O + HNO3 ;
% 2.01D-10*0.09 : MXYCATECH + NO3 = HMXYQONE + HO2 + HNO3 ;
% 2.01D-10*0.91 : H3MXYLENE + NO3 = H3MXYLENE1O + HNO3 ;
% 2.01D-10*0.09 : H3MXYLENE + NO3 = H2MXYQONE + HO2 + HNO3 ;

Appendix C

Additional Information for Chapter 5: A Novel Analysis to Quantify Plume Crosswind Heterogeneity Applied to Biomass Burning Smoke

C.1 Derivation of GOMECH

Given two Gaussians: one with an offset (b) and width (w_i) and another with width w_{CO}.

$$Q_i = A_i e^{-\frac{(y-b)^2}{w_i^2}} \quad \text{(EC.1)}$$

$$Q_{CO} = A_{CO} e^{-\frac{y^2}{w_{CO}^2}} \quad \text{(EC.2)}$$

We have two equations and four variables (y, b, w_i, w_{CO}). We can rearrange these two equations to form one equation with three variables. We will eliminate y.

Starting with EC.1 by expanding the square.

$$Q_i = A_i e^{-\frac{y^2}{w_i^2}+\frac{2by}{w_i^2}-\frac{b^2}{w_i^2}} \quad \text{(EC.3)}$$

Where we consider the first term of the exponent in EC.3 and introduce w_{CO}^2

$$e^{-\frac{y^2}{w_i^2}} = e^{-\frac{y^2}{w_i^2}\times\frac{w_{CO}^2}{w_{CO}^2}} = e^{\frac{w_{CO}^2}{w_i^2}\left[-\frac{y^2}{w_{CO}^2}\right]} \quad \text{(EC.4)}$$

Now, take the natural log of EC.2.

$$-\frac{y^2}{w_{CO}^2} = \ln\frac{Q_{CO}}{A_{CO}} \quad \text{(EC.5)}$$

and substitute this into EC.4

$$= e^{\frac{w_{CO}^2}{w_i^2}\times\ln\frac{Q_{CO}}{A_{CO}}} = A_{CO}^{\frac{w_{CO}^2}{w_i^2}} \times Q_{CO}^{\frac{w_{CO}^2}{w_i^2}} \quad \text{(EC.6)}$$

Next, we solve for y in EC.5

$$y = \sqrt{-w_{CO}^2 \ln \frac{Q_{CO}}{A_{CO}}} = \sqrt{\ln\left(Q_{CO}^{-w_{CO}^2}\right) - \ln\left(A_{CO}^{-w_{CO}^2}\right)} \quad \text{(EC.7)}$$

Finally, we can substitute EC.6 and EC.7 back into EC.3.

$$Q_i = A_i \times A_{CO}^{-\frac{w_{CO}^2}{w_i^2}} \times Q_{CO}^{\frac{w_{CO}^2}{w_i^2}} \exp\left[\frac{2b\left[\sqrt{\ln\left(Q_{CO}^{-w_{CO}^2}\right) - \ln\left(A_{CO}^{-w_{CO}^2}\right)}\right]}{w_i^2} - \frac{b^2}{w_i^2}\right] \quad \text{(EC.8)}$$

The above result is referred to as the Gaussian Observational Model for Edge to Center Heterogeneity (GOMECH).

C.2 Mechanism of Maleic anhydride Formation

Coggon et al. 2019 show that oxidation of furan species by OH was able to explain 90% of maleic anhydride formation in laboratory biomass burning smoke. The formation of maleic anhydride by OH oxidation of furan species begins with the formation of alkene dials and hydroxy furanones (Aschmann et al., 2011, 2014; Yuan et al., 2017). For example, furan oxidizes to form 2-butenedial as well as 5-hydroxy-2(5H)-furanone.

Furan + OH → 5-hydroxy-2(5H)-furanone + 2-butenedial (RC.1)

Subsequent oxidation, or photolysis, of 2-butenedial is then expected to form maleic anhydride (Bierbach et al., 1994).

butenedial + OH → maleic anhydride (RC.2)

butenedial + hv → maleic anhydride (RC.3)

Hydroxy furanones such as 5-hydroxy-2(5H)-furanone are also likely to form maleic anhydride by reaction with OH (Coggon et al., 2019), though no studies have reported mechanisms for these species. In a study of NO_3 oxidation of 3-methylfuran, Tapia et al. determined 2-methylbutendial was one product, among many (Tapia et al., 2011). This result implies that NO_3 oxidation of furan may also form 2-butenedial and thus maleic anhydride as well, however this has not been observed previously. We find similar results when using maleic anhydride and PAN as an OH chemistry proxy. Further, a plume center box model of BB plumes sampled during FIREX-AQ suggests furan compounds are mostly (~95%) oxidized by O_3 and OH as opposed to NO_3 (Decker et al., 2021). Therefore, we expect the contribution of maleic anhydride formation from NO_3 to be negligible.

C.3 Methods of Calculating P(NO_3) Using GOMECH

We show below that the order of operations for determining the plume structure of P(NO_3) produces similar results. The order of operations option for calculating P(NO_3) is 1) using Eq. 5 in the main text to determine P(NO_3) in ppbv h^{-1} and then applying our plume structure method, or 2) applying the plume structure method to observations of NO_2 and O_3 and subsequently calculating P(NO_3) structure as the multiple of the recreated NO_2 and O_3 structures. Option 1 is likely the most accurate method of determining P(NO_3) structure and therefore this method is presented in the main text. Even so, both methods produce similar results as shown in Table C.1 and Figure C.1.

	P(NO_3)				P(NO_3) -Model		NO_2				O_3			
	w	**Center**	**Med. Res.**	**Avg. Res**	**w**	**Center**	***w***	**Center**	**Med. Res.**	**Avg. Res**	***w***	**Center**	**Med. Res.**	**Avg. Res**
Plume 1	0.39	0.59	0.13	0.17 ± 0.14	0.57	0.64	0.78	0.00	0.08	0.10 ± 0.08	0.85	1.40	0.08	0.09 ± 0.07
Plume 2	0.49	0.65	0.12	0.16 ± 0.12	0.50	0.69	0.73	0.00	0.07	0.09 ± 0.09	0.67	1.28	0.09	0.11 ± 0.10
Plume 3	0.37	0.70	0.09	0.11 ± 0.09	0.52	0.58	0.67	0.05	0.04	0.05 ± 0.05	0.82	1.36	0.11	0.12 ± 0.07

Table C.1: Fitting parameters corresponding to Figure C.1 with median and average ($\pm$ standard deviation) residuals.

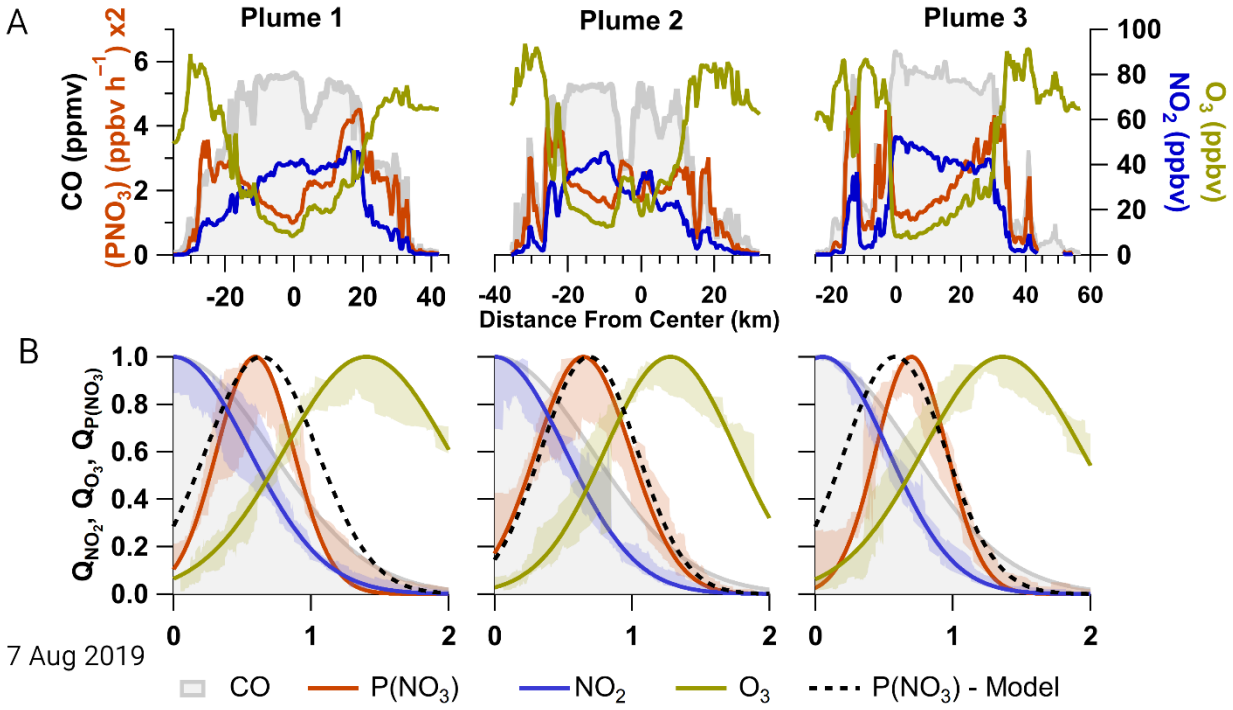

Figure C.1 Panel A: observations of CO (filled grey trace), $P(NO_3)$ (red), NO_2 (blue), and O_3 (gold) for three transects of the Williams Flats Fire sampled by the NASA DC-8. Panel B: recreated plumes using GOMECH for the observations in panel A where P(NO3) in red is calculated by E2.4 and $P(NO_3)$ in black dashes is calculated by the multiplication of the recreated shape of O_3 and NO_2. Shading indicates the average of binned residuals (normalized CO bin width = 0.004).